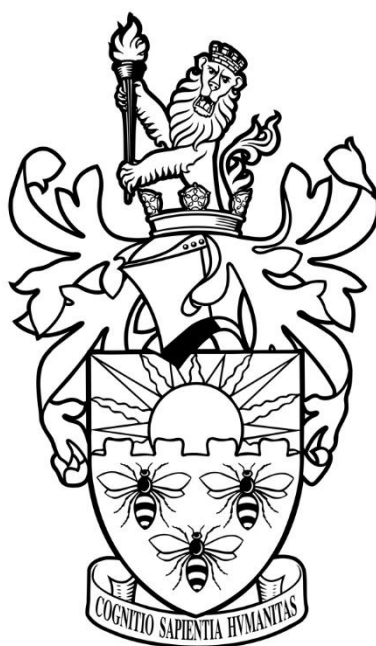


EPR Studies of Magnetic Properties of Coordination Complexes in Solid Host Matrices

A thesis submitted to The University of Manchester for the degree
of Doctor of Philosophy in the Faculty of Science and Engineering

2022



Jonatan B. Petersen

School of Natural Sciences
Department of Chemistry

Institution: University of Manchester
Faculty: Faculty of Science and Engineering
Department: Department of Chemistry, School of Natural Sciences
Degree: Doctor of Philosophy
Author: Jonatan Birch Petersen
Email: jonatan.petersen@manchester.ac.uk
Title: EPR Studies of Magnetic Properties of Coordination Complexes
in Solid Host Matrices

Main supervisor: Prof. Richard E.P. Winpenny
Co-supervisors: Prof. Eric J. L. McInnes & Dr Floriana Tuna
Word count: 27,397
Date of submission: 24-12-2022
Date of resubmission: 10-7-2023

Contents

Abbreviations and Physical Constants.....	5
Abbreviations and Acronyms	5
Physical Constants	6
Abstract.....	7
Declaration and Copyright.....	9
Declaration	9
Copyright Statement	9
Acknowledgements	11
Introduction	13
Rationale for Journal Format and Organisation of Thesis.....	14
1. Methods for Measurement and Modelling of Magnetic Relaxation Parameters	15
1.1 Introduction	15
1.2 Relaxation in EPR Spectroscopy	15
1.3 Measuring Pulsed EPR.....	17
1.4 Spin-lattice Relaxation	18
1.5 Spin-spin Relaxation.....	27
1.6 Concluding Remarks.....	33
2. Magnetic Relaxation Properties of Chromium Nitrido Complexes.....	37
2.1 Preface	37
2.2 Article	39
2.3 Supporting Information	47
3. Playing with the Field: Extending 4f Qubits Beyond Liquid Nitrogen Temperatures	63
3.1 Preface	63
3.2 Article	65
3.3 Supporting Information	73
4. Electron Paramagnetic Resonance Spectra of Pseudo-Pentagonal Bipyramidal Gadolinium Complexes.....	90

4.1	Preface	90
4.2	Article	92
4.3	Supporting Information	100
5.	Conclusions and Future Work	111
5.1	Conclusions	111
5.2	Future Work	112
	Appended Articles	113
	A. Dimerized <i>p</i> -Semiquinone Radical Anions Stabilized by a Pair of Rare-Earth Metal Ions	113
	B. Spin-Lattice Relaxation Decoherence Suppression in Vanishing Orbital Angular Momentum Qubits	136

Word count: 27,397

Abbreviations and Physical Constants

Abbreviations and Acronyms

AC	Alternating Current
CASSCF	Complete Active Space Self-Consistent Field
CF	Crystal Field
CPMG	Carr-Purcell-Meiboom-Gill
cw	Continuous Wave
DFT	Density Functional Theory
EPR	Electron Paramagnetic Resonance
ESEEM	Electron Spin Echo Envelope Modulation
FID	Free Induction Decay
Ln	Lanthanide
m_s	Magnetic spin quantum number
NMR	Nuclear Magnetic Resonance
S	Spin quantum number
SMM	Single Molecule Magnet
TWT	Traveling Wave Tube
ZFS	Zero Field Splitting
SQUID	Superconducting Quantum Interference Device
ArF ₅	Fluorinated Aryl (-C ₆ F ₅)
DCM	Dichloromethane
OTf	Triflate
Ph	Phenyl (-C ₆ H ₅)
Py	Pyridine
Pyrrdtc	Pyrrolidinedithiocarbamate
tBu	Tertbutyl
THF	Tetrahydrofuran
Tol	Toluene
Trensal	2,2',2''-tris(salicylideneimino)triethylamine)

Physical Constants

μ_B	Bohr Magneton	$9.2740100783 \cdot 10^{-24} \text{ J T}^{-1}$
h	Planck's Constant	$6.62607015 \cdot 10^{-34} \text{ J s}$
γ_e	Electron Gyromagnetic Ratio	$28024.9514242 \text{ s}^{-1} \text{ T}^{-1}$
g_e	Electron g-factor	2.00231930436256
R	Ideal Gas Constant	$8.314462618153 \text{ J K}^{-1} \text{ mol}^{-1}$
k_b	Boltzmann Constant	$1.380649 \cdot 10^{-23} \text{ J K}^{-1}$

Abstract

EPR studies of the magnetic properties of coordination complexes in solid state matrices: a thesis submitted to The University of Manchester for the degree of Doctor of Philosophy in the Faculty of Science and Engineering.

This thesis presents a collection of projects directed towards the study of metal complexes in the solid state by Electron Paramagnetic Resonance (EPR) spectroscopy. The properties investigated are related to relaxation of magnetic states of metal complexes of interest in the field of molecular magnetism and quantum information processing.

The first chapter introduces magnetic relaxation and how to measure and fit the relaxation time constants T_1 and T_m experimentally and how to model the temperature dependence of T_1 to extract information on the mechanisms of relaxation. In the second and third chapter these methods are applied, in the former to a chromium nitrido complex in order to ascertain whether its similarities to vanadyl complexes lead to similar properties, and in the latter to Gd(trensal) to understand its relaxation behaviour observed in a previous high field EPR experiment. The chromium nitrido complex is found to have the same desirable relaxation properties possessed by vanadyl: long phase memory time and room temperature quantum coherence. This could make chromium nitrido complexes a system of interest for further qubit research. The spin-lattice relaxation of Gd(trensal) is measured and linked to the direct relaxation mechanism at liquid helium temperature, the Raman mechanism below liquid nitrogen temperature and local mode processes at high temperature. In addition, the long phase memory time from high field EPR is explained by the spin polarization of the lattice making the phase memory time field dependent.

The fourth chapter focuses on cw EPR measurements of the zero field splitting (ZFS) in a series of Gd(III) complexes with near pentagonal bipyramidal coordination spheres, to understand how ZFS relates to geometry and crystal field (CF) strength in this seldom encountered symmetry. An inverse relationship between size of the ZFS and the CF strength of the axial ligands is established and this is extended to a correlation with the barrier for reversal of the magnetic moment (U_{eff}) of the analogous Dy(III) single molecule magnets.

Jonatan Birch Petersen

December 2022

This page is intentionally left blank

Declaration and Copyright

Declaration

No parts of this thesis have been submitted in support of an application for another degree or qualification of this or any other university or other institute of learning. The contribution of the author of this thesis to each manuscript is outlined in the preface.

Copyright Statement

The author of this thesis (including any appendices and/or schedules to this thesis) owns certain copyright or related rights in it (the “Copyright”) and they have given the University of Manchester certain rights to use such Copyright, including for administrative purposes.

Copies of this thesis, either in full or in extracts and whether in hard or electronic copy, may be made **only** in accordance with the Copyright, Designs and Patents Act 1988 (as amended) and regulations issued under it or, where appropriate, in accordance with licensing agreements which the University has from time to time. This page must form part of any such copies made.

The ownership of certain Copyright, patents, designs, trademarks and other intellectual property (the “Intellectual Property”) and any reproductions of copyright works in the thesis, for example graphs and tables (“Reproductions”), which may be described in this thesis, may not be owned by the author and may be owned by third parties. Such Intellectual Property and Reproductions cannot and must not be made available for use without the prior written permission of the owner(s) of the relevant Intellectual Property and/or Reproductions.

Further information on the conditions under which disclosure, publication and commercialisation of this thesis, the Copyright and any Intellectual Property and/or Reproductions described in it may take place is available in the University IP Policy (see

<http://documents.manchester.ac.uk/DocuInfo.aspx?DocID=24420>), in any relevant Thesis

restriction declarations deposited in the University Library, the University Library’s regulations (see

<http://www.library.manchester.ac.uk/about/regulations/>) and in the University’s policy on

Presentation of Theses.

This page is intentionally left blank

Acknowledgements

First of all, I would like to thank my supervisors Prof. Richard E. P. Winpenny, Prof. Eric J. L. McInnes and Dr Floriana Tuna for their helpful advice and also for their patience, especially Richard for spending part of his ERC grant on giving me the chance to study in Manchester.

I owe my gratitude to our technician Adam Brookfield for his practical help with EPR measurements. Without his dedication to his work this thesis would not have been possible.

Since I did not synthesise any of the molecules that I studied, I would like to recognize Dr Christian D. Buch, Dr Kexin Yu, Dr You-Song Ding, Dr Tian Han, Dr Ying-Zhao Ma, Dr Vijay Parmar, Prof. Jesper Bendix and Dr Aurelien Willauer for making samples for me, both those that amounted to gorgeous EPR spectra and those that did not amount to anything.

I am grateful to my collaborators Prof. Jesper Bendix, Dr Stergios Piligkos, Dr Marinella Mazzanti, Prof. Ramaswamy Murugavel and Prof. Yan-Zen Zheng for giving me the chance to work with some of their compounds, notably Stergios whose idea it was that I should go to Manchester in the first place.

I would like to thank Prof. Nick Chilton, Dr Marcus Giansiracusa and Dr Jon Kragoskow for helping me with CAS-SCF calculations, even though none of them made it into my thesis. Marcus also for introducing me to the practical and theoretical setup I used in my early thesis work and for inviting me to join the School of Materials Squash Club, a club I grew very committed to. Jon also deserves extra thanks for introducing me to people and places during my early days in Manchester and for always being ready for some good banter over a pint. I will forever remember his willingness to help a friend in need.

I would also like to thank the post docs Dr Ivana Borilovic, Dr Luisa Ciano and Dr Selena Lockyer who helped me with guidance and friendly advice.

Edmund J. Little deserves special thanks for his personal example of what a real EPR spectroscopist should be and his great sense of humour. Ed was ever the one asking the right questions and sometimes the wrong ones as well.

This thesis is the culmination of almost four years of work at the University of Manchester. I have enjoyed this time in large part due to some of the brilliant people that I have worked with. Of these I would particularly like to thank Daniel Martins, Diana Kuzmina, Thomas Hajdu, Dr Lydia Nodaraki and Dr Alena Sheveleva for brightening my life with their friendship during the lockdowns of 2020 and 2021 and for making everyday life in the office a joy. This is also true of my TNP friends Nathan,

Dave, Lou, Jon, Bern, Andy, Seona and George who kept my spirits up with an online community during lockdowns.

I must acknowledge the support I have had from my family, particularly my mother for sending me care packages, all throughout my time in Manchester, to keep me from being too homesick.

Last, but not least, I need to thank partner Naomi for putting up with me and encouraging me even when I was most lost in my work.

Jonatan Birch Petersen

December 2022

Introduction

The aim of this project is to further the understanding of the electronic structure and relaxation in magnetic molecules using Electron Paramagnetic Resonance (EPR) spectroscopy.

EPR spectroscopy is a powerful experimental technique for investigating magnetic properties of magnetic molecules. Continuous wave (cw) EPR can tell us about the static magnetic properties such as ground state compositions, zero field splitting and magnetic couplings such as exchange and dipolar interactions with other electrons and nuclei in its surroundings. Pulsed EPR has several advantages to cw EPR. It is time resolved, which adds a new dimension, and the possibility of combining several pulses of different length and intensity leads to a multitude of techniques able to probe relaxation times and magnetic couplings with better sensitivity and resolution than cw EPR.

The field of molecular magnetism has split into two main branches each focused on one of two envisioned applications. The first is using the magnetization of Single Molecule Magnets for data storage, which would reduce the space taken up by current data storage technologies by orders of magnitude. The second is the use of molecular spins for spintronics and in particular as quantum bits (qubits), the logical units of quantum computers.

In the Single Molecule Magnetism (SMM) branch EPR often falls short as a technique for a number of reasons: the large energy barriers needed to retain magnetization means that energy levels are too far apart to be excited by microwaves, hence we can only observe transitions within ground state doublets or pseudo doublets. Since the selection rules for these EPR transitions are related to the mixing of the states which also allows the relaxation mechanisms that we are attempting to limit, transition probability in a good SMM is low. Last but not least, a long relaxation time does not work well with a technique where the signal is proportional to the population difference between the two resonant levels, as this means that if there is any transition probability at all the signal will saturate rapidly. All this makes SMMs bad subjects for EPR samples in most cases.

Molecular qubits, on the other hand, are prime subjects for EPR experiments and magnetic resonance has even been suggested as the way to address qubits in the implementation of a quantum computer. The main challenges for molecular qubits are their relatively short-lived quantum coherence, on the order of microseconds, a property related to the relaxation times measured by pulsed EPR.

In this thesis both cw and pulsed EPR has been used in projects in both branches of molecular magnetism. This is carried out by measuring relaxation properties of qubit candidates and by

linking static magnetic properties of EPR active analogues to SMMs to the relaxation of the SMMs themselves.

By studying the magnetic relaxation behaviour of metal complexes we will investigate: if chromium nitrido complexes are equally interesting as their widely used vanadyl counterparts in qubit research, if the cause of the long coherence times measured for gadolinium trensal complexes at high field is an inherent property and if the zero field splitting of gadolinium complexes with pseudo 5-fold symmetry can be modelled according to their idealised point groups.

Rationale for Journal Format and Organisation of Thesis

This thesis is written in journal format. This was chosen to avoid rewriting articles that were already being prepared for publication. The overarching theme of the thesis is EPR spectroscopy and the magnetic relaxation of coordination complexes in the solid state. Chapter 1 is a review of the theory of magnetic relaxation measurements, a relevant topic for Chapter 2 and 3, written as a primer for students starting a project in the field. Chapters 2, 3 and 4 are written as self-contained articles ready for individual publication and typeset using the submission template for the American Chemical Society journals. Before each of the three articles is a short preface, introducing the article topic, its connection to the thesis theme and the contributions of the authors. Chapter 5 contains a summary of the principal findings of the work presented in the previous chapters and outlines future work.

At the end of the thesis two articles are appended. The first is a communication article I co-authored in my first year as a side project sparked from the original focus of my PhD work, which was on the magnetic interactions in lanthanide dimers. The article is therefore not directly linked to the main theme of this thesis.

In the second appended article I had no direct involvement. Chapter 3 is written as a follow up to this article and it was therefore prudent to supply it with the thesis.

To avoid copyright issues, these already published articles are presented as their last drafts resubmitted to the editor after changes requested by the reviewers.

The format of the articles in this thesis was chosen because Chapter 2 and 4 are to be submitted to the ACS journal *Inorganic Chemistry* and the two articles attached at the end are already published in *Inorganic Chemistry* and *Journal of the American Chemical Society* respectively, both ACS journals.

1. Methods for Measurement and Modelling of Magnetic Relaxation Parameters

1.1 Introduction

Each manuscript in the following chapters contain a short review in their introduction of relevant literature and previous works. This chapter contains a short review of methods for the measurement and modelling of EPR relaxation data. This topic has been reviewed extensively in the literature and this is not to be taken as a comprehensive review.¹⁻³ Rather it is an introduction to the main theory needed to obtain numbers for and understand the significance of the two magnetic relaxation characteristics, the longitudinal (spin-lattice) and the transverse (spin-spin) relaxation times, T_1 and T_2/T_m respectively and their underlying mechanisms. With this aim in mind this chapter introduces and describes the main mechanisms of relaxation in solid state matrices as well as methods for modelling the temperature dependence of T_1 . The chapter is written for novice spectroscopists but does assume that the reader has a basic understanding of cw EPR and its terminology.

1.2 Relaxation in EPR Spectroscopy

Relaxation refers to the physical phenomenon, where a perturbed system will seek a return to equilibrium. In the context of magnetism, the system consists of spins, and the relaxation is the returning of the equilibrium distribution in their magnetic levels.

When an unpaired electron is placed in a magnetic field, the z-component (m_s) of intrinsic magnetic moment (spin) will either align with ($m_s = -1/2$) or against ($m_s = +1/2$) the magnetic field vector B_0 and start precessing around it at a rate ω_0 . In an ensemble a small surplus of the magnetic moments will align with the field, this gives rise to magnetization of the system described by the vector M . If you define a coordinate system with the x- and y-axes rotating around the z-axis at a rate of ω_0 (rotating frame), M with components M_x , M_y and M_z can be visualised in the Bloch sphere as shown in Figure 1. The equilibrium magnitude of M_z (M_0) is determined by the field, and the absence of a field along x_R or y_R means that the phases of the individual magnetic moments are evenly distributed and $M_x, M_y = 0$.

When a resonant microwave ($\omega_{mw} = \omega_0$) perturbs this system, the magnetic moments will also start precession around the magnetic field of the microwave, B_1 , flipping the magnetization of the system proportional to the length and power of the pulse. If the phase of the microwave is such that B_1 lies along x_R , M will be flipped towards -z through + y_R . we refer to microwave pulses by their flip angle, a π -pulse will result in M along -z and a $\pi/2$ -pulse will result in M along y_R .

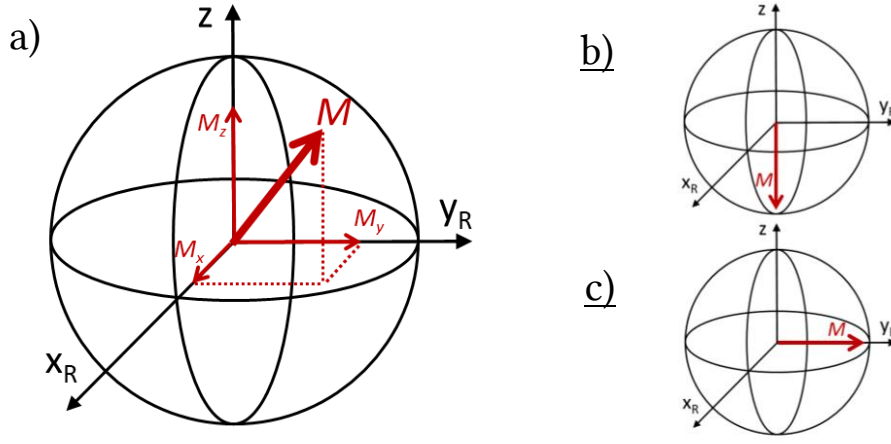


Figure 1. Bloch sphere visualisation of the magnetization vector M a) in an arbitrary orientation with the definition of M_z , M_y and M_x b) after a π -pulse and c) after a $\pi/2$ -pulse.

The fact that the pulse causes $M_y \neq 0$, means that the individual magnetic moments are precessing in the same phase. This is referred to as coherence.

After a pulse the magnetization is now in a perturbed state and will seek equilibrium again, by realigning with the field and losing coherence. That means M_z will go towards M_0 and M_y and M_x will go towards 0, as described by the Bloch equations.^{4,5}

$$\begin{aligned}
 \frac{dM_x}{dt} &= \gamma_e (M_y B_z - M_z B_y) - \frac{M_x}{T_2} \\
 \frac{dM_y}{dt} &= \gamma_e (M_z B_x - M_x B_z) - \frac{M_y}{T_2} \\
 \frac{dM_z}{dt} &= \gamma_e (M_x B_y - M_y B_x) + \frac{(M_0 - M_z)}{T_1}
 \end{aligned} \tag{1}$$

where γ_e is the gyromagnetic ratio of the electron and B_x , B_y and B_z are the magnetic field along x_R , y_R and z . A graphical depiction of the development of the magnetization in time is shown in figure 2. From these equations we get the time constants, T_1 and T_2 , describing the relaxation of the magnetization in time. T_1 is the longitudinal relaxation time of M_z towards M_0 and T_2 is the transverse relaxation time of M_{xy} toward 0. Obtaining these two parameters is the focus of this chapter.

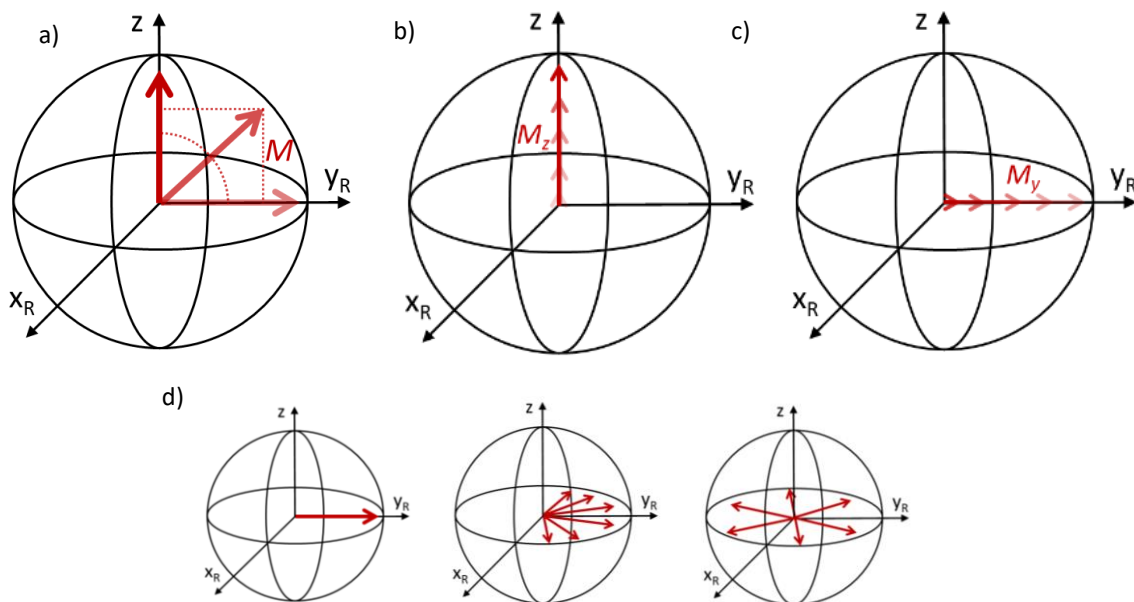


Figure 2. Graphical depictions of relaxation on the Bloch sphere a) Relaxation of the magnetization. b) Relaxation of the magnetization along the z-axis. c) Relaxation of the magnetization along the y_R -axis (bottom). d) Decoherence of the magnetization in the xy-plane. The shading of the arrows indicates the evolution of M_z or M_y in time.

1.3 Measuring Pulsed EPR

Pulsed EPR signal is detected as the magnetization along either x_R or y_R caused by a microwave pulse. Signal is measured in one of two ways either as a Free induction Decay (FID), the direct magnetic response after a pulse, or as an echo.

Since the EPR signal comes from the magnetization in the xy-plane, pulsed EPR can only be measured as long as coherence lasts. This contrasts with cw EPR where signal is detected as the reflected intensity of a standing microwave essentially measuring absorption. The cw experiment thus works as a steady state experiment, where the signal is not linked to the coherence time.

The FID is the decay of the magnetization in the xy-plane in the time after a resonant microwave pulse. The problem with measuring this is that after a pulse there is a time where the leftover power of the pulse dissipates (since the pulse is not perfectly square). During this time no signal can be measured and hence it is referred to as the deadtime. During the deadtime the magnetization will relax and the intensity of the FID after the deadtime is usually very low. To address this problem echo detection is used to obtain more signal intensity.

A spin echo (Hahn echo) occurs after the magnetization is flipped 90° by a $\pi/2$ -pulse to the xy plane, creating coherence, the individual magnetic moments will then precess at their individual Larmor frequencies around the field. The magnetic moments are then flipped 180° by a π -pulse after time, τ , and will keep precessing at their own rates until they meet after 2τ and an echo is

observed. The two-pulse Hahn echo sequence is shown in Figure 3 along with an illustration of the development of the magnetic moments during the sequence.

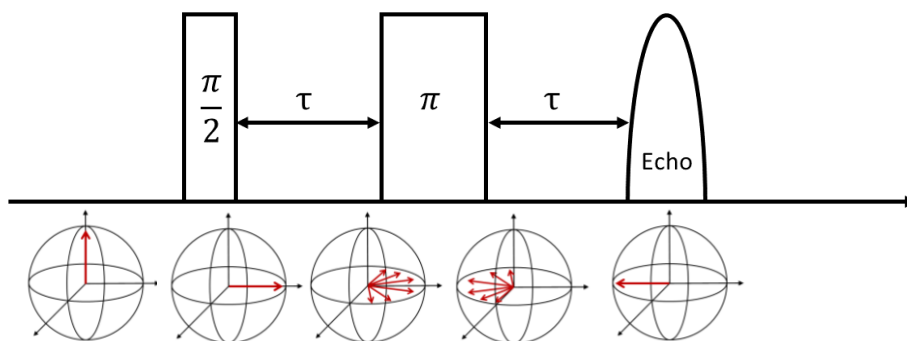


Figure 3. The Hahn echo pulse sequence and vector depiction of the orientation of the magnetization during the sequence

1.4 Spin-lattice Relaxation

Spin-lattice relaxation or longitudinal relaxation is the return of the magnetization to equilibrium along the z-axis as shown in Figure 2a. This happens through interactions between the excited **spins** and the surrounding **lattice**. The time dependence of spin-lattice time dependence is described by T_1 as derived from the Bloch equations (equation 1). This section introduces basic experiments and fitting methods to obtain T_1 and how to fit its temperature dependence to a number of different mechanisms contributing to spin-lattice-relaxation.

1.4.1 Measurement of Spin-lattice Relaxation with EPR

There are several ways to measure T_1 . This section outlines some of the most common and useful methods, though other more exotic methods as well as other versions of those presented do exist. Apart from EPR the most common way to determine T_1 is AC magnetic susceptibility measurements, but this falls beyond the scope of this chapter. We note that T_1 is the relaxation measured for “single molecule magnets”.

1.4.1.1 Saturation Recovery

The intensity of the signal in EPR is dependent on the population difference between the initial and the resulting state of the transition. Saturation happens when the population of the two states get close to equality, and the degree of saturation is described by the saturation factor.

$$S = \frac{1}{1 + \gamma_e^2 B_1^2 T_1 T_2} \quad (2)$$

where γ_e is the gyromagnetic ratio and B_1 is the magnetic field of the pulse. A low saturation factor results in loss of signal. This can be exploited to measure T_1 , since the rate of the signal returning

after **saturation** will be dependent on the **recovery** of the population difference, giving name to the technique: Saturation Recovery.

Saturation recovery can be performed either as a cw or pulsed experiment, detected by a two-pulse echo. In cw the saturation is done by a long “pulse” at high power and the signal detected by cw microwaves at low power to not further saturate the system.⁶ The cw experiment has two advantages, that the saturating pulse can be as long as necessary to get rid of spectral diffusion (see the section on fitting T_1 data) and that it can be performed even when T_2 is too short for detecting an echo. The drawback is that, in order not to notably influence relaxation, the detection microwave must be weak, and the experiment is unmodulated, causing low sensitivity.

Furthermore, most pulsed spectrometers are simply not able to do this experiment due to the limitations of the pulsed TWT amplifier.

The echo detected saturation recovery pulse sequence is shown in Figure 4, first a long low-power pulse saturates the system, then a Hahn-echo sequence picks up the saturated echo, by changing the distance between the saturating pulse and the detection sequence a saturation recovery curve appears. The advantage of pulsed saturation recovery over cw is higher sensitivity as long as T_2 is long enough for an echo to be observed. The drawback is that the data contain spectral diffusion, since amplifiers cannot make pulses long enough to eliminate it. Spectral diffusion can, to some degree, be removed by using several saturation pulses in quick succession.

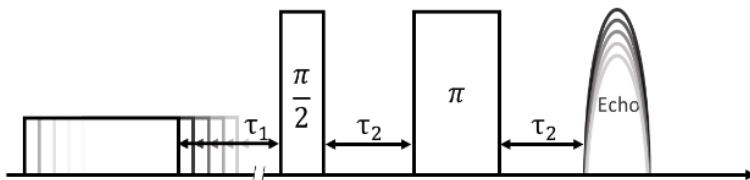


Figure 4. Pulse sequence for echo detected saturation recovery

1.4.1.2 Inversion Recovery

Inversion recovery is the other main method for measuring T_1 . Instead of saturating the system, the first pulse is a π -pulse inverting the magnetization, which is then left to relax for a time, τ_1 , after which the signal is detected by a Hahn echo sequence, as depicted in Figure 5. When τ_1 is shorter than T_1 the echo will be inverted. With longer τ_1 the system relaxes further, and the echo intensity goes from negative to positive and increases until τ_1 is long enough for the magnetization to have relaxed fully between the first pulse and the Hahn echo sequence.

Inversion recovery is easier and faster to set up and measure than saturation recovery, but the recorded recovery curve includes spectral diffusion, and this method has no way to mitigate this.

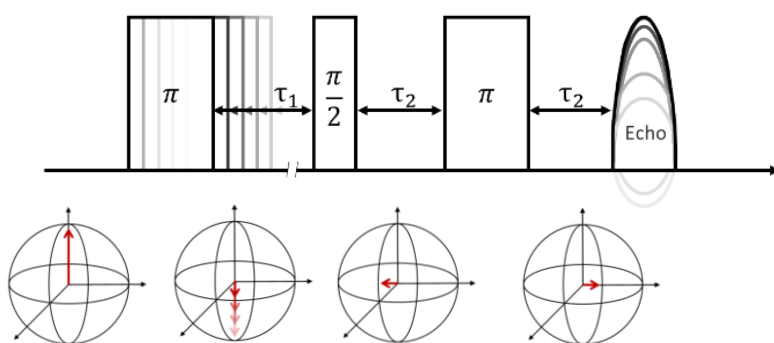


Figure 5. Pulse sequence for echo detected Inversion recovery with depiction of magnetization vectors in the rotating frame.

As in NMR, Inversion recovery could also be performed as a two pulse experiment with FID detection (π - τ_1 - $\pi/2$ -FID) if T_2 is long enough, though this is usually less sensitive than Echo detection.

1.4.1.3 Echo Repetition Rate

Most pulsed spectrometers have a limitation on the maximum length of a pulse sequence, which limits the maximal length of T_1 they can measure.

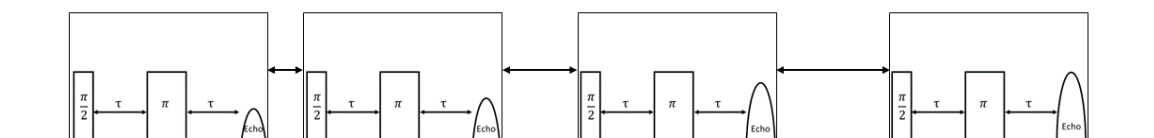


Figure 6. Pulse sequence for the echo repetition rate experiment.

In this situation T_1 can be determined by repeating a two-pulse spin echo sequence with varying repetition rates. If an echo sequence comes close after another some of the magnetization will not have recovered, resulting in loss of signal. The relaxation rate can then be measured by monitoring the echo intensity as a function of the repetition rate as illustrated in Figure 6. This method is good if spin lattice relaxation is very slow, but it is time consuming and yields few datapoints.

1.4.1.4 Phase Cycling

When measuring pulsed EPR with multiple pulses one must be aware that apart from the desired signal, other echoes and FIDs might occur. Each pulse creates an FID, each pair of pulses an echo and each pulse after an echo a refocused echo. Thus, an inversion recovery sequence creates 4 extra echoes at different times. As τ_1 is varied some of these unwanted echoes might come to overlap with the monitored echo causing variations in the intensity. The changes to the inversion recovery curve are rarely severe, but to get an accurate measure of T_1 any distortions should be removed. This is done by cycling the phase of the pulses to average out the effect of the other

echoes. Usually a 4-step phase cycle where the experiment is repeated 4 times with the phase of two of the pulses different in each step. The standard phase of a pulse is +x and so a phase cycling scheme could look like step 1: +x +x +x, step 2: -x +x +x, step 3: +x -x +x and step 4: -x -x +x.

1.4.2 Fitting T_1 Data

The solution to Bloch's differential equations is an exponential function and the data recorded with saturation or inversion recovery ideally fit the function

$$I = I_0 + k \cdot e^{-\left(\frac{\tau_1}{T_1}\right)} \quad (3)$$

where I is the intensity of the signal, I_0 is the intensity of the signal when fully relaxed, k is a negative scaling constant and τ_1 is the time from saturation or inversion until detection. This function sometimes fits the data poorly. This happens when the relaxation is not the only source for the loss of signal. Apart from relaxation, spectral diffusion is the other main contributor. Spectral diffusion is the term used for processes that move spins off resonance without relaxing e.g. a neighbouring spin being excited by the same microwave and changing the resonance frequency through dipolar coupling or a molecular movement changing the energy levels or the orientation of the paramagnet. The effect of spectral diffusion on the curvature of the recorded T_1 data is exemplified in Figure 7.

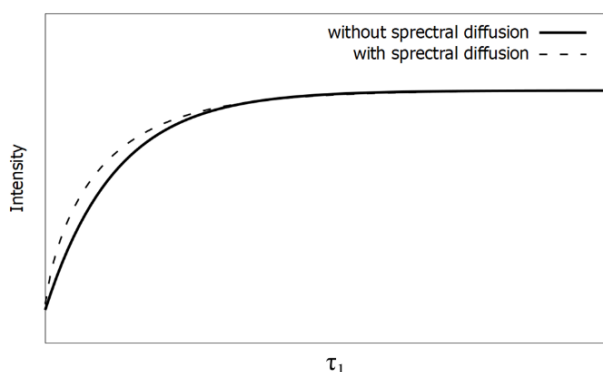


Figure 7. Examples of saturation or inversion recovery curves with and without spectral diffusion.

Spectral diffusion can have a significant effect at low temperature when relaxation is slow.

To fit data with spectral diffusion a stretched exponential is often used.

$$I = I_0 + k \cdot e^{-\left(\frac{\tau_1}{T_1}\right)^{\beta_1}} \quad (4)$$

where the exponential is stretched by the parameter β_1 , representing the spectral diffusion.

The value of β_1 is lower than 1 when spectral diffusion influences the signal and 1 when it does not. Typical values lie at around 0.7 at low temperature.⁷ When β_1 is very low, precise values of T_1 becomes harder to fit as β_1 dominates the curvature. Another way of fitting data with spectral

diffusion is to treat it as a separate relaxation process with its own distinct relaxation rate T_{1f} . This is done with a bi-exponential function

$$I = I_0 + k_1 \cdot e^{-\left(\frac{\tau_1}{T_1}\right)} + k_2 \cdot e^{-\left(\frac{\tau_1}{T_{1f}}\right)} \quad (5)$$

where the first term describes the relaxation of the magnetic moment and the second the spectral diffusion. The bi-exponential function is also used when two competing relaxation processes are observed.

1.4.3 Spin-lattice Relaxation Mechanisms and the Temperature Dependence of T_1

For the excited spins to transition back to the ground state, they need to exchange some energy with the surroundings. Spin-lattice relaxation has its name from the fact that this energy is transferred between the spin and the lattice vibrations, known as phonons. Phonons are vibrations of the lattice and do not in themselves have an electric or magnetic moment and thus are not able to interact with the magnetic states of electrons directly, but the lattice is full of nuclei and other unpaired electrons that will be displaced by vibrations of the lattice. Phonons can also deform the electric field (crystal field) acting on the orbital angular momenta, which are in turn interacting with the spin angular momentum through spin-orbit coupling. These effects combined leads to the interaction known as spin-phonon coupling, which is responsible for the energy transfer between electrons and phonons. Spin lattice relaxation occurs by several different mechanisms, direct transitions by absorption and emission of phonons (direct mechanism), or via different kinds of excited states (Raman, Orbach and local mode mechanisms). Due to the number possible mechanisms, it is often left to the scientist to decide which ones are relevant, depending on other knowledge about the system in question. Some are used more often than others e.g. the Direct, Raman and Orbach processes along with quantum tunnelling are encountered more often in the literature of single molecule magnets. In this section the most important mechanisms are presented.

1.4.3.1 Direct Mechanism

The simplest mechanism is the direct mechanism, where a single phonon is exchanged with the lattice to transition directly between two spin states.⁸ The frequency of the phonon must match the energy difference between the levels (frequency as the exciting microwave), Figure 8 shows a depiction of the transition.

For half integer spins (Kramers system) the two states in question are degenerate in the absence of a magnetic field, hence there is no energy difference and so, no energy can be exchanged to

transition between the states. The transition probability is therefore proportional to the energy splitting between the two states. The energy splitting in EPR is proportional to the field and so the relaxation rate becomes field dependent. For an integer spin (non-Kramers system) the relaxation rate is also field dependent, but to a lesser extent.⁹

The relaxation rate of the direct process is usually expressed with equation 6.

$$T_1^{-1} = A_{dir} \cdot T \cdot B^n \quad (6)$$

where A_{dir} is a parameter used for fitting, T is the temperature, B is the magnetic field and n is a constant, $n=4$ for a half-integer spin and $n=2$ for an integer spin.⁹

A_{dir} incorporates the transition probability and the spin-phonon coupling. As stated above only phonons of a relevant frequency can be involved in the direct process, A_{dir} is therefore often small compared to the probabilities of the other relaxation mechanisms. In the literature the temperature dependence of the direct process is often measured at a single field position, and the field dependence is often ignored leading to an A_{dir} constant incorporating B^n .

The field dependence of direct relaxation arises from the fact that the transition probability of the spin-phonon transition is proportional to the energy splitting between the initial and final state to the n th power (ΔE^n), which is substituted with Zeeman splitting, $((g\mu_B B)^n)$.¹⁰ In EPR the resonance condition is that the splitting is equal to the microwave energy ($g\mu_B B = h \cdot \omega_{mw}$) and equation 6 can thus be rewritten as

$$T_1^{-1} = A_{dir} \cdot T \cdot \omega_{mw}^n \quad (7)$$

where A_{dir} means the same as in equation 6, but with different units. This means that at the same microwave frequency the direct process in EPR is independent of the field position.

In the situation where the resonant phonons are unable to transfer the energy from the relaxing spin to other phonons rapidly, this step then becomes rate determining, forming a phonon bottleneck and the temperature dependence becomes $T_1^{-1} \propto T^2$.¹¹

The Direct mechanism is mainly relevant at low temperatures, because of the first order temperature dependence.

1.4.3.2 Raman Mechanism

The Raman relaxation process is a two-phonon relaxation process, where a phonon is inelastically scattered and the spin transitions either directly (first order) or via a virtual state (second order) to transition between the spin states. The mechanism takes its name from the similarity to Raman

scattering of light, but with phonons rather than photons. The phonons included can be any pair with an energy difference matching the energy between the initial state and the final state. This means that the Raman process is almost always of significance apart from at very low temperatures. In the second order Raman mechanism transitions go through a so-called virtual excited state, that is, a superposition of lattice vibrational modes. The Raman relaxation rate as a function of temperature is written as:⁸

$$T_1^{-1} = A_{Ram} \cdot \left(\frac{T}{\theta_D}\right)^n \cdot J_{n-1}\left(\frac{\theta_D}{T}\right) \quad (8)$$

where A_{Ram} is a parameter encompassing amongst other things the transition probability and θ_D is the Debye temperature, the temperature at which all phonon modes of the lattice are active, θ_D is used as a parameter, n is a constant that is either 9 for a Kramers system or 7 for a non-Kramers system. J_{n-1} is the transport integral defined as¹²

$$J_{n-1}\left(\frac{\theta_D}{T}\right) = \int_0^{\frac{\theta_D}{T}} (x)^{n-1} \cdot \frac{e^x}{(e^x - 1)^2} dx \quad (9)$$

The transport integral is constant when $T \ll \theta_D$, but when $T \geq \theta_D$ it follows $J_n\left(\frac{\theta_D}{T}\right) \propto T^{1-n}$, which leads the temperature dependence of the Raman process rate to be proportional to

$$T_1^{-1} = A_{Ram} \cdot \left(\frac{T}{\theta_D}\right)^n \cdot J_{n-1}\left(\frac{\theta_D}{T}\right) \propto T^n \cdot T^{1-(n-1)} = T^2 \quad (10)$$

at high temperature.

The full expression for the Raman rate is often reduced to the simplified version

$$T_1^{-1} = C \cdot T^n \quad (11)$$

where both c and n are completely phenomenological parameters.⁹

It was suggested early on that the rate of second order Raman relaxation was field dependent and would diminish with increased field, though it is rarely modelled as such.¹³ A transition diagram of the two types of Raman relaxation is shown in figure 8.

1.4.3.3 Orbach Relaxation

The Orbach process is a two-phonon process, where first a phonon is absorbed, exciting the spin into a higher lying m_s state, then another phonon is emitted to relax to the ground state, as shown in figure 8.¹⁴ The need for an intermediate m_s state means the Orbach process is only possible for spins with $S > 1/2$.

The intermediate excited m_s state works as a transition state and the temperature dependence of the Orbach relaxation rate follows the Arrhenius law.

$$T_1^{-1} = A_{Orb} \cdot e^{(\Delta_{orb}/k_b T)} \quad (12)$$

where A_{Orb} is a parameter incorporating the transition probabilities between the states, Δ_{orb} is the energy of the intermediate m_s state and k_b is the Boltzmann constant.

If Δ_{orb} is larger than θ_D relaxation via Orbach is only possible if there are other intermediate m_s states in between with energy differences lower than θ_D . Orbach relaxation then proceeds via a stepwise relaxation process. The relaxation rate still follows Arrhenius law, but is now limited, by the step with the lowest transition probability.

In molecular magnetism Δ_{orb} is to some extent considered a key descriptor of the performance of a single molecule magnet. It is often referred to as the effective barrier to reversal of the magnetic moment or the anisotropy barrier and usually denoted Δ_{eff} or U_{eff} .

1.4.3.4 Local Modes

Spin lattice relaxation can also go through molecular vibrations. A local mode can be excited by a phonon and relax by emitting another phonon, with a difference in energy corresponding to the difference between the starting and initial spin state, as depicted in the transition diagram in figure 8.¹⁵

Local mode relaxation is mainly seen in metal complexes where the vibrations can interact with the orbital angular momentum, by distorting the ligand field. The interaction with the spin goes through spin-orbit coupling and so it has also been found that local mode relaxation is more efficient in metal complexes with larger spin-orbit coupling.¹⁶

$$T_1^{-1} = A_{loc} \cdot \left(\frac{e^{\Delta_{loc}/T}}{(e^{\Delta_{loc}/T} - 1)^2} \right) \quad (13)$$

where A_{loc} is a parameter including the amplitude of the normal mode and its interaction with the spin. Δ_{loc} is the energy of the normal mode.

Relaxation via local modes is typically only relevant at high temperature.

1.4.3.5 Thermally activated processes

Relaxation can be facilitated by random rotational and librational motions of coupled spins.¹⁷ A vibration or oscillation affects relaxation if its frequency comes close to the resonant microwave frequency, this is sometimes referred to as thermally activated processes. In the literature of NMR, spin lattice relaxation from these processes is modelled with spectral density functions of the form.

$$T_1^{-1} = A_{therm} \cdot \left(\frac{2\tau_c}{1 + \omega^2\tau_c^2} \right) \quad (14)$$

where A_{therm} is a parameter, τ_c is the correlation time of the perturbing motion and ω is the Larmor frequency of the resonant spin. τ_c is defined by an Arrhenius law

$$\tau_c = \tau_c^0 e^{E_a/T} \quad (15)$$

Where E_a is the activation energy of the motion and τ_c^0 is the pre-exponential factor (the correlation time as T approaches infinity).

This mechanism is largely irrelevant in frozen solutions and crystalline solids, since in the solid-state vibrations are mostly ordered. There are however some exceptions.¹⁶ If the molecule contains parts that can rotate in the solid state, such as methyl or amino groups, their rotational frequency can come close to ω at high temperature and cause relaxation. When a frozen solution gets close to its melting point, it starts to soften and relaxation via randomized motions needs to be considered.

The thermally activated processes are, as the name suggests, only relevant at high temperature.

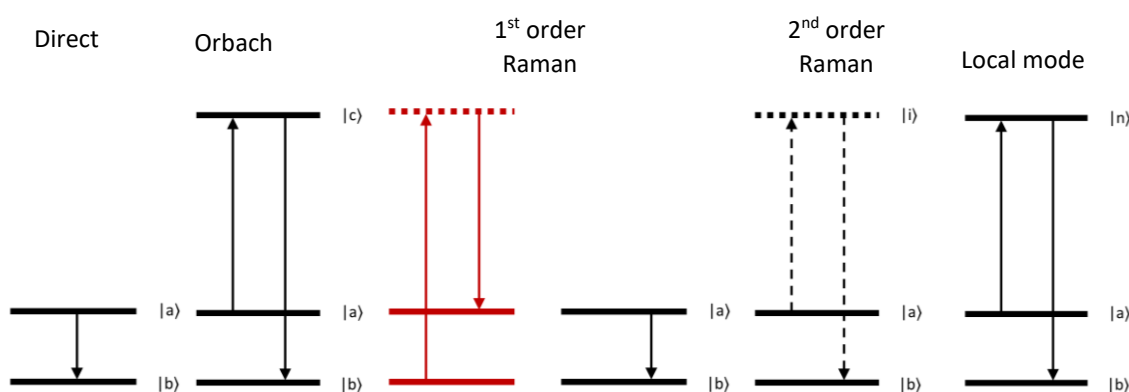


Figure 8. Schematic depiction of the transitions involved in different relaxation mechanisms. $|a\rangle$ and $|b\rangle$ are the spin states involved in the EPR transition, $|c\rangle$ is an intermediate spin state, $|i\rangle$ is a virtual state and $|n\rangle$ is an excited vibrational state. Lines in red are transitions and states of the phonon spectrum and dashed lines are virtual states and transitions.

1.4.3.6 Tunnelling phenomena

In SMMs (i.e. $S > \frac{1}{2}$) tunnelling phenomena are responsible for relaxation at low temperature and low field. Quantum tunnelling of the magnetization is allowed when levels are interacting at avoided level crossings.¹⁸ Tunnelling is not a spin-lattice relaxation mechanism as such, as the transition is made without exchanging energy with the surroundings. This means that the larger the gap is between the levels, the less tunnelling is allowed, which makes it largely irrelevant in relaxation measured by EPR.

1.5 Spin-spin Relaxation

T_2 is the transverse relaxation, that is, the relaxation of the magnetic moment in the xy-plane perpendicular to the z-axis defined by the external magnetic field. It is called spin-spin relaxation since most of the mechanisms leading to decoherence work through interactions with other spins. T_2 is critical to many EPR experiments as it limits the maximum time between pulses if coherence is to be maintained. Long coherence is a prerequisite for quantum computing and specified by the third DiVincenzo criterion, the set of criteria that define the necessary set of properties that are needed for the physical implementation of a qubit.¹⁹ This makes coherence time a main figure of merit in the literature on molecular qubits.

1.5.1 Measuring Spin-spin Relaxation

This section presents the most common ways to measure T_2 in the literature: Linewidths of cw spectra, the Free Induction Decay, Echo decay and CPMG sequences.

1.5.1.1 cw Linewidths

Linewidths are dependent on T_2 and before the advent of time resolved EPR T_2 was estimated from the linewidths observed in cw EPR spectra. If T_2 is the dominant contributor to the linewidth in a cw experiment the two are related by the equation.

$$\Delta B_{pp} = \frac{2}{\sqrt{3}\gamma_e T_2} \quad (16)$$

where ΔB_{pp} is the peak to peak linewidth illustrated in Figure 9 and γ_e is the gyromagnetic ratio of an electron.

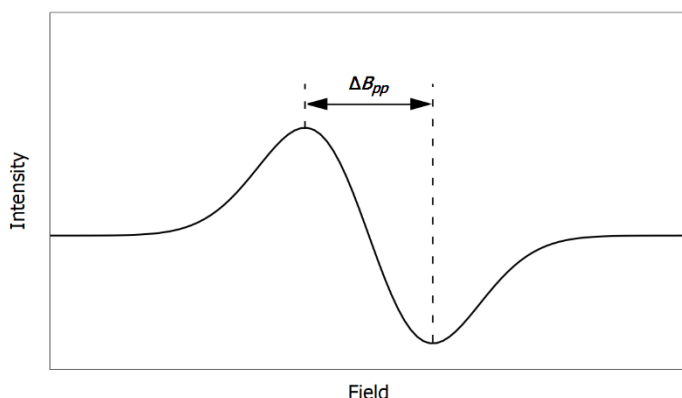


Figure 9. Illustration of peak to peak linewidth in cw EPR.

cw linewidths are more complicated than this, however. Unresolved hyperfine interactions, parameter strain, field inhomogeneity and saturation all add to the linewidth. For this reason, values obtained by this method are usually not accurate.

1.5.1.2 Free Induction Decay

In theory it is possible to measure T_2 from the free induction decay (FID). The FID experiment is the simplest possible pulsed EPR experiment and it can sometimes provide the whole of the spectrum as well as T_2 . In NMR this is a standard experiment and all it requires is a single pulse. The experiment measures decay of the magnetisation along the y-axis of the rotating frame after a single $\pi/2$ -pulse over time. If there is no unresolved hyperfine the decay of the signal is proportional to e^{t/T_2} and the Fourier transform contains the EPR spectrum in the frequency domain or as much of it as the pulse bandwidth is able to excite. If there is unresolved hyperfine or other inhomogeneous broadening of the signal the time constant obtained is referred to as T_2^* which is shorter than T_2 . In EPR this experiment is in most cases less applicable than in NMR. Contrary to a nucleus the unpaired electron is rarely shielded by layers of paired electrons, this leads to a stronger coupling to the lattice and surrounding spins, which in turn leads to larger splitting of the energy levels and shorter relaxation times. The larger splitting of the energy levels has the consequence that a single pulse often cannot excite the whole spectrum at once. The shorter relaxation times of electrons result in a time scale, where most, if not all, of the FID signal is already gone before the end of the deadtime. This makes the experiment next to useless for determining T_2 , but FID detection is sometimes used as an alternative to echo detection in other experiments.

1.5.1.3 Echo Decay

Echo decay is also known as Echo spin envelope decay as the sequence can also be used to get information on hyperfine coupling. The experiment uses a simple Hahn echo sequence, where the time between the pulses, τ , is varied as shown in Figure 10. When τ increases the echo intensity decreases as the individual magnetization has more time to either relax or lose coherence. Monitoring the echo intensity as a function of τ therefore leads to a curve decaying as a function of $T_2(T_m)$.

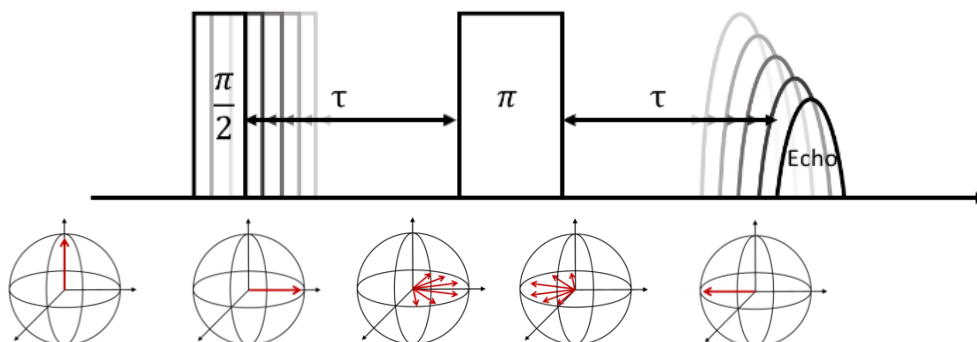


Figure 10. Pulse sequence for the echo decay experiment

1.5.1.3.1 Pulse Lengths and ESEEM

The Echo decay experiment is the same as the two-pulse Electron Spin Echo Envelope Modulation (ESEEM). This means that for some systems the Echo decay curves will exhibit modulation with the nuclear Larmor frequency of coupled nuclei (or coupling constant in strongly coupled cases). The modulation is observed when non-allowed transitions incorporating nuclear spin transitions are also excited by the pulse. This is illustrated in Figure 11 with a spin system with $S = 1/2$ system coupled to a nuclear spin with $I = 1/2$. In a magnetic field the electron spin is split in two levels ($m_s = +1/2$ and $m_s = -1/2$) and further split in two levels by the nuclear spin ($m_s = \pm 1/2, m_I = -1/2$ and $m_s = \pm 1/2, m_I = +1/2$). This means there are now two spin allowed transitions ($\Delta m_s = 1, \Delta m_I = 0$) and two forbidden transitions ($\Delta m_s = 1, \Delta m_I = 1$) as shown in Figure 11a. The first ($\pi/2$) pulse of the sequence will generate coherence, but those spin packets excited via the non-allowed transitions by the second (π) pulse will have a phase offset by the nuclear Larmor frequency times τ (in the weakly coupled case), modulating the echo decay curve when τ is varied.

The modulated echo decay curve can be simulated if there are only a few significant oscillation frequencies. This often fails to give accurate values of T_m (the difference between T_m and T_2 is discussed in the section below), due to both the number of parameters in the equation and the fact that there are often several different nuclei causing the modulation. Therefore, it is often preferable to avoid measuring the modulation altogether.

The excitation bandwidth of a microwave pulse is inversely proportional to the length of the pulse and so modulation can be suppressed by using longer pulses, as these can be made to only excite the allowed transitions. Figure 11b shows an example of the situation where unresolved hyperfine is hidden in what looks like a single peak and illustrates the overlap of the bandwidths of a short and 4 times longer pulse with the transitions.

Using longer pulses does present the obstacle of extending the FIDs.²⁰ The time between pulses (τ) therefore often must start at higher values giving the signal time to decay before the measurement starts.

Longer pulses can also lead to some advantages as the narrower excitation bandwidth of long pulses can also decrease spectral diffusion.²¹

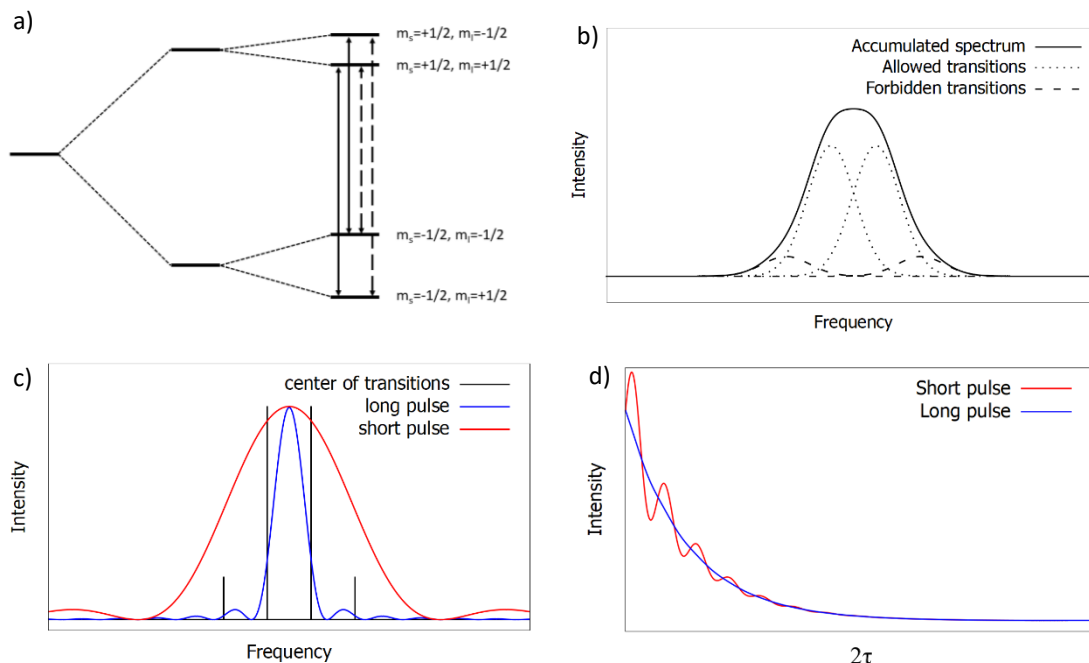


Figure 11. Example $S=1/2$ and $I=1/2$ showing a) the energy levels and transitions, filled arrows indicate an allowed transition, and dashed arrows indicate forbidden transitions. B) the resulting spectrum in the frequency domain showing how a single peak can contain unresolved hyperfine interactions c) examples of excitation profiles of a long (blue) and a short pulse (red) overlaid with the positions of the transitions. D) The resulting echo decay traces of long and short pulses.

1.5.1.4 Carr-Purcell-Meiboom-Gill (CPMG) sequence

To lessen the effect of spectral diffusion on the measured T_m it is common to use the CPMG sequence also known as the echo-train sequence.²² The sequence starts with a $\pi/2$ -pulse followed by a π -pulse and an echo just like the normal echo-decay experiment, but instead of increasing the time between the pulses (τ), the echo is refocused by another π -pulse 2τ after the last one and a refocused echo is observed, the sequence is shown in figure 12. By adding more π -pulses with an interval of 2τ and measuring the intensity of the subsequent refocused echoes, T_2 is measured.

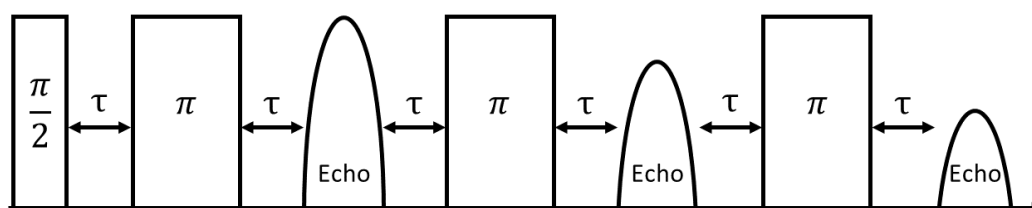


Figure 12. CPMG pulse sequence

1.5.2 Fitting T_2/T_m Data

Solved from the Bloch equations the relaxation profile of T_2 should follow a mono-exponential Decay.

$$I = I_0 + k \cdot e^{-\left(\frac{2\tau}{T_2}\right)} \quad (17)$$

where I_0 is the y-axis offset and k is a positive scaling constant. In practice this function is often inadequate for fitting experimental data. This is due to the influence of coherence loss from mechanisms other than the relaxation of the spins themselves, mechanisms such as instantaneous diffusion and nuclear spin diffusion. The observed T_2 is therefore different in nature to the transverse relaxation time T_2 derived from the Bloch equations. It is instead called the decoherence time or phase memory time and denoted T_m . Instantaneous and nuclear spin diffusion distort the shape of the echo decay, hence functions incorporating these mechanisms must be employed. Just like for T_1 the stretched exponential function (equation 4) is used to fit T_m .

$$I = I_0 + k \cdot e^{-\left(\frac{2\tau}{T_m}\right)^{\beta_m}} \quad (18)$$

where the stretch parameter β_m provides insight into which mechanism limits the phase memory time. Instantaneous diffusion governs when β_m is near or below 1 and nuclear diffusion governs when it is close to or above 2.^{1,23–25} When $\beta_m = 1$ T_m is considered equal to T_2 , because equation 18 is the same as equation 17 and the two can be used interchangeably.²⁶ Examples of relaxation affected by the two kinds of diffusion is shown in Figure 13.

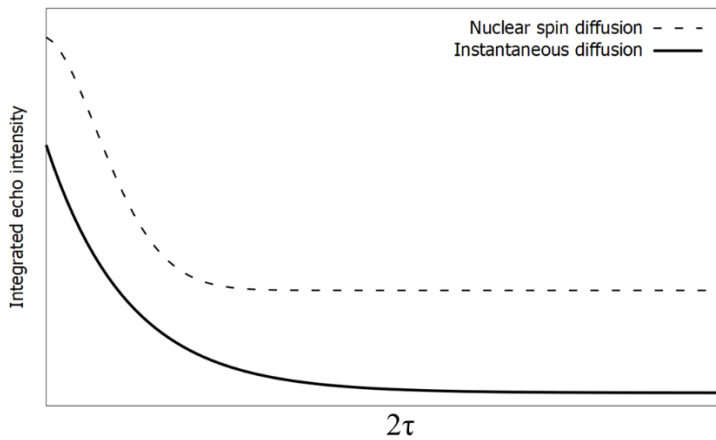


Figure 13. Comparison of spin echo decay curves, when dominated by either instantaneous diffusion or nuclear diffusion.

There could be several reasons for two distinct relaxation processes. Two relaxation times could be observed when there are two species with their own distinct T_1 or an uneven distribution of paramagnets e.g. due to nucleation or other defects when freezing of the solvent in a frozen solution sample.²⁷ The mechanisms of decoherence are often linked to nuclear spins and atoms with several isotopes with different spin can cause different decoherence rates in paramagnets near one or the other isotope.

When two relaxation processes are present a bi-exponential function is used.

$$I = I_0 + k_1 \cdot e^{-\left(\frac{2\tau}{T_{m1}}\right)} + k_2 \cdot e^{-\left(\frac{2\tau}{T_{m2}}\right)} \quad (19)$$

Where each term is equal to equation 17 and describes its own relaxation rate.

In cases when ESEEM is present in the data it can be fitted with equation 20 or an extended version of it

$$I = I_0 + k_m \cdot \left(1 - k_{osc} \cdot \cos\left(\frac{\omega_N \tau}{2} + p\right) \cdot e^{-\left(\frac{\tau}{T_{osc}}\right)}\right) \cdot e^{-\left(\frac{2\tau}{T_m}\right)} \quad (20)$$

where k_m is the normalisation constant, k_{osc} is the modulation amplitude, ω_N is the Larmor frequency of the nucleus causing the oscillation, p is the phase of the oscillation and T_{osc} is the decay time of the oscillation. The function can be extended to include multiple different nuclear frequencies. Due to the large number of parameters in equation 20 it is often unfeasible to get accurate or precise values of T_m .

1.5.3 Spin-spin Relaxation Mechanisms

Spin-spin relaxation is named so because the relaxation comes through the interaction between spins. The T_2 derived by Bloch is supposed to happen through dipolar interactions between neighbouring spins and the relaxation rate should be dependent on the average distance between unpaired spins and the size of their magnetic moments following equation 21.²⁸

$$T_2 \propto \frac{r^3}{\mu^2} \quad (21)$$

where r is the average distance between unpaired electrons and μ is the magnetic moment of the electrons.

For the most part T_2 is hard to measure, since the property we measure in echo decay experiments is effectively the phase memory time, T_m , which is shorter than T_2 . We only measure pure T_2 when the temperature is high enough for spin-lattice relaxation to be faster than other spin-spin relaxation processes, since $2T_1 \geq T_2$, or when there is no spectral diffusion.²⁹

The measured phase memory time, T_m , is shortened mainly by two processes: instantaneous diffusion and nuclear spin diffusion, both of which are contributors to spectral diffusion.

Instantaneous diffusion happens when a spin is flipped by a pulse and changes the resonance frequency of a neighbouring excited spin enough for it not to be outside the excitation bandwidth of the pulses. It arises from interaction with other paramagnetic centres through dipolar coupling. This makes it dependent on the average distance between and thus concentration of paramagnetic centres. Nuclear spin-diffusion works through spin-flips of nuclear spins interacting with the electronic spin, causing phase change. Nuclear spin lattice relaxation happens at rates that are

extremely slow compared to the measured values of T_m , but at low concentration and low temperature the large number of nuclei present often makes it the dominant contribution to phase memory loss. Protons are usually the main source of nuclear spin diffusion due to their abundance and relatively large magnetic moment. It has been shown experimentally that only protons outside a range of $\approx 6 \text{ \AA}$ facilitate decoherence, since the ones close are so strongly coupled that they are unlikely to flip.^{30–32} Outside the 6 \AA the effect of the nuclear spin diffusion from protons slowly diminish with distance, as their coupling becomes too weak to influence the electron spin.

1.5.3.1 Temperature Dependence

In the solid-state matrices T_m is in most cases independent of temperature until high temperature where it becomes limited by T_1 . One exception is in cases where relaxation is largely due to nuclei located in a part of a molecule where certain molecular motions are activated in a specific temperature range. The typical example is when the rate of the rotational motion of a methyl group increases and a dip in T_m is observed.³³ The temperature at which this occurs is determined by the steric hindrance of the methyl group and coupling of the protons to the electron.

1.6 Concluding Remarks

To sum up, T_1 is the longitudinal relaxation time of the magnetization. It is most often measured using an inversion recovery pulse sequence and is supposed to follow a mono-exponential function, but is most often fitted with either a stretched exponential or bi-exponential function to account for spectral diffusion. The temperature dependence of T_1 is dependent on several processes of which the direct, the Raman and when $S > 1/2$ also the Orbach mechanisms are generally used for fitting. T_m is the phase memory time, the relaxation time for the magnetization in the xy-plane to decohere. It is usually measured with an echo decay sequence fitted with a stretched exponential function, from which the dominant mechanism, instantaneous diffusion or nuclear spin diffusion, can also be determined.

References

- (1) Eaton, S. S.; Eaton, G. R. Relaxation Times of Organic Radicals and Transition Metal Ions. In *Distance Measurements in Biological Systems by EPR. Biological Magnetic Resonance, vol 19.*; Springer, 2002; pp 29–154. https://doi.org/10.1007/0-306-47109-4_2.
- (2) Eaton, S. S.; Eaton, G. R. Relaxation Mechanisms. In *eMagRes*; John Wiley & Sons, Ltd, 2016; pp 1543–1556. <https://doi.org/https://doi.org/10.1002/9780470034590.emrstm1507>.

- (3) Jackson, C. E.; Moseley, I. P.; Martinez, R.; Sung, S.; Zadrozny, J. M. A Reaction-Coordinate Perspective of Magnetic Relaxation. *Chem. Soc. Rev.* **2021**, *50* (12), 6684–6699.
<https://doi.org/10.1039/D1CS00001B>.
- (4) Bloch, F. Nuclear Induction. *Phys. Rev.* **1946**, *70* (7–8), 460–474.
<https://doi.org/10.1103/PhysRev.70.460>.
- (5) Spindler, P. E.; Schöps, P.; Bowen, A. M.; Endeward, B.; Prisner, T. F. Shaped Pulses in EPR. In *eMagRes*; John Wiley & Sons, Ltd, 2016; pp 1477–1492.
<https://doi.org/https://doi.org/10.1002/9780470034590.emrstm1520>.
- (6) Eaton S. and Eaton, G. R. Saturation Recovery EPR. In *Biomedical EPR, Part B: Methodology, Instrumentation, and Dynamics*; Eaton S. and Eaton, G. R. and B. L. J., Ed.; Springer US: Boston, MA, 2005; Vol. 24, pp 3–15. https://doi.org/10.1007/0-306-48533-8_1.
- (7) Tesi, L.; Lucaccini, E.; Cimatti, I.; Perfetti, M.; Mannini, M.; Atzori, M.; Morra, E.; Chiesa, M.; Caneschi, A.; Sorace, L.; Sessoli, R. Quantum Coherence in a Processable Vanadyl Complex: New Tools for the Search of Molecular Spin Qubits. *Chem. Sci.* **2016**, *7* (3), 2074–2083.
<https://doi.org/10.1039/C5SC04295J>.
- (8) Kronig, R. de L. On the Mechanism of Paramagnetic Relaxation. *Physica* **1939**, *6* (1), 33–43.
[https://doi.org/https://doi.org/10.1016/S0031-8914\(39\)90282-X](https://doi.org/https://doi.org/10.1016/S0031-8914(39)90282-X).
- (9) Abragam, A.; Bleaney, B. *Electron Paramagnetic Resonance of Transition Ions*, 1st ed.; Oxford: Clarendon press, 1970.
- (10) Shrivastava, K. N. Theory of Spin–Lattice Relaxation. *Phys. status solidi (b)* **1983**, *117* (2), 437–458. <https://doi.org/https://doi.org/10.1002/pssb.2221170202>.
- (11) Scott, P. L.; Jeffries, C. D. Spin-Lattice Relaxation in Some Rare-Earth Salts at Helium Temperatures; Observation of the Phonon Bottleneck. *Phys. Rev.* **1962**, *127* (1), 32–51.
<https://doi.org/10.1103/PhysRev.127.32>.
- (12) Ziman, J. M. Chapter 1: Phonons. In *Electrons and Phonons: The Theory of Transport Phenomena in Solids*; Oxford University Press, 2001.
<https://doi.org/10.1093/acprof:oso/9780198507796.003.0001>.
- (13) van Vleck, J. H. Paramagnetic Relaxation Times for Titanium and Chrome Alum. *Phys. Rev.* **1940**, *57* (5), 426–447. <https://doi.org/10.1103/PhysRev.57.426>.
- (14) Finn, C. B. P.; Orbach, R.; Wolf, W. P. Spin-Lattice Relaxation in Cerium Magnesium Nitrate at Liquid Helium Temperature: A New Process. *Proc. Phys. Soc.* **1961**, *77* (2), 261–268.
<https://doi.org/10.1088/0370-1328/77/2/305>.

- (15) Klemens, P. G. Localized Modes and Spin-Lattice Interactions. *Phys. Rev.* **1962**, *125* (6), 1795–1798. <https://doi.org/10.1103/PhysRev.125.1795>.
- (16) Zhou, Y.; Bowler, B. E.; Eaton, G. R.; Eaton, S. S. Electron Spin Lattice Relaxation Rates for $S = 1/2$ Molecular Species in Glassy Matrices or Magnetically Dilute Solids at Temperatures between 10 and 300 K. *J. Mag. Res.* **1999**, *139* (1), 165–174. <https://doi.org/10.1006/jmre.1999.1763>.
- (17) Atsarkin, V. A.; Demidov, V. v; Vasneva, G. A. Metal-Insulator Transition in RbC₆₀ Polymer Fulleride Studied by ESR and Electron-Spin Relaxation. *Phys. Rev. B* **1997**, *56* (15), 9448–9453. <https://doi.org/10.1103/PhysRevB.56.9448>.
- (18) Thomas, L.; Lioni, F.; Ballou, R.; Gatteschi, D.; Sessoli, R.; Barbara, B. Macroscopic quantum tunnelling of magnetization in a single crystal of nanomagnets. *Nature* **1996**, *383* (6596), 145–147. <https://doi.org/10.1038/383145a0>.
- (19) DiVincenzo, D. P. The Physical Implementation of Quantum Computation. *Fortschr. Phys.* **2000**, *48* (9–11), 771–783.
- (20) Stoll, S. Pulse EPR. In *eMagRes*; John Wiley & Sons, Ltd, 2017; pp 23–38. <https://doi.org/10.1002/9780470034590.emrstm1510>.
- (21) Eaton, S. S.; Eaton, G. R. Irradiated Fused-Quartz Standard Sample for Time-Domain EPR. *J. Mag. Res. A* **1993**, *102* (3), 354–356. <https://doi.org/10.1006/jmra.1993.1116>.
- (22) Harbridge, J. R.; Eaton, S. S.; Eaton, G. R. Comparison of Electron Spin Relaxation Times Measured by Carr–Purcell–Meiboom–Gill and Two-Pulse Spin-Echo Sequences. *J. Mag. Res.* **2003**, *164* (1), 44–53. [https://doi.org/10.1016/S1090-7807\(03\)00182-4](https://doi.org/10.1016/S1090-7807(03)00182-4).
- (23) Mims, W. B. Phase Memory in Electron Spin Echoes, Lattice Relaxation Effects in CaWO₄: Er, Ce, Mn. *Phys. Rev.* **1968**, *168* (2), 370–389. <https://doi.org/10.1103/PhysRev.168.370>.
- (24) Klauder, J. R.; Anderson, P. W. Spectral Diffusion Decay in Spin Resonance Experiments. *Phys. Rev.* **1962**, *125* (3), 912–932. <https://doi.org/10.1103/PhysRev.125.912>.
- (25) Brown, I. M. Electron Spin-Echo Studies of Relaxation Processes in Molecular Solids. In *Time domain electron spin resonance*; Kevan, L., Schwartz, R. N., Eds.; Wiley: New York, 1979.
- (26) Norris, J. R.; Thurnauer, M. C.; Bowman, M. K. Electron Spin Echo Spectroscopy and the Study of Biological Structure and Function. *Adv. Bio. Med. Phys.* **1980**, *17*, 365–416. <https://doi.org/10.1016/B978-0-12-005217-2.50015-4>.

- (27) Zadrozny, J. M.; Niklas, J.; Poluektov, O. G.; Freedman, D. E. Millisecond Coherence Time in a Tunable Molecular Electronic Spin Qubit. *ACS. Cent. Sci.* **2015**, *1* (9), 488–492. <https://doi.org/https://doi.org/10.1021/acscentsci.5b00338>.
- (87) Bloembergen, N.; Purcell, E. M.; Pound, R. v. Relaxation Effects in Nuclear Magnetic Resonance Absorption. *Phys. Rev.* **1948**, *73* (7), 679–712. <https://doi.org/10.1103/PhysRev.73.679>.
- (29) Ladd, T. D.; Jelezko, F.; Laflamme, R.; Nakamura, Y.; Monroe, C.; O’Brien, J. L. Quantum Computers. *Nature* **2010**, *464* (7285), 45–53. <https://doi.org/10.1038/nature08812>.
- (30) Zecevic, A.; Eaton, G. R.; Eaton, S. S.; Lindgren, M. Dephasing of Electron Spin Echoes for Nitroxyl Radicals in Glassy Solvents by Non-Methyl and Methyl Protons. *Mol. Phys.* **1998**, *95* (6), 1255–1263. <https://doi.org/10.1080/00268979809483256>.
- (31) Graham, M. J.; Krzyaniak, M. D.; Wasielewski, M. R.; Freedman, D. E. Probing Nuclear Spin Effects on Electronic Spin Coherence via EPR Measurements of Vanadium(IV) Complexes. *Inorg. Chem.* **2017**, *56* (14), 8106–8113. <https://doi.org/10.1021/acs.inorgchem.7b00794>.
- (32) Graham, M. J.; Yu, C.-J.; Krzyaniak, M. D.; Wasielewski, M. R.; Freedman, D. E. Synthetic Approach To Determine the Effect of Nuclear Spin Distance on Electronic Spin Decoherence. *J. Am. Chem. Soc.* **2017**, *139* (8), 3196–3201. <https://doi.org/10.1021/jacs.6b13030>.
- (33) Nakagawa, K.; Candelaria, M. B.; Chik, W. W. C.; Eaton, S. S.; Eaton, G. R. Electron-Spin Relaxation Times of Chromium(V). *J. Mag. Res.* **1992**, *98* (1), 81–91. [https://doi.org/https://doi.org/10.1016/0022-2364\(92\)90111-J](https://doi.org/https://doi.org/10.1016/0022-2364(92)90111-J).

2. Magnetic Relaxation Properties of Chromium Nitrido Complexes

2.1 Preface

This chapter is a manuscript concerning the relaxation properties of chromium nitrides. Chromium nitrido complexes are isoelectronic and often isostructural with their analogous vanadyl complexes, one of the most popular qubit candidates. Through EPR measurements it is established that a chromium nitrido complex possesses the same advantageous magnetic properties as vanadyl complexes.

The project was first proposed by Prof. Jesper Bendix, who supplied the samples and the crystallographic data. Jonatan B. Petersen measured and interpreted the EPR data and wrote the manuscript under the supervision of Prof. Richard E. P. Winpenny, Prof. Eric J. L. McInnes and Prof. Jesper Bendix. The manuscript is expected to be submitted for publication shortly after the submission of this thesis.

This page is intentionally left blank

Magnetic Relaxation Properties of Chromium Nitrido Complexes

Jonatan B. Petersen,¹ Eric J. L. McInnes,¹ Richard E. P. Winpenny¹ and Jesper Bendix²

¹ Department of Chemistry, School of Natural Sciences, The University of Manchester, Oxford Road, Manchester M13 9PL, United Kingdom

² Department of Chemistry, University of Copenhagen, Universitetsparken 5, DK-2100, Copenhagen, Denmark

KEYWORDS: EPR, quantum bits, Chromium(V), Relaxation properties.

ABSTRACT: Molecular qubits are one candidate systems to realize the quantum computer. One of their biggest challenges in living up to the DiVincenzo criteria is their short quantum coherence times. Vanadium(IV) complexes are some of the most promising qubit candidates, because of their relatively long coherence times, up to room temperature and their chemical versatility. The $\{\text{Cr}(\text{N})\}^{2+}$ unit is iso-electronic with the vanadyl $\{\text{V}(\text{O})\}^{2+}$ unit and expected to have many of the same magnetic properties and their complexes are often iso-structural. In this article we use pulsed Electron Paramagnetic Resonance Spectroscopy to explore the relaxation properties of a chromium(V) nitrido complex, $[\text{Cr}(\text{N})(\text{pyrrdtc})_2]$ (pyrrdtc = pyrrolidinedithiocarbamate). EPR of $[\text{Cr}(\text{N})(\text{pyrrdtc})_2]$ measured in frozen solutions gave coherence times of similar magnitude to published vanadyl complexes and could be extended in deuterated solvents. Solid state dilution into the isomorphous $[\text{Re}(\text{N})(\text{pyrrdtc})_2]$ compound made it possible to show quantum coherence at room temperature by observation of Rabi oscillations. The temperature dependence of T_1 was fitted to models including direct, Raman and local mode terms, producing parameters similar to those of vanadyl complexes.

INTRODUCTION

Quantum information processing promises to revolutionise computational processes and realising the quantum computer has become a primary target for researchers. One proposed approach to this is to use the spin of unpaired electrons in molecular systems. For this to be accomplished the potential qubit will have to live up to DiVincenzo's five criteria for the physical implementation of quantum computation.¹ Molecular qubits are perfect candidates for living up to the first three of the criteria as they are well defined and scalable. Simply cooling the qubits under a field to have it in its pure ground state, should be enough fulfil the second criterion. The third criterion requires the qubit to have coherence times much longer than the gate operation time, this has often been taken to mean that relaxation times on the order of milliseconds are necessary, however it has been shown that shorter times could be sufficient especially when employing quantum error correction protocols.²

The fourth criterion calls for the development of a universal set of quantum gates. Most of the molecular qubit community are focusing on two-body systems, with two interacting molecular qubits, where one acts as the target qubit and another different qubit as the control.³ Molecules are splendid candidates to make such systems due the large number of possible ways to link and combine them and controlling the interaction between the two qubits remains a fascinating challenge for synthetic chemists in the field. The fifth and final criterion involves qubit specific measurement capability and is the frontier of current research. Proposals to use magnetic resonance have been brought forward as a possibility as well as many other techniques, though this question is still to be answered.

In recent years vanadium(IV) complexes, in particular those encompassing the vanadyl moiety, have gained a lot of attention as model systems for qubits. This interest is due to the long quantum coherence times of up to millisecond scale and quantum coherence at room temperature,^{4,5} as well as the chemical robustness and versatility of V(IV) allowing for experiments investigating the nature of spin relaxation.^{6,7}

Vanadyl exhibits T_m values of about 1 μs at room temperature. At these temperatures the magnitude of T_m is at the mercy of T_1 as the limiting factor and hence the temperature dependence of these complexes become of interest. The lessened temperature dependence of T_1 and its increased value in vanadyl complexes compared to other V(IV) complexes has been shown to arise from the rigidity of the $\{\text{VO}\}^{2+}$ component and the more isolated SOMO (d_{xy}).⁸

Chromium nitrides are isoelectronic and in many cases isostructural and isomorphous with their vanadyl counterparts. Furthermore, the nitrido ligand renders these systems quite stable despite the high oxidation state and hence suitable as chemically robust building blocks. This makes them interesting for all the same reasons as vanadyl complexes. The Cr=N bond is at least formally stronger and more rigid and leads to an even more isolated SOMO than the V=O bond. Additionally chromium has only one stable isotope with a nuclear spin, ^{53}Cr which has a nuclear spin of 3/2 and a natural abundance of 9.5%. This makes it possible to probe the influence of the metal nuclear spin on relaxation. Few Cr(V) complexes have previously been investigated with time domain EPR techniques and it has primarily concerned a series of ionic Cr(V) complexes with a terminal oxide ligand and a single nitrido chromium porphyrin complex, though for this complex only the T_1 data were published.^{9,10}

In this article we will investigate the spin relaxation properties of chromium nitrido complexes, specifically of nitrido-bis(pyrrolidinedithiocarbamato)chromium(V) complex ($[\text{Cr}(\text{N})(\text{pyrrdtc})_2]$), using pulsed EPR spectroscopy. This specific complex was chosen from a number of published complexes for the ease of preparation and its g-tensor with small anisotropy and values close to the free electron value g_e , which indicates a well isolated ground state and so the prospect of a long T_1 .

EXPERIMENTAL SECTION

ELECTRON PARAMAGNETIC RESONANCE SPECTROSCOPY. EPR was measured at X-band (ca. 9.6 GHz) on a Bruker Elexsys 580 spectrometer equipped with a Bruker ER 4118X-MD5 Dielectric resonator. The microwave frequency was measured with the built-in digital counter of the spectrometer and the field was corrected against a Bruker strong pitch standard ($g=2.0028$). Temperature was regulated using a Bruker Flexline Cryogen-free system controlled via an Oxford Instruments Mercury ITC.

Pulsed EPR measurements were performed on frozen solutions as well as solid state diluted powder samples. The frozen solutions were 0.1 mM and 1 mM in a 4:1 CH_2Cl_2 :toluene mixture by volume as well as 1 mM CD_2Cl_2 : d_8 -toluene and 0.1 mM d_8 -toluene frozen solutions. The solid-state dilutions were 0.8% and 4% $[\text{Cr}(\text{N})(\text{pyrrdtc})_2]$ in the isostructural $[\text{Re}(\text{N})(\text{pyrrdtc})_2]$ analogue. The lower point of the temperature range was determined by what temperature could be kept stable by the experimental setup at the time and then measured until the signal was too weak to measure or up to 150 K in frozen solution, which was below the calculated melting point of the mixture of 167.5 K (see SI section 3).

Relaxation was measured at the highest intensity peak of the spectrum along the g_{xy} plane of the pseudo axial spectrum for all experiments. The peak at lowest field, originating from hyperfine coupling to the ^{53}Cr isotope (9.5% abundance), was also measured for the 1 mM DCM/toluene solution.

In order to detect quantum coherence, Rabi oscillations were measured using a nutation pulse sequence. Where a nutation pulse was placed before a Hahn-echo sequence and the length of the nutation pulse varied. The Hahn-echo sequence was placed at a minimum of $10T_m$ after the nutation pulses.

SYNTHESIS AND SOLID-STATE DILUTION.

Nitridobis-(pyrrolidinedithiocarbamato)chromium(V) was synthesized by a slight modification of the method reported in the literature.¹¹ Especially, when working at high dilutions it is important to avoid excess of dithiocarbamate, which acts as reductant for the chromium(V) complex. Hence it was synthesized using only 1.8 equivalents of ammonium pyrrolidinedithiocarbamate per chromium and the product was thoroughly washed with small batches of ice-cold methanol.

Nitridobis-(pyrrolidinedithiocarbamato)rhenium(V) was synthesized by essentially the same protocol as used by Fletcher and Skapski¹² for the diethyldithiocarbamate analogue using commercially available ammonium pyrrolidinedithiocarbamate. The identity of the product was confirmed by single crystal X-ray diffraction (See Table S1).

Solid dilutions of Cr@Re with the desired nominal concentrations were made by dissolving separately weighed samples of the pure compounds in weighed amounts of neat DCM and mixing these stock solutions by weight. To the mixture was added ca. 1/3 of the total volume of methanol and the resulting solution was evaporated to near dryness in a nitrogen stream. The precipitate was collected by filtration, washed once with methanol and once with diethyl ether.

CRYSTALLOGRAPHY. Single-crystal X-ray diffraction was performed on a Bruker D8 VENTURE diffractometer with a $\lambda = 0.71073 \text{ \AA}$ wavelength (Mo $K\alpha$) X-ray source and detected by a PHOTON 100 CMOS detector. Crystals were mounted on kapton loops and cooled using an Oxford Cryosystems low temperature device at 100 K.

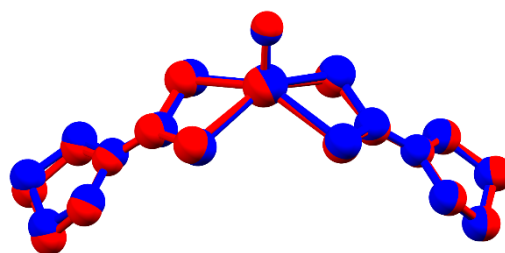


Figure 1. Overlay of the crystal structures of $[\text{Cr}(\text{N})(\text{pyrrdtc})_2]$ (blue) and $[\text{Re}(\text{N})(\text{pyrrdtc})_2]$ (red). Selected bond lengths: Cr-N 1.549(1) Å, Re-N 1.649(3) Å, Cr-S 2.369-2.384(1) Å and Re-S 2.391-2.404(1) Å.

DENSITY FUNCTIONAL THEORY. DFT was performed as an unrestricted Kohn-Sham calculation in the ORCA 4.2.1 program, with the PBE GGA functional and minimally augmented Ahlrich type basis sets of triple zeta quality (ma-def2-TZVP).^{13–16} The geometry was first optimised and vibrational frequencies calculated using the TightSCF and Grid6 keyword settings and a C-PCM solvent model set to use the dielectric constant and refractive index of DCM.¹⁷

RESULTS AND DISCUSSION

CRYSTALLOGRAPHY. $[\text{Re}(\text{N})(\text{pyrrdtc})_2]$ crystallises in the monoclinic spacegroup $P2_1/c$. The single crystal structure of $[\text{Re}(\text{N})(\text{pyrrdtc})_2]$ is isomorphous and isostructural with the structure of $[\text{Cr}(\text{N})(\text{pyrrdtc})_2]$ previously published.¹¹ The rhenium structure exhibits only marginally longer bond lengths, as seen in the overlay of the two molecules in Figure 1.

ELECTRON PARAMAGNETIC RESONANCE SPECTROSCOPY. The continuous wave EPR spectrum

of $[\text{Cr}(\text{N})(\text{pyrrdtc})_2]$ in frozen solution (Figure 2) was measured and compared to the spectrum already published.¹¹ The spectrum was simulated with parameters reflecting the axial nature of the complex, apart from the previously extracted parameters for A_{NL} and A_{CrL} the ^{53}Cr hyperfine in the parallel orientation (A_{CrI}) is visible and simulated to be 122.3 MHz. The parameters used for the simulation were $g_{\parallel}=1.966$, $g_{\perp}=1.996$, $A_{\text{NL}}=10.1$ MHz, $A_{\text{NI}}=10.1$ MHz and $A_{\text{CrL}}=49.5$ MHz and $A_{\text{CrI}}=122.3$ MHz

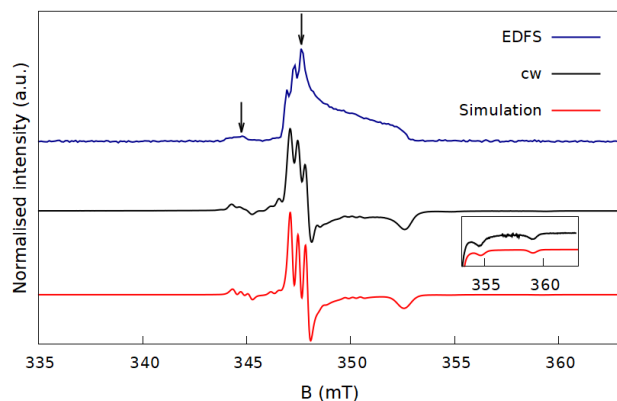


Figure 2. Echo detected Field Sweep of $[\text{Cr}(\text{N})(\text{pyrrdtc})_2]$ in d_8 -toluene (blue) and continuous wave EPR spectrum (black) of $[\text{Cr}(\text{N})(\text{pyrrdtc})_2]$ in DCM/toluene along with a simulation (red). The arrows indicate the two points at which relaxation measurements were done, the lower field transition being the ^{53}Cr hyperfine in the perpendicular orientation. The inset is a zoom-in on the ^{53}Cr hyperfine in the parallel orientation.

RELAXATION MEASUREMENTS. The recorded inversion recovery traces were fitted using a stretched exponential (equation 1)¹⁸

$$I = I_0 + k \cdot e^{-\left(\frac{\tau_1}{T_1}\right)^{\beta_1}} \quad (1)$$

where I_0 is the offset on the y axis, k is the scaling factor, τ_1 is the time between the inversion pulse and the Hahn-echo detection sequence, T_1 is the spin-lattice relaxation time and β_1 is the stretch parameter accounting for spectral diffusion and sources of signal loss other than spin-lattice relaxation.

β_1 values obtained had a general trend of going asymptotically from around 0.7 at low temperature to around 1 at high temperature. The same trend has previously been noted in β_1 of vanadyl complexes.⁴

All experiments gave a similar temperature dependence for T_1 , with the exception of the deuterated toluene solution, which deviates with higher values at low temperature. This could indicate that the direct relaxation mechanism, expected to be dominant at low temperature, is less efficient without dichloromethane present. Fitted relaxation times are reported in Tables S3-S15.

The phase memory time (T_m) was fitted to the intensity of echo decay curves using a stretched exponential (equation 3).¹⁹

$$I = I_0 + k \cdot e^{-\left(\frac{2\tau}{T_m}\right)^{\beta_m}} \quad (3)$$

where τ is the time between pulses in the Hahn echo sequence and β_m is a parameter accounting for nuclear spin diffusion.

Strong modulation of the curves was observed, when measuring T_m using spin-echo decay, due to hyperfine coupling to nitrogen nuclei. In order to get curves that were easier to fit, long pulses of 400 ns/800 ns length were used to narrow the excitation bandwidth and thereby suppress ESEEM effects. These long pulses, meant that the starting value of τ was so large that a significant amount of intensity was lost, and so at higher temperatures it was necessary to revert to shorter pulses (32 ns/64 ns) to be able to bring down τ and increase intensity.

In non-deuterated solvents the fitted values of β_m followed a tendency of being about 1.6-1.8 at low temperature and going to just under $\beta_m = 1$ at 115 K. When $\beta_m \geq 2$ it indicates that nuclear spin diffusion is the dominant relaxation mechanism.²⁰ Thus at low temperature the spin flips of nuclei, most likely the hydrogens of the solvent, determines the spin-spin relaxation rate.

The phase memory times in the non-deuterated solutions were in the range 5-7 μs and temperature independent below 50 K. Above 50 K the shorter T_1 gets to within an order of magnitude of T_m , at which point it starts lowering the value of T_m as shown in Figure 3.

Neither T_1 nor T_m was discernibly different when lowering the concentration from 1 mM to 0.1 mM further demonstrating that effects from nuclear spins were likely to be the limiting factor of T_m . Measurements at the ^{53}Cr hyperfine peak also gave no notable change in relaxation behaviour.

The fact that nuclear diffusion seemed to dominate T_m in non-deuterated solvents prompted us to repeat the experiments in deuterated solvents. In deuterated solvents the T_m relaxation behaviour changes and the echo decay traces at low temperature have visible signal beyond $2\tau \approx 60$ -70 μs suggesting long coherence times. The low temperature measurements have a kink in the early part of the echo decay curves, which suggests that there are two distinct relaxation rates or that some low frequency ESEEM was not entirely suppressed. The stretched exponential function fails to adequately reproduce the echo decay curve shapes at low temperatures and gives unreasonably low and inconsistent values of T_m and β_m at or below 20 K in d_8 -toluene and at all temperatures in a deuterated DCM/toluene mixture (see Tables S6 and S9). The shapes of the echo decay traces were therefore such that it was

appropriate to fit using a bi-exponential function (equation 4).

$$I = I_0 + k_1 \cdot e^{-\left(\frac{2\tau}{T_{m1}}\right)} + k_2 \cdot e^{-\left(\frac{2\tau}{T_{m2}}\right)} \quad (4)$$

Where T_{m1} is the spin-lattice relaxation time and T_{m2} is a pseudo relaxation constant accounting for spectral diffusion and other mechanisms for rapid loss of signal or coherence.

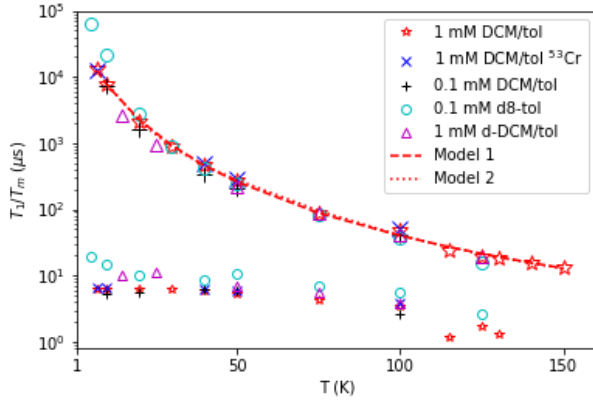


Figure 3. Temperature dependence of T_1 (the higher series of data points) and T_m (the lower series) of $[\text{Cr}(\text{N})(\text{pyrrdtc})_2]$ in frozen solutions. The dashed and dotted lines represent the best fits using eq. 5 and eq. 6 respectively.

The bi-exponential fits yielded values of up to 19.4 μs at 5.5 K in deuterated toluene, which rapidly fall to around 10 μs at 20-50 K before falling steadily as T_1 starts limiting T_m at higher temperatures. The experiment in deuterated DCM/toluene mixture also has a T_m around 10 μs at 15-25 K, which then falls to values around the same magnitude as in non-deuterated solvents at higher temperature.

Table 1. Best fit parameters of model 1 and 2 (with and without local modes) for temperature dependence of T_1 of $[\text{Cr}(\text{N})(\text{pyrrdtc})_2]$ and selected vanadyl and Cr(V) complexes from the literature for comparison

Model 1	a ($\text{s}^{-1} \text{K}^{-1}$)	c ($\text{s}^{-1} \text{K}^{-n}$)	n			Reference
$[\text{Cr}(\text{N})(\text{pyrrdtc})_2]$ (DCM/tol)	9.4	0.051	2.8			This work
$[\text{Cr}(\text{N})(\text{pyrrdtc})_2]$ (d8-tol)	1.4	0.058	2.9			This work
$\text{Cr}@\text{[Re}(\text{N})(\text{pyrrdtc})_2]$ (s)	0.12	0.14	2.6			This work
$\{\text{V}(\text{O})\}@\text{[Ti}(\text{O})\text{Pc}]$ (s)	14	0.038	3			²²
$\{\text{V}(\text{O})\}@\text{[PPh}_4\text{]}_2\text{[Mo}(\text{O})(\text{dmit})_2]$ (s)	-	-	2.8			⁸
Model 2	A_{Dir} ($\text{s}^{-1} \text{K}^{-1}$)	A_{Ram} (10^4 s^{-1})	Θ_D (K)	A_{loc} (10^5 s^{-1})	Δ_{loc} (K)	
$[\text{Cr}(\text{N})(\text{pyrrdtc})_2]$ (DCM/tol)	12.9	5.0	74	6.6	413	This work
$[\text{Cr}(\text{N})(\text{pyrrdtc})_2]$ (DCM/tol)*	13.6	57	163	-	-	This work
$[\text{Cr}(\text{N})(\text{pyrrdtc})_2]$ (d8-tol)	3.0	6.8	74	24	534	This work
$[\text{Cr}(\text{N})(\text{pyrrdtc})_2]$ (d8-tol)*	3.5	22	107	-	-	This work
$\text{Cr}@\text{[Re}(\text{N})(\text{pyrrdtc})_2]$ (s)	5.8	39	136	62	1196	This work
$\text{Cr}@\text{[Re}(\text{N})(\text{pyrrdtc})_2]$ (s)*	5.4	40	132	-	-	This work
$[\text{V}(\text{O})\text{TTP-COOH}]@\text{[ZnTTP]}$ (s)	11.5	6.0	100	4.0	350	¹⁰
$[\text{Cr}(\text{O})(\text{HEBA})_2]$ (H_2O /glycerol)	1.3	13	115	8.7	370	¹⁰
$[\text{Cr}(\text{N})\text{TPP}]$ (toluene/THF)	4.8	12	135	4.3	320	¹⁰
$[\text{V}(\text{O})\text{dmit}_2]^{2-}$ (DMF/tol)*	9.1	38	136	-	-	²⁴

*fitted without local mode term. Abbreviations: Pc=phthalocyanine, dmit=1,3-dithiole-2-thione-4,5-dithiolate, TPP=tetraphenylporphyrinate, TPP-COOH=5-(4-carboxyphenyl)-10,15,20-tri(tolyl)porphyrinate and HEBA=hydroxyl-2-ethylborate.

TEMPERATURE DEPENDENCE OF RELAXATION.

The T_1 and T_m values extracted at a range of temperatures from measurements of the various frozen solutions are shown in Figure 3, along with a fit of the temperature dependence of T_1 . To fit the temperature dependence of T_1 it was modelled with two different models, to compare to results for similar compounds in the literature. The first model used was

$$T_1^{-1} = a \cdot T + c \cdot T^n \quad (5)$$

Where the first term describes the temperature dependence of direct processes with the experimental parameter a and the second term describes the temperature dependence of a Raman type relaxation process with parameters c and n .

The temperature dependence of T_1 was also modelled with equation 6.^{20,21}

$$T_1^{-1} = A_{\text{dir}} \cdot T + A_{\text{Ram}} \cdot \left(\frac{T}{\theta_D}\right)^9 \cdot J_8\left(\frac{\theta_D}{T}\right) + A_{\text{loc}} \cdot \left(\frac{e^{\Delta_{\text{loc}}/T}}{(e^{\Delta_{\text{loc}}/T} - 1)^2}\right) \quad (6)$$

The first term again describes the direct process and is identical to the first term of equation 5, the second term describes the Raman process and the third term represents the relaxation from interactions with local modes. A_{dir} , A_{loc} and A_{Ram} are experimental factors determining the overall contribution of each term, θ_D is the Debye temperature (a fitted parameter) and specifies the temperature at which there all phonon modes are active, $J_8\left(\frac{\theta_D}{T}\right)$ is the transport integral (see SI section 7) and Δ_{loc} is the energy of the local mode responsible for relaxation.

Optimum parameters were found using least squares refinement implemented in a python script. We found that fitting against T_1 heavily favoured fitting the low temperature data points well, while fitting against T_1^{-1} the high temperature data would dominate, hence we opted to fit against the logarithm of T_1 to minimize the influence of the relative magnitudes of the data points.

Both functions were able to reproduce the T_1 data convincingly and the resulting functions are shown as a dashed and a dotted line along with the data in Figure 3.

The parameter values for the first model (equation 5) of $a=9.4 \text{ s}^{-1} \text{ K}^{-1}$ $c=0.051 \text{ s}^{-1} \text{ K}^{-n}$ and $n=2.8$ obtained in 1 mM DCM/toluene are similar to those reported for various vanadyl compounds by the Sessoli group as well as the values of n reported for Cr(V) fitted with only the Raman term by the Eaton group.^{4,8,9,22,23} The T_1 data measured in deuterated matrices deviates from those in protic solutions at low temperature. This is reflected in the value of a , which is significantly lower in d_8 -toluene solution suggesting a reduced efficiency of the direct mechanism. The a parameter is on the other hand higher in deuterated DCM/toluene solution, though the lack of low temperature data for this solution does make this less well established.

The parameters obtained with the second model (eq. 6) for the DCM/toluene glass are listed in Table 1 and may provide more insight into the physical background of the relaxation. A_{dir} , A_{Loc} and A_{Ram} are not unlike literature values for vanadyl fitted with the same method (examples in Table 1) and A_{dir} is of comparable magnitude to the equivalent parameter a from eq. 5, while in deuterated toluene A_{dir} is twice as large as a .^{10,25} The values of θ_D is akin to the 65-80 K found for various species in glasses of DCM/toluene.¹⁰ The local mode vibrational energies Δ_{loc} (413 K and 534 K) are slightly higher than usual, but DFT calculations show plenty of normal modes in this region, most of them incorporating displacement of the donor atoms. This second model includes an extra term accounting for relaxation via local modes, most often left out in the literature. Modelling was also attempted ignoring this term, but it turned out that the local mode term was necessary for accurately reproducing the relaxation behaviour at high temperature. The A_{dir} parameters obtained when removing the third term of equation 6 are similar to those of the full model, but the A_{Ram} deviates by up to a factor of ten. The Debye temperature of the frozen DCM/toluene solution of 163 K obtained with this method is larger than what is normally seen, as the Raman term is compensating for the lack of a third mechanism in this model. The A_{dir} and A_{Ram} parameters obtained with this restricted model resemble those obtained by the Freedman group for V(IV) compounds using the same method (example in Table 1).^{6,7,24} Comparing the function with all three terms to the nested function with only the direct and Raman term using an F-test (see SI) indicated that the use of two extra parameters was justified. The function could have been

further expanded with an extra thermal term, but the three terms used were deemed sufficient.

RELAXATION IN SOLID-STATE DILUTION. In order to look at relaxation properties in the solid state at temperatures above the melting point of the frozen solutions an isostructural rhenium nitride complex was synthesised and $[\text{Cr}(\text{N})(\text{pyrrdtc})_2]$ was doped into it by co-crystallisation.

Two solid state dilution samples of 4% and 0.8% $[\text{Cr}(\text{N})(\text{pyrrdtc})_2]$ doped into $[\text{Re}(\text{N})(\text{pyrrdtc})_2]$ were produced and measured.

In the case of 0.8% $\text{Cr}@[\text{Re}(\text{N})(\text{pyrrdtc})_2]$ the stretched exponential turned out to be insufficient for fitting the inversion recovery experiments. This was evident by fits of the low temperature data showing values of T_1 more than an order of magnitude lower than in solution and more significantly T_1 increasing rather than decreasing between 10 K and 20 K. β_1 values of 0.2-0.3 at the lowest temperatures, compared to 0.7-0.8 for the frozen solutions, could indicate that significant signal intensity was lost by other mechanisms of relaxation, but with dubious estimates of T_1 a different approach was required. To get more reliable estimates of T_1 , the stretch parameter was fixed to $\beta_1=1$. Fitting with the simpler exponential function seemed to yield more consistent results as shown in Figure 4.

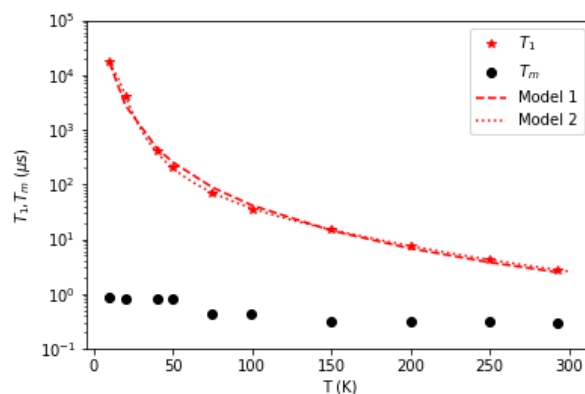


Figure 4. Temperature dependence of T_1 and T_m of 0.8% $[\text{Cr}(\text{N})(\text{pyrrdtc})_2]@[\text{Re}(\text{N})(\text{pyrrdtc})_2]$. The dashed and dotted lines represent the best fits using eq. 5 and eq. 6 respectively.

Fitting the temperature dependence with eq. 5 provides values of $a = 0.12 \text{ s}^{-1} \text{ K}^{-1}$ $c = 0.14 \text{ s}^{-1} \text{ K}^{-n}$ and $n = 2.6$. This means that, at least according to this model, the relaxation is entirely via the Raman mechanism. The best fit parameters found for the second model (eq. 6) $A_{dir} = 5.8 \text{ s}^{-1} \text{ K}^{-1}$, $A_{Ram} = 3.9 \cdot 10^5 \text{ s}^{-1}$, $\theta_D = 136 \text{ K}$, $A_{loc} = 6.2 \cdot 10^6$ and $\Delta_{loc} = 1196 \text{ K}$, presents a different picture. The Raman term is still dominant, but A_{dir} is only half that determined for the DCM/toluene matrix. The Debye temperature is much higher than in frozen solutions, but still within the range often found for molecular solids.²⁰ The local mode parameters differ from the frozen solution. A_{loc} is large, but a relatively larger Δ_{loc} , hints at

the whole of the term being of less importance. Looking at the local modes predicted by DFT in the region of Δ_{loc} , they are primarily related to the hydrogens on the ligands and the nearest mode with any substantial donor atom component would be the Cr-N stretch experimentally determined by IR to lie at 1426 K (991 cm^{-1}).¹¹ Removing the local mode term from model does indeed result in very similar values for the direct and Raman terms. The fit does nonetheless improve markedly when local modes are included, and the F-test value suggests that the goodness of fit is enhanced.

The phase memory times of the solid-state diluted samples were much shorter than in frozen solution, with T_m of the 4% sample at 10 K of only $0.06\text{ }\mu\text{s}$. At 0.8% concentration T_m is around $0.8\text{--}0.9\text{ }\mu\text{s}$ up to 50 K and falling continuously to $0.3\text{ }\mu\text{s}$ at room temperature except for one sudden jump between 50 K and 75 K. This step in T_m coincides with the point at which the signal got too weak for measuring the echo decay with pulses long enough to quench ESEEM modulation of the signal, and the T_m values at 75 K and above are therefore less accurately determined. The increased spin-spin relaxation is due to the higher concentrations of spins in these samples, making the dipolar interactions larger, as 4% and 0.8% corresponds to concentrations about 45 mM and 9 mM respectively.

Rabi oscillations were measured for 0.8% $\text{Cr}@\text{[Re(N)(pyrrdtc)}_2\text{]}$ at room temperature, to show that the system can be initiated in different states. The length of the nutation pulse was gradually increased, which puts the electron spins in different superpositions of $m_s = 1/2$ and $m_s = -1/2$ leading to the echo oscillating as the spin periodically alternates between the states with the length of the pulse. The experiment was repeated with pulses of different power and results are reported in Figure 5a. Fourier transformations of the nutation experiments are shown in Figure 5b, where the peaks give the frequencies of the Rabi oscillations with different power of pulses. The second peak in some of the Fourier transforms comes from hyperfine coupling to hydrogen, which has a Larmor frequency of around 15 MHz at the measured field position. In Figure 5c the Rabi frequencies are plotted against the relative power of the pulses, displaying the linear relationship between them.

CONCLUSION

An experimental investigation of the magnetic relaxation, employing pulsed EPR, on $[\text{Cr(N)(pyrrdtc)}_2]$ in frozen deuterated and non-deuterated solvents as well as solid state dilution in a diamagnetic analogue, has been undertaken. It has shown that this chromium nitrido complex possesses the same interesting properties as isoelectronic vanadyl analogues, namely long phase memory times and room temperature quantum coherence. Further it has been shown, by measuring relaxation at a peak occurring from the 9.5% abundant ^{53}Cr hyperfine, that T_m , just like what has

previously been noted for T_1 , is independent of the spin of the metal nucleus.

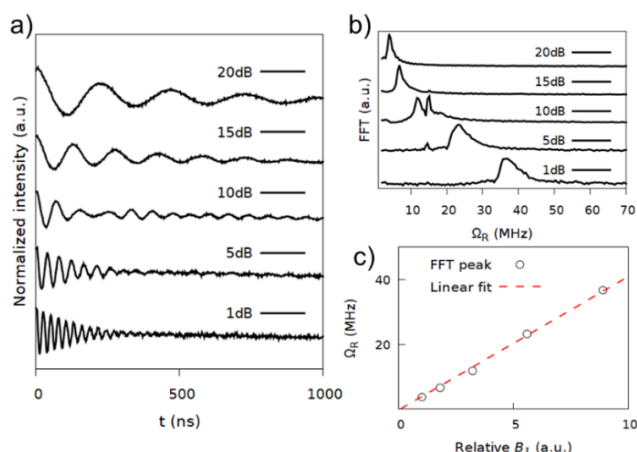


Figure 5. Rabi oscillations of 0.8% $\text{Cr}@\text{[Re(N)(pyrrdtc)}_2\text{]}$ at room temperature a) Rabi oscillations b) Fast Fourier Transform of Rabi oscillations c) Rabi frequency plotted against the relative magnetic field component of microwave pulse.

These discoveries prompt further systematic investigation into the relaxation properties of chromium nitrides. This could be focussed on changing the stiffness of the coordination sphere around chromium as well as the molecular weight, to examine the changes in electron spin relaxation, with respect to the shift of acoustic and optical phonon energies. Further work should also be put into elucidating the effect of the nuclear spin. The ^{53}Cr isotope is commercially obtainable and thus, combined with the two isotopes of nitrogen, this system has several options for isotopic substitution between nuclear spins to investigate the role of these in the magnetic relaxation of transition complexes.

The role of rhenium nitride complexes as an isomorphous host for solid state dilution of chromium nitrides, is expected to be useful in future studies, also of vanadyl complexes.

The relaxation parameters of $[\text{Cr(N)(pyrrdtc)}_2]$ were found to be similar to those of published vanadyl complexes, to the point where isomorphous complexes of the two would be expected have the same relaxation times. Chromium nitrides do have some advantages over vanadyl, namely that the compact spectrum is only 15 mT wide, leading to high intensity peaks, this is beneficial when measuring at room temperature or at very low concentrations.

The close resemblance of the chromium nitrido unit to vanadyl gives the field another paramagnetic module for the chemical toolbox, to be combined with the already existing ones, in order to solve the challenge of realising the first molecular quantum computer.

AUTHOR INFORMATION

Corresponding Author

*Jesper Bendix, bendix@kiku.dk

ACKNOWLEDGMENT

JBP is supported by a European Research Council Advanced Grant to REPW (ERC-2017-ADG-786734). We also thank the EPSRC(UK) EPR National Research Facility (NS/A000055/1) for access to EPR spectrometers.

REFERENCES

- (1) DiVincenzo, D. P. The Physical Implementation of Quantum Computation. *Fortschr. Phys.* **2000**, *48* (9–11), 771–783.
- (2) Devitt, S. J.; Munro, W. J.; Nemoto, K. Quantum Error Correction for Beginners. *Rep. Prog. Phys.* **2013**, *76* (7), 76001. <https://doi.org/10.1088/0034-4885/76/7/076001>.
- (3) Ferrando-Soria, J.; Moreno Pineda, E.; Chiesa, A.; Fernandez, A.; Magee, S. A.; Carretta, S.; Santini, P.; Vitorica-Yrezabal, I. J.; Tuna, F.; Timco, G. A.; McInnes, E. J. L.; Winpenny, R. E. P. A Modular Design of Molecular Qubits to Implement Universal Quantum Gates. *Nat. Commun.* **2016**, *7* (1), 11377. <https://doi.org/10.1038/ncomms11377>.
- (4) Tesi, L.; Lucaccini, E.; Cimatti, I.; Perfetti, M.; Mannini, M.; Atzori, M.; Morra, E.; Chiesa, M.; Caneschi, A.; Sorace, L.; Sessoli, R. Quantum Coherence in a Processable Vanadyl Complex: New Tools for the Search of Molecular Spin Qubits. *Chem. Sci.* **2016**, *7* (3), 2074–2083. <https://doi.org/10.1039/C5SC04295J>.
- (5) Niklas, J.; Poluektov, O. G.; Freedman, D. E.; Zadrozny, J. M. Millisecond Coherence Time in a Tunable Molecular Electronic Spin Qubit. *ACS Cent. Sci.* **2015**, *1* (9), 488–492.
- (6) Graham, M. J.; Krzyaniak, M. D.; Wasielewski, M. R.; Freedman, D. E. Probing Nuclear Spin Effects on Electronic Spin Coherence via EPR Measurements of Vanadium(IV) Complexes. *Inorg. Chem.* **2017**, *56* (14), 8106–8113. <https://doi.org/10.1021/acs.inorgchem.7b00794>.
- (7) Graham, M. J.; Yu, C.-J.; Krzyaniak, M. D.; Wasielewski, M. R.; Freedman, D. E. Synthetic Approach To Determine the Effect of Nuclear Spin Distance on Electronic Spin Decoherence. *J. Am. Chem. Soc.* **2017**, *139* (8), 3196–3201. <https://doi.org/10.1021/jacs.6b13030>.
- (8) Atzori, M.; Morra, E.; Tesi, L.; Albino, A.; Chiesa, M.; Sorace, L.; Sessoli, R. Quantum Coherence Times Enhancement in Vanadium(IV)-Based Potential Molecular Qubits: The Key Role of the Vanadyl Moiety. *J. Am. Chem. Soc.* **2016**, *138* (35), 11234–11244. <https://doi.org/10.1021/jacs.6b05574>.
- (9) Nakagawa, K.; Candelaria, M. B.; Chik, W. W. C.; Eaton, S. S.; Eaton, G. R. Electron-Spin Relaxation Times of Chromium(V). *J. Mag. Res.* **1992**, *98* (1), 81–91. [https://doi.org/https://doi.org/10.1016/0022-2364\(92\)90111-J](https://doi.org/https://doi.org/10.1016/0022-2364(92)90111-J).
- (10) Zhou, Y.; Bowler, B. E.; Eaton, G. R.; Eaton, S. S. Electron Spin Lattice Relaxation Rates for $S = 1/2$ Molecular Species in Glassy Matrices or Magnetically Dilute Solids at Temperatures between 10 and 300 K. *J. Mag. Res.* **1999**, *139* (1), 165–174. <https://doi.org/https://doi.org/10.1006/jmre.1999.1763>.
- (11) Birk, T.; Bendix, J. Atom Transfer as a Preparative Tool in Coordination Chemistry. Synthesis and Characterization of Cr(V) Nitrido Complexes of Bidentate Ligands. *Inorg. Chem.* **2003**, *42* (23), 7608–7615. <https://doi.org/10.1021/ic034777f>.
- (12) Fletcher, S. R.; Skapski, A. C. Crystal and Molecular Structure of the Square-Pyramidal Complex Nitridobis(NN-Diethyldithiocarbamato)Rhenium(V). *J. Chem. Soc., Dalton Trans.* **1972**, No. 10, 1079–1082. <https://doi.org/10.1039/DT9720001079>.
- (13) Neese, F. The ORCA Program System. *Wiley Interdiscip. Rev. Comput. Mol. Sci.* **2012**, *2* (1), 73–78. <https://doi.org/10.1002/wcms.81>.
- (14) Perdew, J. P.; Burke, K.; Ernzerhof, M. Generalized Gradient Approximation Made Simple. *Phys. Rev. Lett.* **1997**, *78* (7), 1396. <https://doi.org/10.1103/PhysRevLett.78.1396>.
- (15) Weigend, F.; Ahlrichs, R. Balanced Basis Sets of Split Valence, Triple Zeta Valence and Quadruple Zeta Valence Quality for H to Rn: Design and Assessment of Accuracy. *Phys. Chem. Chem. Phys.* **2005**, *7* (18), 3297–3305. <https://doi.org/10.1039/B508541A>.
- (16) Zheng, J.; Xu, X.; Truhlar, D. Minimally Augmented Karlsruhe Basis Sets. *Theor. Chem. Acc.: Theory, Computation, and Modeling* **2011**, *128* (3), 295–305. <https://doi.org/10.1007/s00214-010-0846-z>.
- (17) Barone, V.; Cossi, M. Quantum Calculation of Molecular Energies and Energy Gradients in Solution by a Conductor Solvent Model. *J. Phys. Chem. A* **1998**, *102* (11), 1995–2001. <https://doi.org/10.1021/jp9716997>.
- (18) Weibull, W. A Statistical Distribution Function of Wide Applicability. *J. Appl. Mech.* **1951**, 293–297.
- (19) Brown, I. M. Electron Spin-Echo Studies of Relaxation Processes in Molecular Solids. In *Time domain electron spin resonance*; Kevan, L., Schwartz, R. N., Eds.; Wiley: New York, 1979.

- (20) Eaton, S. S.; Eaton, G. R. Relaxation Times of Organic Radicals and Transition Metal Ions. In *Distance Measurements in Biological Systems by EPR. Biological Magnetic Resonance*, vol 19; Springer, 2002; pp 29–154. https://doi.org/10.1007/0-306-47109-4_2.
- (21) Jackson, C. E.; Moseley, I. P.; Martinez, R.; Sung, S.; Zadrozny, J. M. A Reaction-Coordinate Perspective of Magnetic Relaxation. *Chem. Soc. Rev.* **2021**, 50 (12), 6684–6699. <https://doi.org/10.1039/D1CS00001B>.
- (22) Atzori, M.; Tesi, L.; Morra, E.; Chiesa, M.; Sorace, L.; Sessoli, R. Room-Temperature Quantum Coherence and Rabi Oscillations in Vanadyl Phthalocyanine: Toward Multifunctional Molecular Spin Qubits. *J. Am. Chem. Soc.* **2016**, 138 (7), 2154–2157. <https://doi.org/10.1021/jacs.5b13408>.
- (23) Du, J.-L.; Eaton, G. R.; Eaton, S. S. Electron Spin Relaxation in Vanadyl, Copper(II), and Silver(II) Porphyrins in Glassy Solvents and Doped Solids. *J. Mag. Res. A* **1996**, 119 (2), 240–246. <https://doi.org/https://doi.org/10.1006/jmra.1996.0079>.
- (24) Yu, C.-J.; Graham, M. J.; Zadrozny, J. M.; Niklas, J.; Krzyaniak, M. D.; Wasielewski, M. R.; Poluektov, O. G.; Freedman, D. E. Long Coherence Times in Nuclear Spin-Free Vanadyl Qubits. *J. Am. Chem. Soc.* **2016**, 138 (44), 14678–14685. <https://doi.org/10.1021/jacs.6b08467>.
- (25) Fielding, A. J.; Back, D. Bin; Engler, M.; Baruah, B.; Crans, D. C.; Eaton, G. R.; Eaton, S. S. Electron Spin Lattice Relaxation of V(IV) Complexes in Glassy Solutions between 15 and 70 K. In *Vanadium: The Versatile Metal*; ACS Symposium Series; American Chemical Society, 2007; Vol. 974, pp 364–375. <https://doi.org/doi:10.1021/bk-2007-0974.ch026>.

2.3 Supporting Information

Magnetic Relaxation Properties of Chromium Nitrido Complexes

Jonatan B. Petersen,¹ Eric J. L. McInnes,¹ Richard E. P. Winpenny¹ and Jesper Bendix²

¹ Department of Chemistry, School of Natural Sciences, The University of Manchester, Oxford Road, Manchester M13 9PL, United Kingdom

² Department of Chemistry, University of Copenhagen, Universitetsparken 5, DK-2100, Copenhagen, Denmark

KEYWORDS: *EPR, quantum bits, Chromium(V), Relaxation properties.*

1 EPR spectroscopy

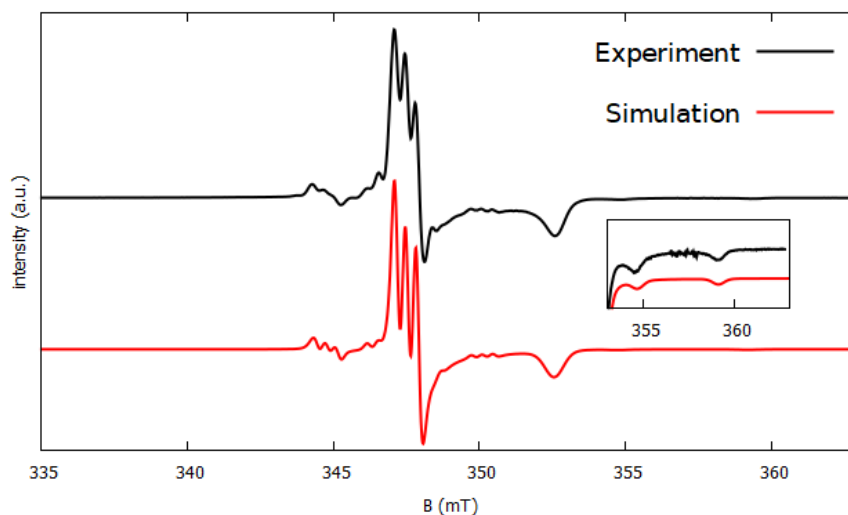


Figure S1. cw X-band EPR spectrum of 1 mM [Cr(N)(pyrrdtc)₂] in DCM/toluene (black) and simulation using Easyspin (red).¹ Inset is 10 times zoomed in on the peaks resulting from hyperfine coupling to ⁵³Cr in the z direction (*A_z*).

EPR spectra were simulated with the following Hamiltonian

$$\hat{H}_1 = \mu_B (B_x \quad B_y \quad B_z) \begin{pmatrix} g_{\perp} & 0 & 0 \\ 0 & g_{\perp} & 0 \\ 0 & 0 & g_{\parallel} \end{pmatrix} \begin{pmatrix} \hat{S}_x \\ \hat{S}_y \\ \hat{S}_z \end{pmatrix} + (\hat{S}_x \quad \hat{S}_y \quad \hat{S}_z) \begin{pmatrix} A_{N,\perp} & 0 & 0 \\ 0 & A_{N,\perp} & 0 \\ 0 & 0 & A_{N,\parallel} \end{pmatrix} \begin{pmatrix} \hat{I}_x \\ \hat{I}_y \\ \hat{I}_z \end{pmatrix}$$

This spectrum was combined with a spectrum normalised to the natural abundance of ⁵³Cr (9.5%) simulated with

$$\hat{H}_2 = \hat{H}_1 + (\hat{S}_x \quad \hat{S}_y \quad \hat{S}_z) \begin{pmatrix} A_{Cr,\perp} & 0 & 0 \\ 0 & A_{Cr,\perp} & 0 \\ 0 & 0 & A_{Cr,\parallel} \end{pmatrix} \begin{pmatrix} \hat{I}_x \\ \hat{I}_y \\ \hat{I}_z \end{pmatrix}$$

2 EPR measurement of relaxation times

The spin-lattice relaxation time (T_1) was measured using an inversion recovery pulse sequence (π - t_1 - $\pi/2$ - τ - π - τ -*echo*) with 64 ns long π pulses and 300 ns long τ . As illustrated in Figure S2, the spins are initially inverted relative to the static magnetic field with a π pulse and then after time t_1 the spins alignment is detected with a Hahn-echo sequence. By varying t_1 the time dependence for the spin to revert to equilibrium is measured.

The phase memory time (T_m) was determined by an echo-decay experiment. Here the time between pulses (τ) in a Hahn-echo sequence ($\pi/2$ - τ - π - τ -*echo*) is gradually increased, leading to a decrease in echo intensity corresponding to more spins going out of phase. Long pulses with $\pi=800$ ns were used to avoid ESEEM effects, the associated longer initial values for τ , meant some loss of signal. In some cases this loss of signal made it unfeasible to measure with long pulses at higher temperatures. In these cases a sequence with $\pi = 64$ ns and $\tau = 300$ ns was used at the highest temperatures. In the case of 4% Cr@[Re(N)(pyrrdte)₂] T_m was so short that a sequence with $\pi = 32$ ns and $\tau = 150$ ns was needed to get a signal.

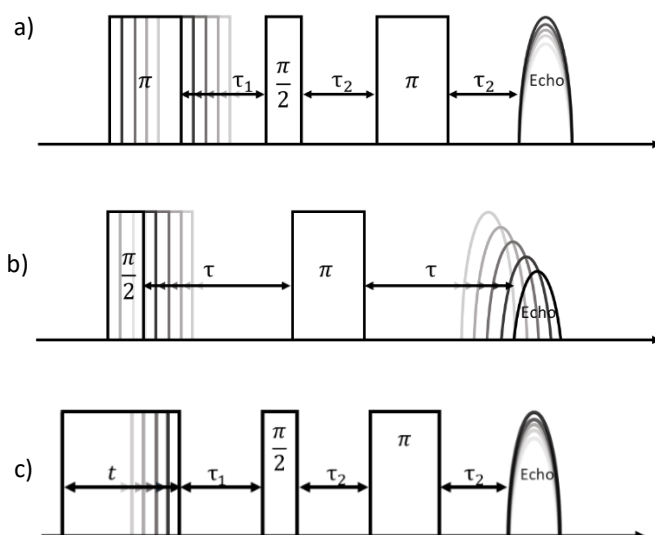


Figure S2. Illustrations of the pulse sequences used a) inversion recovery used to measure T_1 b) Echo decay for measuring T_m c) Nutation sequence for measuring Rabi oscillations.

3 Calculation of freezing point of DCM/toluene mixture

The cryoscopic constant is calculated with:

$$E_f = \frac{R \cdot T_f^2 \cdot M}{\Delta_{fus}H}$$

Where E_f is the cryoscopic constant, R is the gas constant, T_f is the freezing point, M is molar mass and $\Delta_{fus}H$ is the enthalpy of fusion at the melting point.

$\Delta_{fus}H_{DCM}=4.60 \text{ kJ mol}^{-1}$, $T_{f,DCM}=175.95 \text{ K}$ and $M_{DCM}=84.93 \text{ g mol}^{-1}$.^{2,3}

$$E_{f,DCM} = \frac{8.314 \text{ J mol}^{-1} \text{ K}^{-1} \cdot (175.95 \text{ K})^2 \cdot 84.93 \text{ g/mol}^{-1}}{4.60 \text{ kJ mol}^{-1}} = 4.75 \frac{\text{kg} \cdot \text{K}}{\text{mol}}$$

Freezing point depression for a 4:1 DCM:toluene solution

$$\Delta T_f = E_f \cdot m$$

Where ΔT_f is the change in freezing point and m is the molality (mol solute per kg solvent)

$\rho_{tol}=0.867 \text{ g ml}^{-1}$, $\rho_{DCM}=1.327 \text{ g ml}^{-1}$ and $M_{tol}=92.14 \text{ g mol}^{-1}$.⁴

$$m_{tol} = \frac{\left(\frac{1 \text{ ml} \cdot 0.867 \text{ g ml}^{-1}}{92.14 \text{ g mol}^{-1}} \right)}{4 \text{ ml} \cdot \frac{1.327 \text{ g}}{\text{ml}}} = 1.77 \text{ mol/kg}$$

$$T_{f,mixture} = T_f - \Delta T_f = 175.95 \text{ K} - 4.75 \frac{\text{kg} \cdot \text{K}}{\text{mol}} \cdot 1.77 \frac{\text{mol}}{\text{kg}} = 175.95 \text{ K} - 8.42 \text{ K} = 167.53 \text{ K}$$

4 Crystallography

The crystallographic data of $[\text{Re}(\text{N})(\text{pyrrdtc})_2]$ is available free of charge at <https://www.ccdc.cam.ac.uk> as CCDC 2181505. The key crystallographic data are listed in Table S1.

Table S1. Experimental X-ray crystallographic data for $[\text{Re}(\text{N})(\text{pyrrdtc})_2]$ compared to the $[\text{Cr}(\text{N})(\text{pyrrdtc})_2]$ ⁵⁴

	$[\text{Cr}(\text{N})(\text{pyrrdtc})_2]$	$[\text{Re}(\text{N})(\text{pyrrdtc})_2]$
Empirical formula	$\text{C}_{10}\text{H}_{16}\text{CrN}_3\text{S}_4$	$\text{C}_{10}\text{H}_{16}\text{N}_3\text{ReS}_4$
Formula weight (g/mol)	358.51	492.71
Crystal system	monoclinic	monoclinic
Space group	$P2_1/c$	$P2_1/c$
a (Å)	14.859 (1)	14.904 (1)
b (Å)	88.5575 (5)	8.6125 (6)
c (Å)	11.827 (1)	11.89 25 (9)
α (°)	90	90
β (°)	106.528 (7)	107.377 (3)
γ (°)	90	90
V (Å ³)	1441.7(2)	1456.9(2)
Z	4	4
T (K)	122	120
ρ (g cm ⁻³)	1.652	2.246
μ (mm ⁻¹)	1.357	8.899
Θ (°)	1.43-34.95	2.77-30.99
Goodness of fit	1.052	1.129
R1	0.0308	0.0236
wR2	0.0793	0.0523

5 ESEEM

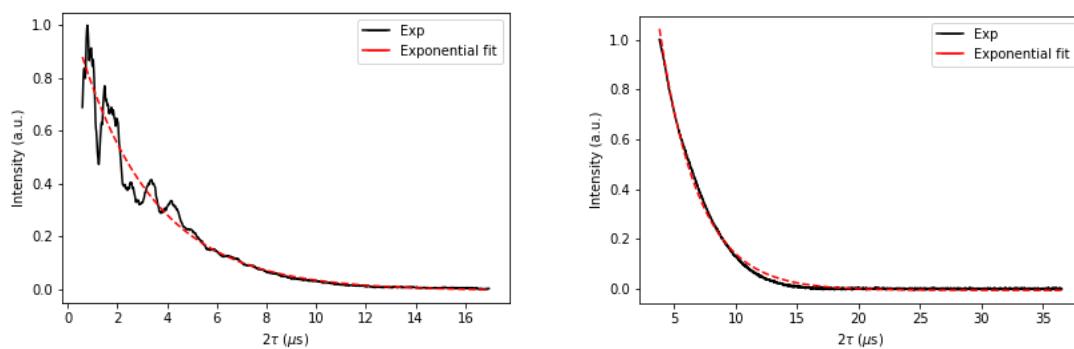


Figure S3. Comparison of echo decay traces of 1 mM $[\text{Cr}(\text{N})(\text{pyrrdtc})_2]$ in DCM/toluene at 50 K measured using Hahn-echo sequences with a π -pulse length of 32 ns (left) and of 800 ns (right) both fitted with a mono-exponential function.

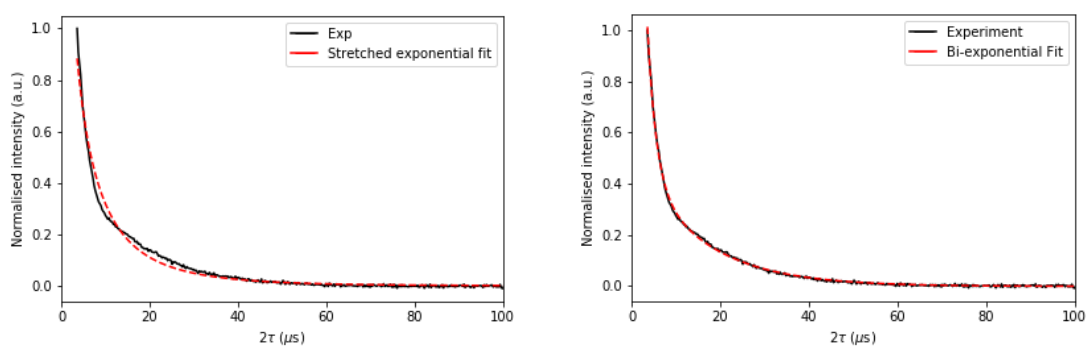


Figure S4. Comparison of echo decay trace of 0.1 mM $[\text{Cr}(\text{N})(\text{pyrrdtc})_2]$ in deuterated toluene at 10 K fitted with a stretched exponential (left) and a bi-exponential function (right).

6 Statistics

We used the F-test to compare the two nested models (equation 6 with or without the local mode term) and estimated the probability that the extra parameters in the full model are statistically sound. F-values were calculated with the following equation:

$$F = \frac{\frac{RSS_1 - RSS_2}{p_2 - p_1}}{\frac{RSS_2}{n - p_2}}$$

Where RSS_i is the residual sum of squares ($RSS_i = \sum_{j=1}^n (y_j - f(x_j)_i)^2$), p_i is the number of parameters of model i , n is the number of observations.

The values were then compared to the F-distribution ($F_{\Delta p, n-p}(s)$) a function of the difference in the number of parameters between the two models (Δp) and the difference between the number of observations and the number of parameters in the full model.

Table S2. F-values calculated for comparison of fits with 3 and 5 parameters of T_1 vs temperature and the value of F-distribution at 5% significance level ($F_{\Delta p, n-p}(0.05)$).

	F-test	$F_{2, n-p}(0.05)$
[Cr(N)(pyrrdc) ₂] (DCM/tol)	27.4	4.46
[Cr(N)(pyrrdc) ₂] (s)	55.6	6.94
[Cr(N)(pyrrdc) ₂] (d8-tol)	42.5	5.79

7 Transport integral

The transport integral is defined as

$$J_8\left(\frac{\theta_D}{T}\right) = \int_0^{\frac{\theta_D}{T}} (x)^8 \cdot \frac{e^x}{(e^x - 1)^2} dx$$

The integral was approximated with the following expression in the python script:

```
np.real(-(x**8/(-1+np.exp(x)))+8*(-(x**8/8)+x**7*cmath.log(1-  
np.exp(x)+0j))+7*x**6*mpmath.polylog(2,np.exp(x))-  
42*x**5*mpmath.polylog(3,np.exp(x))+210*x**4*mpmath.polylog(4,np.exp(x))-  
840*x**3*mpmath.polylog(5,np.exp(x))+2520*x**2*mpmath.polylog(6,np.exp(x))-  
5040*x*mpmath.polylog(7,np.exp(x))+5040*mpmath.polylog(8,np.exp(x)))-  
8*(5040*mpmath.polylog(8,1)))
```

8 Extracted relaxation parameters

Table S3. Relaxation parameters for 1 mM [Cr(N)(pyrrdtc)₂] in DCM/toluene at highest intensity peak. Fitted with a stretched exponential function.

T (K)	T_1 (μs)	95% confidence interval of T_1 fit	β_1	T_m (μs)	95% confidence interval of T_m fit	β_m
7	12961.4	42.66	0.71	6.28	0.06	1.63
10	7770.4	46.41	0.78	6.36	0.09	1.65
20	2148.7	1.11	0.87	6.29	0.07	1.64
30	896.5	0.30	0.91	6.25	0.04	1.65
40	467.2	0.20	0.93	5.77	0.04	1.59
50	269.0	0.16	0.94	5.37	0.05	1.55
75	89.6	0.17	0.94	4.30	0.05	1.43
100	48.3	0.05	0.97	3.37	0.09	1.32
115	24.6	0.67	0.82	1.18	0.64	0.88
125	19.8	0.09	0.97	1.66	0.60	0.96
130	17.9	0.11	0.95	1.30	0.74	0.88
140	15.8	0.22	0.97	-	-	-
150	13.2	0.99	0.97	-	-	-

Table S4. Relaxation parameters for 1 mM [Cr(N)(pyrrdtc)₂] in DCM/toluene at ⁵³Cr peak fitted with a stretched exponential function.

T (K)	T_1 (μs)	95% confidence interval of T_1 fit	β_1	T_m (μs)	95% confidence interval of T_m fit	β_m
7	12231.6	82.68	0.72	6.58	0.09	1.70
10	11860.9*	82.46*	0.80*	6.72	0.16	1.73
40	505.1	0.95	0.92	6.24	0.10	1.70
50	288.9	0.88	0.92	5.83	0.13	1.65
100	52.0	1.03	0.95	3.86	1.14	1.43

* T_1 measurement at 10 K was removed as an outlier. The range of τ used for measurement was too short and the curve was still rising at the end of the range.

Table S5. Relaxation parameters for 0.1 mM [Cr(N)(pyrrdtc)₂] in DCM/toluene at highest intensity peak fitted with a stretched exponential function.

T (K)	T_1 (μs)	95% confidence interval of T_1 fit	β_1	T_m (μs)	95% confidence interval of T_m fit	β_m
10	7226.1	166.71	0.71	5.34	0.24	1.84
20	1579.6	5.45	0.82	5.57	0.28	1.86
40	345.6	1.06	0.91	6.12	0.17	1.94
50	207.7	1.03	0.92	5.86	0.32	1.87
100	41.6	0.35	0.96	2.57	1.83	1.14

Table S6. Relaxation parameters for 0.1 mM [Cr(N)(pyrrdtc)₂] in deuterated toluene at highest intensity peak. Fitted with a stretched exponential function.

T (K)	T_1 (μs)	95% confidence interval of T_1 fit	β_1	T_m (μs)	95% confidence interval of T_m fit	β_m
5.5	62389.8	978.90	0.66	2.94	2.06	0.50
10	22029.6	177.96	0.73	1.54	0.94	0.50
20	2823.7	97.48	0.79	2.41	0.56	0.56
30	898.1	24.53	0.84	-	-	-
40	413.1	11.42	0.88	8.64	0.37	1.01
50	242.6	6.17	0.92	9.78	0.49	0.95
75	84.8	2.64	0.91	4.39	0.46	0.75
100	36.5	3.13	0.92	1.04	0.96	0.50
125	15.9	2.26	1.02	0.50	0.39	0.56

Table S7. Relaxation parameters for 0.1 mM [Cr(N)(pyrrdtc)₂] in deuterated toluene at highest intensity peak. Fitted with an exponential function.

T (K)	T_m (μs)	95% confidence interval of T_m fit
5.5	13.32	0.69
10	7.60	0.42
20	7.84	0.22
40	8.55	0.10
50	10.40	0.15
75	7.02	0.11
100	5.64	0.23
125	2.58	0.07

Table S8. Relaxation parameters for 0.1 mM [Cr(N)(pyrrdtc)₂] in deuterated toluene at highest intensity peak. Fitted with a bi-exponential function.

T (K)	T_{m1} (μs)	95% confidence interval of T_{m1} fit	T_{m2} (μs)	95% confidence interval of T_{m2} fit	k_2/k_1
5.5	19.39	0.81	2.26	0.24	7.2
10	14.63	0.42	1.97	0.09	7.1
20	10.09	0.29	1.81	0.20	2.7
40	8.65	0.14	0.72	0.97	3.4
50	10.66	0.20	0.85	0.57	3.9
75	8.36	0.51	2.70	0.76	0.9
100	7.60	0.97	1.76	0.68	2.8
125	4.29	1.25	1.73	0.41	6.3

Table S9. Relaxation parameters for 1 mM [Cr(N)(pyrrdtc)₂] in deuterated DCM/toluene at highest intensity peak. Fitted with a stretched exponential function.

T (K)	T_1 (μs)	95% confidence interval of T_1 fit	β_1	T_m (μs)	95% confidence interval of T_m fit	β_m
15	2634.1	16.11	0.83	2.55	0.22	0.57
25	935.0	2.21	0.89	3.15	0.20	0.67
50	213.9	0.57	0.93	4.05	0.16	0.81
75	85.4	0.27	0.95	2.40	0.16	0.83
100	41.3	0.12	0.96	0.50	0.21	0.62
125	19.1	0.35	0.97	-	-	-

Table S10. Relaxation parameters for 1 mM [Cr(N)(pyrrdtc)₂] in deuterated DCM/toluene at highest intensity peak. Fitted with an exponential function.

T (K)	T_m (μs)	95% confidence interval of T_m fit
15	7.90	0.12
25	6.77	0.08
50	5.80	0.04
75	3.47	0.02
100	1.99	0.03

Table S11. Relaxation parameters for 1 mM [Cr(N)(pyrrdtc)₂] in deuterated DCM/toluene at highest intensity peak. Fitted with a bi-exponential function.

T (K)	T_{m1} (μs)	95% confidence interval of T_{m1} fit	T_{m2} (μs)	95% confidence interval of T_{m2} fit	k_2/k_1
15	10.28	0.19	2.42	0.16	1.785685
25	11.25	0.79	4.42	0.26	3.01688
50	6.81	0.24	2.84	0.41	0.793951
75	5.44	1.17	2.89	0.26	5.7192
100	3.86	0.98	1.59	0.14	1.690822

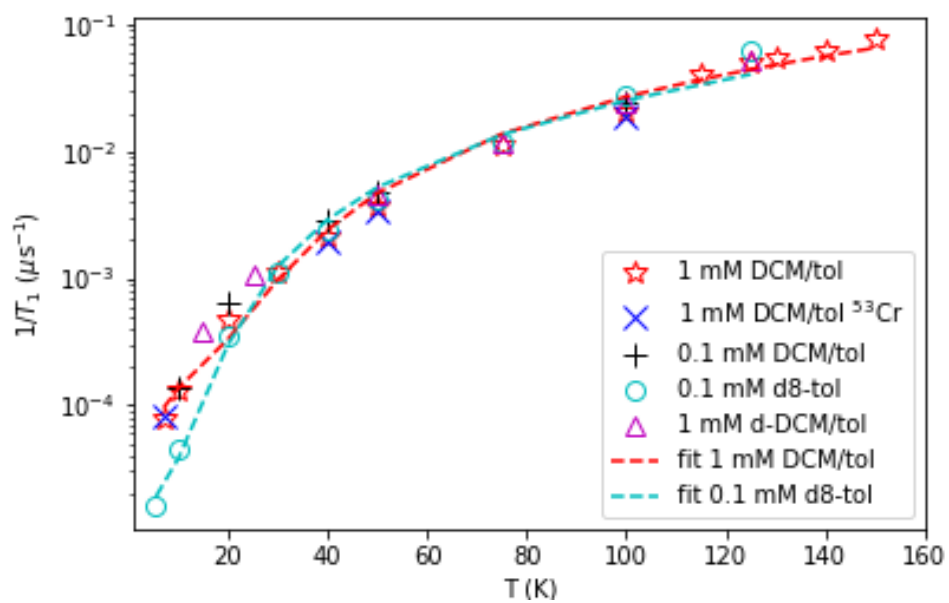


Figure S5. $1/T_1$ vs temperature for $[Cr(N)(pyrrdtc)_2]$ in various frozen solutions. Dashed lines represents best fits using equation 6.

Table S12. Relaxation parameters for 0.8% [Cr(N)(pyrrdtc)₂]₂@[Re(N)(pyrrdtc)₂] at highest intensity peak. Fitted with an exponential function.

T (K)	T_1 (μs)	95% confidence interval of T_1 fit	T_m (μs)	95% confidence interval of T_m fit
10	17280.1	1390.09	0.88	0.04
20	4049.1	250.28	0.83	0.05
40	401.3	20.36	0.81	0.03
50	202.9	8.88	0.81	0.06
75*	71.2	2.16	0.44	0.01
100*	35.0	0.78	0.44	0.02
150*	14.8	0.25	0.31	0.01
200*	7.4	0.18	0.32	0.01
250*	4.4	0.06	0.31	0.01
293*	2.7	0.05	0.30	0.01

* T_m measured with short pulses (64 ns π -pulse)

Table S13. Relaxation parameters for 0.8% [Cr(N)(pyrrdtc)₂]₂@[Re(N)(pyrrdtc)₂] at highest intensity peak. Fitted with a stretched exponential function.

T (K)	T_1 (μs)	95% confidence interval of T_1 fit	β_1	T_m (μs)	95% confidence interval of T_m fit	β_m
10	153.4	42.21	0.20	0.15	0.334736	0.575348
20	366.7	54.80	0.31	0.17	0.522797	0.611478
40	107.3	5.30	0.44	0.18	0.295009	0.621405
50	78.9	1.97	0.51	0.18	0.636566	0.61977
75*	44.3	0.77	0.64	0.28	0.09709	0.83691
100*	26.1	0.43	0.73	0.43	0.260646	0.983707
150*	12.9	0.23	0.85	0.88	0.011656	2.946597
200*	6.7	0.18	0.89	0.90	0.01016	3
250*	4.1	0.06	0.93	0.89	0.008229	3
293*	2.6	0.05	0.95	0.87	0.007675	3

* T_m measured with short pulses (64 ns π -pulse)

Table S14. Relaxation parameters for 0.8% [Cr(N)(pyrrdtc)₂]₂@[Re(N)(pyrrdtc)₂] at highest intensity peak. Fitted with a bi-exponential function.

T (K)	$T_{1,1}$ (μs)	95% confidence interval of $T_{1,1}$ fit	$T_{1,2}$ (μs)	95% confidence interval of $T_{1,2}$ fit	k_2/k_1
10	20764.5	464.65	109.2	7.67	3.125674
20	4866.9	65.32	61.6	2.61	2.166196
40	606.0	6.09	40.3	1.00	1.422468
50	324.6	3.39	33.6	0.81	1.288003
75	106.4	1.98	17.0	0.81	0.904653
100	47.9	1.14	10.8	0.77	0.681926
150	17.4	0.59	5.2	0.92	0.350599
200	8.5	0.56	3.1	1.09	0.327786
250	4.9	0.34	2.5	0.75	0.342583
293	3.0	0.42	1.8	0.88	0.400683

Table S15. Relaxation parameters for 4% [Cr(N)(pyrrdtc)₂]₂@[Re(N)(pyrrdtc)₂] at highest intensity peak. Fitted with an exponential function.

T (K)	T_1 (μs)	95% confidence interval of T_1 fit	T_m (μs)	95% confidence interval of T_m fit
10	3086.5	588.61	0.057	0.0007

9 Density Funtional Theory

Table S16. Calculated IR spectrum of $[Cr(N)(pyrrdtc)_2]$ obtained from DFT calculations. With normal modes in the range of the fitted Δ_{loc} parameters and notes on the affiliation of the most displaced atoms of each normal mode: donor = S or N atoms bound to Cr and ligand = internal vibration of the pyrrolidine dithiocarbamate H, C or N atoms.

Normal mode Nr.	Frequency (cm ⁻¹)	T ² (intensity)	Affiliation of most displaced atoms
18	197.03	0.334209	Donor
19	218.25	0.064727	Donor
20	240.21	3.52427	Donor
21	244.34	6.37228	ligand
22	250.3	0.395222	ligand
23	250.57	1.320571	ligand
24	259.67	0.01328	Donor
25	272.32	0.406854	Donor
26	336.15	6.389994	Donor
27	359.2	15.94491	Donor
28	381.23	216.3084	Donor
29	406.76	0.049493	Donor
30	409.67	13.82229	Donor
31	437.6	0.659672	Donor
32	444.61	0.642519	Donor
33	533.66	0.002157	ligand
34	537.4	0.646201	ligand
35	564.51	1.495835	ligand
36	566	3.150759	ligand
37	691.54	7.59072	ligand
38	691.76	3.668521	ligand
39	818.86	49.86774	ligand
40	819.12	14.67178	ligand
41	849.69	2.815475	ligand
42	850.05	3.273381	ligand
43	876.98	1.006446	ligand
44	877.33	0.542995	ligand
45	893.48	0.043789	ligand
46	893.97	4.80357	ligand
47	909.47	3.063181	ligand
48	909.59	8.697148	ligand
49	927.14	0.30922	ligand
50	931.64	116.1182	ligand
51	980.11	0.067482	ligand
52	985.96	67.87846	ligand
53	1018.28	2.626605	ligand
54	1018.48	3.852542	ligand
55	1078.93	19.46958	ligand
56	1079.22	7.30687	ligand
57	1113.11	243.1262	Cr-N (experimentally 991 cm ⁻¹)

References

- (1) Stoll, S.; Schweiger, A. EasySpin, a Comprehensive Software Package for Spectral Simulation and Analysis in EPR. *J. Magn. Reson.* 2006, 178 (1), 42-55. <https://doi.org/10.1016/j.jmr.2005.08.013>.
- (2) Lide, D. R. ENTHALPY OF FUSION. In *CRC Handbook of Physics and Chemistry*; Lide, D. R., Ed.; CRC Press: Boca Raton, FL, 2005; pp 6–112.
- (3) Lide, D. R. Cryoscopic Constants for Calculation Of Freezing Point Depression. In *CRC Handbook of Physics and Chemistry*; Lide, D. R., Ed.; CRC Press: Boca Raton, FL, 2005; pp 15–28.
- (4) Lide, D. R. Physical Constants of Organic Compounds. In *CRC Handbook of Physics and Chemistry*; Lide, D. R., Ed.; CRC Press: Boca Raton, FL, 2005.
- (5) Birk, T.; Bendix, J. Atom Transfer as a Preparative Tool in Coordination Chemistry. Synthesis and Characterization of Cr(V) Nitrido Complexes of Bidentate Ligands. *Inorg. Chem.* **2003**, 42 (23), 7608–7615. <https://doi.org/10.1021/ic034777f>.

3. Playing with the Field: Extending 4f Qubits Beyond Liquid Nitrogen Temperatures

3.1 Preface

This article investigates the magnetic relaxation properties of the Gd(trensal) complex (trensal = 2,2',2''-tris(salicylideneimino)triethylaminen, $(N(C_2NCC_6O)_3)^{3-}$). It is a continuation of previous work where Gd(trensal) showed long phase memory time (T_m) in high field EPR measurements. In this article the magnetic relaxation properties are measured with X-band EPR, to see how the system behaves at lower field.

The project was initiated by Dr Stergios Piligkos. Synthesis and AC susceptibility experiments were performed by Dr Christian D. Buch under the supervision of Dr Stergios Piligkos. The EPR measurements and fitting and interpretation of data were done by Jonatan B. Petersen.

The introduction of the article is written by Jonatan B. Petersen in collaboration with Dr Christian D. Buch under the supervision of Prof. Richard E. P. Winpenny, Prof. Eric J. L. McInnes and Dr Stergios Piligkos. The rest of the article is written by Jonatan B. Petersen under the supervision of Prof. Richard E. P. Winpenny and Prof. Eric J. L. McInnes. An alternative version, rewritten from this manuscript by Dr Buch and Dr Piligkos, is in progress and expected to be submitted for publication soon after this thesis.

This page is intentionally left blank

Playing with the Field: Extending 4f Qubits Beyond Liquid Nitrogen Temperatures

Christian D. Buch^{1‡}, Jonatan B. Petersen^{2‡}, Richard E. P. Winpenny², Eric J. L. McInnes² and Stergios Piligkos^{1*}

¹ University of Copenhagen, Universitetsparken 5, DK-2100 Copenhagen, Denmark

² Department of Chemistry, School of Natural Sciences, The University of Manchester, Oxford Road, Manchester M13 9PL, United Kingdom

KEYWORDS: *Lanthanides, Crystal Field, Quantum bits, pulse EPR.*

ABSTRACT: Ln(trensal) complexes (Ln=Yb or Gd, H₃trensal = 2,2',2''-tris(salicylideneimino)triethylamine) have previously been investigated as model qubit systems. The Gd(III) complex was studied with pulsed electron paramagnetic resonance spectroscopy at high field and an extra-ordinarily long phase memory time (T_m) for a lanthanide was found: 12 μ s at 3 K. Even at the lowest temperature T_m was restricted by spin-lattice relaxation (T_1), which was likely short due to direct relaxation promoted by the magnetic field. In this paper we study single crystals of Gd(trensal) at lower field with pulsed X-band EPR spectroscopy and AC susceptibility measurements, to clarify its relaxation behavior. With EPR we measured T_1 and T_m at all seven allowed transitions and found that T_m correlated with the strength of the field, while the field dependence of T_1 was more complicated. Analysis of the temperature dependence of T_1 of the $|-1/2\rangle \rightarrow |+1/2\rangle$ and $|-7/2\rangle \rightarrow |-5/2\rangle$ m_s transitions found that below 7 K the direct relaxation dominated, above 10 K the Raman mechanism dominated and above 40 K relaxation via local mode vibrations of the ligand donor atoms are significant contributor. Best fit parameters for all three processes indicate that the difference in relaxation rate between the two transitions is dependent on the specific transition rather than the strength of the field. T_m is lower at X-band than in previous high frequency EPR experiments, and we explain the field dependence of T_m to increasing spin polarization of the system decreasing spin decoherence. Finally, Rabi oscillations were measured to show that Gd(trensal) can be initialized in superposition states at either transition.

INTRODUCTION

Quantum information processing (QIP) promises to be the next revolution within the field of computation. Using quantum algorithms such as Grover's algorithm¹ for searching for entries in large databases or Shor's algorithm² for prime factorization, quantum computers offer tremendous computational improvements over classical computers. Google claimed to have demonstrated this "quantum supremacy" for the first time in 2019.³ Additionally, quantum computers offer the potential of much faster calculations on quantum systems, as they themselves are a quantum system.⁴ The smallest logical part of a quantum computer is the quantum bit (qubit). This is a two-level system, where the two levels can be placed in an arbitrary superposition $|\phi\rangle = \alpha|0\rangle + \beta|1\rangle$.⁵ Many different systems have been proposed as qubit candidates including superconductors,⁶ doped silicon,^{7,8} ion traps,⁹ nitrogen vacancies in diamonds,^{10–12} photons,¹³ quantum dots,¹⁴ atoms on surfaces,¹⁵ and single-molecule magnets (SMMs).^{16–19} SMMs and paramagnetic molecules in general are interesting qubit candidates, as their molecular origin means that they can easily be tuned by small chemical adjustments, be it changing the organic backbone or the paramagnetic center.²⁰ Recently, a number of different studies have been published on molecular spin qubits.^{21–29} Many of these studies are centred around transition metal ions chiefly focused on S=1/2 systems and in particular complexes of vanadium(IV) and copper(II).^{30–34} While the latest

research on SMMs has focused on 4f based complexes, these are less well-studied as molecular qubit candidates. The characteristic photoluminescence of lanthanide systems may be exploited to read out the quantum state of a system, a major advantage of lanthanide complexes over other qubit candidates.³⁵

We have studied the static and dynamic electronic properties of the Ln(trensal) complexes, H₃trensal = 2,2',2''-tris(salicylideneimino)triethylamine).^{36–39} Yb(III) has the ground multiplet $^2F_{7/2}$, which in Yb(trensal) is split into four Kramers doublets by the crystal field (CF) imposed by the trensal ligand.

The ground doublet is thermally isolated from the first excited doublet by ~ 460 cm⁻¹, making Yb(trensal) a pseudo S=1/2 system at low temperatures. Using pulsed EPR the coherence properties of the ground doublet were studied by measuring the spin-lattice relaxation (T_1) and phase-memory time (T_m).³⁶ T_1 describes the time it takes to restore longitudinal magnetization to equilibrium while T_m describes the time it takes to lose phase coherence. The magnitude of the two relaxation times is connected via the relation $2T_1 \geq T_m$, meaning T_1 can be a limit to the extent of T_m . For Yb(trensal) T_m remained almost constant between 3–8 K at 0.5 μ s. Above 8 K the spin lattice relaxation (T_1) starts to limit T_m , which becomes immeasurable above 20 K.

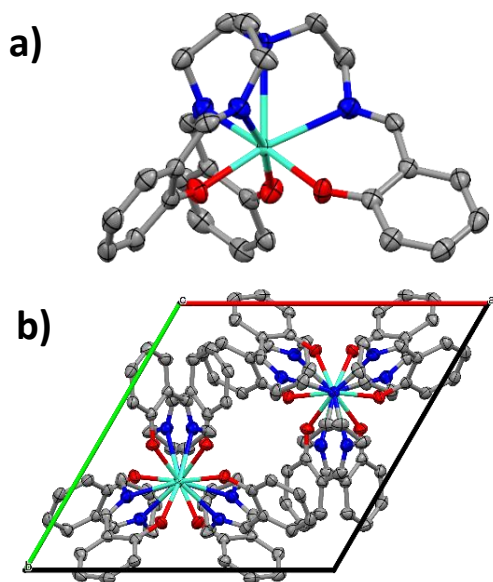


Figure 1. a) Crystal structure of Gd(trensal) viewed perpendicular to the molecular C_3 axis. b) Unit cell of Gd(trensal) viewed along the crystallographic c axis. Ellipsoids are set to 90% probability. Hydrogens have been omitted for clarity. Colour scheme: C, grey; N, blue; O, red; Gd, cyan.

Since T_1 acts as the limiting factor for T_m at high temperatures, we sought a way to extend T_1 by limiting the coupling between the electron spin and the lattice. We did this by exchanging Yb(III) for Gd(III), which has a $^8S_{7/2}$ ground multiplet, with a quenched orbital angular momentum. For such electron configurations the coupling between the electrons and the lattice is greatly reduced.²⁹ In a first study we have investigated the coherence properties of Gd@Y(trensal) doped at 0.5 % (**1**) at 240 GHz (~ 9.88 T).⁴⁰

At the $|-7/2\rangle \rightarrow |-5/2\rangle$ transition at 3 K and 9 T the T_m of **1** is 12 μ s placing it among the 4f qubits with the longest T_m . Contrary to Yb(trensal) the T_m of **1** was not limited by T_1 at high temperatures but instead at low temperatures, with T_1 effectively limiting T_m at 3 K.

It is well-known that T_1 varies greatly with the magnetic field especially if the relaxation mechanism is governed by the direct process.⁴¹ Contrary to our previous study of **1** most molecular qubits are studied in the low field (0.3 – 0.4 T) regime of X-band EPR. In this study we investigate the relaxation of **1** at lower fields to further understand its relaxational behaviour and compare it to the high field experiment.

EXPERIMENTAL SECTION

Synthesis and Crystal Structure. Single crystals of Gd@Y(trensal) with 0.5% (**1**) and 5% (**2**) Gd, were grown according to a literature procedure.³⁹ The Gd(III) ion in Gd(trensal) is heptacoordinated by the trensal ligand, being bonded to a tertiary amine, three imines and three phenoxides. Gd(trensal) crystallizes in the trigonal space group $P\bar{3}c1$ with the crystallographic C_3 axis passing through the metal site, giving the complex perfect

threefold symmetry in the solid state, Figure 1. The crystals of **1** and **2** have the form of elongated hexagonal prisms with the molecular z axis being along the long axis of the crystal.

SQUID Magnetometry. Single crystal AC susceptibility measurements of **2** was performed on a Quantum-Design MPMS-XL SQUID magnetometer with an oscillating field of 3.5 Oe. Measurements were done with a static field of 3000 Oe and varying temperature between 1.9–4.8 K, as well as with varying static fields between 500–4500 Oe at 1.85 K. The crystal was fixed with a tiny amount of grease on a square piece of plastic and oriented with the threefold crystallographic axis parallel to the static magnetic field.

Density Functional Theory. DFT calculations were performed in ORCA version 4.2.1 to get the normal modes and vibrational frequencies of the complex.⁴² The coordinates of the published Yb analogue, with Yb substituted for Lu and Y, was used. Lu and Y were used instead of Gd to simplify the calculations with closed shell systems.⁴³ Numerical frequencies were calculated with the PBE functional with the ma-def2-SVP basis sets using pseudo potentials to correct for the relativistic effects on the lutetium and yttrium.^{44–46}

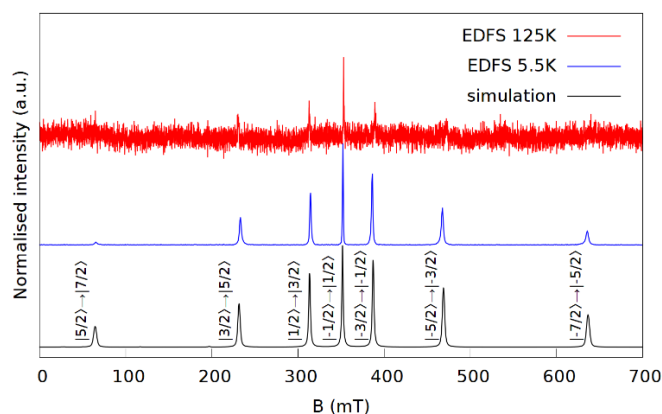


Figure 2. Echo detected field sweeps of **1** with B_0 oriented along z at the highest and lowest temperatures measured: 125 K (red) and 5.5 K (blue), compared to a spectrum simulated using the ZFS parameters previously published (black). For simulation parameters see Table S1.

Pulsed EPR Spectroscopy. Pulsed EPR spectra were recorded at X-band on a Bruker Elexsys E580 spectrometer outfitted with a Bruker ER 4118X-MD5 dielectric resonator. The setup was cooled by a Bruker Flexline Cryogen-free system and the temperature controlled with an Oxford Instruments Mercury ITC. A single crystal of **1** was placed with the unique axis parallel to the magnetic field. To make sure that the crystal was placed correctly echo detected field sweeps (EDFSs) were compared to a simulated spectrum based on the the zero-field splitting parameters obtained in our previous study, Figure 2 (see Table S1 for parameter values). The EDFS spectrum of **1** displays the expected seven allowed transitions ($\Delta m_s = \pm 1$) between the $2S + 1$ states of the $^8S_{7/2}$ Gd(III) ground multiplet. The EDFS also

shows the same relative intensities predicted by the cw EPR spectrum.

T_1 and T_m were measured using inversion recovery and Hahn-echo decay pulse sequences π - t - $\pi/2$ - τ - π - τ -echo and $\pi/2$ - τ - π - τ -echo, respectively. Inversion recovery data were fitted to a simple exponential function, a bi-exponential function was also tried, but did not offer a significant improvement of the fits. In the T_m measurements a large degree of ESEEM was observed with a frequency of $\omega \approx 1$ MHz at 352 mT, due to coupling between the electron spin and the nuclear spin of the nitrogens in the complexes. This coupling was not observed in the previous study, as it was conducted in the high field regime where transitions causing ESEEM are less allowed. The large degree of ESEEM made it difficult to fit the Hahn-echo decay to stretched or bi-exponential functions. These gave inconsistent results, likely due to overparameterization, with bi-exponentials yielding very high numbers and stretched exponentials very low ones. The curves were instead modelled with a more robust mono-exponential decay to extract T_m . At low temperatures the ESEEM effect was suppressed by using long pulses, but due to the decrease in T_m with increasing temperature this was not possible to do this at temperatures above 20 K. In the X-band domain the total energy splitting of the $^8\text{S}_{7/2}$ is only 0.4-3.5 cm^{-1} between 0 - 7000 G. Therefore, the depopulation effects observed below 20 K in our previous high field regime study were not observed here, even at the lowest attainable temperature of 5.5 K. This means that T_1 and T_m could be studied for all seven transitions at the lowest temperature.

RESULTS AND DISCUSSION

In the low field regime SQUID AC susceptibility measurements on a single crystal of $\text{Gd}_{0.05}\text{Y}_{0.95}$ (trensal) (**2**) oriented with the molecular z axis parallel to the static magnetic field of 300 mT revealed that T_1 is about three orders of magnitude larger (~ 10 ms at 3 K) in this field regime compared to the previous measurements at 9 T (~ 30 μs at 3 K). The values of T_1 determined at temperatures between 1.85-4.8 K are shown in Figure 3.

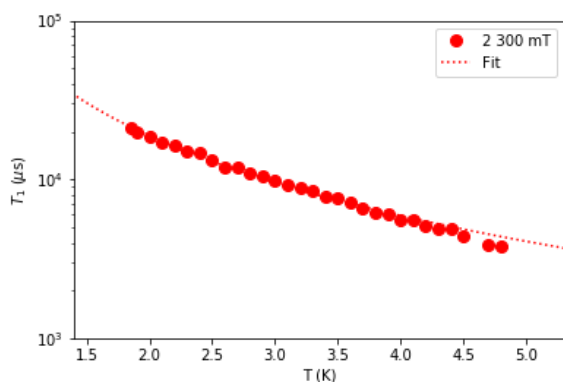


Figure 3. T_1 determined by AC susceptibility measurements of **2** at various temperatures with a static field of 300 mT along the z -axis, the dotted line shows the trend of the

temperature dependence $T_1 = a \cdot T^{-n}$ with $a = 0.066 \text{ s K}^n$ and $n = 1.8$.

The spin lattice relaxation of the Yb analogue followed a temperature dependence of $T_1 \propto T^{-n}$ with $n \approx 6$ and **1** at high field followed $n \approx 0.44$. The temperature dependence of **2** fitted to the same power law approximately gives $n \approx 1.8$. This low value compared to Yb could be caused by a significant direct process, which is to be expected in this temperature range, but must also be incorporating some other processes, likely Raman, since n is larger than in the high field experiment.

With T_1 extended to the ms scale, the limit on T_m from the high field regime is lifted, T_m in the low field regime could be much larger than the 12 μs measured at high field.

In order to study T_m in low field, pulsed EPR studies at X-band frequencies ($\nu = 9.6$ GHz) were performed on a single crystal of **1**. In Figure 4 the field dependence of T_1 and T_m at 5.5 K is shown.

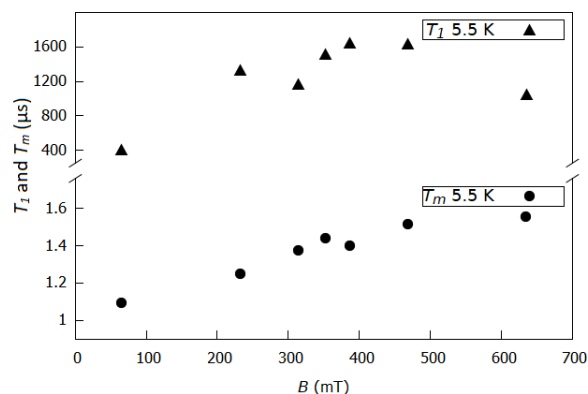


Figure 4. Field dependence of T_1 and T_m for the seven allowed EPR transitions of **1** from EPR at 5.5 K with the unique axis along the magnetic field.

T_1 at 5.5 K varies between 397 μs and 1646 μs at the different transitions, making T_1 only slightly lower than those expected from extrapolating the SQUID data to this temperature (3.2 ms). T_1 of the transitions below 386 mT has a rising trend with the field, it is then the same for the transitions at 386 mT and 468 mT, but falls at the highest field transition. This trend could either be interpreted as transition dependent or field dependent. At first glance this field dependence of T_1 of **1** is like that of the AC susceptibility measurement at 1.85 K (Figure S6), though with a peak at around 400 mT rather than 200 mT. In the AC susceptibility experiment the field dependence is caused by an initial increase of T_1 from suppressing of the quantum tunnelling of the magnetisation (QTM), while the subsequent decrease of T_1 is caused by the increase of the rate of the direct process. For EPR an interpretation with one process being quenched by the field and another being promoted could be valid, but likely not with the same processes involved, since in the EPR experiment we are observing allowed transitions (making QTM less relevant). Furthermore, the field dependence of the direct process

is linked to the increased energy difference between the initial and final state, which is the same for all the transitions, since they are all measured at the same frequency. The trend could be caused by field dependent Raman processes, Van Vleck derived the field dependence of the first order Raman mechanism, which can either be increased or decreased proportional to the field, though this phenomenon is rarely encountered in the literature.^{47–49}

If it is instead due to the nature of the transitions, it means the transitions involving lower m_s states (middle of the spectrum) have lower spin-lattice relaxation rates, than the ones involving higher m_s states (wings of the spectrum).

Surprisingly T_m is lower at X-band than at high field varying between 1.10 – 1.55 μ s compared to 4.3 μ s measured for the $|-7/2\rangle \rightarrow |-5/2\rangle$ transition at 5.5 K and 240 GHz. The variation in T_m seems linked to the magnetic field with the transition at lowest magnetic field (65 mT, $|5/2\rangle \rightarrow |7/2\rangle$) having the shortest coherence time while the transition at highest magnetic field (637 mT, $|-7/2\rangle \rightarrow |-5/2\rangle$) has the longest coherence time, as shown in Figure 4. This effect could be the spins of the matrix, the cause of spin-spin relaxation, being increasingly polarized by the field and thus decreasing T_m . If this is the case, it would explain why the high field EPR measurements found considerably higher values of T_m .

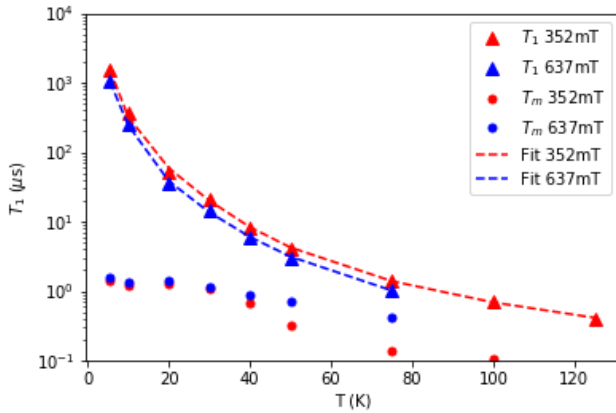


Figure 5. Temperature dependence of the T_1 and T_m EPR measurements of **1**. The measurements were performed at 352 mT (red) and 637 mT (blue) using 64 ns π -pulses.

T_1 and T_m were measured at varying temperatures from 5.5 K up until there was no observable signal, at two transitions: $|-1/2\rangle \rightarrow |1/2\rangle$ (352 mT) and $|-7/2\rangle \rightarrow |-5/2\rangle$ (637 mT) (data shown in figure 5). The lower signal intensity of the 637 mT transition meant that there was no signal above 75 K and for the transition at 352 mT above 125 K. At 352 mT, T_1 goes from 1.5 ms at 5.5 K to 0.4 μ s at 125 K. At 637 mT T_1 is consistently lower by about 30%, which would only be expected at low temperature if this is caused by the field promoting relaxation via the direct process. At both 352 mT and 637 mT, the temperature dependence T_1 of **1** roughly follows

a power law, with $n \approx 2.7$, higher than found for the SQUID measurement, due the lesser influence of the direct process at higher temperature, but again much lower than for Yb(III). A temperature dependence of $T_1 \propto T^{-2.7}$ is very similar to what has been observed for Gd^{3+} doped into CaWO_4 and for $S=1/2$ species like vanadyl.^{31,50}

T_m was measured at the same temperatures as T_1 , except at 125 K where relaxation was so rapid that the value of T_m could not be accurately determined with the same pulse sequence. Below 30 K T_m is largely independent of temperature, but then starts decreasing at higher temperature. At low temperature T_m is the same at the two transitions, at high temperature this is no longer the case. At 50 K T_m is twice as high at 637 mT and at 75 K it is 3 times as high, making T_m of the 352 mT transition far more sensitive to the temperature. This is contrary to what is expected from the relative size of T_1 for the two, where the longer spin lattice relaxation of the first transition would be expected to affect T_m less and not the other way around.

To investigate spin-lattice relaxation in further detail the temperature dependence of T_1 was modelled in detail using equation 1.^{51,52}

$$T_1^{-1} = A_{dir} \cdot T + A_{Ram} \cdot \left(\frac{T}{\theta_D}\right)^9 \cdot J_8 \left(\frac{\theta_D}{T}\right) + A_{loc} \cdot \left(\frac{e^{\Delta_{loc}/T}}{(e^{\Delta_{loc}/T} - 1)^2}\right) \quad (1)$$

Where A_{dir} , A_{Loc} and A_{Ram} are fitting parameters scaling the efficiency of the direct, Raman and local mode relaxation mechanisms respectively, θ_D is the Debye temperature, denoting the temperature at which all phonon modes are populated, Δ_{loc} is the energy of a local mode responsible for the relaxation and J_8 is the transport integral (see SI section 6). The Orbach mechanism was ignored since the magnitude of ZFS is too small to act as a significant barrier to reversal of the magnetization, and the thermally activated processes, relaxation related to the thermal activation of certain modes like the rotation of methyl groups, was neglected, as the three terms were enough to get an adequate fit.

Table 1. Best fit parameters temperature for dependence of spin lattice relaxation with equation 1.

B (mT)	A_{dir} ($10^2 \text{ s}^{-1} \text{ K}^{-1}$)	A_{Ram} (10^6 s^{-1})	θ_D (K)	A_{loc} (10^6 s^{-1})	Δ_{loc} (K)
352	1.1	0.9	47	5.3	204
637	1.6	1.1	44	7.1	202

The parameters obtained by least squares fitting of T_1 to equation 1 are listed in Table 1. The relaxation pathways seem to be almost independent of the transition as parameters found for the two transitions are remarkably similar. As expected, the direct term is more efficient at higher fields, however all three processes are fitted to be more efficient at 637 mT. The Debye temperatures are

low for molecular solids, but still within ranges observed in the literature.⁵¹ Values of Δ_{Loc} of around 200 K (140 cm⁻¹) are in the range where DFT calculation predict vibrations of the ligated oxygen atoms in Y(trensall) and Lu(trensall) (See Table S11 and S12).

From the best fit parameters, the individual contribution of the three terms in equation 1 can be calculated, the result is visualized in Figure 6. At low temperature the direct process is the main relaxation process up until 7 K, where the Raman process becomes co-dominant from 7-10 K. From 10 K the Raman process is dominant until local mode processes become a significant contributor at around 40 K. These two mechanisms then both contribute significantly over the rest of the experimental range with relaxation via local mode processes overtaking the Raman mechanism around 70 K.

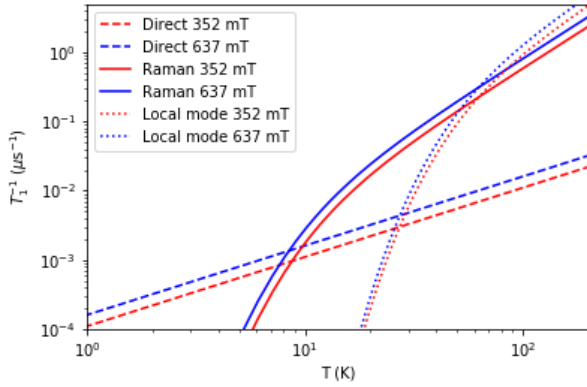


Figure 6. Contributions of the individual relaxation mechanisms calculated from the extracted parameters using the terms in equation 1.

The parameters for all the three spin-lattice relaxation mechanisms are incorporating the increased relaxation rate between 352 mT and 637 mT. The differences in Θ_D and Δ_{Loc} at the two transitions are small enough that they are within the uncertainty of the fit, and they would be expected to be the same since they are properties of the lattice, independent of the spin and the magnetic field. The difference in relaxation must then come from the three scaling parameters, A_{dir} , A_{loc} and A_{Ram} . It seems therefore that the nature of the transitions plays a role in the relaxation rate, since these three parameters incorporate probabilities of the spin-phonon transitions.

In order for a magnetic molecule to be used as a qubit it must be possible to initialize it in any arbitrary superposition of $|0\rangle$ and $|1\rangle$ and retain the information. To show that **1** is able to do this we performed nutation experiments (p-t- $\pi/2$ - τ - π - τ -echo) with microwave pulses of varying power, to observe Rabi oscillations (Figure 7a). The frequencies of the Rabi oscillations (Ω_R) were extracted by finding the peaks in their Fourier transform. The Rabi frequencies are shown in Figure 7b plotted against the relative magnitude of the magnetic field component of the microwave pulse.

The Rabi frequencies of the two transitions both display a linear dependence on B_1 , though with different

gradients as is to be expected with the different spin-state involved in the transitions according to the relation

$$\Omega_R = \frac{2\pi g \mu_B B_1}{\hbar} \sqrt{S(S+1) - m_s(m_s+1)} \quad (2).$$

Where μ_B is the Bohr magneton and \hbar is the Planck constant. In Figure 7 the fit of the obtained values of Ω_R to equation 2 using a scaling factor for the relative B_1 to the effective B_1 as the fitting parameter. This results in perfect agreement of the two datasets using a B_1 scaling factor of 0.086 G.

CONCLUSIONS

We have studied the magnetic relaxation properties of Gd(trensall) using X-band pulsed EPR spectroscopy. We measured T_1 and T_m at all seven allowed transitions at low temperature with the field aligned with the molecular C_3 axis. Spin lattice relaxation between the transitions followed a curve, which could be interpreted in one of two ways. Either T_1 is transition dependent or the curve resembles the field dependence of relaxation mechanisms such as, quantum tunneling or a field dependent Raman Process and direct process. The field dependence of T_1 measured by AC susceptibility has a sharper peak with maximum T_1 at lower field.

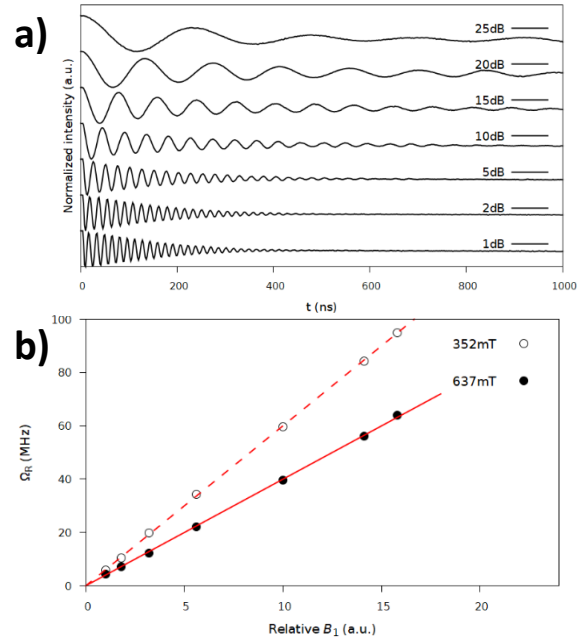


Figure 7. a) Rabi oscillations of **1** recorded at 30 K and 637 mT. b) Rabi frequencies plotted against the relative magnitude of the magnetic field component of the microwave pulse (B_1), lines indicate the best fits with equation 2.

T_1 at the $|-1/2\rangle \rightarrow |1/2\rangle$ (352 mT) and $|-7/2\rangle \rightarrow |-5/2\rangle$ (637 mT) transitions were measured at different temperatures and found to be around 30% lower at the higher field. The temperature dependence was modelled with direct, Raman and local mode mechanisms. It was found that relaxation goes via the direct mechanism below 7 K, Raman mechanism above 10 K and via local mode vibrations of the ligated atoms at high temperature. The parameters indicated that the difference in T_1 between

the transitions arises from the character of the transition rather than the strength of the field. We found that reduced coupling of the Gd(III) $^8S_{7/2}$ ground state to the crystal field compared to the Yb(III) does indeed lead to lower temperature dependence of T_1 .

T_m is lower at X-band ($\sim 1.5 \mu\text{s}$) than at our previous high field experiments, though T_m being less restricted by T_1 should lead to larger values of T_m , in this case these are about an order of magnitude lower than the value of 12 μs previously measured at 9 T. T_m was found to increase with the field strength. We believe this could be due to spin-polarization by the field, which explains the discrepancy between the values found at X-band and high frequency EPR.

AUTHOR INFORMATION

Corresponding Author

*Stergios Piligkos, piligkos@chem.ku.dk

Author Contributions

The manuscript was written through contributions of all authors. All authors have given approval to the final version of the manuscript. ‡These authors contributed equally in the writing process.

ACKNOWLEDGMENT

JBP is supported by a European Research Council Advanced Grant to REPW (ERC-2017-ADG-786734). We also thank the EPSRC(UK) EPR National Research Facility (NS/A000055/1) for access to EPR spectrometers.

REFERENCES

- (1) Grover, L. K. Quantum Computers Can Search Arbitrarily Large Databases by a Single Query. *Phys. Rev. Lett.* **1997**, *79* (23), 4709–4712. <https://doi.org/10.1103/PhysRevLett.79.4709>.
- (2) Shor, P. W. Algorithms for Quantum Computation: Discrete Logarithms and Factoring. In *Proceedings 35th Annual Symposium on Foundations of Computer Science*; 1994; pp 124–134. <https://doi.org/10.1109/SFCS.1994.365700>.
- (3) Arute, F.; Arya, K.; Babbush, R.; Bacon, D.; Bardin, J. C.; Barends, R.; Biswas, R.; Boixo, S.; Brandao, F. G. S. L.; Buell, D. A.; Burkett, B.; Chen, Y.; Chen, Z.; Chiaro, B.; Collins, R.; Courtney, W.; Dunsworth, A.; Farhi, E.; Foxen, B.; Fowler, A.; Gidney, C.; Giustina, M.; Graff, R.; Guerin, K.; Habegger, S.; Harrigan, M. P.; Hartmann, M. J.; Ho, A.; Hoffmann, M.; Huang, T.; Humble, T. S.; Isakov, S. V.; Jeffrey, E.; Jiang, Z.; Kafri, D.; Kchedzhi, K.; Kelly, J.; Klimov, P. V.; Knysh, S.; Korotkov, A.; Kostriksa, F.; Landhuis, D.; Lindmark, M.; Lucero, E.; Lyakh, D.; Mandrà, S.; McClean, J. R.; McEwen, M.; Megrant, A.; Mi, X.; Michielsen, K.; Mohseni, M.; Mutus, J.; Naaman, O.; Neeley, M.; Neill, C.; Niu, M. Y.; Ostby, E.; Petukhov, A.; Platt, J. C.; Quintana, C.; Rieffel, E. G.; Roushan, P.; Rubin, N. C.; Sank, D.; Satzinger, K. J.; Smelyanskiy, V.; Sung, K. J.; Trevithick, M. D.; Vainsencher, A.; Villalonga, B.; White, T.; Yao, Z. J.; Yeh, P.; Zalcman, A.; Neven, H.; Martinis, J. M. Quantum Supremacy Using a Programmable Superconducting Processor. *Nature* **2019**, *574* (7779), 505–510. <https://doi.org/10.1038/s41586-019-1666-5>.
- (4) Lanyon, B. P.; Whitfield, J. D.; Gillett, G. G.; Goggin, M. E.; Almeida, M. P.; Kassal, I.; Biamonte, J. D.; Mohseni, M.; Powell, B. J.; Barbieri, M.; Aspuru-Guzik, A.; White, A. G. Towards Quantum Chemistry on a Quantum Computer. *Nat. Chem.* **2010**, *2* (2), 106–111. <https://doi.org/10.1038/nchem.483>.
- (5) Aromí, G.; Aguilà, D.; Gamez, P.; Luis, F.; Roubeau, O. Design of Magnetic Coordination Complexes for Quantum Computing. *Chem. Soc. Rev.* **2012**, *41* (2), 537–546. <https://doi.org/10.1039/C1CS15115K>.
- (6) Clarke, J.; Wilhelm, F. K. Superconducting Quantum Bits. *Nature* **2008**, *453* (7198), 1031–1042. <https://doi.org/10.1038/nature07128>.
- (7) Morley, G. W.; Warner, M.; Stoneham, A. M.; Greenland, P. T.; van Tol, J.; Kay, C. W. M.; Aepli, G. The Initialization and Manipulation of Quantum Information Stored in Silicon by Bismuth Dopants. *Nat. Mater.* **2010**, *9* (9), 725–729. <https://doi.org/10.1038/nmat2828>.
- (8) Steger, M.; Saeedi, K.; Thewalt, M. L. W.; Morton, J. J. L.; Riemann, H.; Abrosimov, N. V.; Becker, P.; Pohl, H.-J. Quantum Information Storage for over 180 s Using Donor Spins in a 28Si “Semiconductor Vacuum.” *Science* (1979) **2012**, *336* (6086), 1280–1283. <https://doi.org/10.1126/science.1217635>.
- (9) Blatt, R.; Wineland, D. Entangled States of Trapped Atomic Ions. *Nature* **2008**, *453* (7198), 1008–1015. <https://doi.org/10.1038/nature07125>.
- (10) Dutt, M. V. G.; Childress, L.; Jiang, L.; Togan, E.; Maze, J.; Jelezko, F.; Zibrov, A. S.; Hemmer, P. R.; Lukin, M. D. Quantum Register Based on Individual Electronic and Nuclear Spin Qubits in Diamond. *Science* (1979) **2007**, *316* (5829), 1312–1316. <https://doi.org/10.1126/science.1139831>.
- (11) Maurer, P. C.; Kucsko, G.; Latta, C.; Jiang, L.; Yao, N. Y.; Bennett, S. D.; Pastawski, F.; Hunger, D.; Chisholm, N.; Markham, M.; Twitchen, D. J.; Cirac, J. I.; Lukin, M. D. Room-Temperature Quantum Bit Memory Exceeding One Second. *Science* (1979) **2012**, *336* (6086), 1283–1286. <https://doi.org/10.1126/science.1220513>.
- (12) Gulka, M.; Wirtitsch, D.; Ivády, V.; Vodnik, J.; Hruby, J.; Magchiels, G.; Bourgeois, E.; Gali, A.; Trupke, M.; Nesladek, M. Room-Temperature Control and Electrical Readout of

- Individual Nitrogen-Vacancy Nuclear Spins. *Nat. Commun.* **2021**, *12* (1), 4421. <https://doi.org/10.1038/s41467-021-24494-x>.
- (13) Knill, E.; Laflamme, R.; Milburn, G. J. A Scheme for Efficient Quantum Computation with Linear Optics. *Nature* **2001**, *409* (6816), 46–52. <https://doi.org/10.1038/35051009>.
- (14) Hanson, R.; Awschalom, D. D. Coherent Manipulation of Single Spins in Semiconductors. *Nature* **2008**, *453* (7198), 1043–1049. <https://doi.org/10.1038/nature07129>.
- (15) Yang, K.; Paul, W.; Phark, S.-H.; Willke, P.; Bae, Y.; Choi, T.; Esat, T.; Ardavan, A.; Heinrich, A. J.; Lutz, C. P. Coherent Spin Manipulation of Individual Atoms on a Surface. *Science* (1979) **2019**, *366* (6464), 509–512. <https://doi.org/10.1126/science.aay6779>.
- (16) Leuenberger, M. N.; Loss, D. Quantum Computing in Molecular Magnets. *Nature* **2001**, *410* (6830), 789–793. <https://doi.org/10.1038/35071024>.
- (17) Stamp, P. C. E.; Gaita-Ariño, A. Spin-Based Quantum Computers Made by Chemistry: Hows and Whys. *J. Mater. Chem.* **2009**, *19* (12), 1718–1730. <https://doi.org/10.1039/B811778K>.
- (18) Thiele, S.; Balestro, F.; Ballou, R.; Klyatskaya, S.; Ruben, M.; Wernsdorfer, W. Electrically Driven Nuclear Spin Resonance in Single-Molecule Magnets. *Science* (1979) **2014**, *344* (6188), 1135–1138. <https://doi.org/10.1126/science.1249802>.
- (19) Vincent, R.; Klyatskaya, S.; Ruben, M.; Wernsdorfer, W.; Balestro, F. Electronic Read-out of a Single Nuclear Spin Using a Molecular Spin Transistor. *Nature* **2012**, *488* (7411), 357–360. <https://doi.org/10.1038/nature11341>.
- (20) Gaita-Ariño, A.; Luis, F.; Hill, S.; Coronado, E. Molecular Spins for Quantum Computation. *Nat. Chem.* **2019**, *11* (4), 301–309. <https://doi.org/10.1038/s41557-019-0232-y>.
- (21) Aguilà, D.; Barrios, L. A.; Velasco, V.; Roubeau, O.; Repollés, A.; Alonso, P. J.; Sesé, J.; Teat, S. J.; Luis, F.; Aromí, G. Heterodimetallic [LnLn'] Lanthanide Complexes: Toward a Chemical Design of Two-Qubit Molecular Spin Quantum Gates. *J. Am. Chem. Soc.* **2014**, *136* (40), 14215–14222. <https://doi.org/10.1021/ja507809w>.
- (22) Macaluso, E.; Rubín, M.; Aguilà, D.; Chiesa, A.; Barrios, L. A.; Martínez, J. I.; Alonso, P. J.; Roubeau, O.; Luis, F.; Aromí, G.; Carretta, S. A Heterometallic [LnLn'Ln] Lanthanide Complex as a Qubit with Embedded Quantum Error Correction. *Chem. Sci.* **2020**, *11* (38), 10337–10343. <https://doi.org/10.1039/D0SC03107K>.
- (23) Fataftah, M. S.; Zadrozny, J. M.; Coste, S. C.; Graham, M. J.; Rogers, D. M.; Freedman, D. E. Employing Forbidden Transitions as Qubits in a Nuclear Spin-Free Chromium Complex. *J. Am. Chem. Soc.* **2016**, *138* (4), 1344–1348. <https://doi.org/10.1021/jacs.5b11802>.
- (24) Shiddiq, M.; Komijani, D.; Duan, Y.; Gaita-Ariño, A.; Coronado, E.; Hill, S. Enhancing Coherence in Molecular Spin Qubits via Atomic Clock Transitions. *Nature* **2016**, *531* (7594), 348–351. <https://doi.org/10.1038/nature16984>.
- (25) Lenz, S.; Bamberger, H.; Hallmen, P. P.; Thiebes, Y.; Otto, S.; Heinze, K.; van Slageren, J. Chromium(III)-Based Potential Molecular Quantum Bits with Long Coherence Times. *Phys. Chem. Chem. Phys.* **2019**, *21* (13), 6976–6983. <https://doi.org/10.1039/C9CP00745H>.
- (26) Ardavan, A.; Rival, O.; Morton, J. J. L.; Blundell, S. J.; Tyryshkin, A. M.; Timco, G. A.; Winpenny, R. E. P. Will Spin-Relaxation Times in Molecular Magnets Permit Quantum Information Processing? *Phys. Rev. Lett.* **2007**, *98* (5), 57201. <https://doi.org/10.1103/PhysRevLett.98.057201>.
- (27) Ferrando-Soria, J.; Moreno Pineda, E.; Chiesa, A.; Fernandez, A.; Magee, S. A.; Carretta, S.; Santini, P.; Vitorica-Yrezabal, I. J.; Tuna, F.; Timco, G. A.; McInnes, E. J. L.; Winpenny, R. E. P. A Modular Design of Molecular Qubits to Implement Universal Quantum Gates. *Nat. Commun.* **2016**, *7* (1), 11377. <https://doi.org/10.1038/ncomms11377>.
- (28) Ariciu, A.-M.; Woen, D. H.; Huh, D. N.; Nodaraki, L. E.; Kostopoulos, A. K.; Goodwin, C. A. P.; Chilton, N. F.; McInnes, E. J. L.; Winpenny, R. E. P.; Evans, W. J.; Tuna, F. Engineering Electronic Structure to Prolong Relaxation Times in Molecular Qubits by Minimising Orbital Angular Momentum. *Nat. Commun.* **2019**, *10* (1), 3330. <https://doi.org/10.1038/s41467-019-11309-3>.
- (29) Kundu, K.; White, J. R. K.; Moehring, S. A.; Yu, J. M.; Ziller, J. W.; Furche, F.; Evans, W. J.; Hill, S. A 9.2-GHz Clock Transition in a Lu(II) Molecular Spin Qubit Arising from a 3,467-MHz Hyperfine Interaction. *Nat. Chem.* **2022**, *14* (4), 392–397. <https://doi.org/10.1038/s41557-022-00894-4>.
- (30) Yu, C.-J.; Graham, M. J.; Zadrozny, J. M.; Niklas, J.; Krzyaniak, M. D.; Wasielewski, M. R.; Poluektov, O. G.; Freedman, D. E. Long Coherence Times in Nuclear Spin-Free Vanadyl Qubits. *J. Am. Chem. Soc.* **2016**, *138* (44), 14678–14685. <https://doi.org/10.1021/jacs.6b08467>.
- (31) Atzori, M.; Tesi, L.; Morra, E.; Chiesa, M.; Sorace, L.; Sessoli, R. Room-Temperature Quantum Coherence and Rabi Oscillations in Vanadyl Phthalocyanine: Toward Multifunctional Molecular Spin Qubits. *J. Am. Chem. Soc.* **2016**, *138* (7), 2154–2157. <https://doi.org/10.1021/jacs.5b13408>.

- (32) Atzori, M.; Morra, E.; Tesi, L.; Albino, A.; Chiesa, M.; Sorace, L.; Sessoli, R. Quantum Coherence Times Enhancement in Vanadium(IV)-Based Potential Molecular Qubits: The Key Role of the Vanadyl Moiety. *J. Am. Chem. Soc.* **2016**, *138* (35), 11234–11244. <https://doi.org/10.1021/jacs.6b05574>.
- (33) Zadrozny, J. M.; Niklas, J.; Poluektov, O. G.; Freedman, D. E. Millisecond Coherence Time in a Tunable Molecular Electronic Spin Qubit. *ACS Cent. Sci.* **2015**, *1* (9), 488–492. <https://doi.org/https://doi.org/10.1021/acscentsci.5b00338>.
- (34) Bader, K.; Dengler, D.; Lenz, S.; Endeward, B.; Jiang, S.-D.; Neugebauer, P.; van Slageren, J. Room Temperature Quantum Coherence in a Potential Molecular Qubit. *Nat. Commun.* **2014**, *5* (1), 5304. <https://doi.org/10.1038/ncomms6304>.
- (35) Siyushev, P.; Xia, K.; Reuter, R.; Jamali, M.; Zhao, N.; Yang, N.; Duan, C.; Kukharchyk, N.; Wieck, A. D.; Kolesov, R.; Wrachtrup, J. Coherent Properties of Single Rare-Earth Spin Qubits. *Nat. Commun.* **2014**, *5* (1), 3895. <https://doi.org/10.1038/ncomms4895>.
- (36) Pedersen, K. S.; Ariciu, A.-M.; McAdams, S.; Weihe, H.; Bendix, J.; Tuna, F.; Piligkos, S. Toward Molecular 4f Single-Ion Magnet Qubits. *J. Am. Chem. Soc.* **2016**, *138* (18), 5801–5804. <https://doi.org/10.1021/jacs.6b02702>.
- (37) Pedersen, K. S.; Dreiser, J.; Weihe, H.; Sibille, R.; Johannesen, H. v; Sørensen, M. A.; Nielsen, B. E.; Sigrist, M.; Mutka, H.; Rols, S.; Bendix, J.; Piligkos, S. Design of Single-Molecule Magnets: Insufficiency of the Anisotropy Barrier as the Sole Criterion. *Inorg. Chem.* **2015**, *54* (15), 7600–7606. <https://doi.org/10.1021/acs.inorgchem.5b01209>.
- (38) Hussain, R.; Allodi, G.; Chiesa, A.; Garlatti, E.; Mitcov, D.; Konstantatos, A.; Pedersen, K. S.; De Renzi, R.; Piligkos, S.; Carretta, S. Coherent Manipulation of a Molecular Ln-Based Nuclear Qudit Coupled to an Electron Qubit. *J. Am. Chem. Soc.* **2018**, *140* (31), 9814–9818. <https://doi.org/10.1021/jacs.8b05934>.
- (39) Pedersen, K. S.; Ungur, L.; Sigrist, M.; Sundt, A.; Schau-Magnussen, M.; Vieru, V.; Mutka, H.; Rols, S.; Weihe, H.; Waldmann, O.; Chibotaru, L. F.; Bendix, J.; Dreiser, J. Modifying the Properties of 4f Single-Ion Magnets by Peripheral Ligand Functionalisation. *Chem. Sci.* **2014**, *5* (4), 1650–1660. <https://doi.org/10.1039/C3SC53044B>.
- (40) Buch, C. D.; Kundu, K.; Marbey, J. J.; van Tol, J.; Weihe, H.; Hill, S.; Piligkos, S. Spin-Lattice Relaxation Decoherence Suppression in Vanishing Orbital Angular Momentum Qubits. *J. Am. Chem. Soc.* **2022**. <https://doi.org/10.1021/jacs.2c07057>.
- (41) Kronig, R. de L. On the Mechanism of Paramagnetic Relaxation. *Physica* **1939**, *6* (1), 33–43. [https://doi.org/https://doi.org/10.1016/S0031-8914\(39\)90282-X](https://doi.org/https://doi.org/10.1016/S0031-8914(39)90282-X).
- (42) Neese, F. The ORCA Program System. *Wiley Interdiscip. Rev. Comput. Mol. Sci.* **2012**, *2* (1), 73–78. <https://doi.org/10.1002/wcms.81>.
- (43) Bernhardt, P. V.; Flanagan, B. M.; Riley, M. J. Rapid Communication: Completion of the Isomorphous Ln(Trensal) Series. *Aust. J. Chem.* **2001**, *54* (4), 229–232.
- (44) Perdew, J. P.; Burke, K.; Ernzerhof, M. Generalized Gradient Approximation Made Simple. *Phys. Rev. Lett.* **1997**, *78* (7), 1396. <https://doi.org/10.1103/PhysRevLett.78.1396>.
- (45) Weigend, F.; Ahlrichs, R. Balanced Basis Sets of Split Valence, Triple Zeta Valence and Quadruple Zeta Valence Quality for H to Rn: Design and Assessment of Accuracy. *Phys. Chem. Chem. Phys.* **2005**, *7* (18), 3297–3305. <https://doi.org/10.1039/B508541A>.
- (46) Dolg, M.; Stoll, H.; Preuss, H. Energy-adjusted Ab Initio Pseudopotentials for the Rare Earth Elements. *J. Chem. Phys.* **1989**, *90* (3), 1730–1734. <https://doi.org/10.1063/1.456066>.
- (47) van Vleck, J. H. Paramagnetic Relaxation Times for Titanium and Chrome Alum. *Phys. Rev.* **1940**, *57* (5), 426–447. <https://doi.org/10.1103/PhysRev.57.426>.
- (48) Soeteman, J.; Bevaart, L.; van Duynveldt, A. J. The Direct and Raman Spin-Lattice Relaxation Process in YbCl₃·6H₂O. *Physica* **1974**, *74* (1), 126–134. [https://doi.org/https://doi.org/10.1016/0031-8914\(74\)90188-8](https://doi.org/https://doi.org/10.1016/0031-8914(74)90188-8).
- (49) Marchand, R. L.; Stapleton, H. J. Observation of an $H^2T^7\sin^2\theta$ Raman Spin-Lattice Relaxation Rate in a Neodymium Salt. *Phys. Rev. B* **1974**, *9* (1), 14–21. <https://doi.org/10.1103/PhysRevB.9.14>.
- (50) Thorp, J. S.; Ammar, E. A. E. Spin-Lattice Relaxation in Gadolinium-Doped Calcium Tungstate. *J. Mater. Sci.* **1976**, *11* (7), 1215–1219. <https://doi.org/10.1007/BF00545138>.
- (51) Eaton, S. S.; Eaton, G. R. Relaxation Times of Organic Radicals and Transition Metal Ions. In *Distance Measurements in Biological Systems by EPR. Biological Magnetic Resonance*, vol 19; Springer, 2002; pp 29–154. https://doi.org/10.1007/0-306-47109-4_2.
- (52) Jackson, C. E.; Moseley, I. P.; Martinez, R.; Sung, S.; Zadrozny, J. M. A Reaction-Coordinate Perspective of Magnetic Relaxation.

3.3 Supporting Information

Playing with the Field: Extending 4f Qubits Beyond Liquid Nitrogen Temperatures

Christian D. Buch¹, Jonatan B. Petersen², Richard E. P. Winpenny², Eric J. L. McInnes² and Stergios Piligkos^{1*}

¹ University of Copenhagen, Universitetsparken 5, DK-2100 Copenhagen, Denmark

² Department of Chemistry, School of Natural Sciences, The University of Manchester, Oxford Road, Manchester M13 9PL, United Kingdom

KEYWORDS: *Lanthanides, Crystal Field, Quantum bits, pulse EPR*

1 EPR spectroscopy

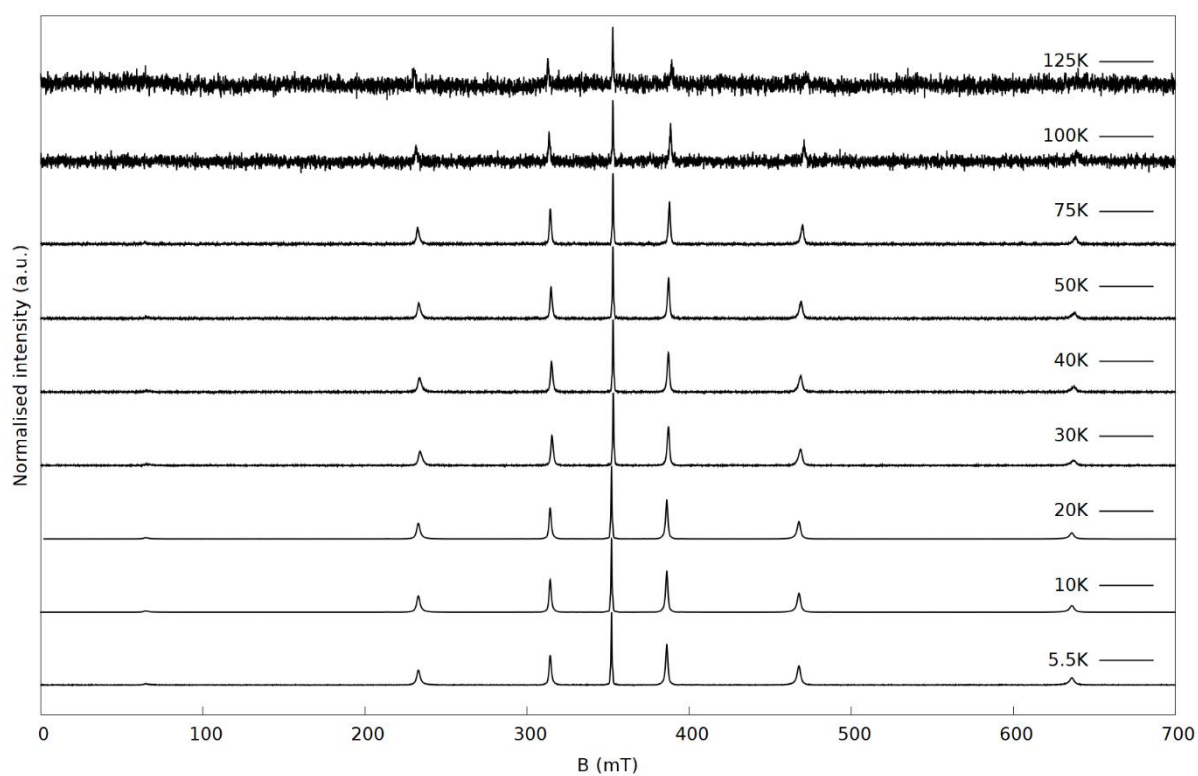


Figure S1. Echo Detected Field sweep spectra of **1** at various temperatures.

At 100 K and 125 K the delay between the pulses in the echo sequence was set to $\tau=200$ ns, to increase the echo intensity.

2 Zero Field Splitting

The spectrum was simulated with the following spin Hamiltonian:

$$\hat{H} = \mu_B B g_{\parallel} \hat{s}_z + \sum_{k,q} B_k^q \hat{O}_k^q$$

Where the first term describes the Zeeman interaction, μ_B is the Bohr magneton, B is the field, g_{\parallel} is the g-value along the unique axis and \hat{s}_z is a spin operator. The second term describes the Zero Field Splitting of the ground state with Stevens operator equivalents \hat{O}_k^q and Stevens parameters B_k^q .

Table S1. Parameters used for simulation of EDFS and Zeeman diagram.¹

g_{\parallel}	B_2^0 10^{-2} cm^{-1}	B_4^0 10^{-5} cm^{-1}	B_6^0 10^{-9} cm^{-1}	B_4^3 10^{-4} cm^{-1}	B_4^{-3} 10^{-4} cm^{-1}
1.992	1.14	4.84	-6.07	5.79	5.57

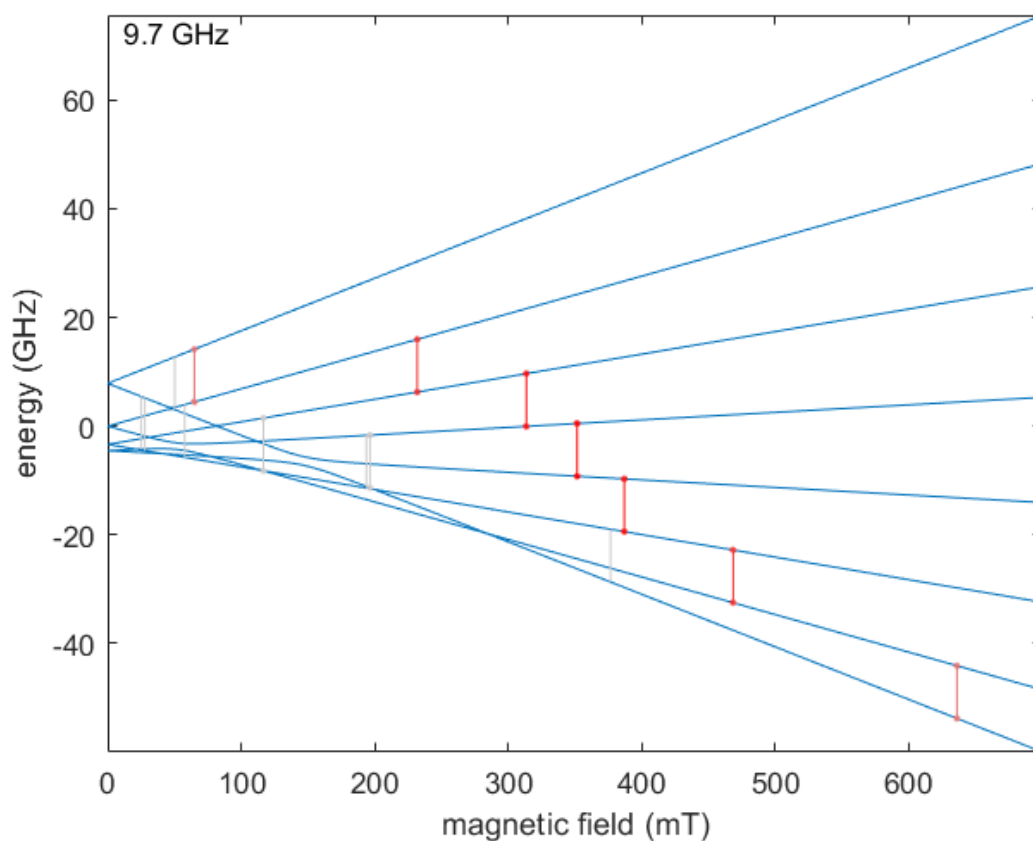


Figure S2. Simulation of the Zeeman splitting diagram of **1** along the z axis calculated with the spin Hamiltonian parameters previously published. Red lines indicate allowed transitions and grey lines indicate forbidden transitions. The order of the allowed transitions is as follows: $|5/2\rangle \rightarrow |7/2\rangle$ (65 mT), $|3/2\rangle \rightarrow |5/2\rangle$ (233 mT), $|1/2\rangle \rightarrow |3/2\rangle$ (314 mT), $|-1/2\rangle \rightarrow |1/2\rangle$ (352 mT), $|-3/2\rangle \rightarrow |-1/2\rangle$ (386 mT), $|-5/2\rangle \rightarrow |-3/2\rangle$ (468 mT) and $|-7/2\rangle \rightarrow |-5/2\rangle$ (637 mT).

3 SQUID relaxation measurements

Relaxation times were extracted from AC susceptibility data using the CC-fit program by Professor Nicholas Chilton.^{2,3}

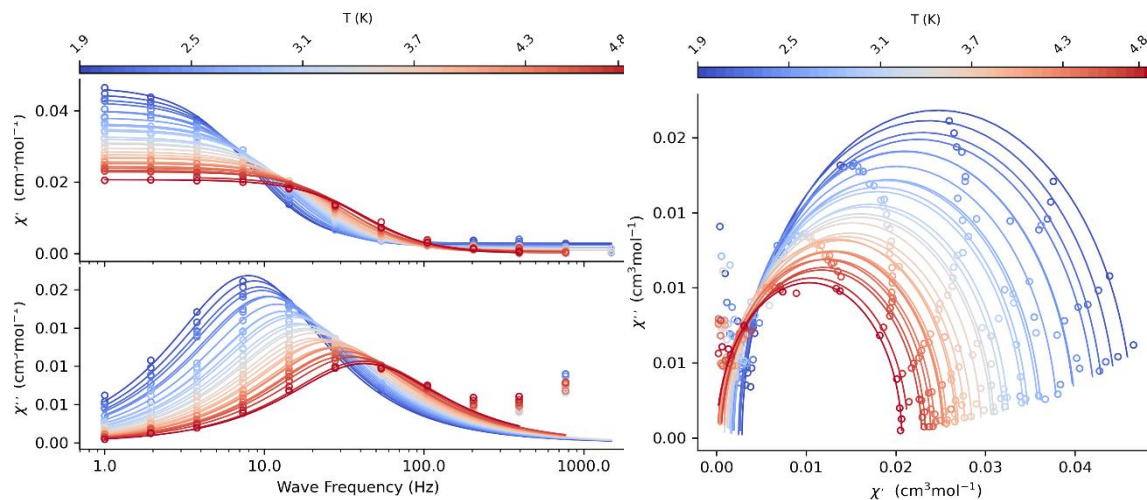


Figure S3. AC susceptibility data for temperature dependence of **2** with a static field of 300 mT.

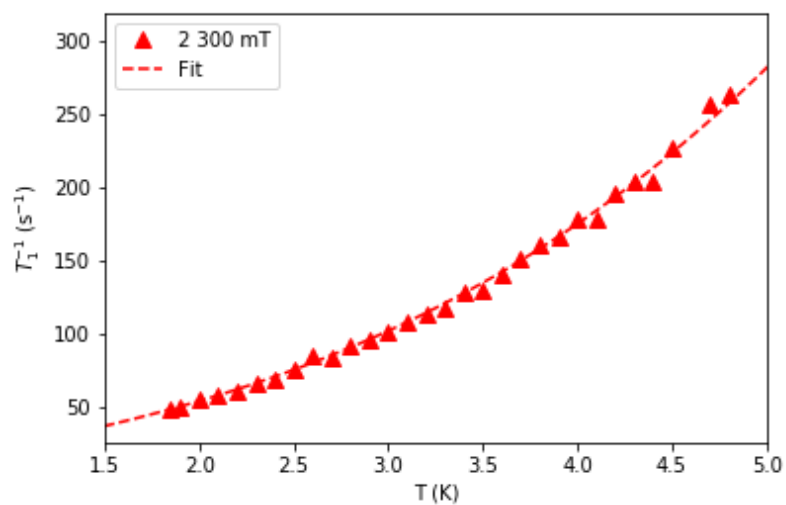


Figure S4. Extracted spin lattice relaxation times of **2** from AC Susceptibility at varying temperature fit with $T_1^{-1} = A_{dir} \cdot T + c \cdot T^n$ with $A_{dir}=21.1 \text{ s}^{-1} \cdot \text{K}^{-1}$, $c=1.46 \text{ s}^{-1} \cdot \text{K}^{-n}$ and $n=2.98$.

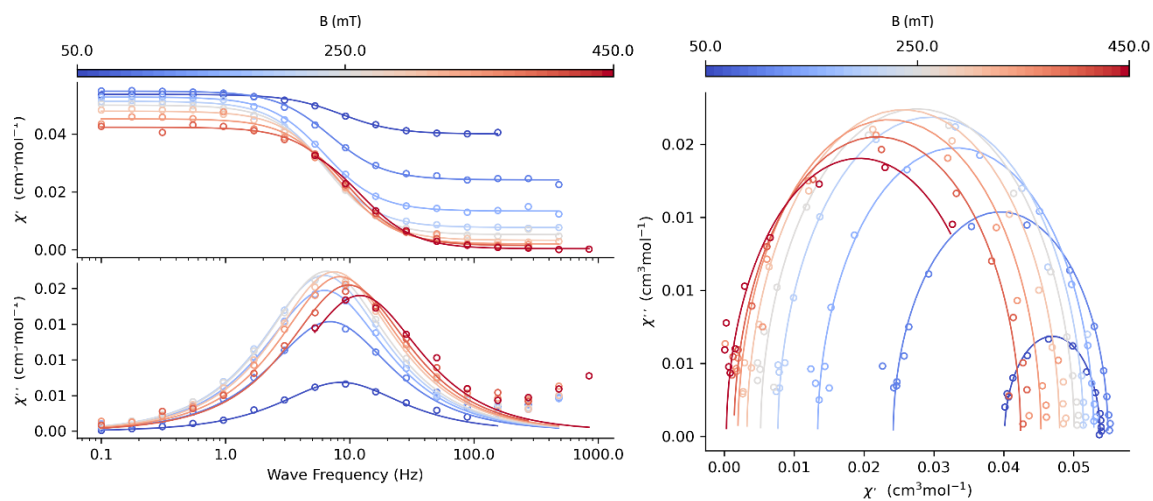


Figure S5. AC susceptibility data for field dependence of **2** at 1.85 K.

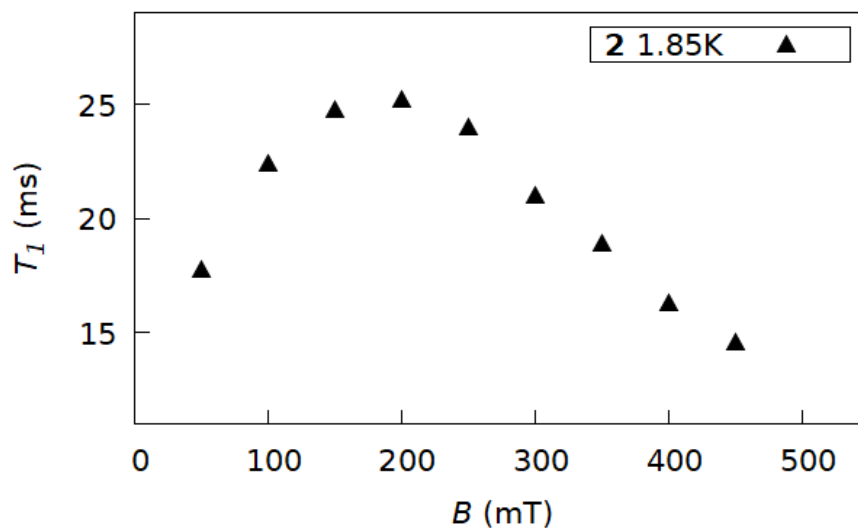


Figure S6. Extracted spin lattice relaxation times of **2** from AC Susceptibility data at varying fields.

Table S2. Spin lattice relaxation parameters for **2** from AC susceptibility at 300 mT.

T (K)	T_1 (ms)	95% confidence interval of T_1 fit
1.85	21.0	2.8
1.9	20.0	5.8
2.0	18.4	6.4
2.1	17.2	3.3
2.2	16.5	4.1
2.3	15.2	3.6
2.4	14.6	3.6
2.5	13.2	2.8
2.6	11.8	2.6
2.7	12.0	4.6
2.8	10.9	2.6
2.9	10.4	3.9
3.0	9.9	1.5
3.1	9.3	2.1
3.2	8.8	2.1
3.3	8.5	2.2
3.4	7.8	3.2
3.5	7.7	1.2
3.6	7.1	1.8
3.7	6.6	1.1
3.8	6.2	1.7
3.9	6.0	1.8
4.0	5.6	2.0
4.1	5.6	1.6
4.2	5.1	1.4
4.3	4.9	1.5
4.4	4.9	1.0
4.5	4.4	1.4
4.6	*	*
4.7	3.9	1.0
4.8	3.8	0.9

*unable to fit a curve in Cole-Cole plot

Table S3. Spin lattice relaxation parameters for **2** from AC susceptibility at 1.85 K.

B (mT)	T_1 (ms)	95% confidence interval of T_1 fit
50	17.8	5.0
100	22.4	7.6
150	24.8	6.5
200	25.2	6.4
250	24.0	5.6
300	21.0	2.8
350	18.9	3.4
400	16.3	1.7
450	14.6	2.5

4 EPR relaxation measurements

EPR relaxation data were fitted to the following mono-exponential functions:

$$I = I_0 + k \cdot e^{-\left(\frac{\tau_1}{T_1}\right)}$$

for T_1 and

$$I = I_0 + k \cdot e^{-\left(\frac{2\tau}{T_m}\right)}$$

for T_m

Where I_0 is the y-offset, k is a proportionality constant, τ_1 is the time between the first pulse and the Hahn echo detection sequence within the inversion recovery sequence, τ is the time between pulses in the echo decay sequence.

For T_1 these are compared to numbers fit with stretched exponential functions and bi-exponential functions

$$I = I_0 + k \cdot e^{-\left(\frac{\tau_1}{T_1}\right)^{\beta_1}}$$

and

$$I = I_0 + k_1 \cdot e^{-\left(\frac{\tau_1}{T_{1,1}}\right)} + k_2 \cdot e^{-\left(\frac{\tau_1}{T_{1,2}}\right)}$$

Table S4. Spin-lattice and spin-spin relaxation parameters for **1** from EPR at 5.5 K fitted with mono-exponentials.

m _s transition	B (mT)	T_1 (μs)	95% confidence interval of T_1 fit	T_m (μs)	95% confidence interval of T_m fit (μs)
$ 5/2\rangle \rightarrow 7/2\rangle$	65	396.5	35.8	1.10	0.06
$ 3/2\rangle \rightarrow 5/2\rangle$	233	1322.6	139.9	1.25	0.01
$ 1/2\rangle \rightarrow 3/2\rangle$	314	1167.0	97.6	1.38	0.02
$ -1/2\rangle \rightarrow 1/2\rangle$	352	1505.8	99.9	1.44	0.02
$ -3/2\rangle \rightarrow -1/2\rangle$	386	1645.7	152.6	1.40	0.01
$ -5/2\rangle \rightarrow -3/2\rangle$	468	1633.4	198.3	1.52	0.02
$ -7/2\rangle \rightarrow -5/2\rangle$	637	1041.3	121.8	1.55	0.02

Table S5. Spin-lattice and spin-spin relaxation parameters for **1** from EPR at 352 mT fitted with a mono-exponential function.

T (K)	T_1 (μ s)	95% confidence interval of T_1 fit (μ s)	T_m (μ s)	95% confidence interval of T_m fit (μ s)
5.5	1505.8	99.86	1.44	0.02
10	370.8	18.92	1.21	0.03
20	52.3	2.28	1.29	0.09
30	21.1	0.59	1.06	0.07
40	8.1	0.25	0.68	0.04
50	4.2	0.15	0.32	0.01
75	1.4	0.10	0.14	0.004
100	0.7	0.19	0.10	0.006
125	0.4	0.15	-	-

Table S6. Spin-lattice relaxation parameters for **1** from EPR at 352 mT fitted with stretched exponentials.

T (K)	T_1 (μ s)	95% confidence interval of T_1 fit (μ s)	β_1
5.5	615.8	21.02	0.49
10	184.8	3.66	0.55
20	29.0	0.59	0.61
30	11.8	0.10	0.63
40	4.2	0.07	0.64
50	1.9	0.07	0.64
75	0.7	0.09	0.70
100	0.4	0.21	0.76
125	0.3	0.15	0.89

Table S7. Spin-lattice relaxation parameters for **1** from EPR at 352 mT fitted with a bi-exponential function.

T (K)	$T_{1,1}$ (μ s)	95% confidence interval of $T_{1,1}$ fit (μ s)	$T_{1,2}$ (μ s)	95% confidence interval of $T_{1,2}$ fit (μ s)	k_2/k_1
5.5	3506.6	192.52	472.4	31.18	1.92
10	644.8	21.87	100.4	6.25	1.24
20	77.2	1.29	12.4	0.54	0.95
30	31.7	0.24	6.9	0.12	1.06
40	12.3	0.13	3.3	0.07	1.32
50	5.8	0.11	1.7	0.07	1.42
75	1.4	1173.56	1.4	1170.94	1.00
100	0.7	1398.46	0.7	1395.22	1.00
125	0.4	1.51	0.4	1.51	1.00

Table S8. Spin-lattice and spin-spin relaxation parameters for **1** from EPR at 637 mT fitted with a mono-exponential function.

T (K)	T_1 (μ s)	95% confidence interval of T_1 fit (μ s)	T_m (μ s)	95% confidence interval of T_m fit (μ s)
5.5	1041.3	121.79	1.55	0.02
10	248.8	10.10	1.31	0.02
20	36.3	1.37	1.42	0.11
30	14.9	0.37	1.14	0.09
40	5.9	0.30	0.87	0.07
50	3.0	0.17	0.71	0.06
75	1.0	0.18	0.42	0.03

Table S9. Spin-lattice relaxation parameters for **1** from EPR at 637 mT fitted with stretched exponentials.

T (K)	T_1 (μ s)	95% confidence interval of T_1 fit (μ s)	β_1
5.5	381.0	41.11	0.49
10	108.7	1.59	0.52
20	26.7	1.12	0.73
30	11.3	0.34	0.77
40	4.3	0.34	0.78
50	1.9	0.18	0.75
75	0.3	0.14	0.58

Table S10. Spin-lattice relaxation parameters for **1** from EPR at 637 mT fitted with a bi-exponential function.

T (K)	$T_{1,1}$ (μ s)	95% confidence interval of $T_{1,1}$ fit (μ s)	$T_{1,2}$ (μ s)	95% confidence interval of $T_{1,2}$ fit (μ s)	k_2/k_1
5.5	2573.4	97.36	117.1	6.27	2.72
10	469.3	7.94	66.8	1.85	1.51
20	61.3	5.41	18.3	2.04	1.45
30	25.8	2.36	9.5	0.71	2.12
40	11.2	2.92	4.3	0.57	3.63
50	6.0	1.38	2.3	0.21	5.57
75	1.4	0.84	0.8	0.62	1.71

5 ESEEM

ESEEM was fitted with the formula

$$I = I_0 + k_m \cdot \left(1 - k_{osc} \cdot \cos\left(\frac{\omega\tau}{2} + p\right) \cdot e^{-\left(\frac{\tau}{T_{osc}}\right)} \right) \cdot e^{-\left(\frac{2\tau}{T_m}\right)}$$

Where I_0 is the y-offset, k_m is a proportionality constant, τ is the time between pulses in the echo decay sequence, k_{osc} is the proportionality constant of ESEEM oscillations, ω is the frequency of oscillation, p is the phase of the oscillations and T_{osc} is the time it takes for the oscillations to die down. The fits in Figure S8 were done with T_m fixed to the value obtained by fitting with a mono-exponential function see Table S5 and Table S8. The fits yielded ω values of 0.99 MHz and 1.87 MHz respectively, very close to the Larmor frequency of ^{14}N at these fields (1.08 MHz and 1.96 MHz).

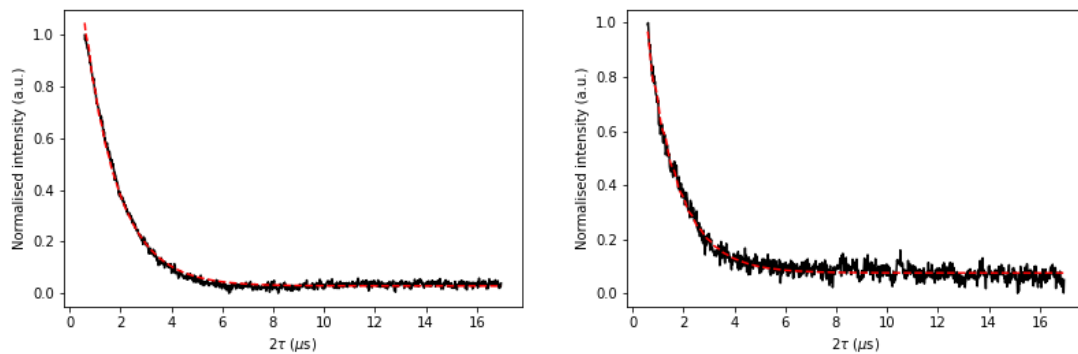


Figure S7. Echo decay curves of **1** (black) fitted with single exponentials (red) measured with 800 ns π -pulses at 10 K at 352 mT and 637 mT respectively.

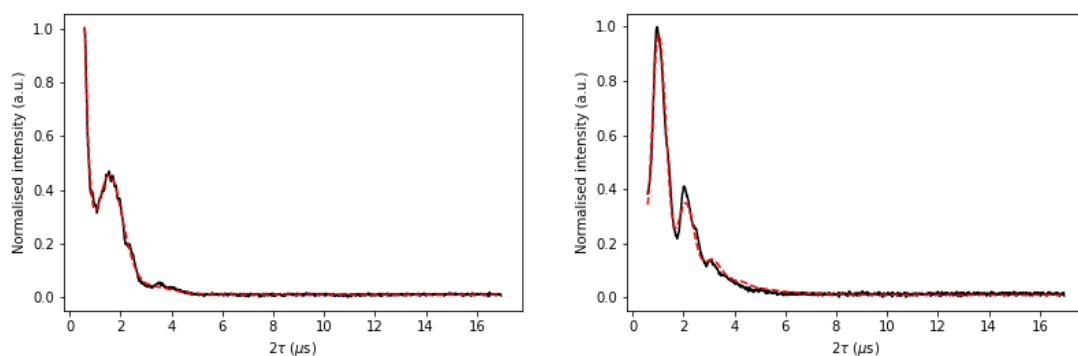


Figure S8. Echo decay curves of **1** (black) with fitted ESEEM (red), measured with 64 ns π -pulses at 10 K at 352 mT (left) and 637 mT (right) respectively.

6 Transport integral

The transport integral is defined as

$$J_8\left(\frac{\theta_D}{T}\right) = \int_0^{\frac{\theta_D}{T}} (x)^8 \cdot \frac{e^x}{(e^x - 1)^2} dx$$

The integral was approximated with the following expression in the python script:

```
np.real(-(x**8/(-1+np.exp(x)))+8*(-(x**8/8)+x**7*cmath.log(1-  
np.exp(x)+0j))+7*x**6*mpmath.polylog(2,np.exp(x))-  
42*x**5*mpmath.polylog(3,np.exp(x))+210*x**4*mpmath.polylog(4,np.exp(x))-  
840*x**3*mpmath.polylog(5,np.exp(x))+2520*x**2*mpmath.polylog(6,np.exp(x))-  
5040*x*mpmath.polylog(7,np.exp(x))+5040*mpmath.polylog(8,np.exp(x)))-  
8*(5040*mpmath.polylog(8,1)))
```

DFT vibrational frequency calculations

Table S11. DFT calculated normal modes of Lu(trensal) in a selected range, normal modes of interest are marked in bold.

Frequency (cm ⁻¹)	Calc. Intensity in IR spectrum	Largest force vectors
14.84	0.110718	C and H
19.18	0.153372	N and H
133.89	7.829197	Lu
136.14	1.627851	O
137.17	1.566421	O
145.95	1.962314	O
174.02	7.995602	Lu and C
174.33	7.303861	Lu and C
176.16	0.247995	Lu, O and C
185.03	37.53749	Lu, O and N
185.75	37.64356	Lu, O and N
274.41	2.384872	O and C

Table S12. DFT calculated normal modes of Y(trensal) in a selected range, normal modes of interest are marked in bold.

Frequency (cm ⁻¹)	Calc. Intensity in IR spectrum	Largest force vectors
96.22	0.110593	C and O
112.83	0.333423	N
136.5	2.252306	O
137.71	2.126938	O
146.78	3.841183	O
189.34	12.08957	Y
209.39	0.06155	C
209.55	0.053139	C
212.83	0.191834	C
247.66	54.40612	O and N
248.54	53.80399	O and N
293	3.35392	O and C

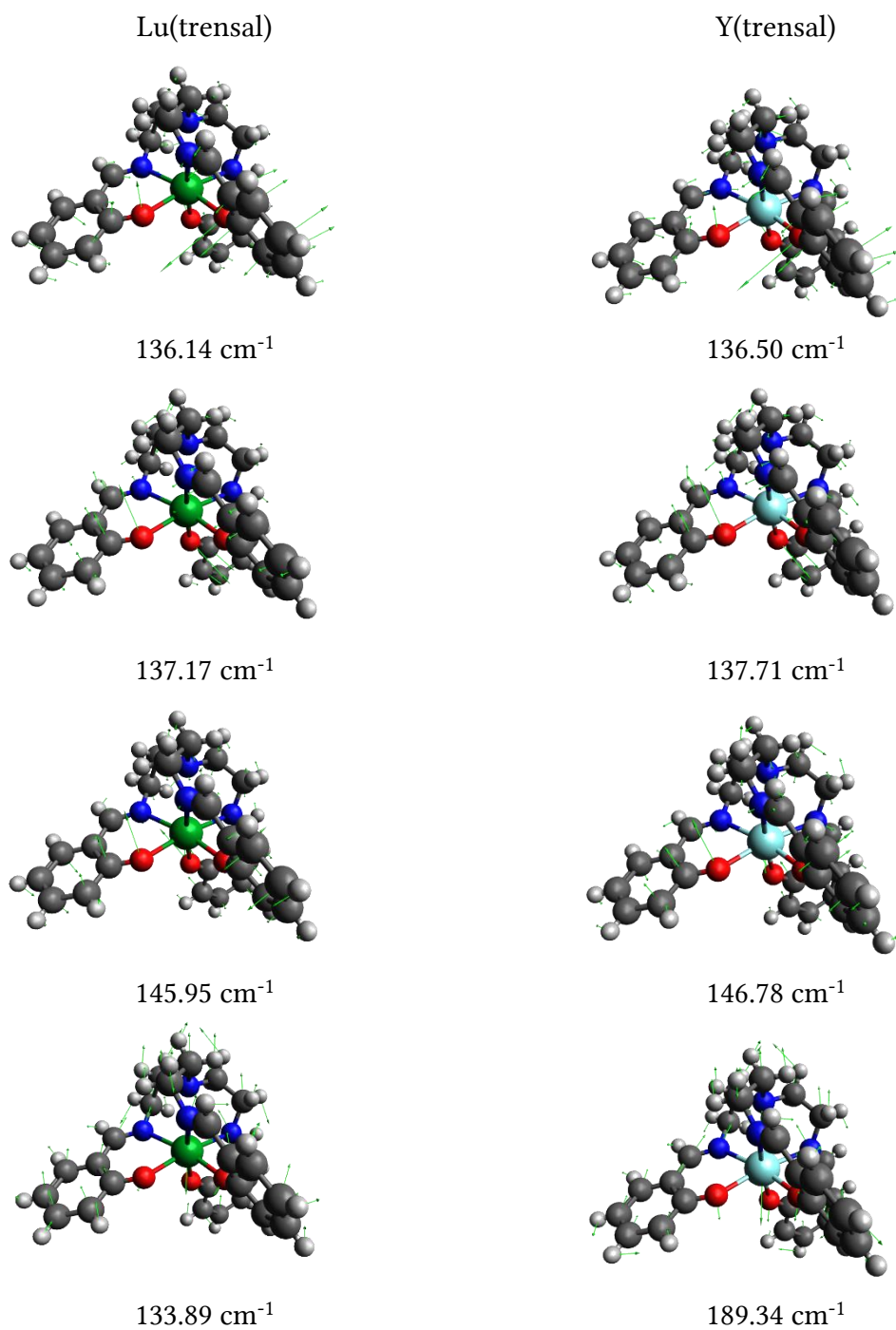


Figure S9. DFT calculated normal modes of Lu(trensal) in the range of Δ_{loc} and corresponding normal modes of Y(trensal). Green arrows are the force vectors. Atom colour code: Lu: Green, Y: Light blue, O: Red, N: Dark blue, C: Grey, H: White/Light grey.

Rabi oscillations

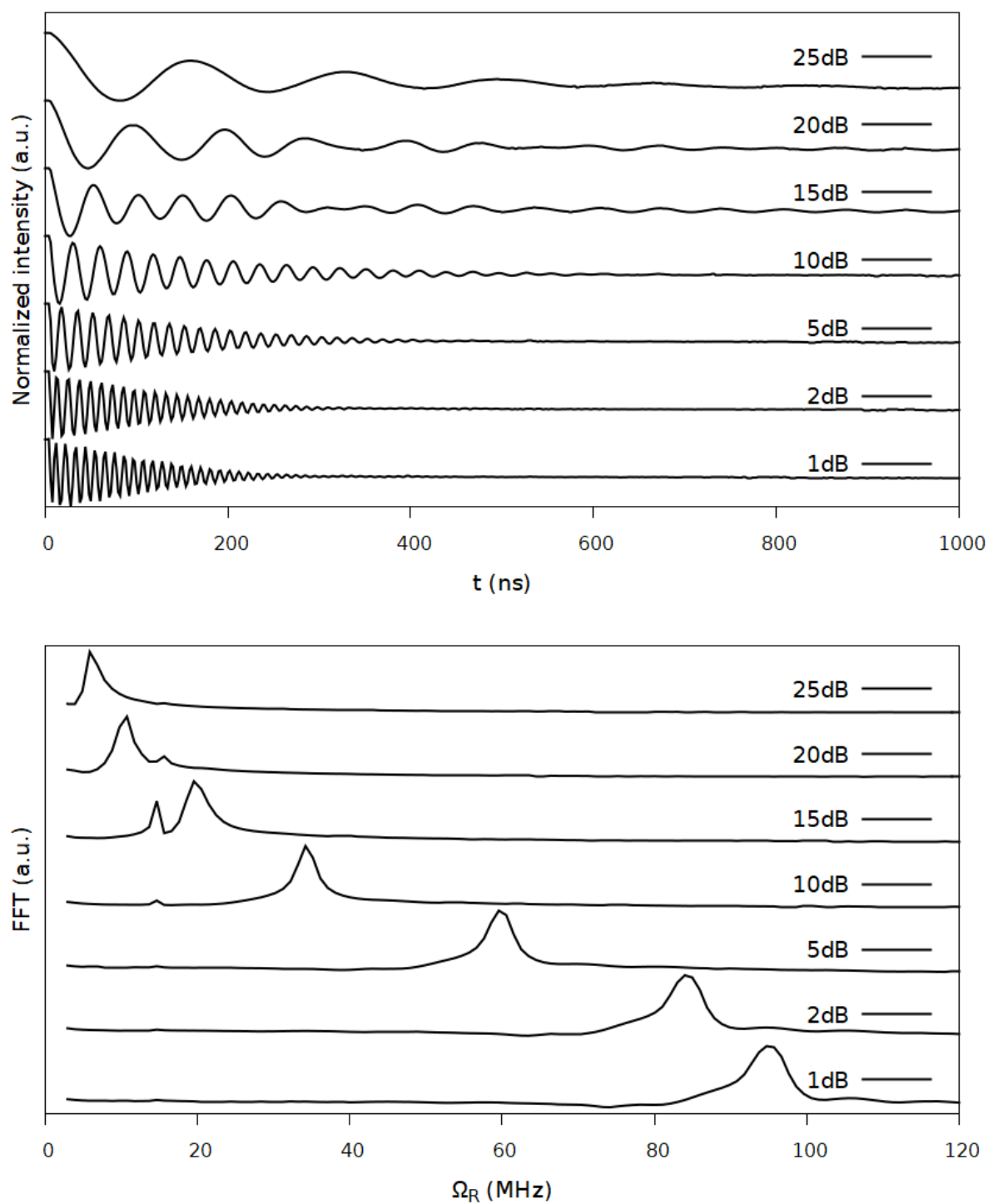


Figure S10. Rabi Oscillations of **1** measured at 352 mT and 30 K with varying microwave attenuation (top) and corresponding Fourier transforms (bottom). The extra peaks at around 15 MHz correspond to the Larmor frequency of ^1H at this field.

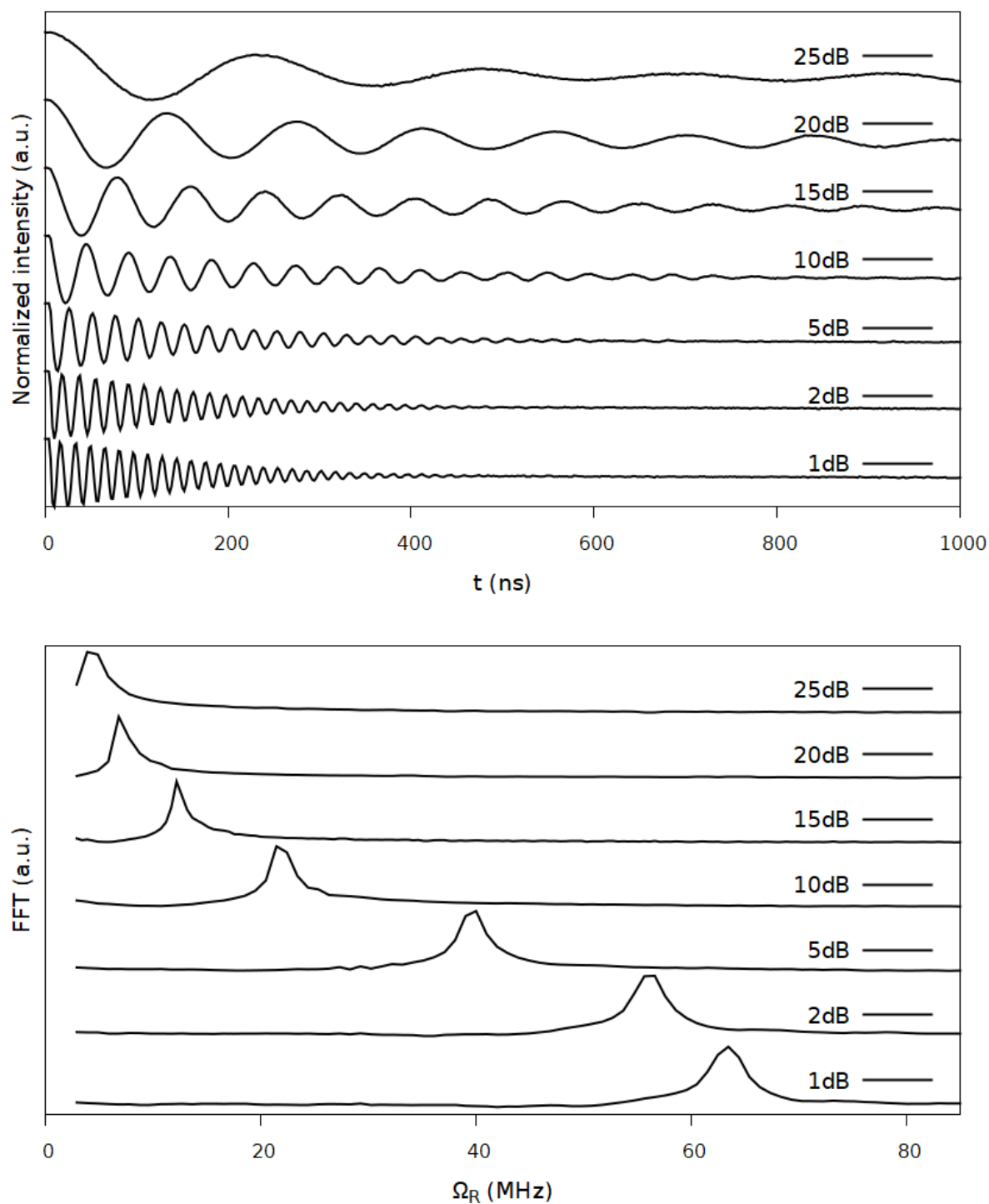


Figure S11. Rabi Oscillations of **1** measured at 637 mT and 30 K with varying microwave attenuation (top) and corresponding Fourier transforms (bottom). The extra small peaks at around 30 MHz correspond to the Larmor frequency of ^1H at this field.

References

- (1) Buch, C. D.; Kundu, K.; Marbey, J. J.; van Tol, J.; Weihe, H.; Hill, S.; Piligkos, S. Spin–Lattice Relaxation Decoherence Suppression in Vanishing Orbital Angular Momentum Qubits. *J. Am. Chem. Soc.* **2022**, 144, 38, 17597–17603. <https://doi.org/10.1021/jacs.2c07057>.
- (2) Reta, D.; Chilton, N. F. Uncertainty Estimates for Magnetic Relaxation Times and Magnetic Relaxation Parameters. *Phys. Chem. Chem. Phys.* 2019, 21 (42), 23567–23575. DOI: 10.1039/C9CP04301B.
- (3) Blackmore, W. J. A.; Gransbury, G. K.; Evans, P.; Kragoskow, J. G. C.; Mills, D. P.; Chilton, N. F. Characterisation of Magnetic Relaxation on Extremely Long Timescales. *Phys. Chem. Chem. Phys.* 2023, 25 (25), 16735–16744. DOI: 10.1039/D3CP01278F.

4. Electron Paramagnetic Resonance Spectra of Pseudo-Pentagonal Bipyramidal Gadolinium Complexes

4.1 Preface

The aim of this article is to find relations between magnetic properties of Gd(III) and the geometry and crystal field. To do this the zero field splitting (ZFS) of Gd(III) in the pseudo five-fold symmetry of a series of five complexes resembling pentagonal bipyramids is determined with cw EPR spectroscopy. This leads to the conclusion that the nature and position of the axial ligands dominates the ZFS. The article also goes on to link the magnitude of the ZFS to the thermal relaxation barrier of the corresponding Dy(III) complexes.

The text of the article was written solely by Jonatan B. Petersen under the supervision of Prof. Richard E. P. Winpenny and Prof. Eric J. L. McInnes. Samples were supplied by Dr You-song Ding, Prof. Yan-Zen Zheng and Prof. Ramaswamy Murugavel. Crystallographic data were supplied by Dr You-song Ding. The EPR measurements, fitting and interpretation of data were performed by Jonatan B. Petersen.

This page is intentionally left blank

Electron Paramagnetic Resonance Spectra of Pseudo-Pentagonal Bipyramidal Gadolinium Complexes

Jonatan B. Petersen,¹ You-Song Ding,^{1,2} Eric J. L. McInnes,¹ Yan-Zhen Zheng,² Ramaswamy Murugavel,³ and Richard E. P. Winpenny^{1*}

¹ Department of Chemistry, School of Natural Sciences, The University of Manchester, Oxford Road, Manchester M13 9PL, United Kingdom

² School of Science, Xi'an Jiaotong University, Xi'an 710049, China

³ Department of Chemistry, Indian Institute of Technology Bombay, Mumbai-400076, India

KEYWORDS: EPR, Pseudo-symmetry, Gadolinium, Zero Field Splitting.

ABSTRACT: Gadolinium is a special case in spectroscopy because of the near isotropic nature of the $4f^7$ configuration of the $3+$ oxidation state. Gd^{3+} complexes have been studied in several symmetries to understand the underlying mechanisms of the ground state splitting. The aim is often to possibly apply the abundance of information in Gd^{3+} spectra to a probe for properties of the other rare earth ions in the same complexes. Since 5-fold symmetry does not occur in crystallographic space groups, the behavior of Gd^{3+} in this pseudo symmetry is hitherto uncharted. In this work the Zero-Field Splitting (ZFS) of a series of Gd^{3+} complexes of the form $[GdX^1X^2(L_{eq})_5]^+$ (X = axial ligands: Cl^- , $-O^tBu$, $-OArF_5$ or $^tBuPO(NH^iPr)_2$, L_{eq} = equatorial ligand: Py , THF or H_2O) with near 5-fold symmetry axes along X^1-Gd-X^2 was investigated. The ZFS parameters were determined by fitting of room-temperature continuous wave Electron Paramagnetic Resonance (EPR) spectra (at X, K and Q-band) to a spin Hamiltonian incorporating extended Stevens operators compatible with C_5 symmetry. Examination of the acquired parameters led to the conclusion that the ZFS is dominated by the B_2^0 term and that the magnitude of B_2^0 is almost entirely dependent on, and inversely proportional to, the donor strength of the axial ligands. Surveying the Continuous Shape Measure (CSHM) and the X^1-Gd-X^2 angle of the complexes showed that there is some correlation between the proximity of each complex to D_{5h} symmetry and the magnitude of the B_6^5 parameter, but that the deformation of the X^1-Gd-X^2 angle is more significant than other distortions. Finally the magnitude of B_2^0 was found to be inversely proportional to the thermal barrier for reversal of the magnetic moment (U_{eff}) of the corresponding isostructural Dy^{3+} complexes.

INTRODUCTION

For many years gadolinium(III) has intrigued spectroscopists, with its combination of shielded $4f$ orbitals and a half-filled shell in the $+3$ oxidation and the resulting $L = 0$ ground state with no orbital angular momentum and therefore no first order spin-orbit coupling. This special case leads to very little ground state splitting compared to most lanthanides.¹ This results in ground state splitting of typically less than 1 cm^{-1} which is the perfect magnitude for rich EPR spectra as well as relaxation times that are still relatively long.²

Crystal fields determine many of the properties of lanthanide ions and completely dominate their magnetic behaviour. Understanding the crystal field is therefore of paramount importance when working with lanthanides. For example, the crystal field determines the barrier for reversal of the magnetic moment via the Orbach mechanism in lanthanide single ion magnets (SIMs),³ and the symmetry of the crystal field influences the rate of quantum tunnelling of the magnetization circumventing this barrier.⁴

Even though it has no formal orbital angular momentum, the splitting of the gadolinium(III) $^8S_{7/2}$ ground state still happens through spin-orbit coupling through excited states with $L \neq 0$ and this splitting adheres to the same symmetry restrictions as crystal

field splitting.⁵ It has therefore been suggested that the ZFS parameters obtained for gadolinium can help elucidate how close a family of lanthanide complexes comply with their approximate symmetry.⁶

Most investigations of lanthanide crystal field and zero field splitting have been performed in high symmetry environments to ensure the number of parameters needed is low enough to determine a unique best set of parameters from experimental data. In low symmetry the elucidation of the crystal field parameters often requires *ab initio* calculations for a meaningful understanding of ground state compositions. Methods used such as Density Functional Theory and Complete Active Space Self-Consistent Field employ approximations that introduce significant errors and for $4f^7$ configurations like Gd^{3+} these errors are on the order of magnitude of the total splitting, rendering theoretical calculations useless for obtaining accurate parameters for the ground state splitting in these systems.^{7,8}

Five-fold symmetry does not exist in regular crystals and it follows that five-fold point symmetry is not crystallographically enforceable. However, molecules with near 5-fold symmetry occur. Within the lanthanide series, dysprosium(III) compounds with pseudo-pentagonal bipyramidal coordination geometries are important as many compounds with this geometry are

single-molecule magnets (SMMs) with high thermal barriers for loss of magnetisation.^{9,10}

In this work we set out to investigate five gadolinium complexes with pentagonal bipyramidal coordination geometries (e.g. Figure 1); gadolinium in this geometry has not previously been investigated by EPR spectroscopy. The complexes have strongly donating and/or negatively charged ligands on their axis and weaker donating neutral ligands in the plane, and thus the dysprosium analogues (and in one case even a neodymium analogue) are SMMs.^{10–14} This geometry is ideal for stabilising the highest M_J doublet in Dy^{3+} complexes, giving large barriers for reversal of the magnetic moment.^{9–13} For the current investigation we measured the room temperature EPR spectra of Gd^{3+} doped into isostructural Y^{3+} complexes at multiple frequencies, and examined how well they could be reproduced using a spin Hamiltonian consistent with the approximate symmetry.

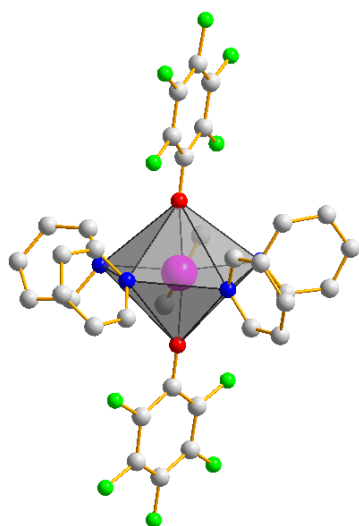


Figure 1. Solid state structure of $[Y(OArF_5)_2(Py)_5]^+$ (**4**) with a grey polyhedron drawn between ligand donor atoms, almost forming a pentagonal bipyramid. Colour code: Y (magenta), F (green), O (red), N (blue) and C (grey). H atoms omitted.

EXPERIMENTAL SECTION

Six samples were produced for EPR measurements: $Gd@[YCl_2(Py)_5]BPh_4 \cdot THF$ **1**; $Gd@[YCl_2(THF)_5]BPh_4$ **2**; $Gd@[Y(O^tBu)Cl(THF)_5]BPh_4 \cdot 2THF$ **3**; $Gd@[Y(OArF_5)_2(Py)_5]B(ArF_5)_4 \cdot 0.5C_6H_{14}$ **4**; $Gd@[Y(^tBuPO(NH^iPr)_2)_2(H_2O)_5]I_3 \cdot H_2O \cdot 2(^tBuPO(NH^iPr))$ **5a**; $[Gd(^tBuPO(NH^iPr)_2)_2(H_2O)_5]I_3 \cdot H_2O \cdot 2(^tBuPO(NH^iPr))$ **5b** (Py = pyridine, THF = tetrahydrofuran, Me = methyl, Ph = phenyl, ArF₅ = pentafluorophenyl, ^tBu = *tert*-butyl and ⁱPr = *iso*-propyl).

The samples were synthesised by modified versions of the procedures previously published for the analogous dysprosium complexes with DyX_3 substituted for YX_3

and GdX_3 (X = Cl or I).^{11–13,15} Doping was done by using a mixture of $GdCl_3$ and YCl_3 (1-5% Gd) in the initial synthetic step.

All samples were studied as crystalline powders of yttrium compounds doped their gadolinium analogue, with the exception of **5** where the neat gadolinium compound was also measured.

X-band and Q-band EPR spectra were measured on a Bruker EMXplus spectrometer equipped with ER 4122 SHQ or ER 5106 QT resonators. K-band EPR spectra were recorded on a Bruker E500 spectrometer equipped with an ER 6706 KT resonator. All spectra were measured at room temperature with modulation frequencies of 100 kHz and modulation amplitudes of 5-10 G. The recorded spectra were baseline corrected with a first or second order polynomial and field corrected against a strong pitch standard sample supplied by Bruker. The samples were measured in sealed quartz tubes as samples **1-4** are moisture sensitive.

The spectra were modelled with a spin Hamiltonian of the form:

$$\hat{H} = \mu_B (B_x \quad B_y \quad B_z) \begin{pmatrix} g_{\perp} & 0 & 0 \\ 0 & g_{\perp} & 0 \\ 0 & 0 & g_{\parallel} \end{pmatrix} \begin{pmatrix} \hat{S}_x \\ \hat{S}_y \\ \hat{S}_z \end{pmatrix} + \sum_{k,q} B_k^q \hat{O}_k^q \quad (1)$$

where μ_B is the Bohr magneton. The first term describes the Zeeman interaction between the magnetic moment of the spin (with spin operators \hat{S}_x , \hat{S}_y and \hat{S}_z) and the external magnetic field (with components B_x , B_y and B_z) through an axial g-tensor with principal values parallel (g_{\parallel}) and perpendicular (g_{\perp}) to the unique axis. The second term describes the Zero Field Splitting of the ground state with Stevens operator equivalents \hat{O}_k^q , which are polynomials of spin operators of order $q < k$, parameterised with Stevens parameters B_k^q .¹⁶ To adhere to the approximate C_5 symmetry of the complexes, only B_2^0 , B_4^0 , B_6^0 and B_6^5 were allowed non-zero values as these are the only allowed operators in the C_5 point group.¹⁷ Line widths were modelled assuming unresolved hyperfine interactions and strain in the g-factors and the dominant ZFS parameter, by using axially anisotropic linewidths lw_{\perp} and lw_{\parallel} and a Gaussian distribution (strain) around the value of the B_2^0 parameter.

Spin Hamiltonian parameters were obtained by Levenberg-Marquardt least squares fitting using the multi-purpose EPR software written by Høgni Weihe.^{18,19} The parameters were fitted against the spectra of all three frequencies simultaneously, except **5a** and **5b** where each frequency was fit separately with the spectra of both samples simultaneously.

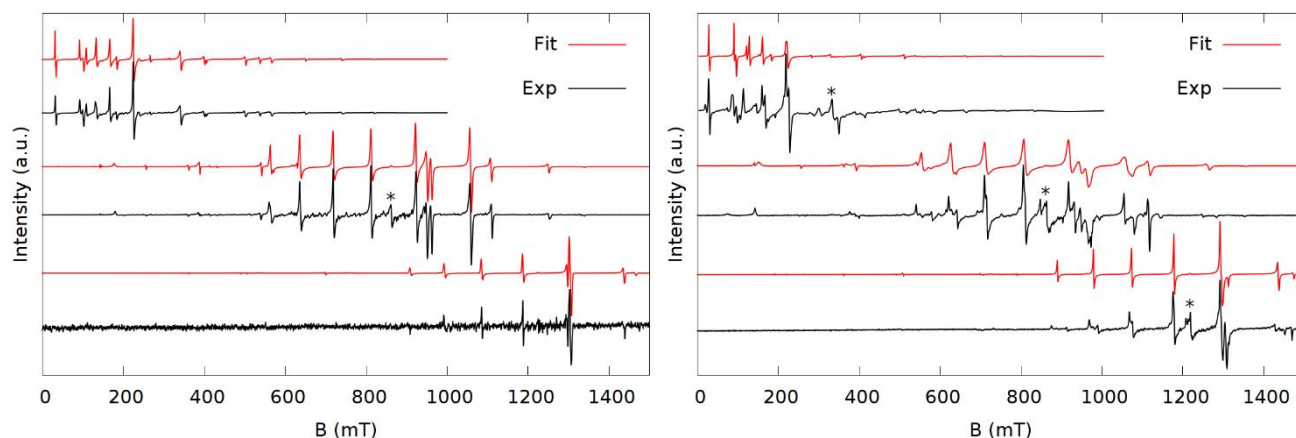


Figure 2. Spectra (black) and simulations (red) at X (top), K (middle) and Q-band (bottom) of **1** (left) and **2** (right). Simulation parameters are based on the parameters in Table 1 and exact frequencies of measurements are given in supplementary information. The stars indicate an impurity.

Single crystals of **1**, **2** (Gd analogue) and **4** (Y analogue) for crystal structure determination were obtained by recrystallisation of the neat compounds from hexane. X-ray diffraction was measured on a Bruker Apex CCD II diffractometer using Mo- K_{α} radiation.

RESULTS AND DISCUSSION

The experimental spectra of **1-5b** are shown along with the best fit simulations in Figures 2-5. All the samples gave intense EPR signals and spectra with many observable transitions. In the K-band spectra both $\Delta m_s = \pm 1$ and $\Delta m_s = \pm 2$ (<500 mT) transitions are observed for all samples, with the exception of **3**, where the smaller sample size meant that the field range was cut short to focus on the main part of the spectrum. The $\Delta m_s = \pm 2$ transitions are also accurately reproduced in the simulations, substantiating the validity of the model.

The spectra of **1** and **2** contain several intense narrow peaks and are presented in Figure 2. The simulation parameters used are given in Table 1. Both have the $\Delta m_s = \pm 1$ transitions spread over a wide range of as much as 800 mT, indicating large ZFS. The multitude of small peaks, between the more intense peaks are caused by polycrystallinity effects, meaning that larger crystallites give more weight to certain orientations rather than a true average of the orientations. To prove this, the sample was turned 10° and a new spectrum measured where the position and shape of these minor peaks changed. This effect was seen even though the sample was thoroughly ground, which is likely due to the extraordinarily narrow linewidths and wide spectral range of **2**.

As seen in the right panel of Figure 2 the spectra of **2** exhibits more peaks than the simulations based on an axial spin Hamiltonian. This could be because the

asymmetric unit of the crystal structure contains two gadolinium complexes with slightly different geometries. The main peaks are at positions noticeably similar to those in the spectra of **1** and the best fit parameters of **1** were therefore used as the starting point for fitting of **2**. The resulting simulated spectra do resemble the experimental data, but the fitted parameters are less reliable. An attempt at fitting the spectra with two independent sets of parameters failed, as the spectra are too convoluted. Even though the extra peaks in these spectra probably emerge from the two different Gd sites, we also found that on exchanging B_6^5 for B_2^2 in the spin Hamiltonian, i.e. decreasing the symmetry, the spectra can be simulated almost to perfection (see Figure S2). The off-diagonal part of this model is hard to compare with the axial model used for the other samples, but yields very similar values of B_2^0 and B_4^0 .

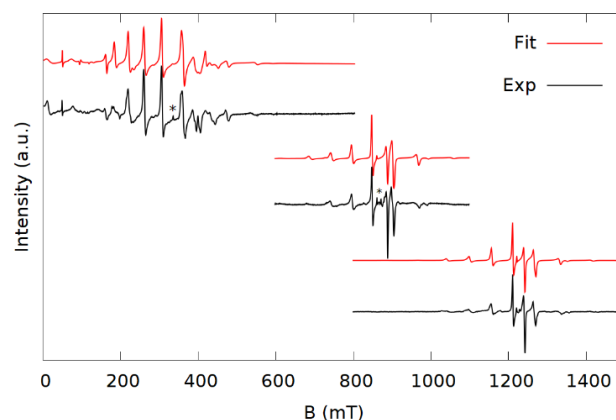


Figure 3. Spectra (black) and simulations (red) of **3** at X (top), K (middle) and Q-band (bottom). The stars indicate an impurity. Simulation parameters in table 1.

Table 1. Best fit spin Hamiltonian parameters for **1-5** from EPR spectra and structural data from gadolinium crystal structures. Numbers in parenthesis are estimated standard deviations of the last digit. The last two columns are the total energy difference from the lowest to the highest m_s doublet (ΔE) and the B_6^5 parameter normalised by ΔE .

	g_{\perp}	g_{\parallel}	B_2^0 (10^{-2} cm^{-1})	B_4^0 (10^{-5} cm^{-1})	B_6^0 (10^{-7} cm^{-1})	B_6^5 (10^{-5} cm^{-1})	$X_1\text{-Gd-X}_2$ ($^{\circ}$)	CShM D_{5h}	ΔE (cm^{-1})	$B_6^5/\Delta E$ (10^{-5})
1	1.994(1)	-	3.63(1)	-1.3(1)	0	0.6(5)	176.8	0.093	1.308	0.46
2^a	1.993(1)	-	3.76(1)	-1.2(1)	0	5.0(4)	179.3 176.2	0.244 0.224	1.356	3.7
3	1.992(1)	-	1.86(2)	-1.6(2)	0	-1.7(4)	178.7 ^b	0.274 ^b	0.673	-2.5
4	1.997(1)	1.991(2)	1.01(8)	-2(1)	-10(7)	-8(2)	178.4 ^b	0.979 ^b	0.361	-22
5^c	1.994(3)	1.999(5)	1.58(8)	-3(1)	-6(5)	-7(2)	174.5 ^b	0.173 ^b	0.568	-12

^aCrystal structure contains two Gd sites in the asymmetric unit. ^bData from Y analogue crystal structure. ^cSpin-Hamiltonian parameters from simultaneous fit of **5a** and **5b** K-band spectra.

The spectra of **3** also shows several well resolved peaks in particular at X-band (Figure 3). At K-band the measured field range was narrowed to only include the main part of the spectrum. This was a necessary compromise for increasing the intensity, as the size of the sample was smaller than for the other samples.

In contrast to **1** and **2**, the signals of **3** are found in a much narrower field range, indicating smaller ZFS, though still large enough that all features are resolved. The spectra could be modelled with the same set of axial ZFS terms as used for **1**. An attempt was made to fit **3** with the B_6^5 parameter exchanged with B_2^2 , as was necessary for **2**, but this made no significant improvement. Hence, the ZFS of **3** conforms to the approximate C_5 symmetry.

In some of the spectra of **1**, **2** and **3** a peak corresponding to a g value of 1.993-1.995 is seen. This peak does not fit with the simulations, and we attribute it to a small impurity of an amorphous Gd species giving rise to an isotropic signal.

The spectra of **4** are unusual in that they are less well resolved than for the other compounds as seen in Figure 4. The observed signal only extends over roughly 200 mT and, apart from one transition in the middle, the transitions have broader linewidths than the other spectra. The narrow spectral range is a result of a small ZFS of the ground state. The spectra can be simulated with a relatively large B_6^5 parameter, though to reproduce the linewidths a significant strain of the B_2^0 parameter with a standard deviation of 7.3% was needed. This is a great deal more than necessary for the other samples (>1%)

5 was measured both as a doped (**5a**) and neat (**5b**) compound. Both samples give rich spectra (Figure 5), which is surprising as neat gadolinium complexes often have line widths so broad that few transitions are observable. For comparison Figure S3 shows the

spectrum of neat $\text{GdCl}_2(\text{THF})_5$, which has linewidths so immense that the spectrum resembles a single transition. The narrow line widths of **5b**, could be the result of the crystal structure containing both water and two additional uncoordinated ligand molecules and their iodine counterions leading to increased distance between neighbouring molecules and a lower density of paramagnetic species. Like **4** and to some degree **3** the transitions of **5a** are narrower towards the middle of the spectrum than at the edges, which again suggests an influential B_6^5 parameter or strain on B_2^0 . This effect is not seen in the spectrum of **5b**. The spectra of **5a** and **5b** complement each other nicely this way, with **5a** having narrow line width on the central transitions, giving a good measure of the g -values and **5b** relatively even linewidths and thus giving a better fit of the splitting. The two samples contain the same complex and approximately the same ZFS would be expected, since the ionic size of yttrium is not dissimilar to gadolinium (102 pm and 105 pm, respectively, in eight coordinate complexes).²⁰ They were therefore fitted together to give a single set of spin-Hamiltonian parameters.

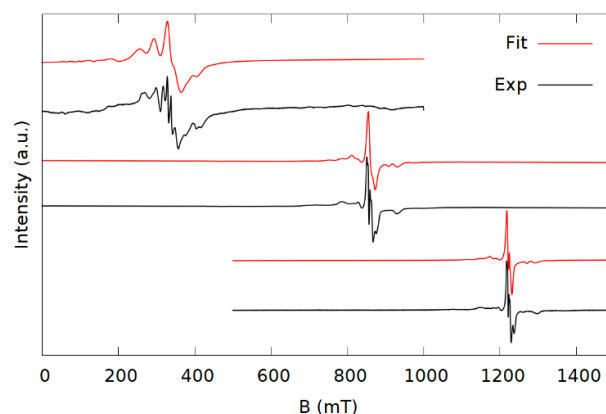


Figure 4. Spectra (black) and simulations (red) of **4** at X (top), K (middle) and Q-band (bottom) simulation parameters in table 1.

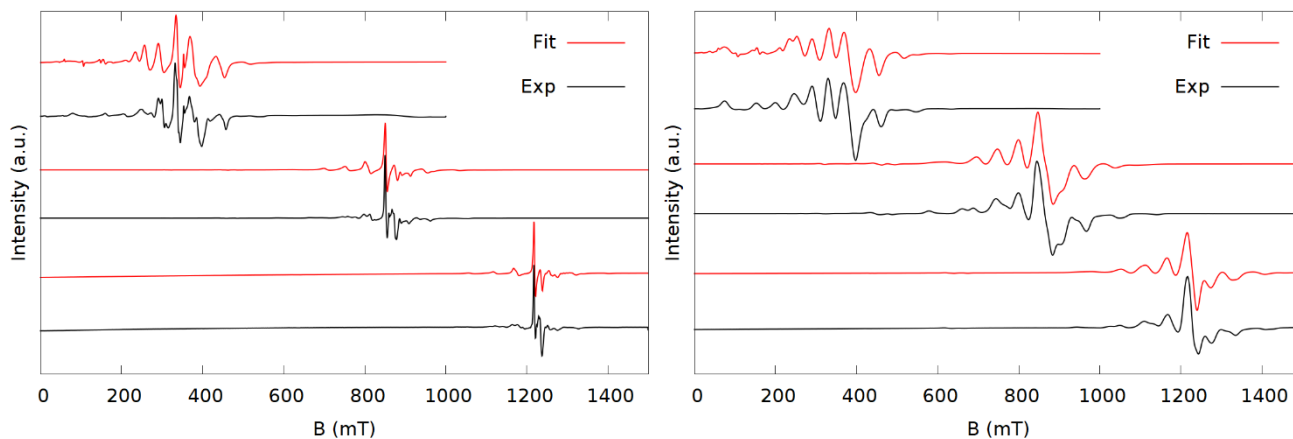


Figure 5. Spectra (black) and simulations (red) at X (top), K (middle) and Q-band (bottom) of **5a** (left) and **5b** (right). Simulation parameters in Table 1.

As fitting six datasets at a time was too cumbersome, the spectra were fitted in pairs of **5a** and **5b** at each frequency, starting with K-band and then using the resulting parameters as a starting point at X- and Q-band. The best fit parameters are presented in Table S3. The ZFS parameters obtained this way are mostly consistent, apart from B_4^0 which is an order of magnitude lower at X-band. The Zeeman parameters give conflicting values. X- and Q-band g -values (see Table S3) are lower than those from the K-band spectrum, partly due to an experimental error causing the Q-band spectra to not be field corrected. The three parameter sets have the same trend with $g_{\perp} < g_{\parallel}$ by 0.005-0.009.

Overall, the fits match the experimental data well and give robust parameters which are reported in Table 1. Since the spectra were measured at room temperature, the sign of the ZFS parameters cannot be determined, though their magnitude and relative signs can. The parameters in Table 1 are arbitrarily written with positive values of B_2^0 .

Due to the high energy of the excited states of Gd^{3+} , its g -factors are usually very close to the free electron g -value, with typical values in the range 1.99-2. The values of g_{\perp} and g_{\parallel} are reported along with the rest of the best fit parameters in Table 1 and fall in the normal range for Gd^{3+} .¹ In the case of **1**, **2** and **3** the g -value was modelled as isotropic because the values of g_{\parallel} were close to those of g_{\perp} and the standard deviations were significantly larger than the difference between the two. **4** and **5** were modelled with anisotropic g -values. The direction of the g -anisotropy is opposite in the two compounds: **4** has $g_{\perp} > g_{\parallel}$ and **5** the reverse. No explanation for this behaviour presents itself, except the standard errors of the g -values of **5** allows for them to be isotropic.

As a measure of the magnitude of the ground state ZFS, the total energy difference from the lowest to the highest m_s doublet (ΔE) was calculated from the ZFS parameters and is given in the last column of Table 1. For f^7 complexes ZFS is most often dominated by the second

order parameters and this series of complexes is no exception. The value of ΔE is found to be dominated by this second order term and roughly linearly dependent on B_2^0 . The magnitude of B_2^0 and ΔE follows the order opposite to the crystal field strength expected of the axial ligands. This observation is in line with already established results in the literature.²¹ The uncharged ligands in the plane of the bipyramid on the other hand play a minor role.

The two remaining axial ZFS parameters B_4^0 and B_6^0 have less influence on the spectra and ΔE , compared to B_2^0 . Especially B_6^0 is of little to no importance and was so inadequately determined in the fits of **1**, **2** and **3** that it was removed from the model.

The role of the \hat{O}_6^5 operator is to mix the m_s states five steps apart ($\Delta m_s = \pm 5$): in the case of gadolinium that is mixing of the $|\pm 7/2\rangle$ state with the $|\mp 3/2\rangle$ state and the intermixing of the $|\pm 5/2\rangle$ states. B_6^5 is the only off-diagonal parameter allowed to be non-zero under C_5 symmetry, so these states are therefore the only ones interacting at zero field. The compositions of the eigenstates derived from the ZFS parameters are written in Tables S5-S10.

Since B_6^5 is not allowed in D_{5h} symmetry, which is the ideal symmetry of the complexes other than **3**, a correlation between the magnitude of B_6^5 and the deviation from this symmetry is proposed. In order to test this hypothesis, continuous shape measures (CShM) are used as a parameter to describe the deviation of the first coordination sphere from the shape of a pentagonal bipyramid. To compare the B_6^5 parameters between the complexes, they were normalised by the overall splitting ΔE (final column in Table 1). At first glance there is no obvious connection between CShM and B_6^5 . Considering that the high B_6^5 value of **2** is likely caused by the extra peaks of the two Gd sites, and that the rest of the parameters are remarkably like those of **1**, we have ignored this complex in attempting to find a correlation.

This order is then $1 < 5 < 3 < 4$ for CShM, while it is $1 < 3 < 5 < 4$ for B_6^0 . Thus, the ordering fails with regards to 3 and 5. Looking closer at 5 it is found that despite it having a low CShM value, the positions of the axial ligands are the furthest from 180° of the five complexes. The deformation of the axiality seems therefore to influence the off-diagonal ZFS more than distortions to the equatorial ligands, possibly due to the higher charge.

The thermal energy barrier (U_{eff}) of Dy^{3+} single molecule magnets is proportional to the axial crystal field. Since the magnitudes of B_2^0 and ΔE for the Gd^{3+} complexes appear inversely proportional to the axial crystal field, we attempted to correlate them with thermal energy barrier (U_{eff}) of the corresponding Dy^{3+} compounds. 2, 3 and 5 all have Dy^{3+} analogues with published values of U_{eff} .¹² No Dy^{3+} analogues of 1 or 4 have been published, but a version of 4 with non-fluorinated phenoxide ligands is known and was used for the purpose of comparison, though fluorinating the ligand is expected to change the U_{eff} somewhat.^{12,22} The comparison of B_2^0 and U_{eff} can be seen in Figure 6 and shows an almost linear correlation between the two.

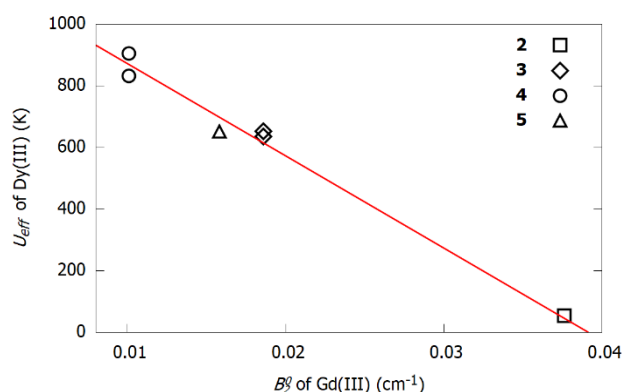


Figure 6. Comparison of the magnitude of B_2^0 and the barrier to reversal of the magnetic moment determined for the corresponding Dy^{3+} complex. $[Dy(OPh)_2Py_5]^+$ is used as analogue to $[Gd(OArF_5)_2Py_5]^+$ (4). The red line is a trendline to guide the eye. When there are two values of U_{eff} it is due to two relaxation rates being observed in the AC susceptibility experiments from which they are extracted.

CONCLUSIONS

Six crystalline powder samples of pseudo 5-fold symmetric complexes of pure Gd^{3+} and Gd^{3+} doped into Y^{3+} have been produced and investigated with EPR at various frequencies. They were found to give intense spectra with a wealth of observable transitions.

The EPR spectra of the gadolinium complexes were generally found to be reproducible by splitting of the ground state with a spin-Hamiltonian in accordance with the restrictions of this symmetry. Some correlation between the continuous shape measure of the complex toward D_{5h} point group symmetry and the relative magnitude of the off-diagonal parameter of the ZFS was found. However, it was found that distortions in the positions of the axial ligands have more impact than

distortions of the ligands in the plane, possibly due to the greater charge of the axial ligands. Furthermore, the nature of the axial ligands is the determining factor for the magnitude of the B_6^5 parameter.

The magnitude of B_2^0 is inversely proportional to the crystal field strength expected for the axial ligands. Comparing this with the thermal energy barrier (U_{eff}) for the Dy^{3+} analogues of these compounds we find an inverse correlation.

To build upon this project, measuring the spectra at a range of temperatures, to reveal the sign of B_2^0 , would be beneficial for a better understanding of the crystal field's influence on the ZFS of gadolinium(III).

AUTHOR INFORMATION

Corresponding Author

*Richard E. P. Winpenny,
richard.winpenny@manchester.ac.uk

ACKNOWLEDGMENT

JBP is supported by a European Research Council Advanced Grant to REPW (ERC-2017-ADG-786734). We also thank the EPSRC(UK) EPR National Research Facility (NS/A000055/1) for access to EPR spectrometers.

REFERENCES

- (1) Abragam, A.; Bleaney, B. *Electron Paramagnetic Resonance of Transition Ions*, 1st ed.; Oxford: Clarendon Press, 1970.
- (2) Buckmaster, H. A.; Shing, Y. H. A Survey of the EPR Spectra of Gd^{3+} in Single Crystals. *Phys. status solidi (a)* **1972**, 12 (2), 325–361.
<https://doi.org/https://doi.org/10.1002/pssa.2210120202>.
- (3) Blagg, R. J.; Ungur, L.; Tuna, F.; Speak, J.; Comar, P.; Collison, D.; Wernsdorfer, W.; McInnes, E. J. L.; Chibotaru, L. F.; Winpenny, R. E. P. Magnetic Relaxation Pathways in Lanthanide Single-Molecule Magnets. *Nat. Chem.* **2013**, 5, 673.
- (4) Gatteschi, D.; Sessoli, R. Quantum Tunneling of Magnetization and Related Phenomena in Molecular Materials. *Angew. Chem., Int. Ed.* **2003**, 42 (3), 268–297.
<https://doi.org/https://doi.org/10.1002/anie.200390099>.
- (5) Newman, D. J. Origin of the Ground State Splitting of Gd^{3+} in Crystals. *Chem. Phys. Lett.* **1970**, 6 (4), 288–290.
[https://doi.org/https://doi.org/10.1016/0009-2614\(70\)85077-1](https://doi.org/https://doi.org/10.1016/0009-2614(70)85077-1).
- (6) Sørensen, M. A.; Weihe, H.; Vinum, M. G.; Mortensen, J. S.; Doerr, L. H.; Bendix, J. Imposing High-Symmetry and Tuneable Geometry on Lanthanide Centres with Chelating Pt and Pd Metalloligands. *Chem. Sci.* **2017**, 8 (5), 3566–3575. <https://doi.org/10.1039/C7SC00135E>.

- (7) Senn, F.; Helm, L.; Borel, A.; Daul, C. A. Electronic Fine Structure Calculation of [Gd(DOTA)(H₂O)] – Using LF-DFT: The Zero Field Splitting. *C. R. Chim.* **2012**, *15* (2), 250–254. <https://doi.org/https://doi.org/10.1016/j.crci.2011.10.008>.
- (8) Lasoroski, A.; Vuilleumier, R.; Pollet, R. Vibrational Dynamics of Zero-Field-Splitting Hamiltonian in Gadolinium-Based MRI Contrast Agents from Ab Initio Molecular Dynamics. *J. Chem. Phys.* **2014**, *141* (1), 14201. <https://doi.org/10.1063/1.4885848>.
- (9) Liu, J.; Chen, Y.-C.; Liu, J.-L.; Vieru, V.; Ungur, L.; Jia, J.-H.; Chibotaru, L. F.; Lan, Y.; Wernsdorfer, W.; Gao, S.; Chen, X.-M.; Tong, M.-L. A Stable Pentagonal Bipyramidal Dy(III) Single-Ion Magnet with a Record Magnetization Reversal Barrier over 1000 K. *J. Am. Chem. Soc.* **2016**, *138* (16), 5441–5450. DOI: 10.1021/jacs.6b02638.
- (10) Ding, Y.-S.; Chilton, N. F.; Winpenny, R. E. P.; Zheng, Y.-Z. On Approaching the Limit of Molecular Magnetic Anisotropy: A Near-Perfect Pentagonal Bipyramidal Dysprosium(III) Single-Molecule Magnet. *Angew. Chem., Int. Ed.* **2016**, *55* (52), 16071–16074. <https://doi.org/10.1002/anie.201609685>.
- (11) Ding, Y.-S.; Yu, K.-X.; Reta, D.; Ortu, F.; Winpenny, R. E. P.; Zheng, Y.-Z.; Chilton, N. F. Field- and Temperature-Dependent Quantum Tunnelling of the Magnetisation in a Large Barrier Single-Molecule Magnet. *Nat. Commun.* **2018**, *9* (1), 3134. <https://doi.org/10.1038/s41467-018-05587-6>.
- (12) Ding, Y.-S.; Han, T.; Zhai, Y.-Q.; Reta, D.; Chilton, N. F.; Winpenny, R. E. P.; Zheng, Y.-Z. A Study of Magnetic Relaxation in Dysprosium(III) Single-Molecule Magnets. *Chem. Eur. J.* **2020**, *26* (26), 5893–5902. <https://doi.org/10.1002/chem.202000646>.
- (13) Gupta, S. K.; Rajeshkumar, T.; Rajaraman, G.; Murugavel, R. An Air-Stable Dy(III) Single-Ion Magnet with High Anisotropy Barrier and Blocking Temperature. *Chem. Sci.* **2016**, *7* (8), 5181–5191. <https://doi.org/10.1039/C6SC00279J>.
- (14) Gupta, S. K.; Rajeshkumar, T.; Rajaraman, G.; Murugavel, R. An Unprecedented Zero Field Neodymium(III) Single-Ion Magnet Based on a Phosphonic Diamide. *Chem. Commun.* **2016**, *52* (44), 7168–7171. <https://doi.org/10.1039/C6CC03066A>.
- (15) Gupta, S. K.; Rajeshkumar, T.; Rajaraman, G.; Murugavel, R. Is a Strong Axial Crystal-Field the Only Essential Condition for a Large Magnetic Anisotropy Barrier? The Case of Non-Kramers Ho(III) versus Tb(III). *Dalton Trans.* **2018**, *47* (2), 357–366. <https://doi.org/10.1039/C7DT04020B>.
- (16) Stevens, K. W. H. Matrix Elements and Operator Equivalents Connected with the Magnetic Properties of Rare Earth Ions. *Proc. Phys. Soc. A* **1952**, *65* (3), 209.
- (17) Newman, D.; Ng, B. Empirical Crystal Fields. In *Crystal Field Handbook*; Newman, D., Ng, B., Eds.; Cambridge University Press: Cambridge, 2000; pp 26–42. DOI: 10.1017/CBO9780511524295.004.
- (18) Jacobsen, C. J. H.; Pedersen, E.; Villadsen, J.; Weihe, H. ESR Characterization of Trans-Diacidatotetrakis(Pyridine)Vanadium and -Manganese Trans-V(II)(Py)₄X₂ and Trans-Mn(II)(Py)₄X₂ (X = NCS, Cl, Br, I; Py = Pyridine). *Inorg. Chem.* **1993**, *32* (7), 1216–1221. <https://doi.org/10.1021/ic00059a031>.
- (19) Husein Mor, H.; Weihe, H.; Bendix, J. Fitting of EPR Spectra: The Importance of a Flexible Bandwidth. *J. Mag. Res.* **2010**, *207* (2), 283–286. <https://doi.org/https://doi.org/10.1016/j.jmr.2010.09.011>.
- (20) Shannon, R. D. Revised Effective Ionic Radii and Systematic Studies of Interatomic Distances in Halides and Chalcogenides. *Acta Crystallogr. A* **1976**, *32* (5), 751–767. <https://doi.org/10.1107/S0567739476001551>.
- (21) Levin, L. I.; Gorlov, A. D. Gd³⁺ Crystal-Field Effects in Low-Symmetric Centres. *J. Phys. Condens. Matter* **1992**, *4* (8), 1981–1992. <https://doi.org/10.1088/0953-8984/4/8/013>.
- (22) Ma, Y.; Zhai, Y.-Q.; Luo, Q.-C.; Ding, Y.-S.; Zheng, Y.-Z. Ligand Fluorination to Mitigate the Raman Relaxation of Dy(III) Single-Molecule Magnets: A Combined Terahertz, Far-IR and Vibronic Barrier Model Study. *J. Angew. Chem., Int. Ed.* **2022**, *61* (26), e202206022. <https://doi.org/https://doi.org/10.1002/anie.202206022>.

This page is intentionally left blank

4.3 Supporting Information

Electron Paramagnetic Resonance Spectra of Pseudo-Pentagonal Bipyramidal Gadolinium Complexes

Jonatan B. Petersen,¹ You-Song Ding,^{1,2} Eric J. L. McInnes,¹ Yan-Zhen Zheng,² Ramaswamy Murugavel,³ and Richard E. P. Winpenny^{1*}

¹ Department of Chemistry, School of Natural Sciences, The University of Manchester, Oxford Road, Manchester M13 9PL, United Kingdom

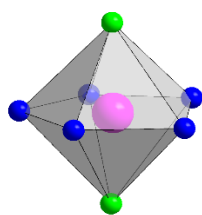
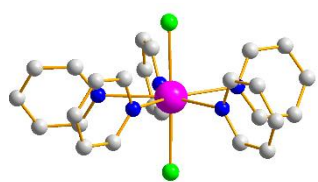
[§]School of Science, Xi'an Jiaotong University, Xi'an 710049, China

² Department of Chemistry, Indian Institute of Technology Bombay, Mumbai-400076, India

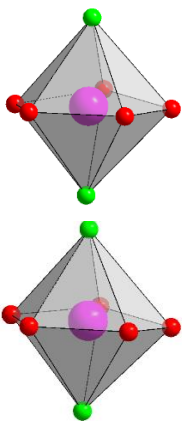
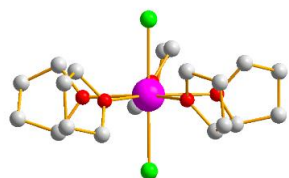
Crystallography

Table S1. X-ray crystallographic data

	[GdCl ₂ (Py) ₅] BPh ₄ ·THF (1)	2[GdCl ₂ (THF) ₅] 2BPh ₄ · THF (2)	[Y(O ^t Bu)Cl (THF) ₅] BPh ₄ ·2THF (3)	[Y(OArF ₅) ₂ (Py) ₅] B(ArF ₅) ₄ ·0.5C ₆ H ₄ 4 (4)	[Y(^t BuPO(NH ^t Pr) ₂) ₂ (H ₂ O) ₅]I ₃ ·H ₂ O ·2(^t BuPO(NH ^t Pr) (5)
Reference	This work	This work	^{1,2}	This work	³
Sum formula	GdC ₄₉ H ₄₅ BCl ₂ N ₅	Gd ₂ C ₉₂ H ₁₂₈ B ₂ C ₁₄ O ₁₁	YC ₅₆ H ₈₅ BClO ₈	YC ₆₄ H ₃₂ BF ₃₀ N ₅ O ₂	YC ₄₀ H ₁₁₂ I ₃ N ₈ O ₁₀ P ₄
Formula weight (g/mol)	942.9	1887.9	1021.4	1572.7	1458.9
Crystal system	Orthorhombic	Triclinic	Monoclinic	Triclinic	Triclinic
Space group	<i>Pca</i> 2 ₁	<i>P</i> $\bar{1}$	<i>P</i> 2 ₁ / <i>n</i>	<i>P</i> $\bar{1}$	<i>P</i> $\bar{1}$
<i>T</i> (K)	150	150	100	150	-
<i>a</i> (Å)	19.9112(5)	12.5445(7)	13.636(1)	11.965(1)	13.743(2)
<i>b</i> (Å)	12.5805(3)	12.7740(7)	12.434(2)	14.515(1)	14.745(2)
<i>c</i> (Å)	17.9843(5)	29.309(2)	32.618(4)	19.428(2)	20.690(4)
α (°)	90	79.520(5)	90	73.514(7)	92.44(1)
β (°)	90	79.800(5)	90.434(2)	77.693(6)	108.16(1)
γ (°)	90	82.567(4)	90	79.769(6)	114.93(1)
<i>V</i> (Å ³)	4504.9	4522.3	5530.1	3136.3	3538.3
<i>Z</i>	4	2	4	2	2
ρ_{calc} (g cm ⁻³)	1.390	1.386	1.227	1.665	1.369
μ (mm ⁻¹)	1.63	1.628	1.145	1.069	2.269
<i>F</i> ₀₀₀	1908	1948	2184	1562	1492
θ (°)	2.784-29.06	2.685-29.185		2.712-28.961	
Goodness of fit	1.013	1.096		1.064	
<i>R</i> ₁ (%)	3.79	9.96	5.85	9.36	8.04
w <i>R</i> ₂ (%)	6.22	20.91		22.89	

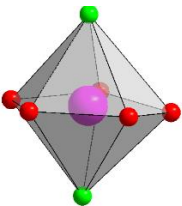
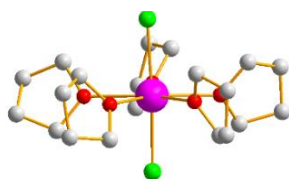


[GdCl₂(Py)₅]BPh₄·THF (**1**)

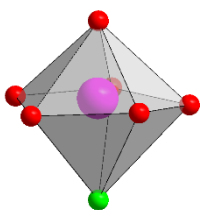
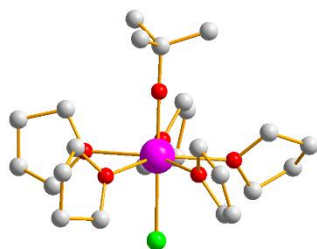


2[GdCl₂(THF)₅]2BPh₄·THF (**2**)

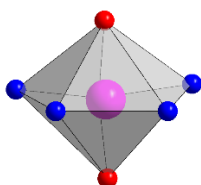
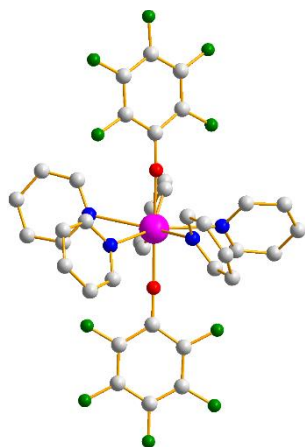
Site 1



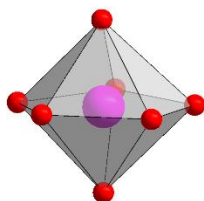
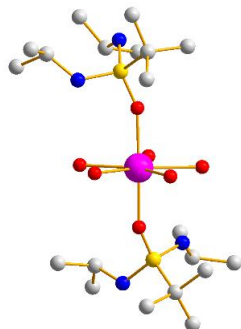
Site 2



[Y(O'Bu)Cl(THF)₅]BPh₄·2THF (**3**)



[Y(OArF₅)₂(Py)₅]B(ArF₅)₄·0.5C₆H₁₄ (**4**)



[Y('BuPO(NH'Pr)₂)(H₂O)₅]I₃·H₂O·2('BuPO(NH'Pr) (**5**)

Figure S1. Solid state structures of the 5 complexes, excluding counterions and solvent. Colour code: Gd/Y=magenta, P=yellow, Cl=light green, F=dark green, O=red, N=Blue and C=grey. Hydrogen is not shown

EPR spectroscopy

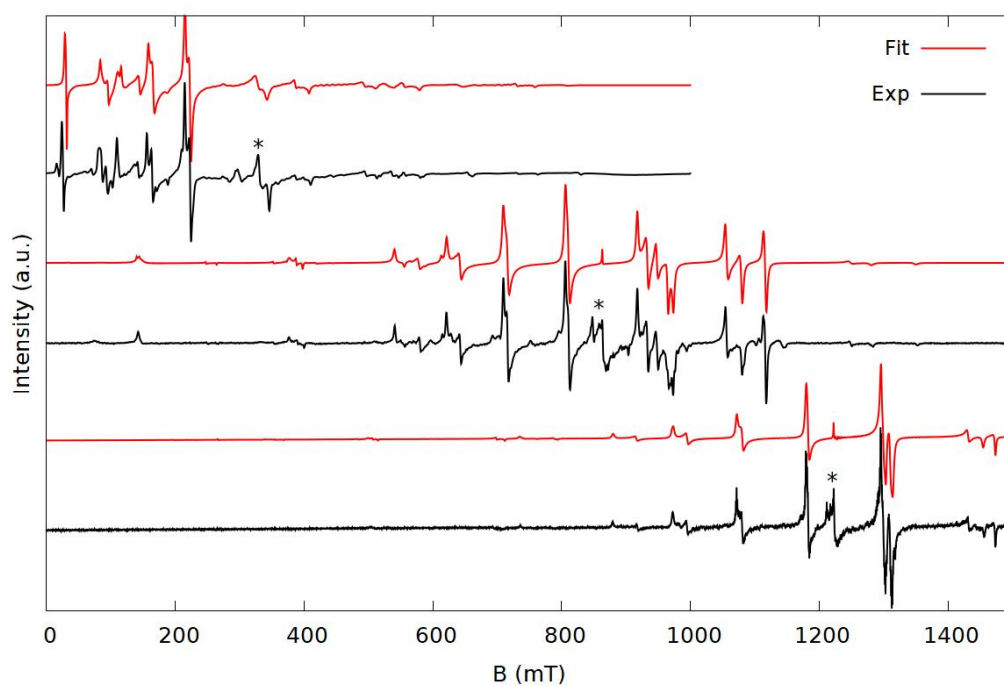


Figure S2. Spectra (black) and simulations (red) of **2** at X (top), K (middle) and Q-band (bottom). Fitted with the spin Hamiltonian of equation 1 with an added B_2^2 term. Simulation parameters in Table S2

Table S2. Best fit spin Hamiltonian parameters for **2** from fit of EPR spectra using alternative spin Hamiltonian. Numbers in parenthesis are estimated standard deviations of the last digit.

	g_{\perp}	g_{\parallel}	B_2^0 10^{-2} cm^{-1}	B_2^2 10^{-3} cm^{-1}	B_4^0 10^{-5} cm^{-1}
2	1.9910(2)	-	3.705(2)	1.83(5)	-0.92(4)

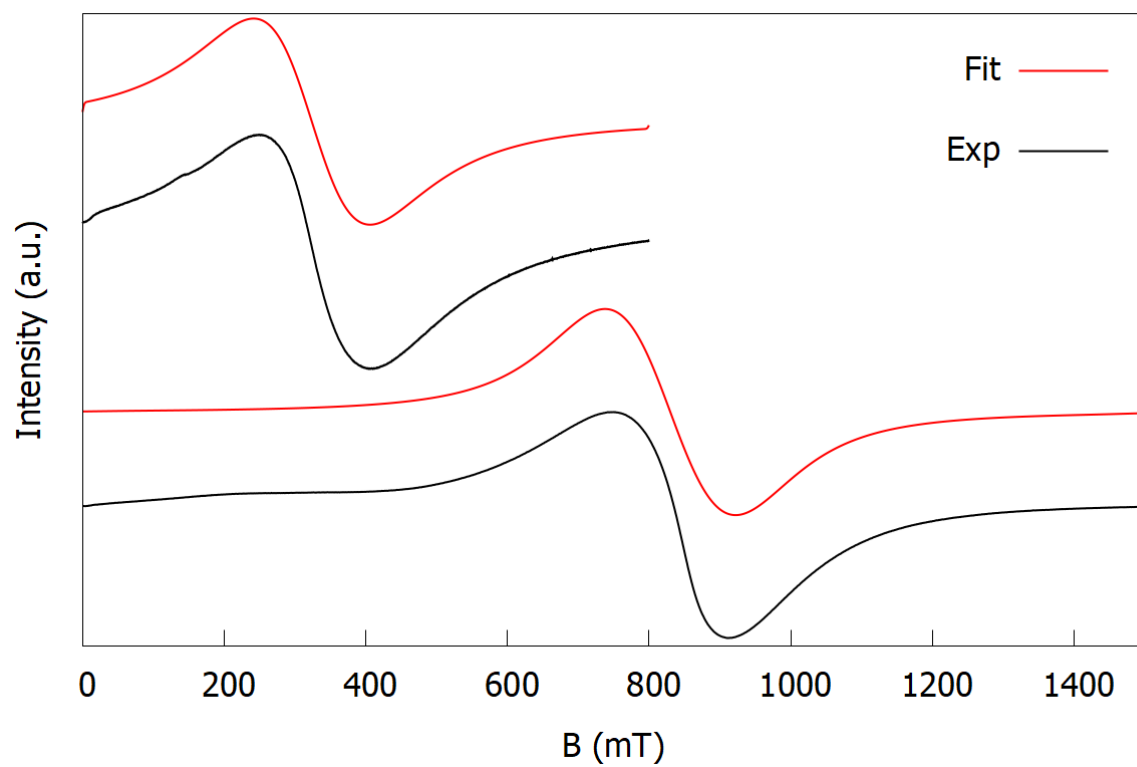


Figure S3. Spectra (black) and simulations (red) of neat $[\text{GdCl}_2(\text{THF})_5]_2\text{BPh}_4$ at X (top) and K (bottom). Simulated with $S=1/2$ and $g_{\text{iso}}=1.99$.

Table S3. Best fit spin Hamiltonian parameters for **5** from fit of X- and Q-band EPR spectra. Numbers in parenthesis are estimated standard deviations of the last digit. The last two columns are the total energy difference from the lowest to the highest m_s doublet (ΔE) and the B_6^5 parameter normalised by ΔE

5	g_{\perp}	g_{\parallel}	B_2^0 10^{-2} cm^{-1}	B_4^0 10^{-5} cm^{-1}	B_6^0 10^{-7} cm^{-1}	B_6^5 10^{-5} cm^{-1}	ΔE (cm^{-1})	$B_6^5/\Delta E$ (10^{-5})
X-band	1.988(4)	1.997(7)	1.47(2)	-0.3(2)	-4(1)	7.2(7)	0.527	14
Q-band*	1.989(3)*	1.995(6)*	1.6(1)	-3(1)	-4(5)	6(2)	0.58	10

*not field corrected

Parameter conversion

In order to convert the P_k^q parameters obtained via the multi purpose EPR fitting program to the B_k^q parameters as originally defined by Stevens we used the relation.^{4,5}

$$B_{q,Wybourne}^k = \frac{P_k^q}{2^k} \sqrt{\frac{(2S + k + 1)!}{(2S - k)!}}$$

Which results in parameters normalised in Wybourne's notation. These were then divided by the ratios listed in Table S4 to convert them to Stevens parameters.⁶

$$B_{k,Stevens}^q = \frac{B_{q,Wybourne}^k}{\lambda_{k,q}}$$

Table S4. Conversion factors between Stevens and Wybourne normalised parameters.

k	q	$\lambda_{k,q}$
2	0	2
2	2	$\frac{2}{\sqrt{6}}$
4	0	8
6	0	16
6	5	$\frac{-8}{3\sqrt{77}}$

Ground state compositions

Table S5. Composition of the eigenstates obtained from the best fit ZFS of **1** in the m_s state basis.

$m_s \backslash E(\text{cm}^{-1})$	0.000	0.000	0.227	0.227		0.671	0.671	1.308	1.308
-3.5			0.00016					99.99984	
-2.5							100		
-1.5				99.99984					0.00016
-0.5	100								
0.5		100							
1.5			99.99984					0.00016	
2.5						100			
3.5				0.00016					99.99984

Table S6. Composition of the eigenstates obtained from the best fit ZFS of **2** in the m_s state basis.

$M_s \backslash E(\text{cm}^{-1})$	0.000	0.000	0.234	0.234	0.693	0.693	1.356	1.356
-3.5			0.0153				99.9847	
-2.5						100		
-1.5				99.9847				0.0153
-0.5	100							
0.5		100						
1.5			99.9847				0.0153	
2.5					100			
3.5				0.0153				99.9847

Table S7. Composition of the eigenstates obtained from the best fit ZFS of **2** in the m_s state basis using alternative spin-hamiltonian including the B_2^2 parameter term.

$m_s \backslash E(\text{cm}^{-1})$	0.000	0.000	0.234	0.234	0.691	0.691	1.357	1.357
-3.5		0.00001		0.00554			99.99444	
-2.5	0.03139		0.00026		99.96833	0.00001		
-1.5	0.00005	0.36631		99.62805		0.00003	0.00556	
-0.5	99.58996	0.01228	0.36614		0.03163			
0.5	0.01228	99.58996		0.36614		0.03163		
1.5	0.36631	0.00005	99.62805		0.00003			0.00556
2.5		0.03139		0.00026	0.00001	99.96833		
3.5	0.00001		0.00554					99.99444

Table S8. Composition of the eigenstates obtained from the best fit ZFS of **3** in the m_s state basis.

$m_s \backslash E(\text{cm}^{-1})$	0.000	0.000	0.123	0.123	0.356	0.356	0.673	0.673
-3.5			0.0071				99.9929	
-2.5						100		
-1.5				99.9929				0.0071
-0.5	100							
0.5		100						
1.5			99.9929				0.0071	
2.5					100			
3.5				0.0071				99.9929

Table S9. Composition of the eigenstates obtained from the best fit ZFS of **4** in the m_s state basis.

$m_s \backslash E(\text{cm}^{-1})$	0.0000	0.0000	0.0551	0.0551	0.2078	0.2078	0.3611	0.3611
-3.5			0.4964				99.5036	
-2.5					100			
-1.5				99.5036				0.4964
-0.5	100							
0.5		100						
1.5			99.5036				0.4964	
2.5						100		
3.5				0.4964				99.5036

Table S10. Composition of the eigenstates obtained from the best fit ZFS of **5** in the m_s state basis.

$m_s \backslash E(\text{cm}^{-1})$	0.000	0.000	0.106	0.106	0.323	0.323	0.568	0.568
-3.5			0.1624				99.8376	
-2.5						100		
-1.5				99.8376				0.1624
-0.5		100						
0.5	100							
1.5			99.8376				0.1624	
2.5					100			
3.5				0.1624				99.8376

Table S11. Best fit B_2^0 parameters and strain parameters. Numbers in brackets are the estimated standard deviations of the last digit.

	B_2^0 10^{-2} cm^{-1}	B_2^0 strain 10^{-2} cm^{-1}	B_2^0 strain %
1	3.63(1)	0.0023 (5)	0.06
2	3.76(1)	0.021(10)	0.56
3	1.86(2)	0.0059(12)	0.32
4	1.01(8)	0.074 (11)	7.3
5	1.58(8)	0.013(7)	0.82

References

- (1) Ding, Y.-S.; Yu, K.-X.; Reta, D.; Ortu, F.; Winpenny, R. E. P.; Zheng, Y.-Z.; Chilton, N. F. Field- and Temperature-Dependent Quantum Tunnelling of the Magnetisation in a Large Barrier Single-Molecule Magnet. *Nat. Commun.* **2018**, *9* (1), 3134. <https://doi.org/10.1038/s41467-018-05587-6>.
- (2) Evans, W. J.; Olofson, J. M.; Ziller, J. W. Synthesis and Structure of the Cationic Tert-Butoxide Complexes $Y_3(OR)_7Cl(THF)_3^+$, $Y_2(OR)_4Cl(THF)_4^+$, and $Y(OR)Cl(THF)_5^+$: Representatives of a New Class of Yttrium Alkoxides. *J. Am. Chem. Soc.* **1990**, *112* (6), 2308–2314. <https://doi.org/10.1021/ja00162a035>.
- (3) Gupta, S. K.; Rajeshkumar, T.; Rajaraman, G.; Murugavel, R. An Air-Stable Dy(III) Single-Ion Magnet with High Anisotropy Barrier and Blocking Temperature. *Chem. Sci.* **2016**, *7* (8), 5181–5191. <https://doi.org/10.1039/C6SC00279J>.
- (4) Rudowicz, C.; Chung, C. Y. The Generalization of the Extended Stevens Operators to Higher Ranks and Spins, and a Systematic Review of the Tables of the Tensor Operators and their Matrix Elements. *J. Phys. Condens. Matter* **2004**, *16* (32), 5825–5847. <https://doi.org/10.1088/0953-8984/16/32/018>.
- (5) Smith, D.; Thornley, J. H. M. The Use of 'Operator Equivalents'. *Proc. Phys. Soc.* **1966**, *89* (4), 779. <https://doi.org/10.1088/0370-1328/89/4/301>.
- (6) Newman, D. J.; Ng, B.. Empirical Crystal Fields. In *Crystal Field Handbook*; Cambridge University Press, 2000. <https://doi.org/10.1017/CBO9780511524295>.

5. Conclusions and Future Work

5.1 Conclusions

A number of coordination complexes have been studied using EPR techniques to investigate their magnetic properties and electronic structure.

Nitridobis-(pyrrolidinedithiocarbamato)chromium(V) ($[\text{Cr}(\text{N})(\text{pyrrdtc})_2]$) was explored as a representative of chromium nitrido complexes as analogues of vanadyl complexes.

A thorough examination of the relaxation properties of $[\text{Cr}(\text{N})(\text{pyrrdtc})_2]$ in frozen solutions produced results: both spin-lattice and phase memory times are, as expected, of similar magnitude to those of vanadyl. The temperature dependence of T_1 was modelled and found to be dependent on direct, Raman and local mode relaxation, while T_m was restricted by T_1 at higher temperature. It has previously been proposed that the nuclear spin of the paramagnetic centre could have an influence on some relaxation mechanisms such as direct processes. Comparison between measurements at the maximum intensity peak and at one of the ^{53}Cr hyperfine peaks in the same orientation showed that neither T_1 nor T_m are dependent on the nuclear spin of chromium. Thus at least the dominant Raman mechanism is independent of the nuclear spin of chromium in the temperature range explored. For the direct process the amount of data at the lowest temperatures might be too small to conclude that the nuclear spin has no effect, though there is no indication that it does.

The iso-structural nitridobis-(pyrrolidinedithiocarbamato)rhenium(V) complex was synthesized and used as a diamagnetic host for doping with the chromium compound. In this solid-state dilution sample the Debye temperature was higher and the local mode relaxation was less influential leading to T_1 large enough at room temperature to not restrict T_m . This allowed us to record EPR signals all the way up to room temperature. Quantum coherence at room temperature was demonstrated by measurement of Rabi oscillations. All this comes together to validate the chromium nitrido moiety as the equal of vanadyl as a qubit candidate in terms of relaxational and spectroscopic behaviour.

Pulsed EPR and AC susceptibility experiments were conducted on $\text{Gd}(\text{trensal})$ at lower field than in the previous project to study (see appendix B) its relaxation properties. Spin-lattice relaxation proved to be transition dependent and the temperature variation was modelled with direct, Raman and local mode relaxation. T_1 was longer than at high field, but T_m was

shorter even though it was no longer restricted by T_1 . It was shown that the remarkably long T_m measured at high field was likely caused by polarization effects from the field.

The zero field splitting of a series of five pentagonal bi-pyramidal gadolinium(III) complexes, doped into their yttrium(III) congeners, was determined using multifrequency cw EPR at room temperature and certain trends extracted. The ZFS was dominated by the position and crystal field strength of the negatively charged axial ligands. The magnitude of the off-diagonal term of the ZFS seemed linked to the deviation from ideal D_{5h} symmetry but was more susceptible to deviations in the positions of the axial ligands. The overall extent of the ZFS was dominated by the axial second order Stevens parameter B_2^0 which was found to be inversely proportional to the expected CF strength of the axial ligands. This was expanded to the discovery of an inverse relationship between B_2^0 and the effective barrier for reversal of the magnetic moment (U_{eff}) of the corresponding dysprosium(III) SMMs. Due to the inherent complexity of the gadolinium ZFS, rationalising its behaviour can be a challenge. The crystal field splitting of dysprosium on the other hand is more systematic. This result could therefore be considered somewhat surprising.

5.2 Future Work

The properties of $[\text{Cr}(\text{N})(\text{pyrrdtc})_2]$ opens a few interesting paths for further research of other $\{\text{Cr}(\text{N})\}^{2+}$ complexes and for combinations and comparisons with vanadyl.

Coupling $\{\text{Cr}(\text{N})\}^{2+}$ with $\{\text{V}(\text{O})\}^{2+}$ could be used as a CNOT quantum gate with the two working as similar but magnetically inequivalent qubits. This could be done by linking them together with a ligand of sufficient length to get an interaction of the right magnitude.

Another thing to look at could be a direct comparison of iso-structural vanadyl and chromium nitride complexes doped into the same matrix, possibly a solid-state dilution in iso-structural rhenium nitrido or gallium chlorido complexes. This would give us the opportunity to study and compare the two in the exact same environment with the same phonon spectrum and nuclear spins apart from those on the $\{\text{VO}\}^{2+}$ and $\{\text{CrN}\}^{2+}$ units and clarify whether the higher vibrational frequency of the $\text{Cr}\equiv\text{N}$ bond makes T_1 less temperature dependent. On the same theme chromium nitrido complexes with more rigid

ligands could decrease the temperature dependence of T_1 even more and allow larger values of T_m at high temperature.

The effect of the nuclear spin (or lack thereof) can be more thoroughly investigated by preparing isotope pure ^{50}Cr and ^{53}Cr compounds. This experiment is being contemplated.

Since Ln(trensal) complexes are being proposed as model system for qubits any research improving our understanding of their relaxation behaviour is a valuable addition to the field. A topic that has received some research attention recently is the potential of linking two different lanthanides together using molecular cages based on trensal. This leads to an interest in how geometric changes around the lanthanide ion affect the relaxation behaviour. Future projects therefore include a systematic survey of the effect of substituents e.g. methoxy groups in different positions on the aromatic ring, on the relaxation dynamics, to see if this has any systematic effect.

The correlation between B_2^0 of the fivefold symmetric gadolinium(III) complexes and U_{eff} of their dysprosium(III) analogues gives EPR some predictive power for the relaxation rates in SMMs. Since the ZFS parameters of gadolinium are in many cases easier to obtain experimentally than those of other lanthanides, understanding this correlation better could be an approach for screening of possible dysprosium SMMs. If this can be expanded to general trends for other series of Gd and Dy complexes it could turn out to be a valuable tool in SMM characterisation and design. Furthermore it would be of great interest to investigate if gadolinium(III) parameters have any correlation with the properties of SMMs of other lanthanides.

Appended Articles

A. Dimerized *p*-Semiquinone Radical Anions Stabilized by a Pair of Rare-Earth Metal Ions

Preface

This is a communication paper published in Inorganic Chemistry, that I co-authored, during the first year of my PhD, as a side project to my original project (which was focused on

magnetic interactions in lanthanide dimers). It is not meant to be taken as a part of the main part of the thesis as I did not have a leading role in the project. I was involved with the measurement and simulation of EPR data and interpretation of the magnetometry data. In terms of writing, I contributed to the article with the three paragraphs and the figures related EPR spectroscopy. It is published as:

Han, T., Petersen, J. B., Li, Z.-H., Zhai, Y.-Q., Kostopoulos, A., Ortu, F., McInnes, E. J. L., Winpenny, R. E. P., & Zheng, Y.-Z. (2020). Dimerized p-Semiquinone Radical Anions Stabilized by a Pair of Rare-Earth Metal Ions. *Inorganic Chemistry*, 59(11), 7371–7375. <https://doi.org/10.1021/acs.inorgchem.0c00503>

This page is intentionally left blank

Dimerized *p*-Semiquinone Radical Anions Stabilized by a Pair of Rare-Earth Metal Ions

Tian Han,¹ Jonatan B. Petersen,² Zi-Han Li,¹ Yuan-Qi Zhai,¹ Andreas Kostopoulos,² Fabrizio Ortu,² Eric J. L. McNnes,² Richard E. P. Winpenny^{2,*} and Yan-Zhen Zheng^{1,*}

¹ School of Science, Frontier Institute of Science and Technology (FIST), Research Institute of Xi'an Jiaotong University (Zhejiang), State Key Laboratory for Mechanical Behavior of Materials, MOE Key Laboratory for Nonequilibrium Synthesis and Modulation of Condensed Matter, Xi'an Key Laboratory of Sustainable Energy and Materials Chemistry, Xi'an Jiaotong University, Xi'an 710049, China

² School of Chemistry, The University of Manchester, Oxford Road, Manchester M13 9PL, United Kingdom

ABSTRACT: Here we report stable *para*-quinone-radical bridged rare-earth complexes involving the ligands tetramethylquinone ($\text{QMe}_4^{\bullet-}$). The complexes, $\{\text{Y}[(\text{QMe}_4^{\bullet-})\text{Cl}_2(\text{THF})_3]_2\}$ **1** and $\{\text{Gd}[(\text{QMe}_4^{\bullet-})\text{Cl}_2(\text{THF})_3]_2\}$ **2**, are sufficiently stable that we can measure the single-crystal structures and perform magnetic and electron paramagnetic resonance (EPR) measurements. These studies show the presence of a semiquinone form and that the magnetic interaction between the radicals in the dimer is strong and antiferromagnetic.

Quinones, widely found in nature, are capable of transferring electrons and participating in electrochemical reactions for energy transduction and storage such as photosynthesis and respiration, which is requisite for life.¹ Quinones can also coordinate to metal ions in the form of catecholate, semiquinone or hydroquinone; amongst these, semiquinone complexes are important molecules in chemical and biological redox processes, like an iron-quinone complex involved in type II bacterial photosynthetic reaction center.² Despite only one electron transport pathway available to form this odd-electron radical, the redox properties of semiquinones are profoundly affected by the functional groups and coordination environments. Thus, semiquinone complexes have extensive applications in optical, electrical and magnetic sciences due to their fascinating electronic structures and adjustable redox properties.³

In contrast to the well-developed chemistry of *o*-semiquinone complexes,⁴ there are a few examples of *p*-semiquinone complexes. To the best of our knowledge, apart from the terminal *p*-semiquinone-radical systems,⁵ only three *p*-semiquinone-radical-bridged complexes have been

structurally characterized. These are a $[\text{BQ}]^{\bullet-}$ -bridged Mn(II) dimer with π - π stacking interaction between radicals ($\text{BQ} = 1,4$ -benzoquinone), $[\text{BQ}]^{\bullet-} / [\text{p-B}_2\text{Q}]^{\bullet-}$ -bridged K(I) infinite chains ($\text{p-B}_2\text{Q} = 2,5$ -di-*tert*-butyl-1,4-benzoquinone), and a $[\text{QCl}_4]^{\bullet-}$ -bridged one-dimensional linear Mn(III) chain ($\text{QCl}_4 = \text{tetrachloro-1,4-benzoquinone}$).⁶ No single crystal structure of *p*-semiquinone-radical-bridged Rare Earth (RE) complex has been determined, although two *p*-semiquinone-radical-bridged Sc(III) compounds have been proposed.⁷ In these few examples the *p*-semiquinone radicals were obtained *via* reduction of the corresponding benzoquinone.

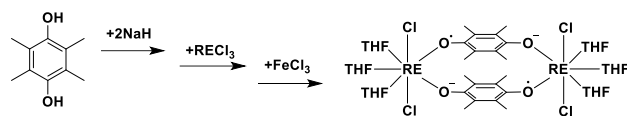
Moreover, incorporating radical bridges into lanthanide complexes has attracted much attention of scientists in the field of single-molecule magnets (SMMs).⁸ One prime example is the N_2^{3-} radical-bridged lanthanide dimers, where strong exchange interactions are transmitted, giving a high blocking temperature $T_B = 20$ K and record coercive field $H_c = 7.9$ T (10 K) in a Tb₂ compound.⁹ Other systems like $[\text{Dy-radical}]_2$ pair / bptz radical-bridged dilanthanide / metallacyclic triangle complexes also exhibit interesting SMM behaviour.¹⁰

Here we report *p*-semiquinone-radical-bridged rare-earth complexes involving the ligand *para*-tetramethylquinone ($\text{QMe}_4^{\bullet-}$). In these complexes two $\text{QMe}_4^{\bullet-}$ act as bridges between two Gd or Y centres, and show π -stacking. EPR studies of Y, Gd and diluted Gd analogues reveal a strong antiferromagnetic coupling between two stacking radicals.

The H_2QMe_4 ligand was deprotonated with sodium hydride (NaH), and reacted with anhydrous RECl_3 ($\text{RE} = \text{Y, Gd}$) in THF at room temperature for one day. The solution was then oxidised with one equivalent of FeCl_3 . The resulting blue-black

powder was washed and recrystallized from $\text{CH}_2\text{Cl}_2/\text{THF}$ to give dark blue crystals of compounds $[\{\text{Y}(\mu\text{-QMe}_4^{\cdot-})_2\text{Cl}_2(\text{THF})_3\}_2]$ (**1**), $[\{\text{Gd}(\mu\text{-QMe}_4^{\cdot-})_2\text{Cl}_2(\text{THF})_3\}_2]$ (**2**) and 10 % Gd@**1** (**3**) (Scheme 1). The dimers are very air-sensitive, and the color changes to red when exposed to air for few seconds, but both crystals and solutions are stable under inert gas.

Scheme 1. Syntheses of *p*-semiquinone-radical-bridged RE complexes **1** and **2**.



RE = Y (**1**), Gd (**2**)

Single-crystal X-ray diffraction analysis shows that **1** and **2** are isomorphous; the structure of **1** is described here (Table S1). Complex **1** crystallizes in the monoclinic space group P21/c as a centrosymmetric dimer. Each Y(III) ion is seven-coordinate with two oxygen atoms from two *p*-semiquinone radical anions, two Cl⁻ anions and three THF molecules, while each *p*-semiquinone radical bridges two Y(III) ions (Figure 1). Thus, two Y(III) ions are linked by two *p*-semiquinone radicals. Such a dimerized *p*-semiquinone radical anions is also found in the rare crystalline *p*-semiquinone-radical-bridged Mn(II) dimer.^{6a} The Shape value for the local coordination geometry is estimated to be 0.729 from ideal pentagonal bipyramid with D5h symmetry, confirming five oxygen atoms in the equatorial plane with two Cl⁻ in the axial positions.¹¹ The Y–OTHF bond lengths range from 2.405 to 2.502 Å, with the Y–O_{rad} distances of 2.239 Å, while Y–Cl distances are around 2.62 Å (Table S2). The bond lengths in **1** is compared with that in Yb(III)-ketyl complexes.¹² After calibrating the ionic radius change by comparing Yb–OTHF (2.35 Å) with Y–OTHF (2.46 Å) bond lengths, the Y–O_{rad} is lengthened from Yb–O_{rad} (2.07 Å) by ca. 0.06 Å. Significant lengthening is further observed in Yb complexes of radicals derived from α -diketones where the charge and the radical spread over the two O-donors as against one in the Yb-ketyl complexes.^{12b} Thus, the negative charge for the bridging ligand in **1** is proposed to spread over the two O-donors.

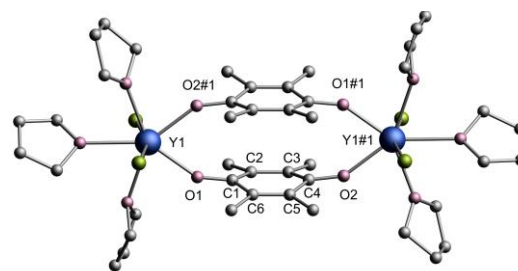


Figure 1. Molecular structure of complex **1**. All the H atoms are omitted for clarity. Colour codes: blue, Y; green, Cl; pink, O and grey, C. C1–C2: 1.448(5) Å, C2–C3: 1.374(5) Å, C3–C4: 1.449(5) Å, C4–C5: 1.456(5) Å, C5–C6: 1.367(5) Å, C6–C1: 1.446(5) Å. Symmetry code: #1 1-*x*, 1-*y*, 1-*z*.

The charge within complex **1** is balanced if the bridging ligand is the monoanion radical $\text{QMe}_4^{\cdot-}$. Further confirmation is found from the C–O and C–C bond lengths within the ligand. The C–O bond lengths in $\text{QMe}_4^{\cdot-}$ in **1** are 1.290(4) and 1.288(4) Å, falling in the range expected in semiquinone complexes (1.29 Å),^{5a,6a} and shorter than the corresponding distances in the 1,4-hydroquinone dianion bridged metal complexes (1.314–1.369 Å).^{5a,13,14} The C1–C2 and C1–C6 bond lengths are 1.448(5) and 1.446(5) Å, respectively, close to the expected value in semiquinone complexes (1.44 Å).^{5a,6a} The C–C bond lengths also vary in a different way in quinones, semiquinones and benzene-like species. If we consider the lengths *b* and *c* in Figure 2, and compare with the QCl_4 ligand as an analogy,¹⁴ the C–C bonds are almost equal in the benzenoid form of QCl_4^{2-} with $\Delta(b-c)$ close to 0 Å, whilst for $\text{QCl}_4^{\cdot-}$ $\Delta(b-c) \approx 0.1$ Å. In **1** the average of $\Delta(b-c)$ for the bridging ligand is 0.079 Å, almost a same value in the *p*-semiquinone-radical-bridged Mn(II) dimer,^{6a} indicating the semiquinonate form of $\text{QMe}_4^{\cdot-}$. As such, we can conclude that the QMe_4 in **1** is a radical anion.

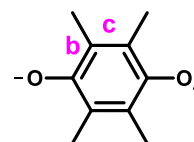


Figure 2. Representative of *b* and *c* in semiquinone radical.

In **1**, there are two equatorial $\text{QMe}_4^{\cdot-}$ ligands around each Y(III) ion, having an O_{rad}–Y–O_{rad} bond angle of 72.89(8)°, close to an ideal PB geometry. These two $\text{QMe}_4^{\cdot-}$ ligands stack in a face-to-face manner, with the dihedral angle between the two benzene planes of 0.02°. The centroid–centroid distance (Cg...Cg) between the rings is 3.097 Å.

Such a type of structure is known as π -dimer radical anion with strong $\pi\cdots\pi$ repulsion. Rotating this dimer in Fig. 1 along the centroid-centroid direction by 90° , we can find that the semiquinone anion has a slightly bent, boat-like conformation, typical of π -dimerized pancake-bonded systems (Figure S1 and S2).¹⁵

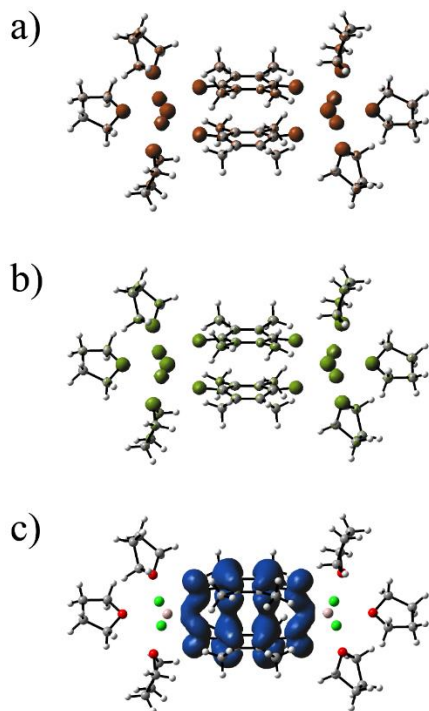


Figure 3. (a) α -spin density shown at a 0.1 isovalue in brown; (b) β -spin density shown at a 0.1 isovalue in green and (c) total spin density shown at a 0.03 isovalue in blue.

Density functional theory calculations were carried out to provide greater insight into the origin of the strong coupling between two radicals in **1**. The magnetic orbitals, as determined by DFT methods (B3LYP-D3/def2-TZVP/def2-SVP), show that the α -spin density is primarily localized on two Y^{III} ions as well as the coordinated atoms to them, as shown in Figure 3a at a 0.1 isovalue. The location of β -spin density is similar to the former one at the same isovalue but some different shape of β -spin density if obtained (Figure 3b). Thus, the overlap of the magnetic pair (Figure 3c) at 0.03 isovalue presents with strong mixing between the face of two radicals, demonstrating strong antiferromagnetic coupling. This result is in accord with a bonding model in which strong π -bonding from upper semiquinone radical to the nether one's π orbitals. Meanwhile, visual inspection of the canonical orbitals in **1** also reveals the existence of radical-radical π -bonding with the presence of two orthogonal orbitals in the complex (Figure S3).

Temperature-dependent direct-current (dc) susceptibility data collected under 5 kOe applied field suggest compound **1** is diamagnetic over the temperature range 300–2 K (Figure S4 and S5). Similar diamagnetic behavior is also found in some pure radical systems at low temperature due to strong π -dimerization, the same effect in **1**. In comparison with the dimeric phase, essentially diamagnetic phase in the organic radical crystals, along with using the Bleaney-Bowers equation for an exchange-coupled dimer of $S = \frac{1}{2}$ ions, a very large singlet-triplet energy gap is estimated to be larger than 1300 K, in consistent with the DFT calculation (Table S3).¹⁶ For **2**, temperature-dependent dc susceptibility data were collected under 1 kOe applied field. The χT value at 300 K is $15.13 \text{ cm}^3 \text{ mol}^{-1} \text{ K}$, slightly lower the expected value of $15.76 \text{ cm}^3 \text{ mol}^{-1} \text{ K}$ for two uncoupled Gd(III) ions.¹⁷ Upon cooling the χT values remain almost unchanged, and then a slight decrease to $14.06 \text{ cm}^3 \text{ mol}^{-1} \text{ K}$ (at 2 K) below 16 K occurs (Figure S6). The saturation magnetization value is $13.24 \text{ N}\beta$ at 50 kOe and 2 K (Figure S7). χT vs. T and M vs. H plots are then fitted simultaneously via the PHI program¹⁸ based on the following spin Hamiltonian (1):

$$\hat{H} = -2J_{\text{Gd-Gd}}\hat{S}_{\text{Gd}} \cdot \hat{S}_{\text{Gd}} + 2\mu_{\text{B}}g_{\text{iso}}\hat{S}_{\text{Gd}} \cdot B \quad (1)$$

where μ_{B} is the Bohr magneton, g_{iso} is the Landé factor and B is the magnetic induction. With the introduction of 4 % noncoupled Gd species, the best fitting gives $g_{\text{iso}} = 1.98$ and $J_{\text{Gd-Gd}} = -0.012 \text{ cm}^{-1}$. The dc susceptibility data for diluted sample **3** were also performed, which are identical to those for **2** (Figure S8 and S9).

To identify the electronic properties, electron paramagnetic resonance (EPR) spectra of these compounds were measured. Both powder and solution EPR spectra of **1** show a single resonance with $g \approx 2$, the intensity of which grows larger at lower temperature (Figure S10). This indicates that the signal originates from an impurity of one uncoupled radical, which was confirmed by simulating the hyperfine coupling in the solution spectrum (Figure S11), with $g = 2.003$ and $A_{\text{H}} = 5.46 \text{ MHz}$. No signal from an $S = 1$ state was observed even at room temperature (Figure S12), suggesting a strong antiferromagnetic interaction between the two radicals. This is consistent with the diamagnetic behaviour of **1** in the SQUID measurements and DFT calculations.

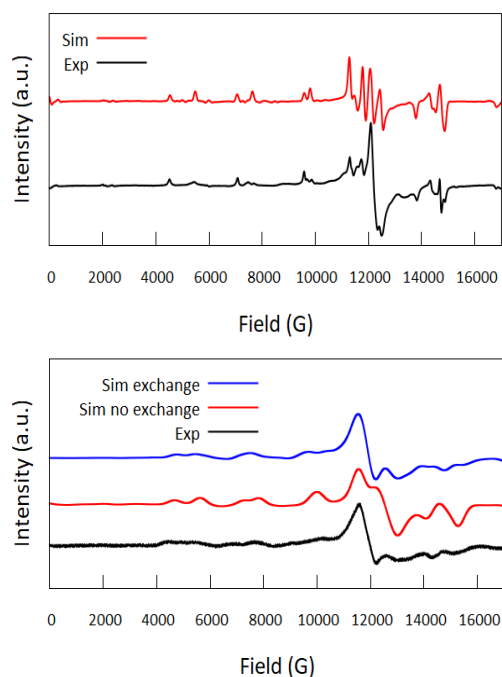


Figure 4. (top) Q-band EPR spectrum of **3** measured at 10 K (black) and simulation (red). (down) Q-band EPR spectrum of **2** measured at 10 K (black) and simulations using only one Gd (red) or using two Gd and $J_{\text{Gd-Gd}} = -0.004 \text{ cm}^{-1}$ (blue).

The EPR spectra of **3** (Figure 4 top, S13 and S14) show for an uncoupled gadolinium ion. They can be modelled employing the Hamiltonian (2):

$$\hat{H} = \mu_B g_{\text{iso}} B \hat{S}_z + D \left(\hat{S}_z - \frac{1}{3} S(S+1) \right) + E (\hat{S}_x^2 - \hat{S}_y^2) \quad (2)$$

where the Zeeman Effect was modelled with an isotropic g -value, the parameters D and E ($3B_2^0$ and B_2^2) were used to describe the zero-field splitting. Higher order terms were not included to avoid over-parameterization. The optimized simulation parameters across X, K and Q-band were $g = 1.99$, $D = 1.22 \times 10^{-1} \text{ cm}^{-1}$ and $E = 3.27 \times 10^{-2} \text{ cm}^{-1}$. At all three frequencies the central transitions (about $g = 2.05$) are broadened compared to the simulation. This may be due to the presence of a small amount of the Gd-Gd dimer (**2**) and or possibly due to a weak interaction with the radicals. It might also be due to additional crystal field terms that we have not included.

The spectra of **2** (Figure 4 bottom, S15 and S16) can with some degrees of success be modelled with the same parameters for each gadolinium ion, as they are related by symmetry. Simulations of **2** are improved by the addition of an isotropic exchange interaction between the two Gadolinium ions, using the formalism of the first term in

Hamiltonian (1). An accurate value of $J_{\text{Gd-Gd}}$ was not determined, but the best fit was obtained with a $J_{\text{Gd-Gd}}$ in the range of -0.003 to -0.004 cm^{-1} which is also antiferromagnetic, though 3–4 times smaller than the static magnetic fitting value.

In conclusion, we reported the first structurally characterized *p*-semiquinone-bridged rare-earth complexes. The synthesis by oxidation of QMe_4^{2-} by FeCl_3 is an unusual route to such radicals; previous work tends to involve reduction. A strong antiferromagnetic coupling between radicals is revealed by DFT calculation, SQUID and EPR studies due to the formation of the face-to-face stacking π -dimer radical anion in this dimer complex.

ASSOCIATED CONTENT

Supporting Information

Full experimental details, crystallographic and additional magnetic data. This material is available free of charge via the Internet at <http://pubs.acs.org>.

AUTHOR INFORMATION

Corresponding Author

zheng.yanzhen@xjtu.edu.cn;
richard.winpenny@manchester.ac.uk

Notes

The authors declare no competing financial interests.

ACKNOWLEDGMENT

This work was supported by NSFC (21871219 and 21773130), Joint Fund of the Natural Science Foundation of Zhejiang Province and Qingshan Lake (LQY18B010001), Key Laboratory Construction Program of Xi'an Municipal Bureau of Science and Technology (201805056ZD7CG40), the China Postdoctoral Science Foundation (2017M623150), the Shaanxi Postdoctoral Science Foundation (2017BSHTDZZ08), China Scholarship Council.

REFERENCES

- (a) Allen, J. F.; Martin, W. Out of Thin Air. *Nature* **2007**, 445, 610–612. (b) Osyczka, A.; Moser, C. C.; Daldal, F.; Dutton, P. L. Reversible Redox Energy Coupling in Electron Transfer Chains. *Nature* **2004**, 427, 607–612.
- D. Astruc, *Electron Transfer and Radical Processes in Transition-Metal Chemistry*, Wiley VCH, **1995**.

- (a) Kitagawa, S.; Kawata, S. Coordination Compounds of 1,4-Dihydroxybenzoquinone and its Homologues. Structures and Properties. *Coord. Chem. Soc.* **2002**, *224* (1–2), 11–34. (b) Son, E. J.; Kim, J. H.; Kim, K. Park, C. B. Quinone and its Derivatives for Energy Harvesting and Storage Materials. *J. Mater. Chem. A* **2016**, *4*, 11179–11202. (c) Jeon, I.-R.; Negru, B.; Duyne, R. P. Van; Harris, T. D. A 2D Semiquinone Radical-Containing Microporous Magnet with Solvent-Induced Switching from $T_c = 26$ to 80 K. *J. Am. Chem. Soc.* **2015**, *137* (50), 15699–15702.
- (a) Zhang, P.; Perfetti, M.; Kern, M.; Hallmen, P. P.; Ungur, L.; Lenz, S.; Ringenberg, M. R.; Frey, W.; Stoll, H.; Rahn, G.; Slagere, J. V. Exchange Coupling and Single Molecule Magnetism in Redox-Active Tetraoxolene-Bridged Dilanthanide Complexes. *Chem. Sci.* **2018**, *9*, 1221–1230. (b) Min, K. S.; DiPasquale, A. G.; Golen, J. A.; Rheingold, A. L.; Miller, J. S. Synthesis, Structure, and Magnetic Properties of Valence Ambiguous Dinuclear Antiferromagnetically Coupled Cobalt and Ferromagnetically Coupled Iron Complexes Containing the Chloranilate(2–) and the Significantly Stronger Coupling Chloranilate(•3–) Radical Trianion. *J. Am. Chem. Soc.* **2007**, *129* (8), 2360–2368. (c) Demir, S.; Jeon, I.-R.; Long, J. R.; Harris, T. D. Radical Ligand-Containing Single-Molecule Magnets. *Coord. Chem. Rev.* **2015**, *289–290*, 149–176. (d) Pierpont, C. G.; Buchanan, R. M. Transition Metal Complexes of o-Benzoquinone, o-Semiquinone, and Catecholate Ligands. *Coord. Chem. Rev.* **1981**, *38* (1), 45–87.
- (a) Domingos, Â.; Lopes, I.; Waerenborgh, J. C.; Marques, N.; Lin, G. Y.; Zhang, X. W.; Takats, J.; McDonald, R.; Hillier, A. C.; Sella, A.; Elsegood, M. R. J.; Day, V. W. Trapping of Anionic Organic Radicals by $(\text{Tp}^{\text{Me}_2})_2\text{Ln}$ (Ln = Sm, Eu). *Inorg. Chem.* **2007**, *46* (22), 9415–9424. (b) Takats, J. Hydrotris(pyrazolyl)borates. Versatile Ligands for f-Element Complexation. *J. Alloy Compd.* **1997**, *249* (1–2), 52–55.
- (a) Nakumori, H.; Matsumoto, T.; Yatabe, T.; Yoon, K.-S.; Nakai, H.; Ogo, S. Synthesis and crystal structure of a dinuclear, monomeric Mn^{II} p-semiquinonato complex. *Chem. Commun.* **2014**, *50*, 13059–13061. (b) Lü, J.-M.; Rosokha, S. V.; Neretin, I. S.; Kochi, J. K. Quinones as Electron Acceptors. X-Ray Structures, Spectral (EPR, UV–vis) Characteristics and Electron-Transfer Reactivities of Their Reduced Anion Radicals as Separated vs Contact Ion Pairs. *J. Am. Chem. Soc.* **2006**, *128* (51), 16708–16719. (c) Brandon, E. J.; Rogers, R. D.; Burkhart, B. M.; Miller, J. S. The Structure and Ferrimagnetic Behavior of meso-Tetraphenylporphyrinatomanganese(III) Tetrachloro-1,4-Benzoquinonide, $[\text{Mn}^{\text{III}}\text{TPP}]^+[\text{QCl}_4]^- \cdot \text{PhMe}$: Evidence of a Quinoidal Structure for $[\text{QCl}_4]^-$. *Chem. Eur. J.* **1998**, *4* (10), 1938–1943.
- (a) Yuasa, J.; Suenobu, T.; Fukuzumi, S. Highly Self-Organized Electron Transfer from an Iridium Complex to p-Benzoquinone Due to Formation of a π -Dimer Radical Anion Complex Triply Bridged by Scandium Ions. *J. Am. Chem. Soc.* **2003**, *125* (40), 12090–12091. (b) Yuasa, J.; Fukuzumi, S. Reversible Formation and Dispersion of Chiral Assemblies Responding to Electron Transfer. *J. Am. Chem. Soc.* **2007**, *129* (43), 12912–12913.
- Demir, S.; Jeon, I.-R.; Long, J. R.; Harris, T. D. Radical Ligand-Containing Single-Molecule Magnets. *Coord. Chem. Rev.* **2015**, *289–290*, 149–176.
- (a) Rinehart, J. D.; Fang, M.; Evans, W. J.; Long, J. R. Strong Exchange and Magnetic Blocking in N_2^{3-} -Radical-Bridged Lanthanide Complexes. *Nature Chem.* **2011**, *3*, 538–542. (b) Rinehart, J. D.; Fang, M.; Evans, W. J.; Long, J. R. A N_2^{3-} Radical-Bridged Terbium Complex Exhibiting Magnetic Hysteresis at 14 K. *J. Am. Chem. Soc.* **2011**, *133* (36), 14236–14239. (c) Demir, S.; Gonzalez, M. I.; Darago, L. E.; Evans, W. J.; Long, J. R. Giant Coercivity and High Magnetic Blocking Temperatures for N_2^{3-} Radical-Bridged Dilanthanide Complexes Upon Ligand Dissociation. *Nature Commun.* **2017**, *8*, 2144.
- (a) Fatila, E. M.; Rouzières, M.; Jennings, M. C.; Lough, A. J.; Clérac, R.; Preuss, K. E. Fine-Tuning the Single-Molecule Magnet Properties of a $[\text{Dy}(\text{III})\text{-Radical}]_2$ Pair. *J. Am. Chem. Soc.* **2013**, *135* (26), 9596–9599. (b) Dolinar, B. S.; Gómez-Coca, S.; Alexandropoulos, D. I.; Dunbar, K. R. An Air Stable Radical-Bridged Dysprosium Single Molecule Magnet and its Neutral Counterpart: Redox Switching of Magnetic Relaxation Dynamics. *Chem. Commun.* **2017**, *53*, 2283–2286. (c) Dolinar, B. S.; Alexandropoulos, D. I.; Vignesh, K. R.; James, T.; Dunbar, K. R. Lanthanide Triangles Supported by Radical Bridging Ligands. *J. Am. Chem. Soc.* **2018**, *140* (3), 908–911.
- Llunell, P.; Casanova, M.; Cirera, D.; Bofill, J.; Alemany, J. M.; Alvarez, D.; Pinsky, S.; Avnir, M. *SHAPE 2.1*, Universitat de Barcelona and The Hebrew University of Jerusalem, Barcelona and Jerusalem, **2003**.
- (a) Hou, Z.; Fujita, A.; Zhang, Y.; Miyano, T.; Yamazaki, H.; Wakatsuki, Y. One-Electron Reduction of Aromatic Ketones by Low-Valent Lanthanides. Isolation, Structural Characterization, and Reactivity of Lanthanide Ketyl Complexes. *J. Am. Chem. Soc.* **1998**, *120* (4), 754–766. (b) Werner, D.; Zhao, X.; Best, S. P.; Maron, L.; Junk, P. C.; Beacon, G. B. Bulky Ytterbium Formamidinates Stabilise Complexes with Radical Ligands, and Related Samarium

“Tetracyclone” Chemistry. *Chem. Eur. J.* **2017**, *23* (9), 2084–2102.

(a) Werner, D.; Deacon, G. B.; Junk, P. C.; Anwander, R. Cerium(III/IV) Formamidinate Chemistry, and a Stable Cerium(IV) Diolate. *Chem. Eur. J.* **2014**, *20* (15), 4426–4438. (b) Robinson, J. R.; Booth, C. H.; Carroll, P. J.; Walsh, P. J. Schelter, E. J. Dimeric Rare-Earth BINOLate Complexes: Activation of 1,4-Benzoquinone through Lewis Acid Promoted Potential Shifts. *Chem. Eur. J.* **2013**, *19* (19), 5996–6004. (c) Lopes, I.; Dias, R.; Domingos, Â.; Marques, N. Organo-f-Element Chemistry with Multidentate Nitrogen Ligands. *J. Alloy Compd.* **2002**, *344* (1–2), 60–64. (d) Nie, K.; Feng, T.; Song, F.-K.; Zhang, Y.; Sun, H.-M.; Yuan, D.; Yao, Y.-M.; Shen, Q. Bimetallic Amine-Bridged Bis(Phenolate) Lanthanide Aryloxides and Alkoxides: Synthesis, Characterization, and Application in the Ring-Opening Polymerization of *rac*-Lactide and *rac*- β -Butyrolactone. *Sci. China Chem.* **2014**, *57*, 1106–1116.

Itoh, M.; Asai, Y.; Kamo, H.; Miura, A.; Miyasaka, H. A Dimer-of-dimers Composed of Paddlewheel Diruthenium(II, III) Complexes and a Bridge of Tetrachlorohydroquinonate(2-) Derived by Intramolecular Charge Transfers. *Chem. Lett.* **2012**, *41* (1), 26–28.

(a) Preuss, K. E. Pancake Bonds: π -Stacked Dimers of Organic and Light-Atom Radicals. *Polyhedron* **2014**, *79* (5), 1–15. (b) Molčanov, K.; Stilinović, V.; Šantić, A.; Maltar-Strmečki, N.; Pajić, D.; Kojić-Prodić, B.

Fine Tuning of π -Stack Separation Distances of Semiquinone Radicals Affects Their Magnetic and Electric Properties. *Cryst. Growth Des.* **2016**, *16* (9), 4777–4782. (c) Molčanov, K.; Jelsch, C.; Landeros, B.; Hernández-Trujillo, J.; Wenger, E.; Stilinović, V.; Kojić-Prodić, B.; Escudero-Adán, E. C. Partially Covalent Two-Electron/Multicentric Bonding between Semiquinone Radicals. *Cryst. Growth Des.* **2019**, *19* (1), 391–402.

(a) Fujita, W.; Awaga, K. Room-Temperature Magnetic Bistability in Organic Radical Crystals. *Science* **1999**, *286* (5438), 261–262. (b) Fujita, W.; Awaga, K.; Matsuzaki, H.; Okamoto, H. Room-temperature magnetic bistability in organic radical crystals: Paramagnetic-diamagnetic phase transition in 1,3,5-trithia-2,4,6-triazapentalenyl. *Phys. Rev. B* **2002**, *65* (6), 064434. (c) McManus, G. D.; Rawson, J. M.; Feeder, N.; Duijn, J. van; McInnes, E. J. L.; Novoa, J. J.; Burriel, R.; Palacio, F.; Olliete, P. Synthesis, crystal structures, electronic structure and magnetic behaviour of the trithiatriazapentalenyl radical, C2S3N3. *J. Mater. Chem.* **2001**, *11*, 1992–2003.

Kahn, O. *Molecular Magnetism*, VCH Publishers, Cambridge, **1993**.

Chilton, N. F.; Anderson, R. P.; Turner, L. D.; Soncini, A.; Murray, K. S. PHI: A powerful new program for the analysis of anisotropic monomeric and exchange-coupled polynuclear d- and f-block complexes. *J. Comput. Chem.* **2013**, *34* (13), 1164–1175.

Dimerized *p*-Semiquinone Radical Anions Stabilized by a Pair of Rare-Earth Metal Ions

Tian Han,¹ Jonatan B. Petersen,² Zi-Han Li,¹ Andreas kostopoulos,² Fabrizio Ortu,² Eric J. L. McInnes,² Nicholas F. Chilton,² Richard E. P. Winpenny^{2,*} and Yan-Zhen Zheng^{1,*}

¹ School of Science, Frontier Institute of Science and Technology (FIST), Research Institute of Xi'an Jiaotong University (Zhejiang), State Key Laboratory for Mechanical Behavior of Materials, MOE Key Laboratory for Nonequilibrium Synthesis and Modulation of Condensed Matter, Xi'an Key Laboratory of Sustainable Energy and Materials Chemistry, Xi'an Jiaotong University, Xi'an 710049, China

² School of Chemistry, The University of Manchester, Oxford Road, Manchester M13 9PL, United Kingdom

Experimental Section

1.1 Materials and method

All reactions were carried out under a dry and oxygen-free argon atmosphere by using Schlenk techniques or in a glovebox. All solvents were dried and degassed by standard techniques. Anhydrous YCl_3 and GdCl_3 salts were prepared according to the literature procedure. The ligand H_2QMe_4 (2,3,5,6-tetramethylhydroquinone) was used as received without further purification. Elemental analyses were performed on a Flash 2000 elemental analyzer.

1.2 Syntheses of complexes 1–3

Complex $\{\text{Y}[\text{QMe}_4^-\text{Cl}_2(\text{THF})_3]\}_2 \cdot 2\text{CH}_2\text{Cl}_2$ (**1**·2 CH_2Cl_2):

To a THF solution of H_2QMe_4 (1 mmol), NaH (2.0 mmol) was added. The reaction mixture was stirred overnight at ambient temperature, after which YCl_3 (1 mmol) was added. The resulting mixture was stirred for 20 h at room temperature, and then a THF solution of FeCl_3 (1 mmol) was added. The reaction mixture became blue immediately. After stirring for 4 h at ambient temperature, the reaction was halted and then filtered. The obtained blue-black powder was washed with THF more than 4 times. The powder was then dissolved in a mixture of CH_2Cl_2 and THF to give a dark blue solution. After filtration, slow diffusion of THF to the filtrate at -35°C gave dark blue, air-sensitive crystals of **1**. The crystals were then collected and washed with THF for 4 times (ca. 22 % yield). Elemental analysis calcd (%) for **1** ($\text{C}_{44}\text{H}_{72}\text{Cl}_4\text{O}_{10}\text{Y}_2$): C 48.90, H 6.72; found: C 48.52, H 6.78.

Complex $\{\text{Gd}[(\text{QMe}_4)^-\text{Cl}_2(\text{THF})_3]\}_2 \cdot 2\text{CH}_2\text{Cl}_2$ (**2**·2 CH_2Cl_2):

The synthesis is the same as **1**·2 CH_2Cl_2 with anhydrous YCl_3 replaced by 1 mmol of anhydrous GdCl_3 . Yield 33 %. Elemental analysis calcd (%) for **2** ($\text{C}_{44}\text{H}_{72}\text{Cl}_4\text{O}_{10}\text{Gd}_2$): C 43.41, H 5.96; found: C 43.26, H 6.04.

Complex 10 % Gd @ **1** (**3**·2 CH_2Cl_2):

The synthesis is the same as **1**·2 CH_2Cl_2 with anhydrous YCl_3 replaced by 0.1 mmol of anhydrous GdCl_3 and 0.9 mmol of anhydrous YCl_3 . Yield 28 %. Elemental analysis calcd (%) for **3** ($\text{C}_{44}\text{H}_{72}\text{Cl}_4\text{O}_{10}\text{Gd}_{0.2}\text{Y}_{1.8}$): C 48.29, H 6.63; found: C 47.84, H 6.62.

X-ray Crystallography Data

Single-crystal X-ray diffraction data were recorded on a Bruker Apex CCD II area-detector diffractometer with MoK α radiation. Diffraction data for fresh crystal of **1**·2CH₂Cl₂ and **2**·2CH₂Cl₂ were collected at 150 K, after which the same crystal of **1**·2CH₂Cl₂ was warmed up to 300 K for 30 minutes under N₂ and the diffraction data of **1** were then collected at 300 K. The structure was solved by direct method and refined by full-matrix least-squares method on F^2 with anisotropic thermal parameters for all non-hydrogen atom. Hydrogen atoms were located geometrically and refined isotropically. CCDC 1981913 (**1**·CH₂Cl₂), 1981914 (**1**) and 1981915 (**2**·CH₂Cl₂) contain the supplementary crystallographic data, which can be obtained free of charge via www.ccdc.cam.ac.uk/conts/retrieving.html (or from the Cambridge Crystallographic Data Centre, 12 Union Road, Cambridge CB21EZ, UK; fax: (+44)1223-336-033; or deposit@ccdc.cam.ac.uk).

Magnetic measurements

Direct-current (dc) magnetic susceptibilities were measured on a Quantum Design MPMS XL-7 SQUID magnetometer. Diamagnetic corrections were made with Pascal's constants for all the constituent atoms and sample holder.

Electron paramagnetic resonance measurements

EPR was measured on microcrystalline powder samples of **1**, **2** and **3** and a sample of **1** dissolved in a mixture of CH₂Cl₂ and THF, all in sealed quartz tubes. The X- and Q-band spectra were recorded using a Bruker EMXplus spectrometer equipped with an ER 4122 SHQ and an ER 5106 QT respectively, cooled by liquid helium with an Oxford Instruments ESR-900 or CF-935 cryostat respectively. The K-band spectra were recorded on an Elecsys 580 equipped with an ER 6706 KT resonator and cooled with a CRYOGENIC CFVTC for EPR.

For the measurements at K-band saturation effects were observed at 10 K and K-band spectra were therefore measured at higher temperature.

The solution of **1** in CH₂Cl₂/THF had a small amount of precipitation, and was therefore heated to 50°C on a water bath and sonicated until everything was dissolved before being flash-frozen with liquid nitrogen and placed in the resonator at 50 K. The CH₂Cl₂/THF mixture has a melting point between 150K and 200K and measurements the sample at 200 K and beyond are expected to be of a liquid solution.

Simulations were done using the pepper and garlic functions and fits were done with the esfit

function in the Easyspin software package for MATLAB.

The reported g -values were corrected by use of a Bruker strong pitch standard, measured after each measurement

Table S1. Crystallographic data and structure refinement for **1**·2CH₂Cl₂, **1** and **2**·2CH₂Cl₂.

Compound	1 ·2CH ₂ Cl ₂	1	2 ·2CH ₂ Cl ₂
Formula	C ₄₆ H ₇₆ Cl ₈ O ₁₀ Y ₂	C ₄₄ H ₇₂ Cl ₄ O ₁₀ Y ₂	C ₄₆ H ₇₆ Cl ₈ O ₁₀ Gd ₂
<i>M</i> , g mol ⁻¹	1250.48	1080.63	1387.16
Temperature, K	150	300	150
Space group	<i>P</i> 2 ₁ / <i>c</i>	<i>P</i> 2 ₁ / <i>n</i>	<i>P</i> 2 ₁ / <i>c</i>
<i>a</i> , Å	9.146(4)	9.119(3)	9.151(4)
<i>b</i> , Å	14.821(7)	15.201(5)	14.841(6)
<i>c</i> , Å	20.895(10)	19.716(6)	20.936(9)
<i>α</i> , deg	90	90	90
<i>β</i> , deg	99.390(6)	102.967(5)	99.172(6)
<i>γ</i> , deg	90	90	90
<i>V</i> , Å ³	2794(2)	2663.3(15)	2807(2)
<i>Z</i>	2	2	2
<i>d</i> _{cal} , g cm ⁻³	1.486	1.348	1.641
2 θ range, deg	3.384 to 50.016	3.416 to 49.692	4.508 to 50.014
Completeness	0.999	0.979	0.993
Final indices [<i>I</i> > 2 σ (<i>I</i>)]	<i>R</i> ₁ = 0.0404, <i>wR</i> ₂ = 0.1041	<i>R</i> ₁ = 0.0607, <i>wR</i> ₂ = 0.1310	<i>R</i> ₁ = 0.0477, <i>wR</i> ₂ = 0.1058
<i>R</i> indices (all data)	<i>R</i> ₁ = 0.0549, <i>wR</i> ₂ = 0.1137	<i>R</i> ₁ = 0.1515, <i>wR</i> ₂ = 0.1641	<i>R</i> ₁ = 0.0638, <i>wR</i> ₂ = 0.1132
Goodness-of-fit on <i>F</i> ²	1.068	1.048	1.071
Residual map, e Å ⁻³	1.11/-0.79	0.62/-0.28	1.97/-1.17

Table S2. Selected bond lengths (Å) and angles (deg) for compound **1**.

Y1-Cl1	2.6066(12)	Cl1-Y1-Cl2	162.60(3)
Y1-Cl2	2.6302(13)	O1-Y1-Cl1	94.32(8)
Y1-O1	2.239(2)	O1-Y1-Cl2	100.19(7)
Y1-O2#1	2.239(3)	O1-Y1-O2#1	72.89(8)
Y1-O3	2.405(3)	O2#1-Y1-O3	73.41(8)
Y1-O4	2.502(2)	O3-Y1-O4	70.39(8)
Y1-O5	2.466(3)	O4-Y1-O5	71.85(8)
O1-C1	1.290(4)	O5-Y1-O1	72.03(8)
O2-C4	1.288(4)	O1-C1-C2	119.8(3)
C1-C2	1.448(5)	O1-C1-C6	120.5(3)
C2-C3	1.374(5)	C6-C1-C2	119.5(3)
C3-C4	1.449(5)		
C4-C5	1.456(5)		
C5-C6	1.367(5)		
C6-C1	1.446(5)		

^aSymmetry code: #1 1-x,1-y,1-z

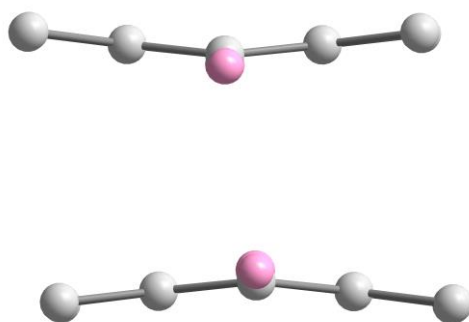


Figure S1 Rotating the dimer along the centroid–centroid direction by 90°.

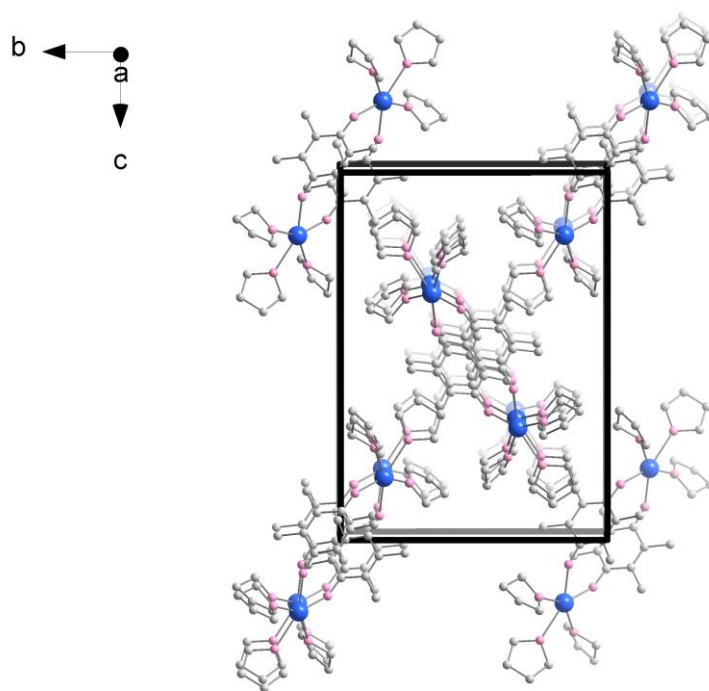


Figure S2 3D packing diagram for **1**. All the hydrogen atoms and lattice solvents are omitted.

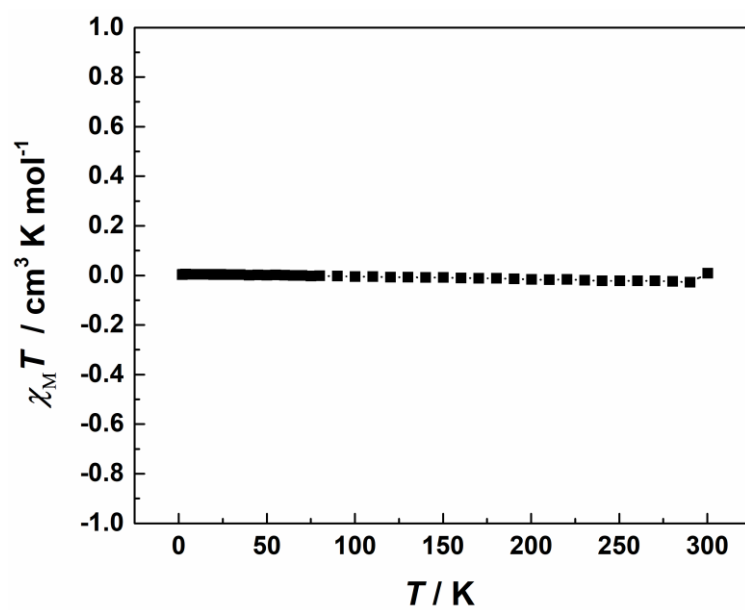


Figure S3 $\chi_M T$ as a function of temperature in an applied field of 5 kOe for **1**.

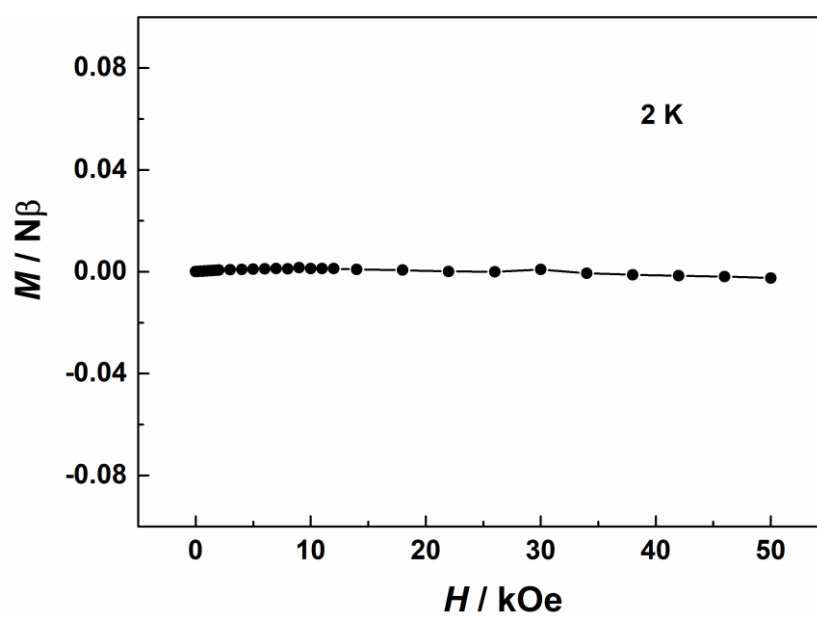


Figure S4 The plot of M vs. H at 2 K for **1**.

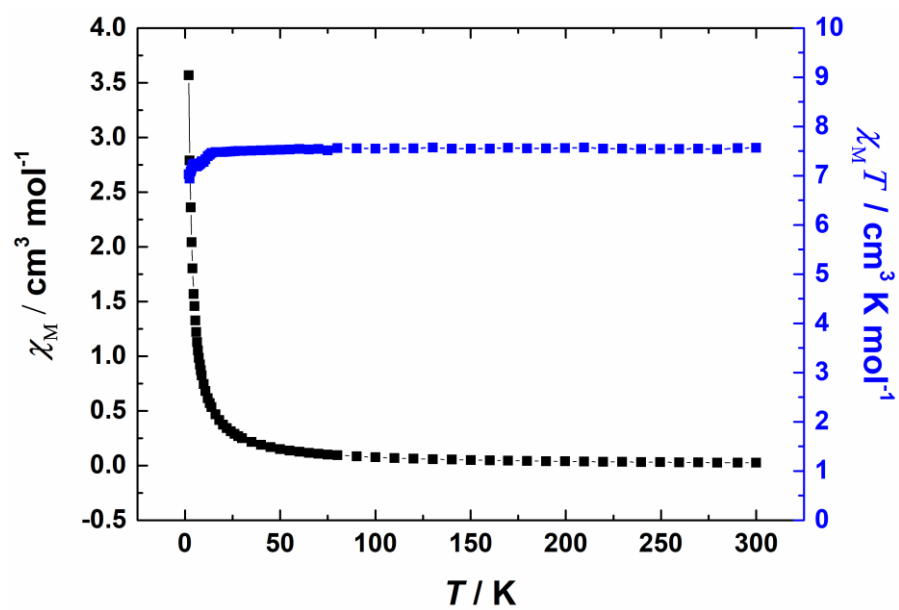


Figure S5 χ_M and $\chi_M T$ as a function of temperature in an applied field of 1 kOe for **2**.

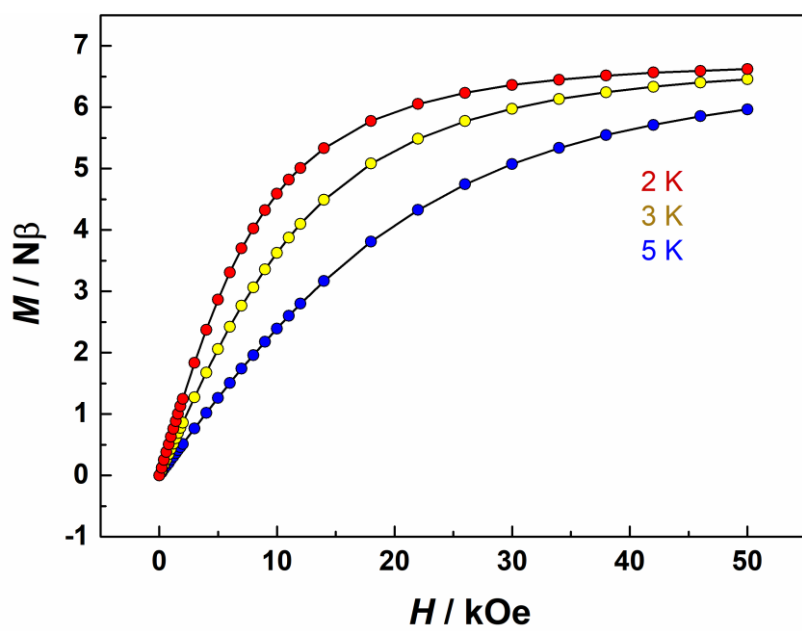


Figure S6 The plots of M vs. H at various temperatures for **2**.

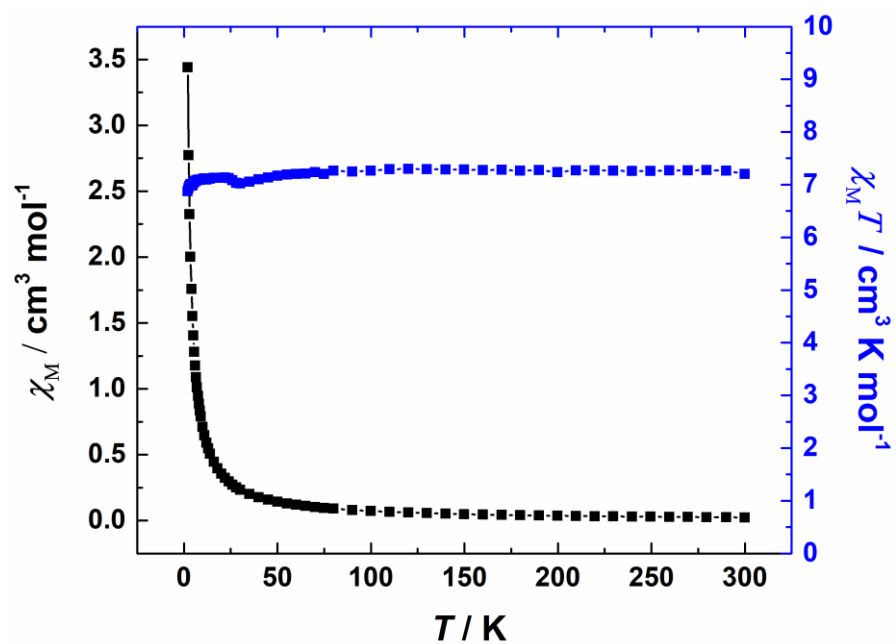


Figure S7 χ_M and $\chi_M T$ as a function of temperature in an applied field of 1 kOe for **3**

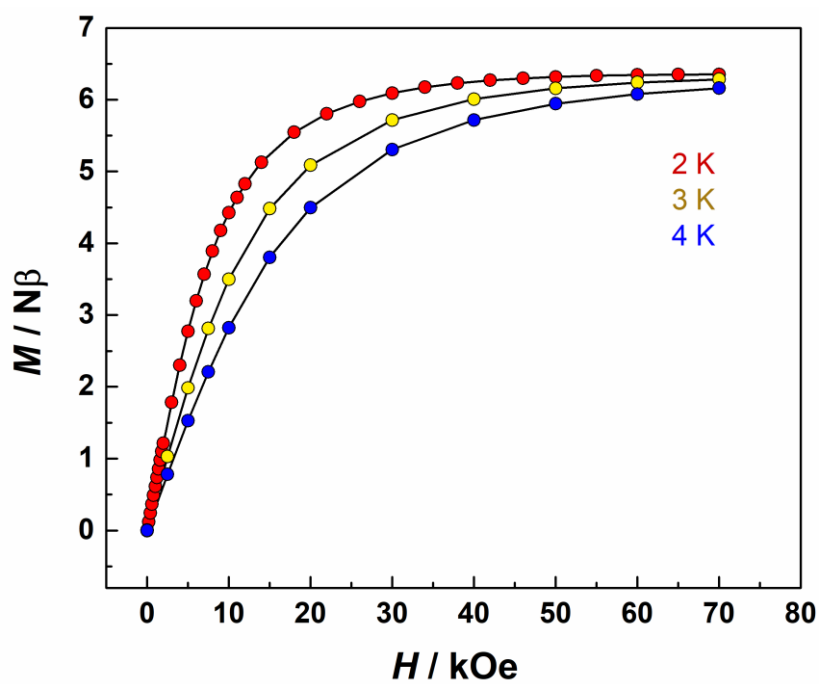


Figure S8 The plots of M vs. H at various temperatures for **3**.

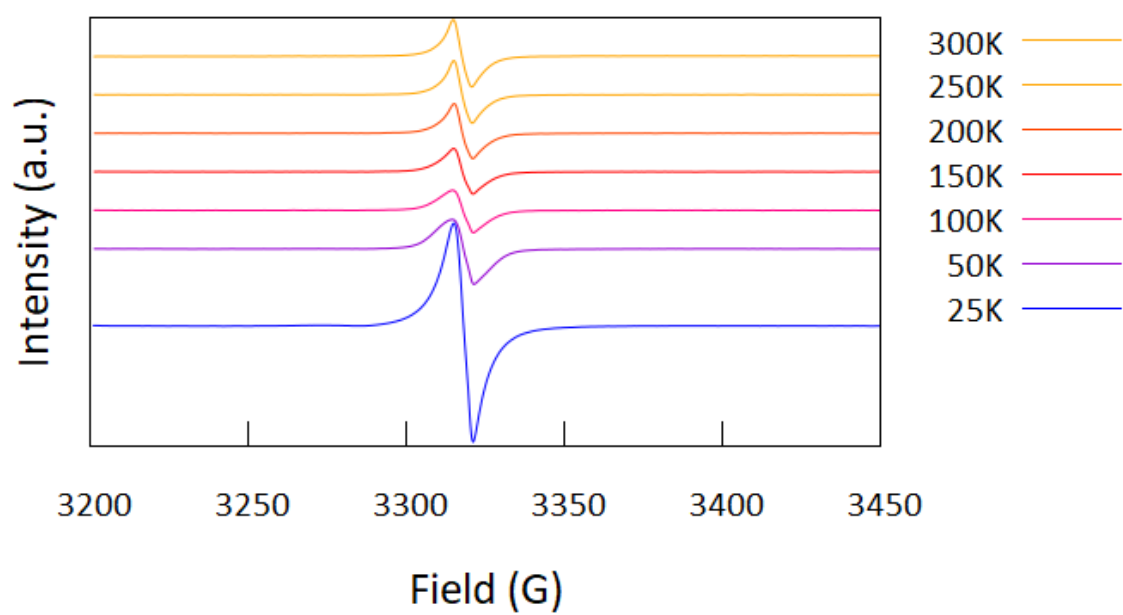


Figure S9 X-band EPR spectrum of **1** at varying temperatures.

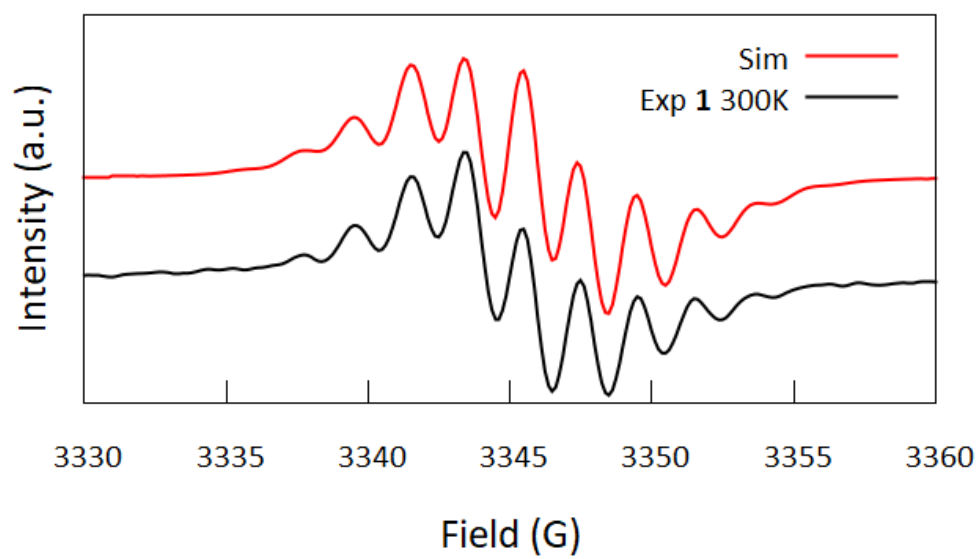


Figure S10 X-band EPR spectrum of **1** dissolved in DCM/THF 300k (black) and simulation (red).

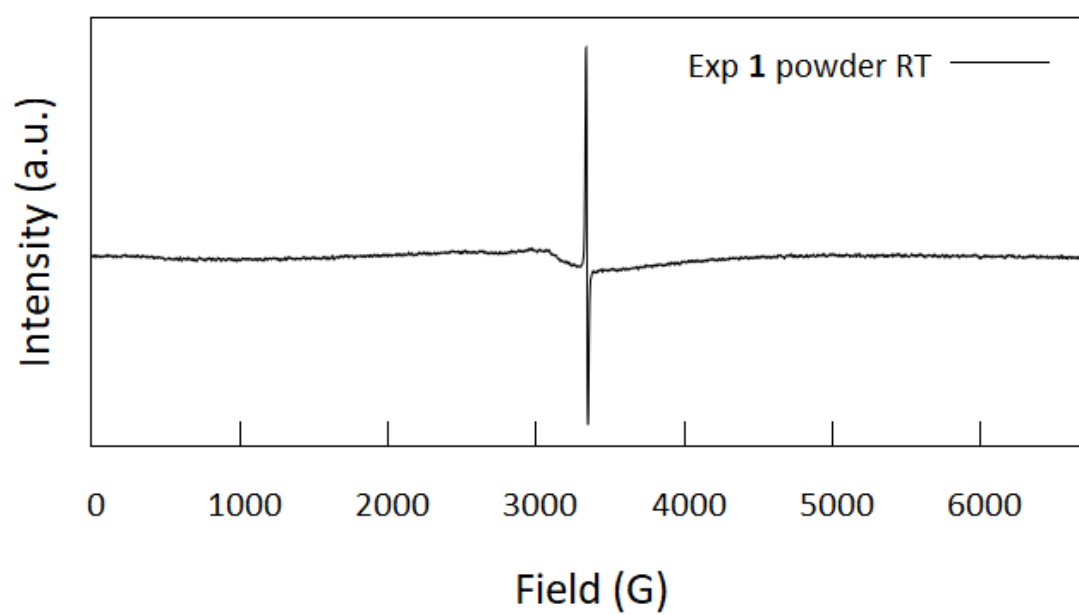


Figure S11 X-band EPR spectrum of **1** at room temperature, full field range.

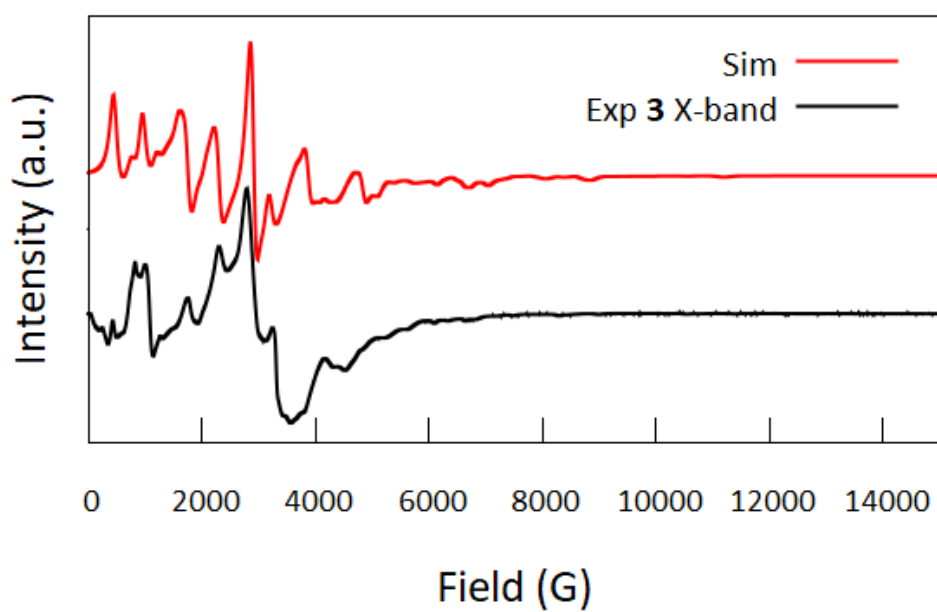


Figure S12 X-band EPR spectrum of **3** at 10 K (black) and simulation (red)

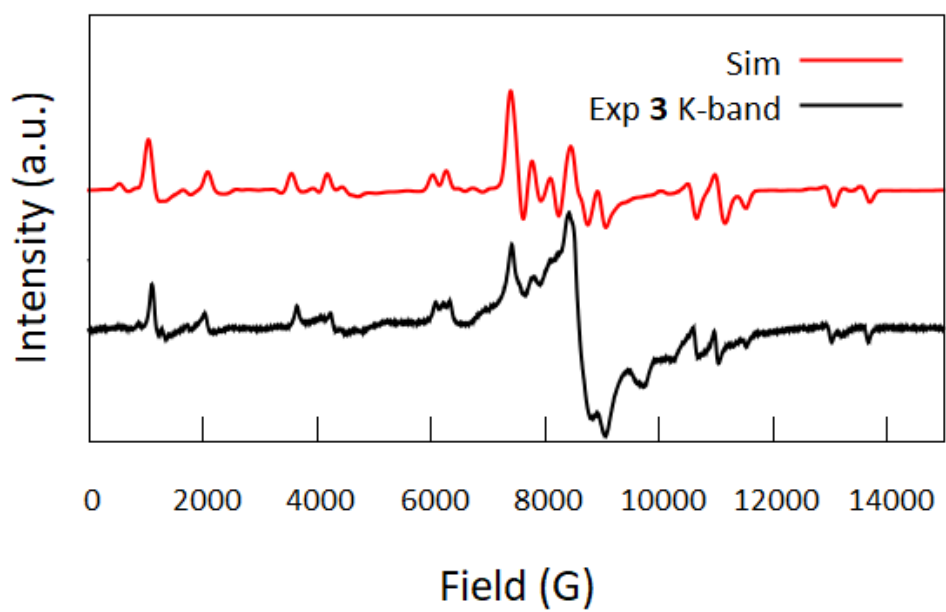


Figure S13 K-band EPR spectrum of **3** at 20K (black) and simulation (red)

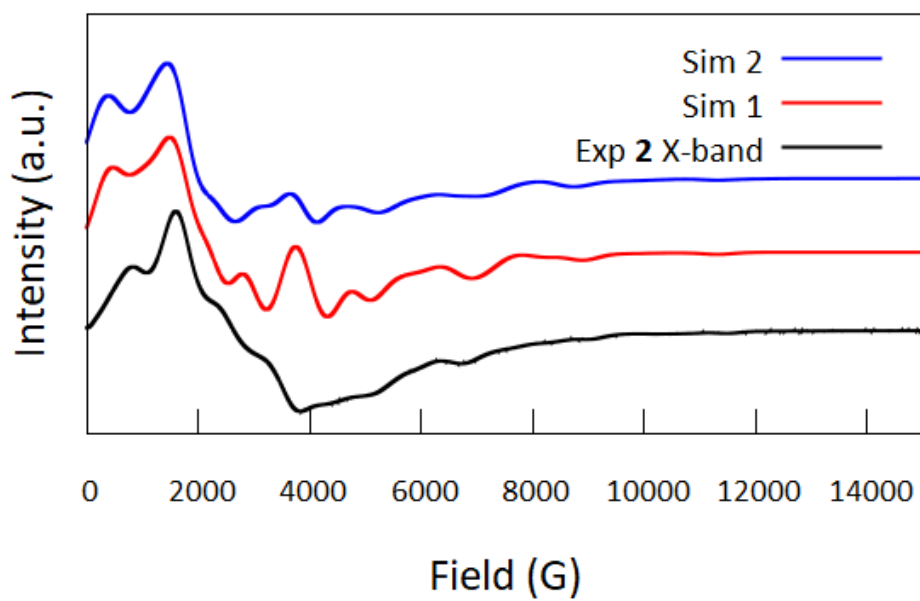


Figure S14 X-band EPR spectrum of **2** measured at 10 K (black) and simulations using only one Gd (red) or using two equivalent Gd and $j=7 \times 10^{-3} \text{ cm}^{-1}$ (blue)

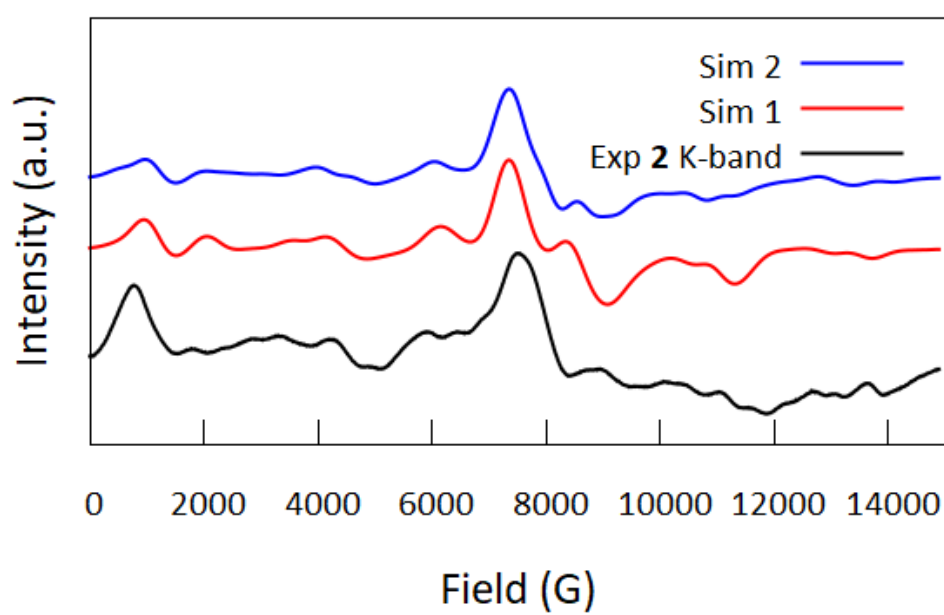


Figure S15 K-band EPR spectrum of **2** measured at 10 K (black) and simulations using only one Gd (red) or using two equivalent Gd and $j=6 \times 10^{-3} \text{ cm}^{-1}$ (blue)

B. Spin-Lattice Relaxation Decoherence Suppression in Vanishing Orbital Angular Momentum Qubits

Preface

This is the article to which chapter 3 is written to follow up on and it is therefore included. I have had no direct involvement in writing it. It is published as:

Buch, C. D., Kundu, K., Marbey, J. J., van Tol, J., Weihe, H., Hill, S., & Piligkos, S. (2022). Spin–Lattice Relaxation Decoherence Suppression in Vanishing Orbital Angular Momentum Qubits. *Journal of the American Chemical Society*. <https://doi.org/10.1021/jacs.2c07057>

This page is intentionally left blank

Spin-Lattice Relaxation Decoherence Suppression in Vanishing Orbital Angular Momentum Qubits

Christian D. Buch,¹ Krishnendu Kundu,² Jonathan J. Marbey,² Johan van Tol,² Høgni Weihe,¹ Stephen Hill,² and Stergios Piligkos*¹

¹ Department of Chemistry, University of Copenhagen, DK-2100 Copenhagen, Denmark

² National High Magnetic Field Laboratory, Tallahassee, Florida, 32310, United States of America

KEYWORDS *Quantum Technologies, molecular magnetic materials, molecular qubits, quantum gates.*

ABSTRACT: Multifrequency Electron Paramagnetic Resonance spectroscopy on oriented single crystals of magnetically dilute Gd(III) ions in Gd_{0.004}Y_{0.996}(trensol) is used to determine the Hamiltonian parameters of the ground $^8S_{7/2}$ term and its phase memory time, T_m , characterizing its coherent spin dynamics. The vanishing orbital angular momentum of the $^8S_{7/2}$ term makes it relatively insensitive to spin-lattice relaxation mediated by magnetoelastic coupling and leads to a T_m of 12 μ s at 3K which is not limited by spin-lattice relaxation.

INTRODUCTION

We are currently experiencing the advent of Quantum Technologies, as defined within the context of the “Second Quantum Revolution”.¹⁻³ These emerging technologies, amongst which Quantum Computing, Simulators, Communications, Sensing, Metrology, Cryptography and Imaging, are based on the exploitation of genuine quantum properties of matter, such as superposition and entanglement. In particular, the realization of a general purpose Quantum Computer⁴⁻⁸ (QC) is currently one of the most ambitious technological goals,⁹⁻¹⁰ since QCs will outperform classical computers (*Quantum Advantage*) for some specific types of computations, such as prime number factorization,¹¹ search of large databases,¹² and the accurate simulation of quantum many-body systems.¹³ Attaining *Quantum Advantage* will change the way in which we process, search and share information and will have a transformative impact on the development of novel materials and chemicals with applications in energy (magnets, batteries, superconductors), agriculture (efficient and sustainable fertilizers) and biomedicine and biotechnologies via the simulation of the conformational structures of proteins, leading to the discovery of new binding sites for custom designed drugs or vaccines.

Very recently, superconducting and photonic quantum processing units (QPUs) were announced to have attained *Quantum Advantage*.¹⁴⁻¹⁶ Although these are very impressive and encouraging achievements, the number of qubits included in these QPUs is still not

sufficient to address practical problems, to which purpose the estimated number of incorporated qubits amounts to several thousand or even millions, in order to be able to deal with quantum error correction.¹⁷ Thus, the realization of future general purpose QCs will not be solely based on superconducting or photonic qubits but will require additional, or entirely different, components offering more efficient ways to fight against quantum error.

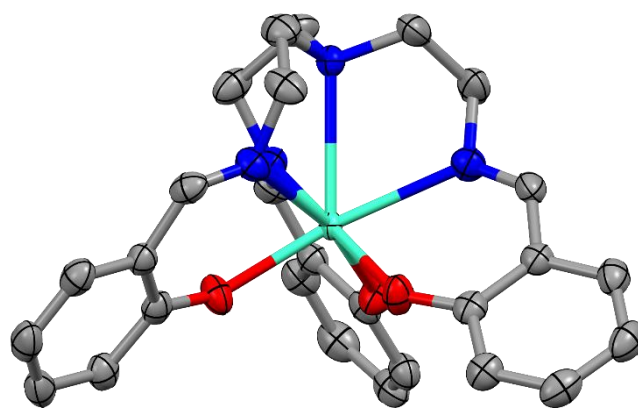


Figure 1. Molecular structure of Gd(trensol) determined by SCXRD. Hydrogens have been omitted for clarity. Color code: C, gray; N, blue; O, red; Gd, cyan. Thermal ellipsoids are set to 90 % probability.

Molecular magnetic materials offer possibilities to circumvent some of these limitations and therefore constitute a very promising avenue for the next generation *Quantum Information* technology devices.¹⁸⁻²³ Unlike many other candidates, molecular magnetic materials routinely display many low energy states

compatible with the encoding of qubits and even acting as integrated quantum processors, the additional levels providing the capability to expand the dimension of the computational space or to efficiently encode quantum error correction algorithms.²⁴⁻²⁹ The critical parameter for the suitability of such materials to be used in *Quantum Information* devices is the phase memory time, T_m , reflecting the time for which the information encoding state retains its phase coherence.³⁰ Decoherence,³¹ the interaction of the quantum system with its environment, results in loss of superposition and/or entanglement, collapsing the dynamic state of the system to its thermal equilibrium static eigenvectors. Strategies to reduce decoherence in molecular magnetic materials include magnetic dilution to reduce magnetic dipolar interactions, isotopic enrichment to modify the nuclear spin composition of the environment, and chemically engineered systems displaying magnetic clock transitions (CTs). In the case of CTs, the vanishing magnetic field derivative of the energy of the information encoding states leads to insensitivity of the resonance frequency with respect to fluctuations of the local magnetic field and thus, to an increased coherence of these states, reflected in their high T_m .³²⁻³³ Furthermore, previous studies showed that the extent to which a quantum state is isotropic, or of S-character, is a factor affecting its T_m . In this context divalent isotropic (or minimally anisotropic) d-shell ions were studied targeting an 2S ground term, resulting in T_m s of the order of microsecond.³⁴

RESULTS AND DISCUSSION

Lanthanide (Ln) complexes are a rather unexplored but very interesting class of molecular spin qubits.^{20,24,28-29,32,35-36} Some of us have recently demonstrated that the ground Kramers doublet of the $^2F_{7/2}$ ground term of the trigonally symmetric Yb(trensal)³⁷ is an excellent electronic qubit.²⁴ Yb(trensal) is also a prototypical coupled electronic-qubit–nuclear-qudit where efficient quantum error correction algorithms can intrinsically be implemented.²⁵ However, the orbital angular momentum ($L = 3$) of the $^2F_{7/2}$ term of Yb(III) limits its T_m via spin-lattice (SL) relaxation contributions to decoherence.^{24,37} This prompted us to study Gd(trensal), since the ground $^8S_{7/2}$ term of Gd(III) is devoid of first order orbital angular momentum with small high order contributions from excited states possessing orbital angular momentum.³⁸ The ground $^8S_{7/2}$ term of Gd(III) mixes via spin orbit coupling to primarily the $^6P_{7/2}$ and $^6D_{7/2}$ excited states, introducing at high order an orbital component to the ground $^8S_{7/2}$ term, reflected mainly in the splittings, and also g -factor, of c.w.-EPR spectra of Gd(III) ions.³⁸ However, as these excited states lie 33000 and 40000 cm^{-1} above the ground state, respectively, the amount of orbital momentum transmitted to the ground state is minimal, even for a relatively large spin-orbit coupling matrix element as in Gd(III).³⁸

The energy spectrum of the ground $^8S_{7/2}$ term of Gd(III), due to the electrostatic potential of the ligands (ligand field, LF) and the Zeeman (ZE) interaction with the

external magnetic field, \vec{B} , can phenomenologically be parametrised via the effective Hamiltonian:

$$\hat{H} = \hat{H}_{LF} + \hat{H}_{ZE} = \sum_{k, -k \leq q \leq k} B_q^k \hat{O}_q^k + \mu_B \vec{B} \tilde{g} \hat{S} \quad (1)$$

where B_q^k, \hat{O}_q^k are the Stevens parameters and operators, respectively, μ_B is the electron Bohr magneton, \tilde{g} is the g -tensor and \hat{S} the spin angular momentum operator of the ground term. The SL interaction is mediated by vibrations that modulate the LF via magnetoelastic coupling terms. These terms, when considering their effect on the electronic functions to first order in displacement, are of the form³⁹:

$$\hat{H}_{SL} \propto \sum_i \frac{\partial \hat{H}_{LF}}{\partial R_i} \quad (2)$$

with ∂R the displacement of the i^{th} neighboring atom participating in the relevant vibration. Since \hat{H}_{LF} expresses the electrostatic potential created by the ligands at the metal, it acts only on the orbital component of the eigenfunctions of the metal since this component expresses the charge distribution of the metal electrons. Thus, a vanishing orbital angular momentum component for the Ln functions leads to an insensitivity of the Ln centre to SL relaxation via equation (2). This effect can be viewed as equivalent to magnetic CTs³² where the resonance frequency is insensitive to local fluctuations of the magnetic field. Here, the resonance frequency is insensitive to local fluctuations of the LF. To assess the effect of the above on the coherent spin dynamics of the eigenstates of the $^8S_{7/2}$ term of Gd(III) in Gd(trensal), we first accurately determine the parameters entering (1) by multifrequency c.w.-EPR spectroscopy on single crystals and then probe the coherent spin dynamics of the ground $^8S_{7/2}$ term by pulse EPR spectroscopy.

As previously reported,⁴⁰⁻⁴² Gd(trensal), as other members of the Ln(trensal) family,^{37,40-47} crystallises in the $P\bar{3}c1$ space group as large pencil-shaped crystals in which the Gd(III) ion and the apical tertiary amine nitrogen atom (Figure 1) define the molecular C_3 axis and both lie on the crystallographic C_3 axis. Furthermore, two different molecular orientations are found along the trigonal crystallographic axis, corresponding to a relative rotation of two Gd(trensal) molecules by 48° around the C_3 axis (Figure S1). Gd(trensal) was magnetically diluted in its isostructural diamagnetic host, Y(trensal), at 0.4% level [$\text{Gd}_{0.004}\text{Y}_{0.996}(\text{trensal})$, **1**], as determined by ICP-MS (SI section), to minimize dipolar interactions between paramagnetic Gd(III) centres. The c.w. X-band EPR spectra of **1** at 15 K, with the magnetic field parallel or perpendicular to the C_3 axis, are shown in Figures 2a and 2b, respectively. A group of 7 intense allowed lines centered around “ $g = 2$ ” can be observed at both orientations. In addition, numerous lower intensity forbidden lines as well as “dimer” lines, originating from Gd(III) sites where the first neighbor is not a diamagnetic

Y(III) centre but rather a Gd(III), are observed. Similar “dimer” lines have been observed in both the c.w. and pulse EPR spectra of Yb(trensal).^{24,37} Upon rotation of the crystal about an axis perpendicular to the C_3 axis, a splitting of each of the allowed lines is observed for all orientations where the magnetic field is not along the C_3 axis orientation or perpendicular to it. This is due to the two different molecular orientations in the crystal

(Figure S1) being magnetically inequivalent at general orientations of the magnetic field. The angular dependence of the single crystal X-band c.w.-EPR spectra of **1** in a plane containing the C_3 axis is shown in Figure 3. The determination of the parameters entering Hamiltonian (1) was performed by numerical fitting of the observed resonance fields by use of the Simplex algorithm.⁴⁸

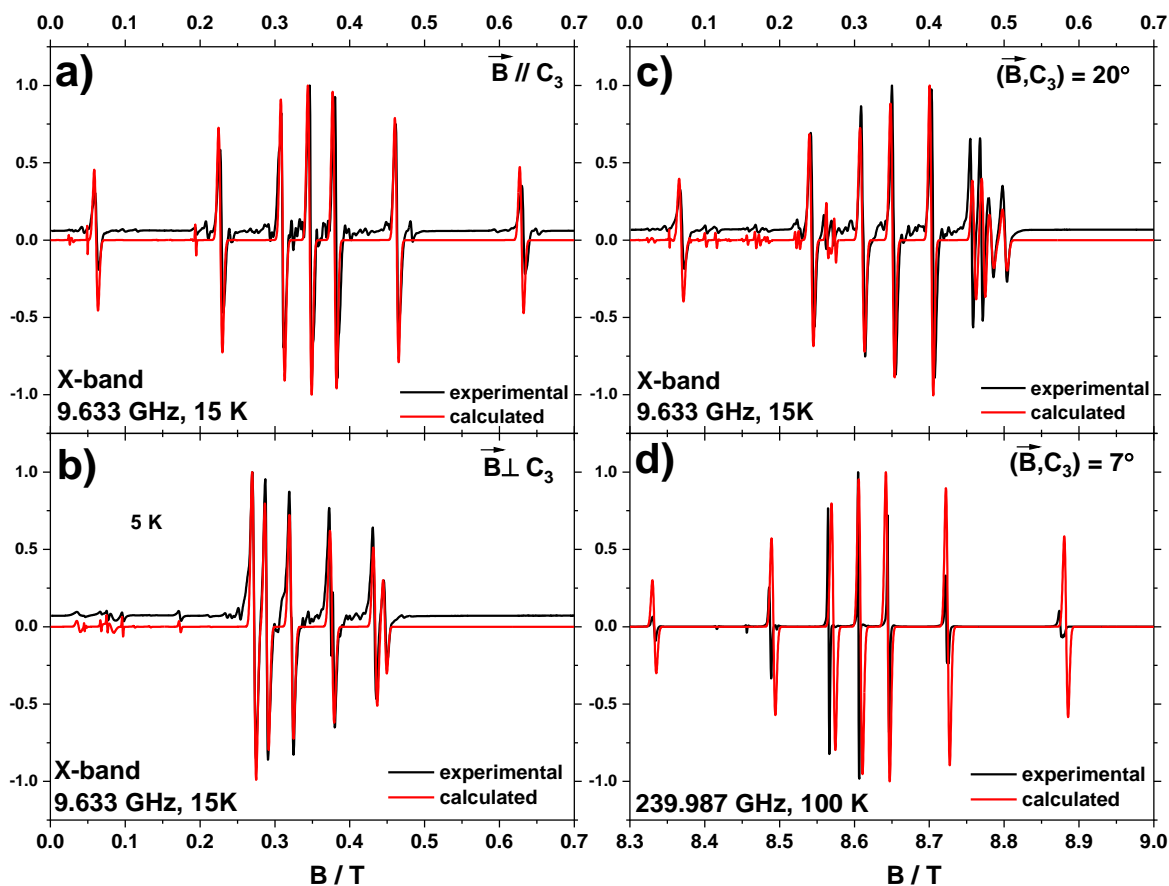


Figure 2. Multifrequency c.w.-EPR spectra on oriented single crystals of **1** at X-band and 240 GHz. Simulations were made as described in the text.

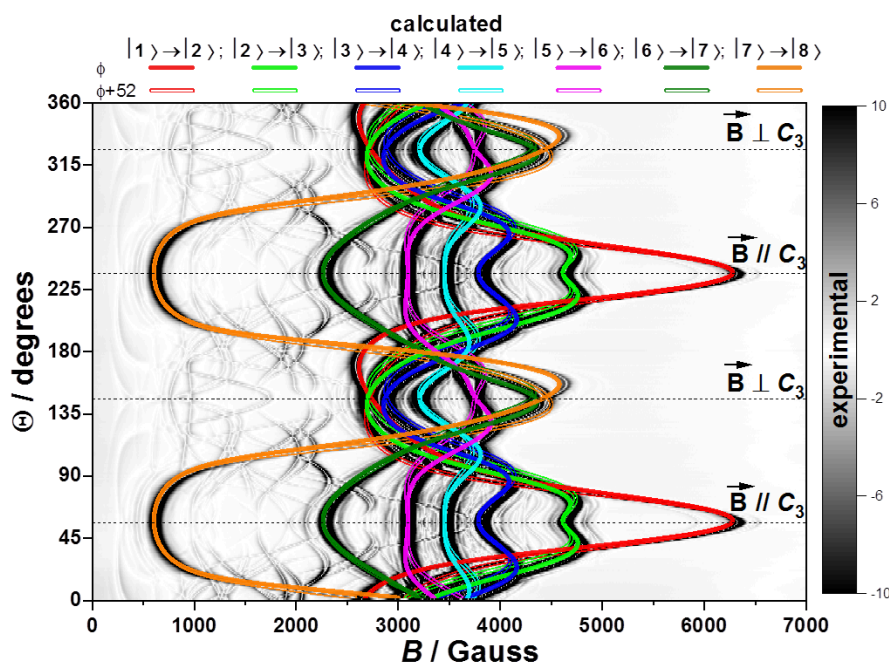


Figure 3. Angular variation of the X-band c.w.-EPR spectrum of **1** in a plane containing the C_3 axis and at 15K. The $|i\rangle$ labels refer to the eigenvectors given in Table S3. Simulations concern the allowed transitions.

Anticipating the discussion relevant to the determination of the relative splitting of the m_s sublevels of the $^8S_{7/2}$ term, we also recorded single crystal c.w.-EPR spectra of **1** at higher frequency (240 GHz). When resonance fields of allowed transitions for an orientation of the magnetic field along C_3 (Fig. 2a), close to it (Fig. 2d), or perpendicular to C_3 (Fig. 2b) are taken into account, only diagonal ($k=2,4,6$; $q=0$) Stevens parameters entering Hamiltonian (1), as well as the $g_{||}$ and g_{\perp} factors, can be determined (Figures S2a,b,d). However, use of only diagonal Stevens parameters fails to reproduce the spectra at intermediate orientations (Fig. S2c). Thus, to reproduce the observed resonance fields at general orientations of the magnetic field, use of off-diagonal ($q \neq 0$) Stevens parameters is required. To this purpose we also included in the fitting the observed X-band allowed transition resonance fields for an angle of the magnetic field of 20 degrees with respect to the C_3 axis (Fig. S3). This was done for one of the two magnetically inequivalent species (Fig. S1). This resulted in the best fit parameters: $B_0^2 = +1.14 \cdot 10^{-2} \text{ cm}^{-1}$, $B_0^4 = +4.84 \cdot 10^{-5} \text{ cm}^{-1}$, $B_0^6 = -6.07 \cdot 10^{-9} \text{ cm}^{-1}$, $B_3^4 = +5.79 \cdot 10^{-4} \text{ cm}^{-1}$, $B_{-3}^4 = -5.57 \cdot 10^{-4} \text{ cm}^{-1}$, $g_{||} = 1.992$ and $g_{\perp} = 1.985$. The two off-diagonal parameters corresponding to real ($q=3$) and imaginary ($q=-3$) matrix elements can be replaced by their vector sum in the complex plane. By imposing that this vector sum is a real number, one can reduce the number of parameters by one. Keeping the parameters entering (1) constant, a rotation of the laboratory coordinate frame by 52 degrees, which is very close to 48 degrees which is the angle of relative rotation of the two magnetically inequivalent species as defined by the C_3 axis and the phenolic oxygens (Figure S1), results in the reproduction of the resonant fields of the other magnetically inequivalent site (Figure 2c). Most importantly the determined best-fit parameters excellently reproduce the full angular variation of the observed spectra at X-band for both allowed (Fig. 3) and forbidden (Fig. S4) transitions. The resulting energy level spectrum of the sublevels (Table S3) of the ground $^8S_{7/2}$ term with the obtained best-fit parameters (Figures S5 and S6) reveals that the smallest m_s projections are lowest in energy at zero magnetic field. To verify this result, we recorded the temperature dependence of the c.w.-EPR spectrum at 240 GHz (Fig. S7) where significant depopulation effects can be observed, given the splitting of the $^8S_{7/2}$ term sublevels at zero magnetic field. The temperature dependence of the observed intensities (Fig. S7) is in agreement with our assignment of the observed transitions.

The study and exploitation by magnetic resonance techniques of the spin dynamics of Ln coordination complexes, and more specifically of Gd-containing ones, is a vast research topic encompassing large research areas such as Magnetic Resonance Imaging,⁴⁹ Dynamic Nuclear Polarisation,⁵⁰⁻⁵⁴ and spin labeling for distance measurements,⁵⁴⁻⁵⁸ an extensive review of which is outside the scope of this study. Thus, several previous

investigations on frozen solutions or polycrystalline powders of Gd coordination complexes revealed that Gd(III) centres in such complexes display relatively long relaxation times and in some cases T_m 's of the order of tens of microseconds. To probe the coherent spin dynamics of **1**, we measured pulse EPR spectra on single crystals of **1** at 240 GHz. The temperature dependence of the observed echo-detected field-swept (EDFS) spectra of **1** for an orientation of the applied magnetic field very close to the C_3 axis (Figure S8) reveal that EDFs spectra can be recorded for temperatures as high as 70 K. Hahn echo⁵⁹ and stimulated echo⁶⁰⁻⁶¹ sequences were used to determine the T_m and T_1 (Figures S9-S13), respectively, of the observed EDFs transitions. The determined parameters are given in Tables S4 and S5. At the lowest temperature (3K) the T_m and T_1 of only the highest field transition can be determined because of the previously mentioned thermal depopulation effects at 240 GHz. At 3K, we observe that the dynamic state described as a superposition of the two lowest sublevels ($m_s = -5/2$ and $m_s = -7/2$) of the $^8S_{7/2}$ term displays coherent spin dynamics characterized by a $T_1 = 30 \mu\text{s}$ and by a phase memory time $T_m = 12 \mu\text{s}$ (Table S4). The determined T_m is amongst the longest observed for purely f-electron molecular systems. By increasing the temperature (Fig. 4), T_m decreases faster than T_1 , indicating that coherent spin dynamics within the studied temperature and field range is not limited by spin-lattice induced decoherence. The temperature dependence of T_1 is linear in a double log plot, indicating a power law $T_1 = D T^{-m}$, with $m = 0.44$ and $D = 46.4 \text{ s K}^{-0.44}$, likely corresponding to a direct process that is promoted at high magnetic fields since for Kramers ions a direct process determined T_1 is inversely proportional to the fourth power of the external magnetic field, \vec{B} .³⁹

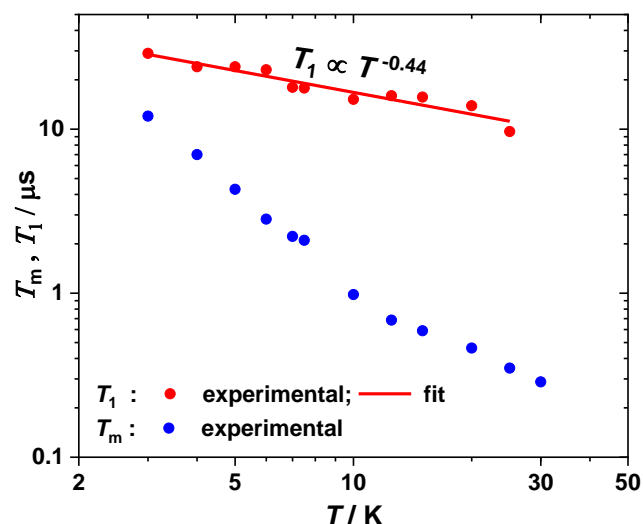


Figure 4. T_1 (red) and T_m (blue) at different temperatures. The measurements were performed at 240 GHz and 8.89 T for a single crystal of **1** with the magnetic field oriented as described in the main text.

We have shown herein, that long phase memory times can be achieved in purely f-electron systems essentially devoid of orbital angular momentum since local fluctuations of the LF cannot couple via magnetoelastic coupling terms to the wave functions of the electronic system. These results are in agreement with previous studies on d- or f-shell molecular systems where isotropic states, thus devoid of orbital angular momentum, have been probed.^{20,34,62} Furthermore, they are also in agreement with recent experimental and theoretical studies⁶³ in which we demonstrated the importance of the magnetoelastic coupling and the role of the trigonal symmetry to the dynamic magnetic properties of the isostructural (displaying thus the same phonon spectrum) Yb(trensals) complex.²⁴ In addition, in previous coherent dynamics studies of Yb(trensals) we have shown that the ground term displays a phase memory time of a few hundred nanoseconds for Yb_{0.07}Lu_{0.93}(trensals) at X-band, which gets T_1 limited and of the order of 0.1 μ s at around 20 K. Preliminary measurements on single crystals of Yb_{0.01}Lu_{0.99}(trensals) at 240 GHz (Figure S14) show similar T_m characteristics as those previously determined for Yb(III) at X-band.²⁴ In the case of Gd(trensals) the coherent spin dynamics is characterized by a T_m of 12 μ s at 3K and is still detectable at temperatures up to 70 K (Figure S8). Based on the results obtained herein and in previous studies,^{20,34,62} a general strategy for the optimization of the coherence characteristics of molecular magnetic materials should be based on the minimization of the partial derivatives of all parameters entering the time dependent Hamiltonian of the systems.

ASSOCIATED CONTENT

Experimental details, characterization and EPR data. This material is available free of charge via the Internet at <http://pubs.acs.org>. Crystallographic data (including structure factors) for Yb(trensals) have been deposited with the Cambridge Crystallographic Data Centre (CCDC 2183899). Copies of the data can be obtained, free of charge, on application to Cambridge Crystallographic Data Centre, 12 Union Road, Cambridge CB2 1EZ, UK, (fax: +44-(0)1223-336033 or email: deposit@ccdc.cam.ac.uk).

AUTHOR INFORMATION

Corresponding Author

*piligkos@chem.ku.dk

Author Contributions

The manuscript was written through contributions of all authors. All authors have given approval to the final version of the manuscript.

Funding Sources

Novo Nordisk Foundation research grant NNF20OC0065610. US Department of Energy (under DE-SC0020260 to SH). Work performed at the NHMFL

is supported by the US National Science Foundation (DMR-1644779) and by the State of Florida.

Notes

Any additional relevant notes should be placed here.

ACKNOWLEDGMENT

SP thanks the Novo Nordisk Foundation for research grant NNF20OC0065610. SH thanks the US Department of Energy (under DE-SC0020260 to SH), the US National Science Foundation (DMR-1644779) and the State of Florida.

REFERENCES

- (1) Riedel, M. F.; Bloch, I.; Debuisschert, T.; Wilhelm-Mauch, F.; Pruneri, V.; Vitanov, N. V.; Wehner, S.; Calarco, T., 'Europe's Quantum Flagship is taking off', *Europhysics News* **2018**, 49, 30-34.
- (2) Atzori, M.; Sessoli, R., 'The Second Quantum Revolution: Role and Challenges of Molecular Chemistry', *Journal of the American Chemical Society* **2019**, 141, 11339-11352.
- (3) MacFarlane, A. G. J.; Dowling, J. P.; Milburn, G. J., 'Quantum technology: the second quantum revolution', *Philosophical Transactions of the Royal Society of London. Series A: Mathematical, Physical and Engineering Sciences* **2003**, 361, 1655-1674.
- (4) Feynman, R. P., 'Quantum-Mechanical Computers', *Found. Phys.* **1986**, 16, 507-531.
- (5) Awschalom, D.; Samarth, N.; Loss, D. Semiconductor Spintronics and Quantum Computation; Springer: Berlin **2002**.
- (6) Barnett, S. M. Quantum information; Oxford University Press: Oxford, 16 **2009**.
- (7) Preskill, J., 'Quantum Computing in the NISQ era and beyond', *Quantum* **2018**, 2, 1-20.
- (8) Gibney, E., 'Physics: Quantum computer quest', *Nature* **2014**, 516, 24-26.
- (9) DiCarlo, L.; Reed, M. D.; Sun, L.; Johnson, B. R.; Chow, J. M.; Gambetta, J. M.; Frunzio, L.; Girvin, S. M.; Devoret, M. H.; Schoelkopf, R. J., 'Preparation and measurement of three-qubit entanglement in a superconducting circuit', *Nature* **2010**, 467, 574-578.
- (10) Thiele, S.; Balestro, F.; Ballou, R.; Klyatskaya, S.; Ruben, M.; Wernsdorfer, W., 'Electrically driven nuclear spin resonance in single-molecule magnets', *Science* **2014**, 344, 1135-1138.
- (11) Shor, P. W. Algorithms for quantum computation: discrete logarithms and factoring **1994**.

- (12) Grover, L. K., 'Quantum Mechanics Helps in Searching for a Needle in a Haystack', *Physical Review Letters* **1997**, 79, 325-328.
- (13) Cirac, J. I.; Zoller, P., 'Goals and opportunities in quantum simulation', *Nat. Phys.* **2012**, 8, 264-266.
- (14) Arute, F. et al., 'Quantum supremacy using a programmable superconducting processor', *Nature* **2019**, 574, 505-510.
- (15) Wu, Y. et al., 'Strong Quantum Computational Advantage Using a Superconducting Quantum Processor', *Physical Review Letters* **2021**, 127, 180501.
- (16) Zhong, H.-S. et al., 'Phase-Programmable Gaussian Boson Sampling Using Stimulated Squeezed Light', *Physical Review Letters* **2021**, 127, 180502.
- (17) Terhal, B. M., 'Quantum error correction for quantum memories', *Rev. Mod. Phys.* **2015**, 87, 307-346.
- (18) Rocha, A. R.; Garcia-Suarez, V. M.; Bailey, S. W.; Lambert, C. J.; Ferrer, J.; Sanvito, S., 'Towards molecular spintronics', *Nat. Mater.* **2005**, 4, 335-339.
- (19) Bogani, L.; Wernsdorfer, W., 'Molecular spintronics using single-molecule magnets', *Nat. Mater.* **2008**, 7, 179-186.
- (20) Gaita-Ariño, A.; Luis, F.; Hill, S.; Coronado, E., 'Molecular spins for quantum computation', *Nat. Chem.* **2019**, 11, 301-309.
- (21) Sessoli, R., 'All in one', *Nat. Phys.* **2021**, 17, 1192-1193.
- (22) Sessoli, R., 'Tackling the challenge of controlling the spin with electric field', *National Science Review* **2020**, 8, nwaa267.
- (23) Bonizzoni, C.; Ghirri, A.; Santanni, F.; Atzori, M.; Sorace, L.; Sessoli, R.; Affronte, M., 'Storage and retrieval of microwave pulses with molecular spin ensembles', *npj Quantum Information* **2020**, 6, 68.
- (24) Pedersen, K. S.; Ariciu, A. M.; McAdams, S.; Weihe, H.; Bendix, J.; Tuna, F.; Piligkos, S., 'Toward Molecular 4f Single-Ion Magnet Qubits', *Journal of the American Chemical Society* **2016**, 138, 5801-5804.
- (25) Hussain, R.; Allodi, G.; Chiesa, A.; Garlatti, E.; Mitcov, D.; Konstantatos, A.; Pedersen, K. S.; De Renzi, R.; Piligkos, S.; Carretta, S., 'Coherent Manipulation of a Molecular Ln-Based Nuclear Qudit Coupled to an Electron Qubit', *Journal of the American Chemical Society* **2018**, 140, 9814-9818.
- (26) Gimeno, I.; Urtizberea, A.; Román-Roche, J.; Zueco, D.; Camón, A.; Alonso, P. J.; Roubeau, O.; Luis, F., 'Broad-band spectroscopy of a vanadyl porphyrin: a model electronuclear spin qudit', *Chem. Sci.* **2021**, 12, 5621-5630.
- (27) Carretta, S.; Zueco, D.; Chiesa, A.; Gómez-León, Á.; Luis, F., 'A perspective on scaling up quantum computation with molecular spins', *Appl. Phys. Lett.* **2021**, 118, 240501.
- (28) Jenkins, M. D.; Duan, Y.; Diosdado, B.; García-Ripoll, J. J.; Gaita-Ariño, A.; Giménez-Saiz, C.; Alonso, P. J.; Coronado, E.; Luis, F., 'Coherent manipulation of three-qubit states in a molecular single-ion magnet', *Physical Review B* **2017**, 95, 064423.
- (29) Martínez-Pérez, M. J.; Cardona-Serra, S.; Schlegel, C.; Moro, F.; Alonso, P. J.; Prima-García, H.; Clemente-Juan, J. M.; Evangelisti, M.; Gaita-Ariño, A.; Sesé, J.; van Slageren, J.; Coronado, E.; Luis, F., 'Gd-Based Single-Ion Magnets with Tunable Magnetic Anisotropy: Molecular Design of Spin Qubits', *Physical Review Letters* **2012**, 108, 247213.
- (30) Goldfarb, D.; Stoll, S. *EPR Spectroscopy: Fundamentals and Methods*; Wiley: **2018**.
- (31) Takahashi, S.; Tupitsyn, I. S.; van Tol, J.; Beedle, C. C.; Hendrickson, D. N.; Stamp, P. C. E., 'Decoherence in crystals of quantum molecular magnets', *Nature* **2011**, 476, 76-79.
- (32) Shiddiq, M.; Komijani, D.; Duan, Y.; Gaita-Ariño, A.; Coronado, E.; Hill, S., 'Enhancing coherence in molecular spin qubits via atomic clock transitions', *Nature* **2016**, 531, 348-351.
- (33) Kundu, K.; White, J. R. K.; Moehring, S. A.; Yu, J. M.; Ziller, J. W.; Furche, F.; Evans, W. J.; Hill, S., 'A 9.2-GHz clock transition in a Lu(II) molecular spin qubit arising from a 3,467-MHz hyperfine interaction', *Nat. Chem.* **2022**, 14, 392-397.
- (34) Ariciu, A.-M.; Woen, D. H.; Huh, D. N.; Nodaraki, L. E.; Kostopoulos, A. K.; Goodwin, C. A. P.; Chilton, N. F.; McInnes, E. J. L.; Winpenny, R. E. P.; Evans, W. J.; Tuna, F., 'Engineering electronic structure to prolong relaxation times in molecular qubits by minimising orbital angular momentum', *Nature Communications* **2019**, 10, 3330.
- (35) Aguila, D.; Barrios, L. A.; Velasco, V.; Roubeau, O.; Repolles, A.; Alonso, P. J.; Sese, J.; Teat, S. J.; Luis, F.; Aromi, G., 'Heterodimetallic [LnLn] Lanthanide Complexes: Toward a Chemical Design of Two-Qubit Molecular Spin Quantum Gates', *J. Am. Chem. Soc.* **2014**, 136, 14215-14222.
- (36) Luis, F.; Repolles, A.; Martinez-Perez, M. J.; Aguila, D.; Roubeau, O.; Zueco, D.; Alonso, P. J.; Evangelisti, M.; Camon, A.; Sese, J.; Barrios, L. A.; Aromi, G., 'Molecular Prototypes for Spin-Based CNOT and SWAP Quantum Gates', *Phys. Rev. Lett.* **2011**, 107, 117203/117201-117203/117205.
- (37) Pedersen, K. S.; Dreiser, J.; Weihe, H.; Sibille, R.; Johannesen, H. V.; Sørensen, M. A.; Nielsen, B. E.; Sigrist, M.; Mutka, H.; Rols, S.; Bendix, J.; Piligkos, S., 'Design of Single-Molecule Magnets: Insufficiency of the Anisotropy Barrier as the Sole Criterion', *Inorganic Chemistry* **2015**, 54, 7600-7606.

- (38) Wybourne, B. G., 'Energy Levels of Trivalent Gadolinium and Ionic Contributions to the Ground-State Splitting', *Physical Review* **1966**, 148, 317-327.
- (39) Shrivastava, K. N., 'Theory of Spin-Lattice Relaxation', *physica status solidi (b)* **1983**, 117, 437-458.
- (40) Bernhardt, P. V.; Flanagan, B. M.; Riley, M. J., 'Completion of the Isomorphous Ln(trensal) Series', *Aust. J. Chem.* **2001**, 54, 229 - 232.
- (41) Habib, M.; Sain, S.; Das, B.; Chandra, S. K., 'Benign routes for the syntheses of polydentate Schiff base and their lanthanide complexes', *J. Indian Chem. Soc.* **2011**, 88, 1501.
- (42) Kanesato, M.; Yokoyama, T., 'Synthesis and Structural Characterization of Ln(III) Complexes (Ln = Eu, Gd, Tb, Er, Tm, Lu) of Tripodal Tris[2-(salicylideneamino)ethyl]amine', *Chem. Lett.* **1999**, 28, 137-138.
- (43) Kanesato, M.; Mizukami, S.; Houjou, H.; Tokuhisa, H.; Koyama, E.; Nagawa, Y., 'Comparison of the bond lengths for the lanthanide complexes of tripodal heptadentate ligands', *J. Alloys Compd.* **2004**, 374, 307-310.
- (44) Pedersen, K. S.; Ungur, L.; Sigrist, M.; Sundt, A.; Schau-Magnussen, M.; Vieru, V.; Mutka, H.; Rols, S.; Weihe, H.; Waldmann, O.; Chibotaru, L. F.; Bendix, J.; Dreiser, J., 'Modifying the properties of 4f single-ion magnets by peripheral ligand functionalisation', *Chem. Sci.* **2014**, 5, 1650-1660.
- (45) Kanesato, M.; Yokoyama, T.; Itabashi, O.; Suzuki, T. M.; Shiro, M., 'Synthesis and Structural Characterization of Praseodymium(III) and Neodymium(III) Complexes of Tripodal Tris[2-(salicylideneamino)ethyl]amine', *Bull. Chem. Soc. Jpn.* **1996**, 69, 1297-1302.
- (46) Kanesato, M.; Yokoyama, T., 'Crystal Structures of Dysprosium(III) and Holmium(III) Complexes of Tripodal Tris[2-(salicylideneamino)ethyl]amine', *Anal. Sci.* **2000**, 16, 335-336.
- (47) Bernhardt, P. V.; Flanagan, B. M.; Riley, M. J., 'Isomorphous Lanthanide Complexes of a Tripodal N4O3 Ligand', *Aust. J. Chem.* **2000**, 53, 229 - 231.
- (48) Press, W. H.; Teukolsky, S. A.; Vetterling, W. T.; Flannery, B. P. *Numerical Recipes in C: The Art of Scientific Computing*; 2nd ed.; Cambridge University Press: Cambridge **1992**.
- (49) Wahsner, J.; Gale, E. M.; Rodríguez-Rodríguez, A.; Caravan, P., 'Chemistry of MRI Contrast Agents: Current Challenges and New Frontiers', *Chem. Rev.* **2019**, 119, 957-1057.
- (50) Corzilius, B.; Smith, A. A.; Barnes, A. B.; Luchinat, C.; Bertini, I.; Griffin, R. G., 'High-Field Dynamic Nuclear Polarization with High-Spin Transition Metal Ions', *Journal of the American Chemical Society* **2011**, 133, 5648-5651.
- (51) Stevanato, G.; Kubicki, D. J.; Menzildjian, G.; Chauvin, A.-S.; Keller, K.; Yulikov, M.; Jeschke, G.; Mazzanti, M.; Emsley, L., 'A Factor Two Improvement in High-Field Dynamic Nuclear Polarization from Gd(III) Complexes by Design', *Journal of the American Chemical Society* **2019**, 141, 8746-8751.
- (52) Kaushik, M.; Qi, M.; Godt, A.; Corzilius, B., 'Bis-Gadolinium Complexes for Solid Effect and Cross Effect Dynamic Nuclear Polarization', *Angew Chem Int Ed Engl* **2017**, 56, 4295-4299.
- (53) Capozzi, A.; Patel, S.; Wenckebach, W. T.; Karlsson, M.; Lerche, M. H.; Ardenkjær-Larsen, J. H., 'Gadolinium Effect at High-Magnetic-Field DNP: 70% ¹³C Polarization of [U-¹³C] Glucose Using Trityl', *The Journal of Physical Chemistry Letters* **2019**, 10, 3420-3425.
- (54) Nagarajan, V.; Hovav, Y.; Feintuch, A.; Vega, S.; Goldfarb, D., 'EPR detected polarization transfer between Gd³⁺ and protons at low temperature and 3.3 T: The first step of dynamic nuclear polarization', *The Journal of Chemical Physics* **2010**, 132, 214504.
- (55) Goldfarb, D., 'Gd³⁺ spin labeling for distance measurements by pulse EPR spectroscopy', *Physical Chemistry Chemical Physics* **2014**, 16, 9685-9699.
- (56) Giannoulis, A.; Ben-Ishay, Y.; Goldfarb, D. In *Methods Enzymol.*; Cotruvo, J. A., Ed.; Academic Press: 2021; Vol. 651, p 235-290.
- (57) Raitsimring, A. M.; Gunanathan, C.; Potapov, A.; Efremenko, I.; Martin, J. M. L.; Milstein, D.; Goldfarb, D., 'Gd³⁺ complexes as potential spin labels for high field pulsed EPR distance measurements', *Journal of the American Chemical Society* **2007**, 129, 14138 - 14139.
- (58) Yagi, H.; Banerjee, D.; Graham, B.; Huber, T.; Goldfarb, D.; Otting, G., 'Gadolinium Tagging for High-Precision Measurements of 6 nm Distances in Protein Assemblies by EPR', *Journal of the American Chemical Society* **2011**, 133, 10418-10421.
- (59) Hahn, E. L., 'Spin Echoes', *Physical Review* **1950**, 80, 580-594.
- (60) Takahashi, S.; van Tol, J.; Beedle, C. C.; Hendrickson, D. N.; Brunel, L.-C.; Sherwin, M. S., 'Coherent Manipulation and Decoherence of $S=10$ Single-Molecule Magnets', *Physical Review Letters* **2009**, 102, 087603.
- (61) Schweiger, A.; Jeschke, G. *Principles of Pulse Electron Paramagnetic Resonance*; Oxford University Press: New York **2001**.

(62) Handzlik, G.; Magott, M.; Arczyński, M.; Sheveleva, A. M.; Tuna, F.; Sarewicz, M.; Osyczka, A.; Rams, M.; Vieru, V.; Chibotaru, L. F.; Pinkowicz, D., 'Magnetization Dynamics and Coherent Spin Manipulation of a Propeller Gd(III) Complex with the Smallest Helicene Ligand', *The Journal of Physical Chemistry Letters* **2020**, *11*, 1508-1515.

(63) Kragoskow, J. G. C.; Marbey, J.; Buch, C. D.; Nehrkorn, J.; Ozerov, M.; Piligkos, S.; Hill, S.; Chilton, N. F., 'Analysis of vibronic coupling in a 4f molecular magnet with FIRMS', *Nature Communications* **2022**, *13*, 825.

Spin-Lattice Relaxation Decoherence Suppression in Vanishing Orbital Angular Momentum Qubits

Christian D. Buch,¹ Krishnendu Kundu,² Jonathan J. Marbey,² Johan van Tol,²

Høgni Weihe,¹ Stephen Hill,² and Stergios Piligkos*¹

¹Department of Chemistry, University of Copenhagen, DK-2100 Copenhagen, Denmark

²National High Magnetic Field Laboratory, Tallahassee, Florida, 32310, United States of America

Contents

Experimental	2
Crystallographic Table.....	4
C.-w. single crystal Electron Paramagnetic Resonance	6
Pulsed single crystal Electron Paramagnetic Resonance	12
References.....	18

Experimental

Materials and methods

Acetonitrile, tris(2-aminoethyl)amine and salicylaldehyde were obtained from commercial sources and used as received. $\text{Gd}(\text{OTf})_3 \cdot 9\text{H}_2\text{O}$ and $\text{Y}(\text{OTf})_3 \cdot 9\text{H}_2\text{O}$ were synthesised from the corresponding Ln_2O_3 following a literature procedure.¹ The water content was determined *via* an EDTA titration using xylenol orange as the indicator. Gd_2O_3 and Y_2O_3 were obtained commercially and used as received.

Inductively coupled plasma mass spectrometry (ICP-MS) was performed to determine the actual Gd concentration. The measurements were performed on a Bruker Aurora Elite at The Department of Chemistry, University of Copenhagen. The instrument was tuned and calibrated (using calibration points spanning the range of concentrations encountered in the samples) prior to use. The calibration solutions were made by diluting a reference solution from Inorganic Ventures such that the concentrations of Y and Gd were between 0 – 15 ng/ml (9 calibration solutions were made in total). The reference solution was diluted using 2 % nitric acid of TraceSelect grade. The sample solution was prepared by dissolving single crystals (2.77 mg) of $\text{Gd@Y}(\text{trensal})$ (from the same batch as the ones used for the EPR measurements) in boiling conc. nitric acid (ca. 20 ml). After boiling the solution was diluted to 100 ± 0.1 ml using a measuring flask. As the concentrations of Gd and Y in the crystal are very different two subsequent dilutions were made for the ICP-MS measurements to ensure that the Gd and Y concentrations were within the calibration range. From the analysis, mass percentages of 0.12 % for Gd and 16.1 % for Y were found, giving a molar ratio of 0.4 % Gd to 99.6 % Y. The mass percentages found are close to the ones predicted for $\text{Gd}_{0.004}\text{Y}_{0.996}\text{C}_{27}\text{H}_{27}\text{N}_4\text{O}_3$ which affords Gd: 0.12 % and Y: 16.3 %.

Continuous wave Electron Paramagnetic Resonance (c.w.-EPR) measurements at X-band frequencies were measured on a Bruker Elexsys E500 equipped with an automatic goniometer for rotations of single crystals. c.w.-EPR measurements at 240 GHz were performed on a custom built instrument at The National High Magnetic Field Laboratory in Tallahassee, Florida, USA.^{2, 3}

Pulsed EPR was performed at 240 GHz on a custom built instrument at The National High Magnetic Field Laboratory in Tallahassee, Florida, USA.^{2, 3} To determine the spin-lattice relaxation time (T_1) at the magnetic field positions given in the main text a three-pulse stimulated echo sequence ($\pi/2$ - τ - $\pi/2$ - t - $\pi/2$ - τ -echo) was used. T_1 was extracted from the measurements by fitting a monoexponential [$I(t) = I_0 + A \cdot \exp(t/T_1)$] to the data. In the monoexponential A is a preexponential factor. To determine the phase memory time (T_m) at the magnetic field positions given in the main text a standard Hahn echo sequence ($\pi/2$ - τ - π - τ -echo) with pulse lengths of 400 ns ($\pi/2$) and 800 ns (π) was employed. At the given magnetic field position, the decay of the Hahn echo was measured as a function of the inter

pulse time τ . Depending on the temperature of the sample T_m was extracted either by fitting the measurements to a monoexponential decay [$I(\tau) = I_0 + A \cdot \exp(-2\tau/T_m)$] or to a stretched monoexponential decay [$I(\tau) = I_0 + A \cdot \exp(-2\tau/T_m)^b$], where b is the stretching factor. For measurements below 10 K the data were fitted to a stretched monoexponential decay while at temperatures above 10 K the data were fitted to a standard monoexponential decay. Echo-detected field-swept (EDFS) EPR spectra were obtained using a standard Hahn-echo sequence ($\pi/2$ - τ - π - τ -echo) while sweeping the magnetic field. For the measurements pulse lengths of 400 ns ($\pi/2$) and 800 ns (π) were used except for the EDFs at 10 K where pulse lengths of 500 ns ($\pi/2$) and 1000 ns (π) were used.

Synthesis

Single crystals of Gd(trensal) were prepared analogously to a literature procedure.⁴ **1** was prepared similarly to Gd(trensal) but employing a molar ratio of 5:995 for Gd(OTf)₃·9H₂O and Y(OTf)₃·9H₂O, respectively.

Crystallography

Single crystals suitable for single crystal X-ray diffraction were mounted on a BRUKER D8VENTURE diffractometer, which is equipped with a PHOTON 100 CMOS detector, a Mo K α high-brilliance I μ S S3 radiation source ($\lambda = 0.71073$) and an Oxford cryosystem solution. The diffraction was performed at 120 K. The instrument was controlled using the APEX2 software package. Data reduction and absorption corrections were performed using SAINT⁵ and SADABS,⁶ respectively. SHELXT⁷ with intrinsic phasing was used to solve the structure and SHELXL^{8,9} (least squares) was used for the data refinement. OLEX2^{10,11} was used to visualize the data during refinement. All atoms except hydrogen were refined anisotropically. All hydrogen atoms in the structure have been placed using the “Add H” command in OLEX2, and are thus only placed at calculated positions.

Crystallographic Tables

Table S1 Crystallographic data for Gd(trensal)

Empirical formula	C ₂₇ H ₂₇ GdN ₄ O ₃
Formula weight	612.78
Temperature/K	120
Crystal system	Trigonal
Space group	$P\bar{3}c1$
a/Å	13.0268(6)
b/Å	13.0268(6)
c/Å	16.3361(8)
$\alpha/^\circ$	90
$\beta/^\circ$	90
$\gamma/^\circ$	120
Volume/Å ³	2400.8(3)
Z	4
ρ_{calc} , g cm ⁻³	1.695
μ/mm^{-1}	2.800
$F(000)$	1220.0
Crystal size/mm ³	0.61 × 0.544 × 0.292
$\lambda(\text{MoK}\alpha)$	0.71073
2 Θ range for data collection/ $^\circ$	3.61 to 54.944
Reflections collected	73514
Independent reflections	1840 [$R_{\text{int}} = 0.0403$, $R_{\text{sigma}} = 0.0089$]
Data/restraints/parameters	1840/0/106
Goodness-of-fit on F^2	1.194
R_1 , wR_2 [$I \geq 2\sigma(I)$]	0.0200, 0.0508
R_1 , wR_2 [all data]	0.0242, 0.0549
Residual electron density / e Å ⁻³	0.39/-0.93

Table S2 Selected bond lengths and angles in Gd(trensal)

Atom	Atom	Length / Å	Atom	Atom	Atom	Angle / °
Gd	O1	2.2331(16)	N1	Gd	N2	66.09(4)
Gd	N1	2.737(3)	N1	Gd	O1	121.15(4)
Gd	N2	2.5157(19)	O1	Gd	O1*	95.66(6)
			O1	Gd	N2	72.83(6)
			N2	Gd	N2*	104.70(5)

* Symmetry generated by the C_3 axis

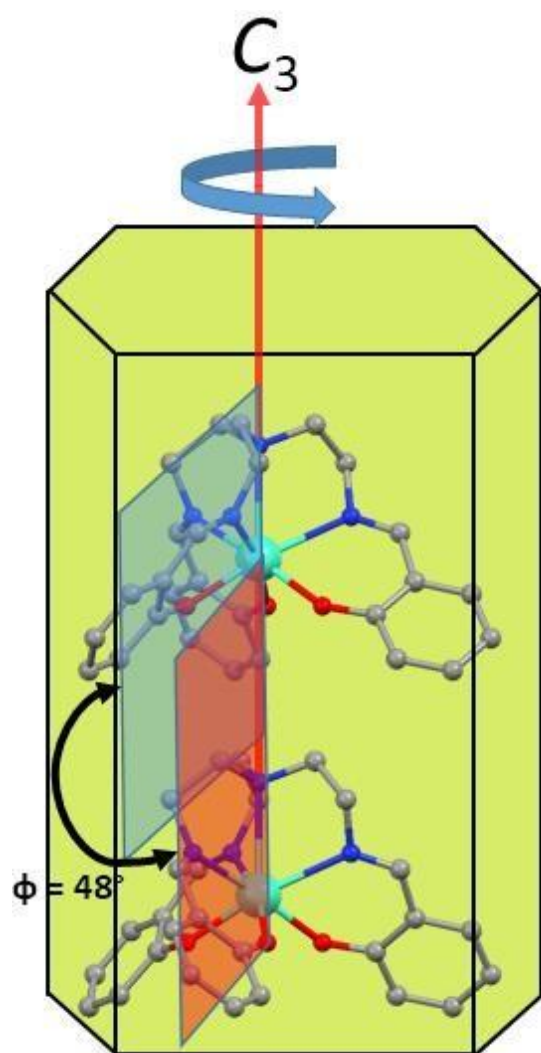


Figure S1 Orientation of the molecular C_3 axis in the crystal of Gd(trensal). The two planes indicate the 48° angle between the two magnetic nonequivalent sites in the unit cell. Hydrogens have been omitted for clarity. Color code: C, grey; O, red; N, blue and Gd, cyan.

C.-w. single crystal Electron Paramagnetic Resonance

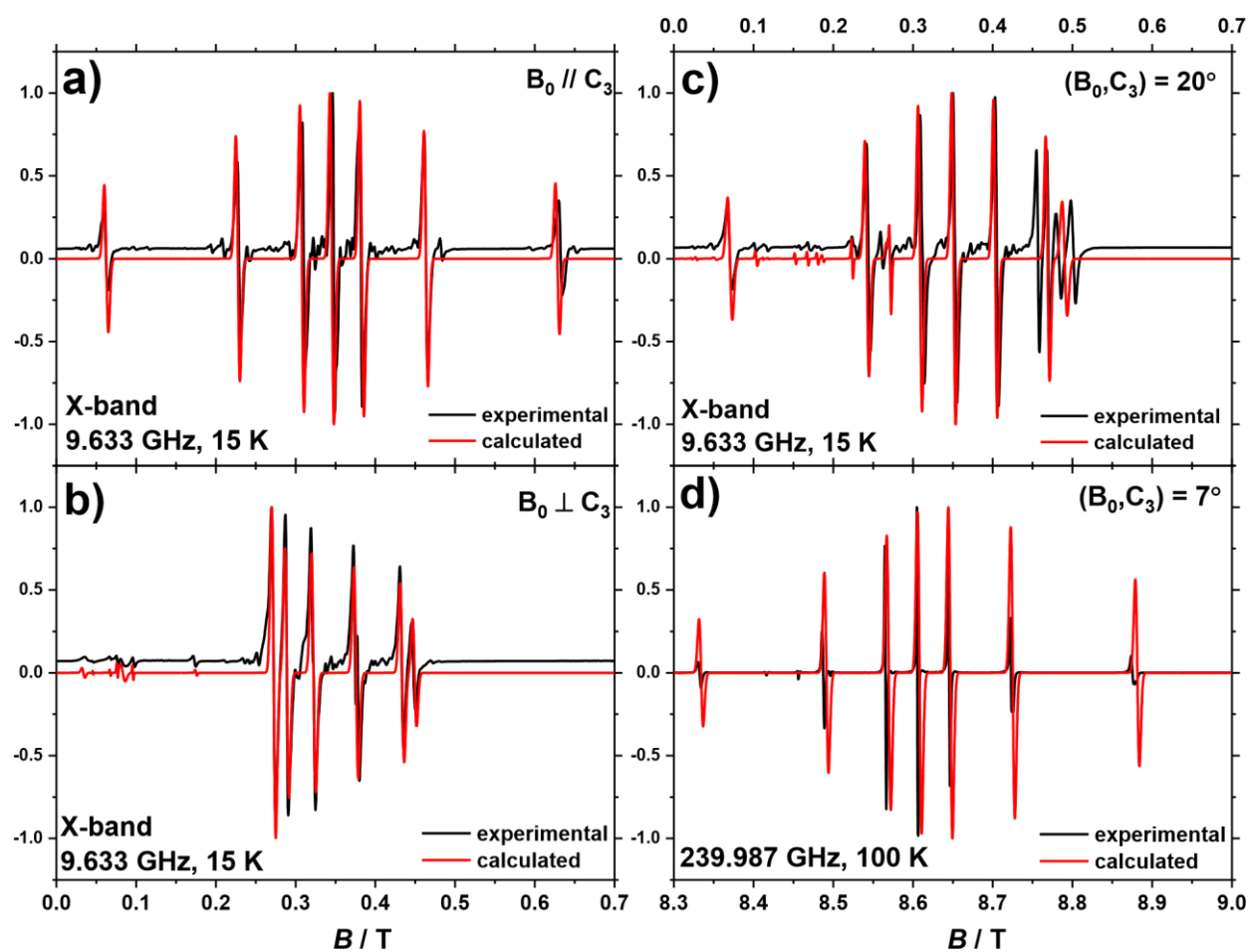


Figure S2 Multifrequency c.w.-EPR spectra on oriented single crystals of **1** at X-band and 240 GHz. Simulations were made as described in the main text for one species and only diagonal parameters.

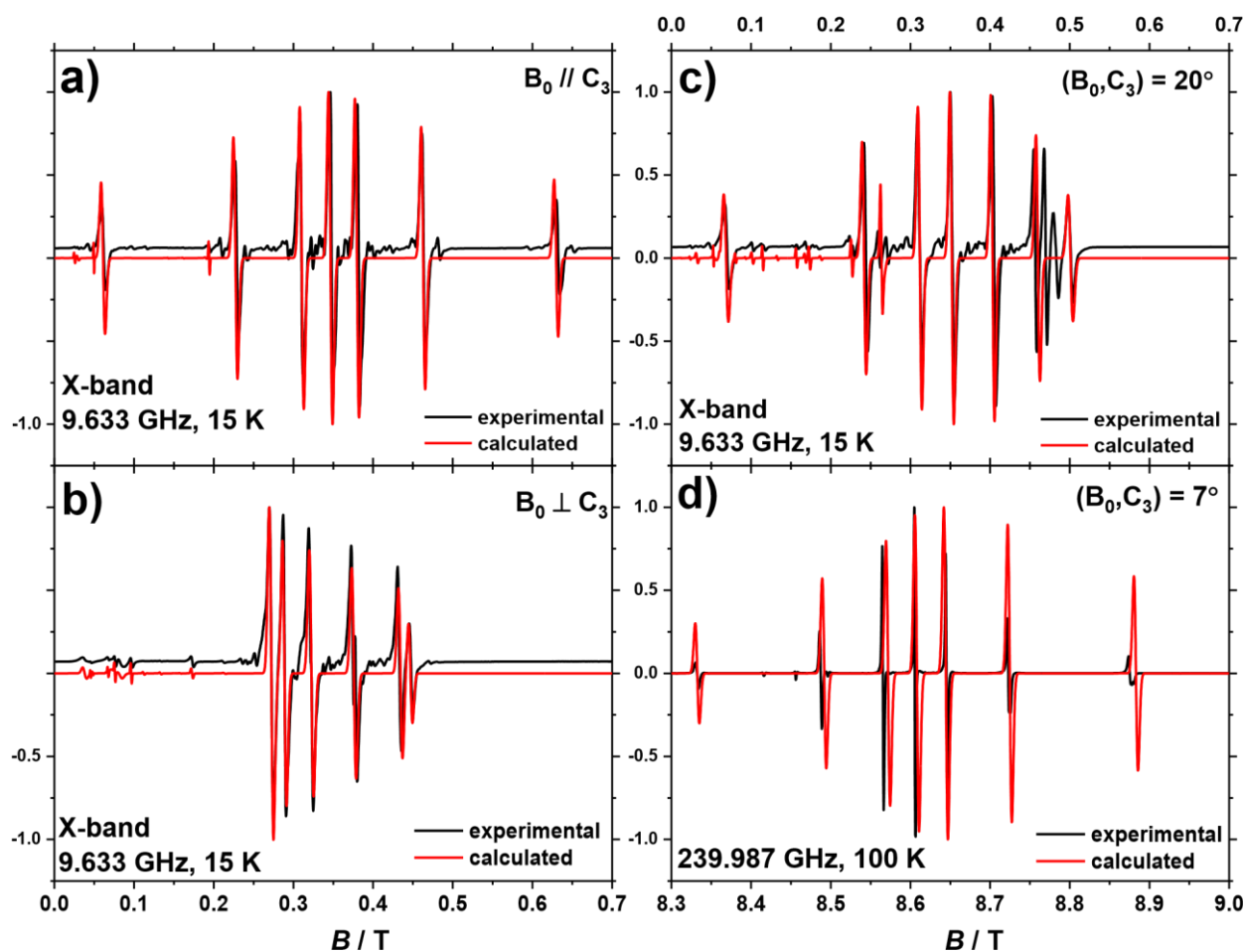


Figure S3 Multifrequency c.w.-EPR spectra on oriented single crystals of **1** at X-band and 240 GHz. Simulations were made as described in the main text for one species and with off-diagonal parameters.

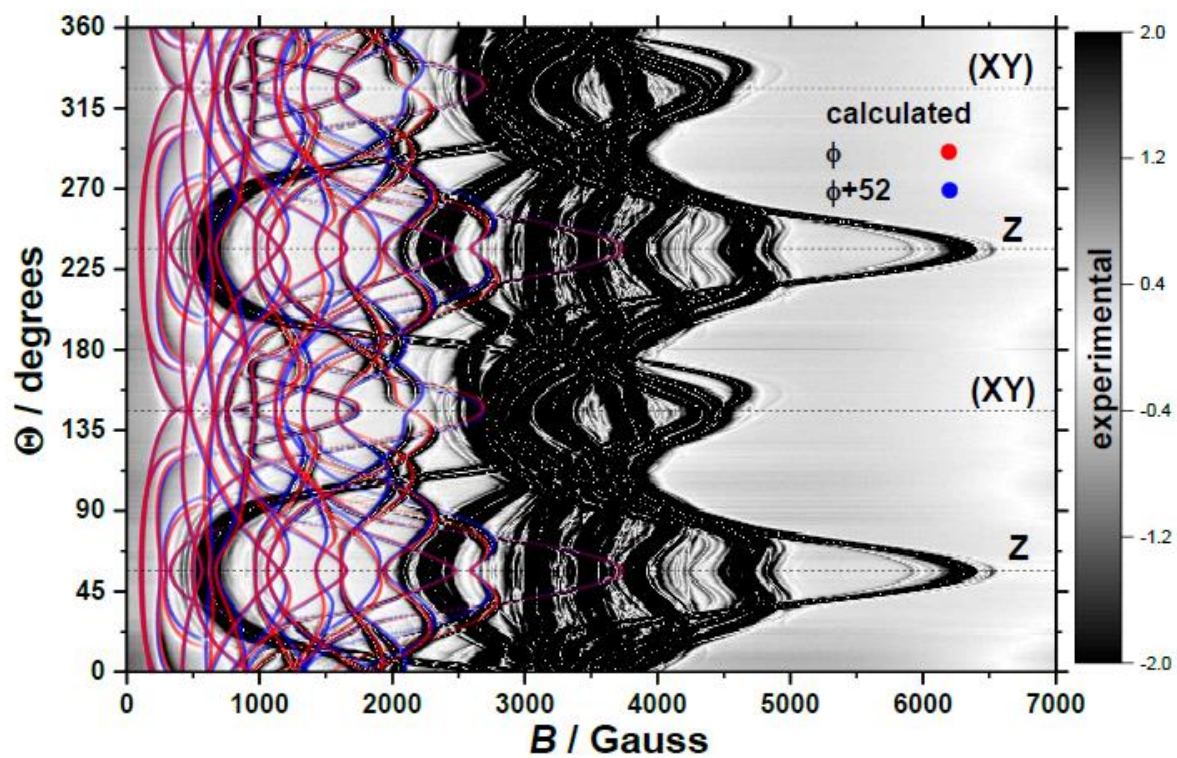


Figure S4 Angular variation of the X-band c.w.-EPR spectrum of **1** in a plane containing the C_3 axis and at 15K. Simulations concern forbidden transitions.

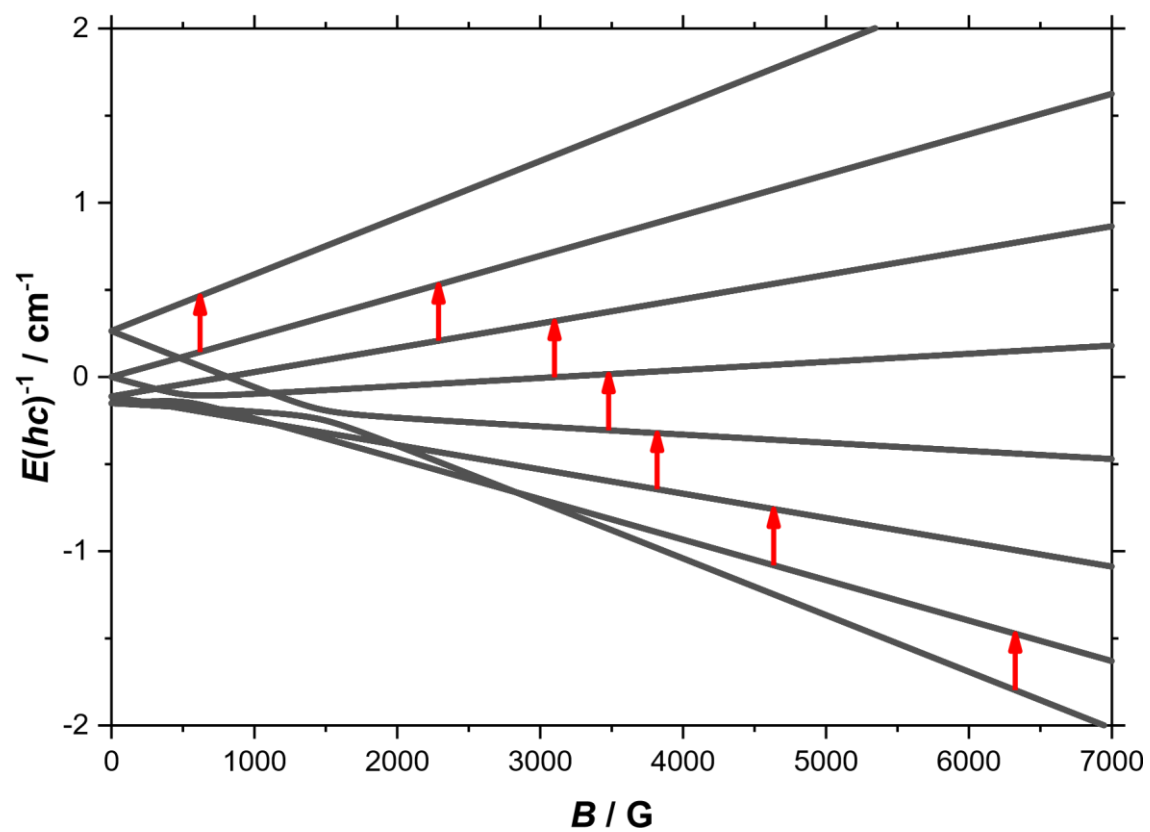


Figure S5 Energy spectrum of **1** and X-band allowed transitions (red arrows) for a magnetic field oriented along the C_3 axis.

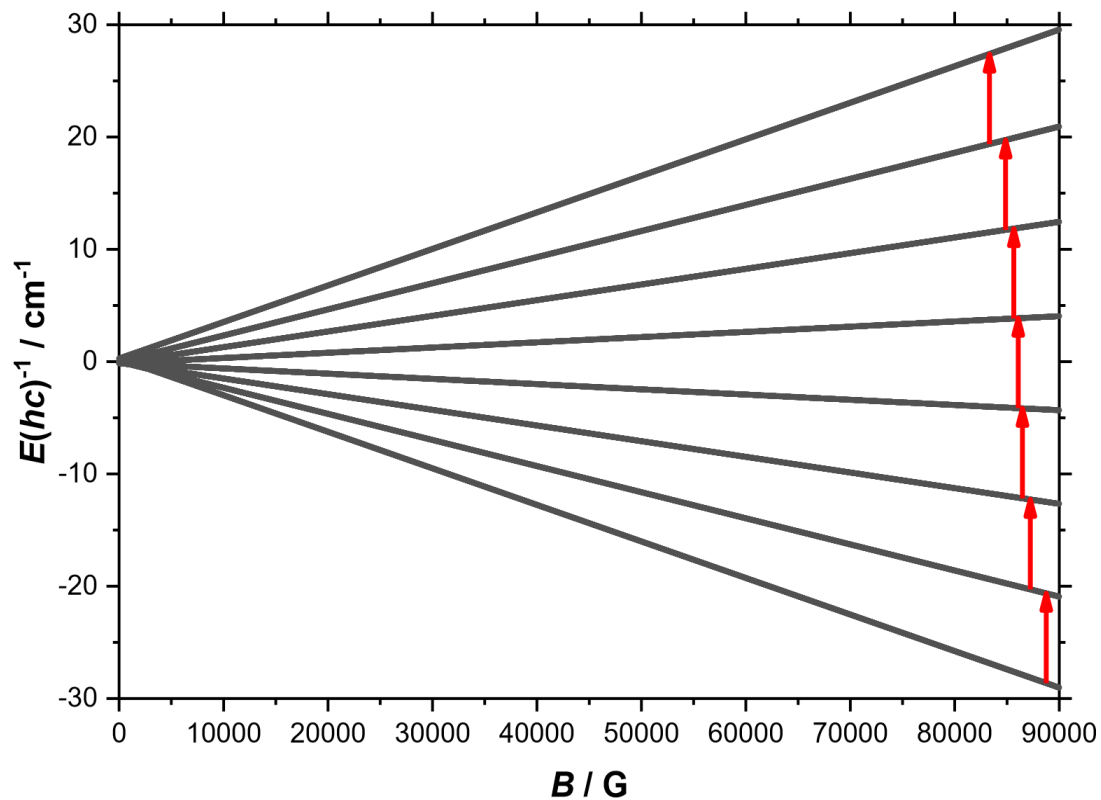


Figure S6 Energy spectrum of **1** and 240 GHz allowed transitions (red arrows) for a magnetic field oriented along the C_3 axis.

Table S3 Zero magnetic field eigenvalues and eigenvector compositions (square coefficients) in terms of $|S, m_S\rangle$ for the sublevels of the ground $^8S_{7/2}$ term of **1** obtained with the parameters in the main text.

	$E(hc) / \text{cm}^{-1}$	$\begin{vmatrix} 7 & 7 \\ 2 & 2 \end{vmatrix}$	$\begin{vmatrix} 7 & 5 \\ 2 & 2 \end{vmatrix}$	$\begin{vmatrix} 7 & 3 \\ 2 & 2 \end{vmatrix}$	$\begin{vmatrix} 7 & 1 \\ 2 & 2 \end{vmatrix}$	$\begin{vmatrix} 7 & -1 \\ 2 & -2 \end{vmatrix}$	$\begin{vmatrix} 7 & -3 \\ 2 & -2 \end{vmatrix}$	$\begin{vmatrix} 7 & -5 \\ 2 & -2 \end{vmatrix}$	$\begin{vmatrix} 7 & -7 \\ 2 & -2 \end{vmatrix}$
1⟩	-0.1512	0.0000	0.0207	0.0000	0.0000	0.9746	0.0000	0.0000	0.0047
2⟩	-0.1512	0.0047	0.0000	0.0000	0.9746	0.0000	0.0000	0.0207	0.0000
3⟩	-0.1121	0.0000	0.0000	0.0000	0.0000	0.0000	1.0000	0.0000	0.0000
4⟩	-0.1121	0.0000	0.0000	1.0000	0.0000	0.0000	0.0000	0.0000	0.0000
5⟩	-0.0001	0.0002	0.0000	0.0000	0.0205	0.0000	0.0000	0.9792	0.0000
6⟩	-0.0001	0.0000	0.9792	0.0000	0.0000	0.0205	0.0000	0.0000	0.0002
7⟩	0.2634	0.0000	0.0000	0.0000	0.0000	0.0049	0.0000	0.0000	0.9951
8⟩	0.2634	0.9951	0.0000	0.0000	0.0049	0.0000	0.0000	0.0000	0.0000

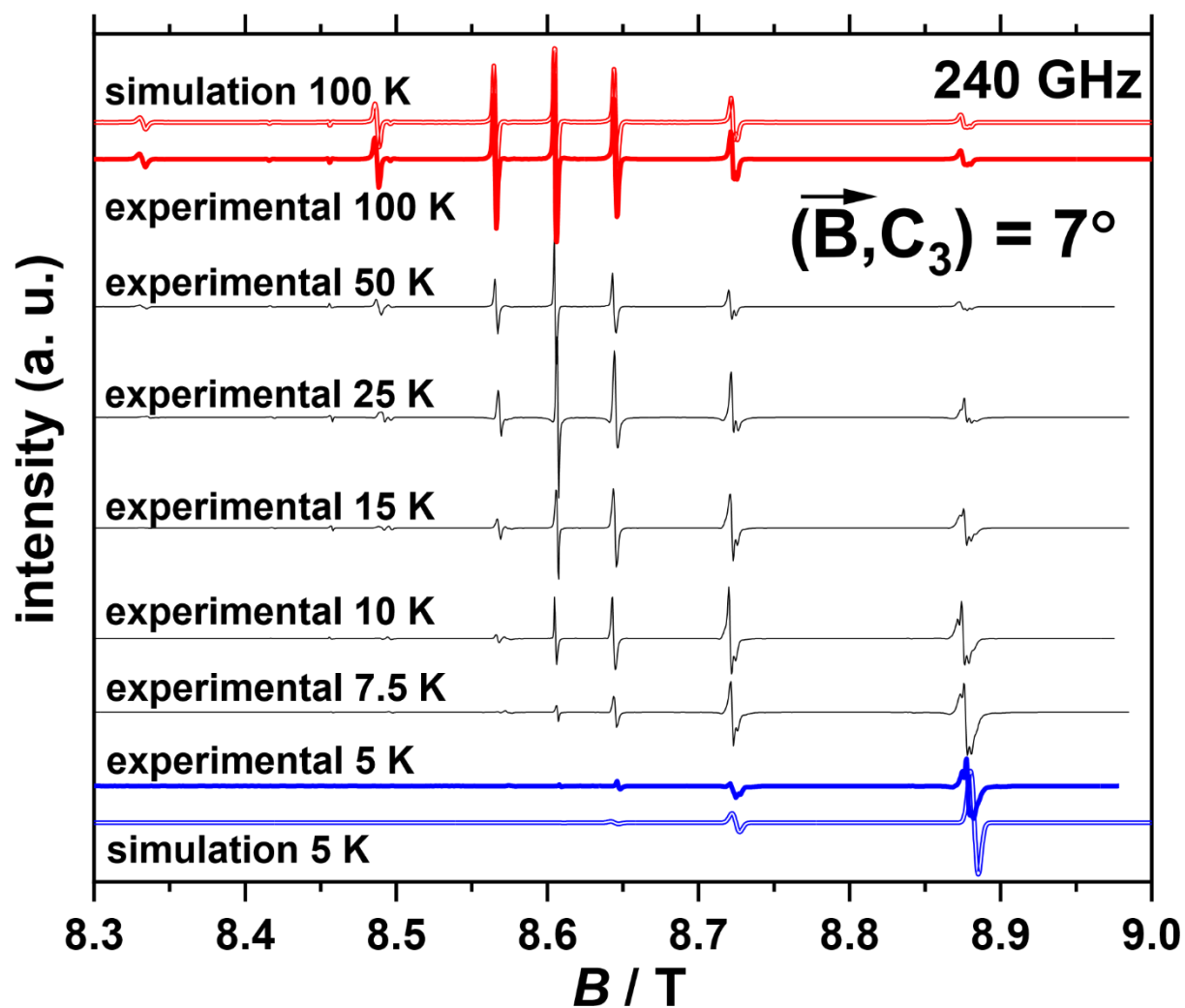


Figure S7. Variable temperature 240 GHz c.w.-EPR spectra for the determination of the relative splitting of the sublevels of the ground $^8S_{7/2}$ term of Gd(III) in **1**.

Pulsed single crystal Electron Paramagnetic Resonance

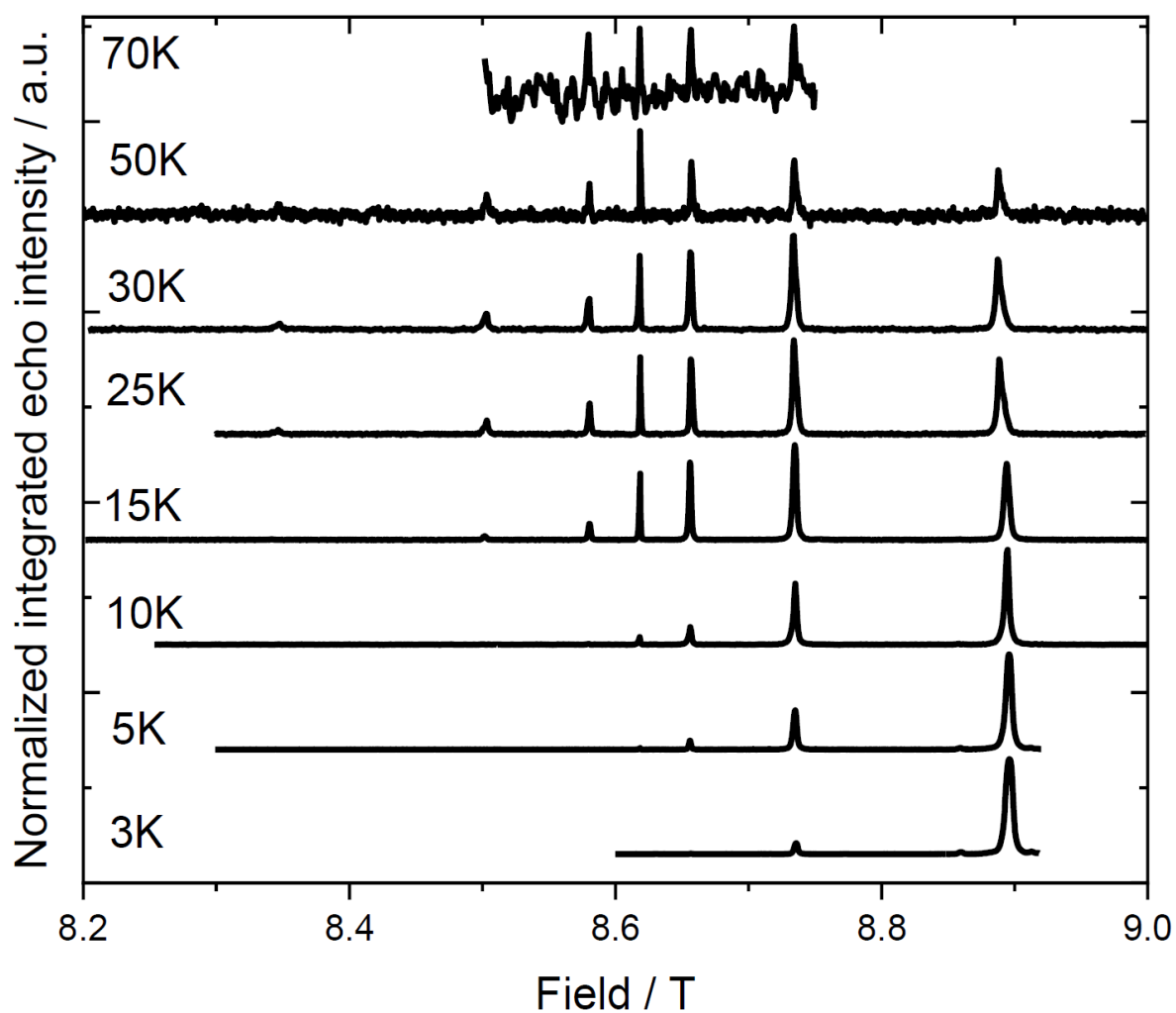


Figure S8 Temperature dependence of the 240 GHz EDFS of a single crystal of **1** measured with the magnetic field at an angle of 7 degrees to the C_3 axis.

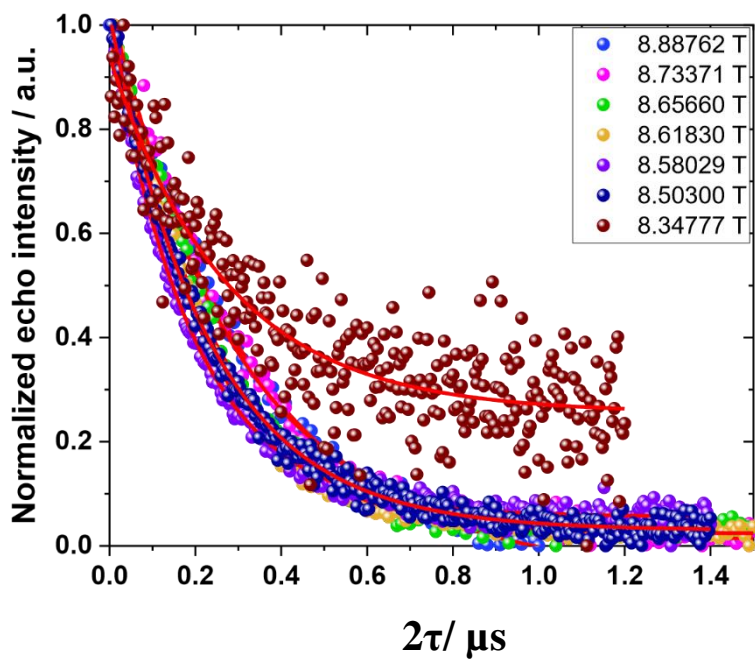


Figure S9 Normalized Hahn echo intensities (scatter) as a function of 2τ for **1** at 30 K measured at different magnetic field positions as indicated in the legend. The measurements were performed at 240 GHz. The red lines are fits to the mono-exponential described in the methods section.

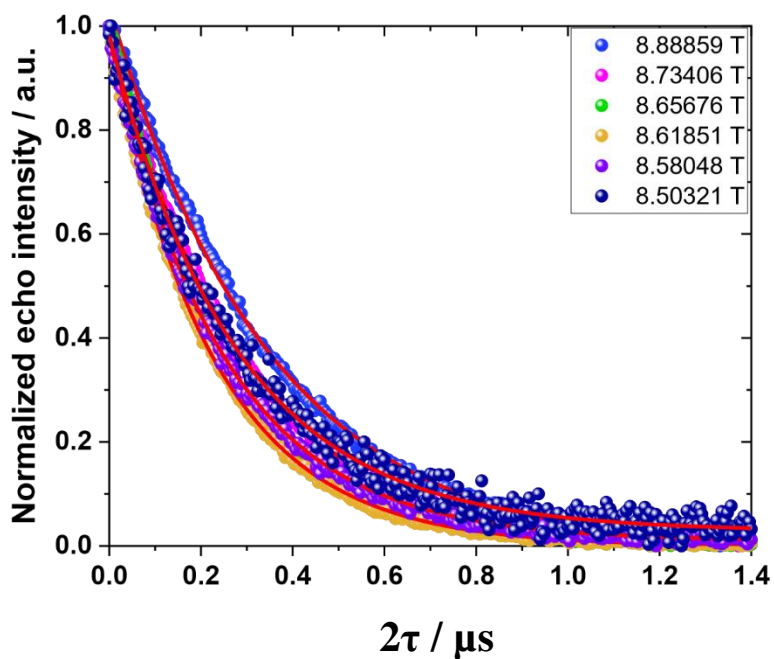


Figure S10 Normalized Hahn echo intensities (scatter) as a function of 2τ for **1** at 25 K measured at different magnetic field positions as indicated in the legend. The measurements were performed at 240 GHz. The red lines are fits to the mono-exponential described in the methods section.

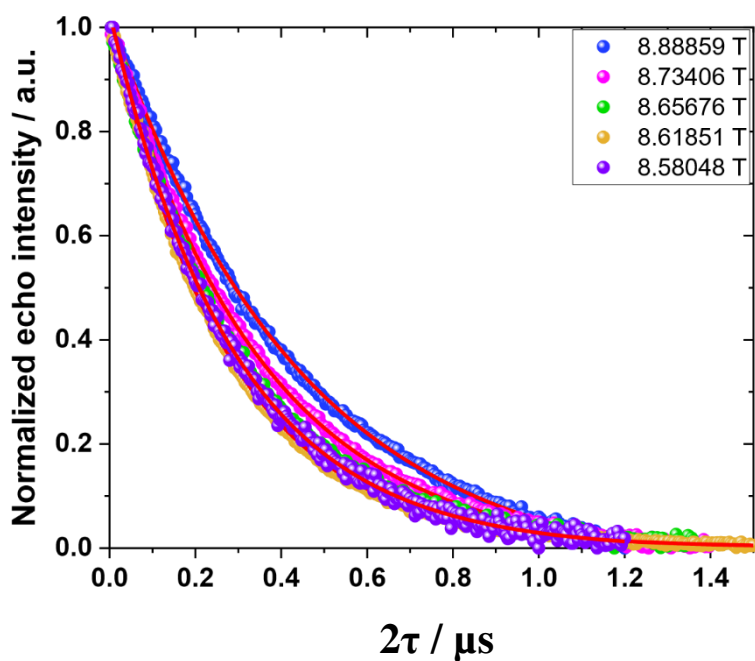


Figure S11 Normalized Hahn echo intensities (scatter) as a function of 2τ for **1** at 20 K measured at different magnetic field positions as indicated in the legend. The measurements were performed at 240 GHz. The red lines are fits to the mono-exponential described in the methods section.

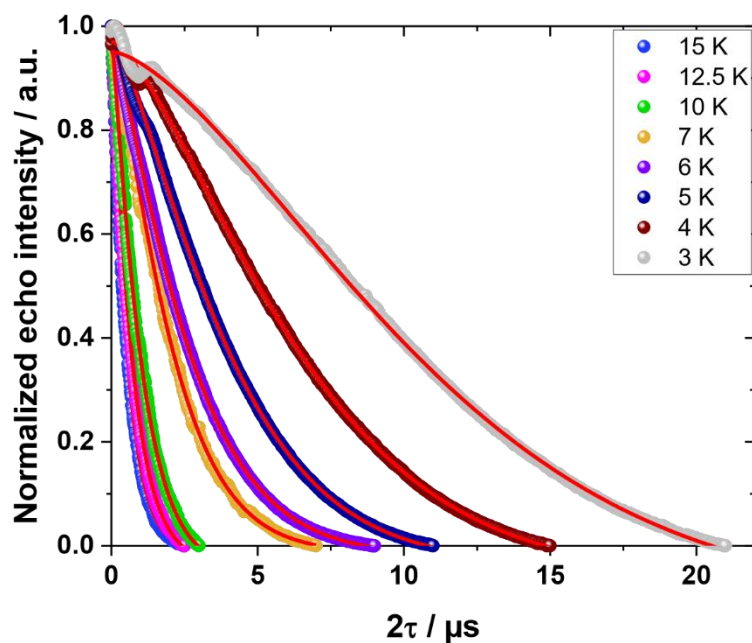


Figure S12 Normalized Hahn echo intensities (scatter) as a function of 2τ for **1** at $B = 8.89400$ T measured at different temperatures as indicated in the legend. The measurements were performed at 240 GHz. The red lines are fits to the mono-exponentials described in the methods section.

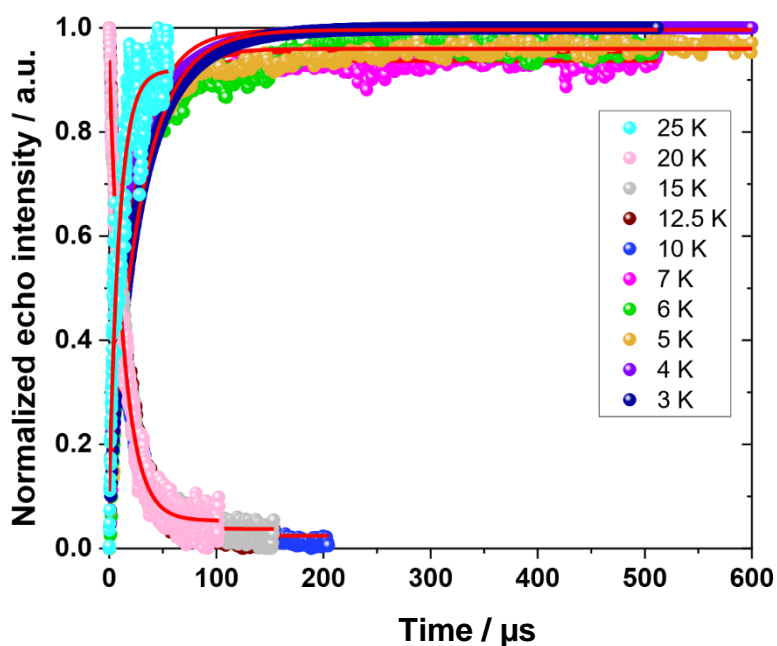


Figure S13 Normalized stimulated echo intensities (scatter) as a function of t for **1** at $B = 8.89400$ T measured at different temperatures as indicated in the legend. The measurements were performed at 240 GHz. The red lines are fits to the mono-exponentials described in the methods section.

Table S4 Extracted T_2 values with errors at different temperatures and at different magnetic fields

30 K	25 K	20 K			
B / T	T_2 / ns	B / T	T_2 / ns	B / T	T_2 / ns
8.88762	337 ± 7	8.88859	349 ± 2	8.88859	445 ± 2
8.73371	281 ± 6	8.73406	287 ± 1	8.73406	352 ± 1
8.65660	235 ± 4	8.65676	236 ± 1	8.65676	300 ± 1
8.61830	214 ± 2	8.61851	228 ± 1	8.61851	271 ± 1
8.58029	195 ± 2	8.58048	249 ± 1	8.58048	291 ± 2
8.50300	233 ± 2	8.50321	277 ± 3		
8.34777	270 ± 18				

Table S5 Extracted T_1 and T_2 values with errors measured at the transition at highest magnetic field (8.89 T) and at different temperatures.

T / K	$T_1 / \mu\text{s}$	T_2 / ns
30 K	-	337 ± 7
25 K	9.67 ± 0.3	349 ± 2
20 K	13.9 ± 0.1	445 ± 2
15 K	15.7 ± 0.1	546 ± 2
12.5 K	16.0 ± 0.1	720 ± 3
10 K	15.2 ± 0.1	$1,064 \pm 4$
7 K	17.8 ± 0.2	$2,223 \pm 8$
6 K	23.0 ± 0.3	$2,823 \pm 5$
5 K	24.1 ± 0.3	$4,303 \pm 8$
4 K	25.4 ± 0.2	$7,071 \pm 20$
3 K	29.9 ± 0.1	$12,014 \pm 48$

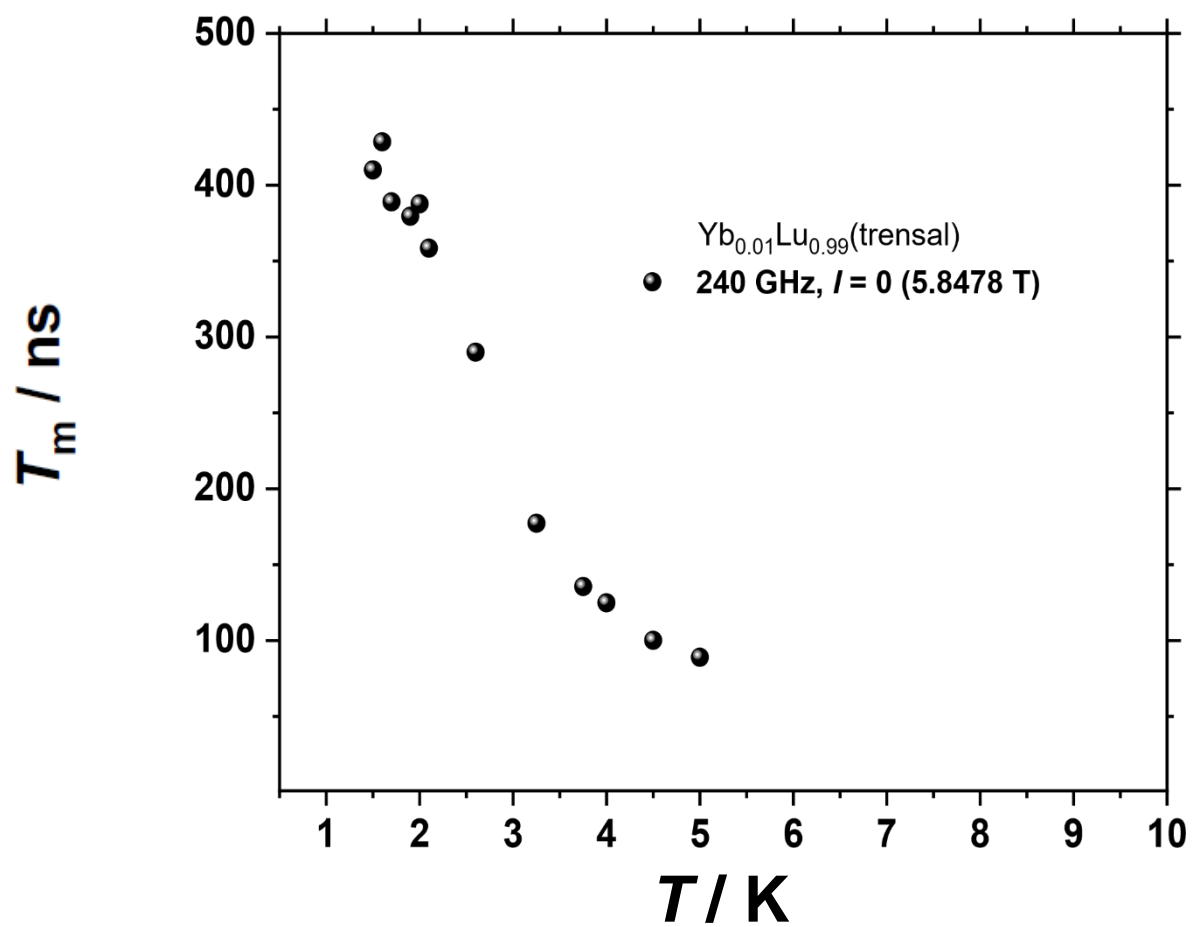


Figure S14 Temperature dependence of T_m for the $I = 0$ line of a single crystal of Yb_{0.01}Lu_{0.99}(trensai) with the magnetic field along the C_3 axis, at 240 GHz.

References

1. Vesborg, P. C.; Chorkendorff, I.; Brock-Nannestad, T.; Dethlefsen, J. R.; Bendix, J. Note: simple means for selective removal of the 365 nm line from the Hg spectrum using Dy. *Rev Sci Instrum* **2011**, 82 (9), 096102.
2. van Tol, J.; Brunel, L. C.; Wylde, R. J. A quasioptical transient electron spin resonance spectrometer operating at 120 and 240 GHz. *Review of Scientific Instruments* **2005**, 76 (7),
3. Morley, G. W.; Brunel, L. C.; van Tol, J. A multifrequency high-field pulsed electron paramagnetic resonance/electron-nuclear double resonance spectrometer. *Rev Sci Instrum* **2008**, 79 (6), 064703.
4. Pedersen, K. S.; Ungur, L.; Sigrist, M.; Sundt, A.; Schau-Magnussen, M.; Vieru, V.; Mutka, H.; Rols, S.; Weihe, H.; Waldmann, O.; Chibotaru, L. F.; Bendix, J.; Dreiser, J. Modifying the properties of 4f singleion magnets by peripheral ligand functionalisation. *Chem. Sci.* **2014**, 5 (4), 1650-1660.
5. Bruker. *Bruker AXS, Inc. SAINT, Version 7.68A; Bruker AXS: Madison, WI, 2009.*
6. Sheldrick, G. M. *SADABS, Version 2008/2; University of Göttingen: Germany, 2003.* Vol. .
7. Sheldrick, G. M. SHELXT - integrated space-group and crystal-structure determination. *Acta Crystallogr A Found Adv* **2015**, 71 (Pt 1), 3-8.
8. Sheldrick, G. M. A short history of SHELX. *Acta Crystallogr A* **2008**, 64 (Pt 1), 112-22.
9. Sheldrick, G. M. Crystal structure refinement with SHELXL. *Acta Crystallogr C Struct Chem* **2015**, 71 (Pt 1), 3-8.
10. Bourhis, L. J.; Dolomanov, O. V.; Gildea, R. J.; Howard, J. A.; Puschmann, H. The anatomy of a comprehensive constrained, restrained refinement program for the modern computing environment - Olex2 dissected. *Acta Crystallogr A Found Adv* **2015**, 71 (Pt 1), 59-75.
11. Dolomanov, O. V.; Bourhis, L. J.; Gildea, R. J.; Howard, J. A. K.; Puschmann, H. OLEX2: a complete structure solution, refinement and analysis program. *Journal of Applied Crystallography* **2009**, 42 (2), 339-341.